DEVELOPMENT OF AMBIENT IONIZATION MASS SPECTROMETRY FOR INTRAOPERATIVE CANCER DIAGNOSTICS AND SURGICAL MARGIN ASSESSMENT

by

Clint Miles Alfaro

A Dissertation

Submitted to the Faculty of Purdue University

In Partial Fulfillment of the Requirements for the degree of

Doctor of Philosophy

Department of Chemistry

West Lafayette, Indiana

May 2019

THE PURDUE UNIVERSITY GRADUATE SCHOOL
STATEMENT OF COMMITTEE APPROVAL

Dr. R. Graham Cooks, Chair

    Department of Chemistry

Dr. Kavita Shah

    Department of Chemistry

Dr. Garth J. Simpson

    Department of Chemistry

Dr. Julia Laskin

    Department of Chemistry

Approved by:

    Dr. Christine A. Hrycyna

      Head of the Graduate Program

This dissertation is dedicated to those that contributed to my success and continue to light my way: my family, friends, mentors, and mentees

ACKNOWLEDGMENTS

I am indebted to the surgical teams of the Goodman Campbell Brain and Spine Neurosurgeons; Dr. Mahua Dey, Dr. Charles Kulwin, Dr. James Miller, Dr. Troy Payner, Dr. Mitesh Shah, Dr. Scott Shapiro, are gratefully acknowledged for continuing contributions to our DESI-MS study. Our study could not have progressed if not for the efforts of the neurosurgeons that balanced research time in addition to fulfilling their clinical duties. The extraordinary time and effort dedicated to our project is greatly appreciated.

The support provided by the Indiana Clinical and Translational Sciences Institute is greatly appreciated. The pre-doctoral training program has provided me with complementary experiences that have enriched my graduate school experience and will benefit my scientific career. I am emerging from Purdue with a solid background in analytical chemistry, and the ICTSI introduced me to clinical translational science, and I hope to continue working at the interface of these fields for years to come.

Thank you to my graduate school friends, Sam and Stacey Ewan, Susie and Matt Banziger, Emilio Cárdenas, Stevie Norcross, and Spencer Gardeen for helping keep me centered. Thank you to my North Carolina friends for keeping contact with me. I am grateful to see some of you during the Holidays and hope we can all grow happy and old together.

I am extremely grateful for the support from my undergraduate research advisor, Prof. Nadja Cech, for being an inspiring scientist, mentor, role model, and friend. I would not be studying mass spectrometry or writing this dissertation if not for your contagious enthusiasm. Your ability to inspire your students is an amazing skill that I hope to adopt in my career.

I am incredibly grateful for the support from my family in pursuing my career goals. My parents, Sonia and Michael Alfaro, provide unwavering moral support and convince me that I can achieve anything despite how difficult the journey may be. My grandparents, Flor and Carlos Garayar, give me constant reassurance and remind me that I am valued. Thank you to Joe and Michelle Soler, and Patti and Toby Bunton for your encouragement.

I am thankful for Joshua Mazur for encouraging me to do well and being a constant pillar of support. My time in graduate school would have been much more difficult if I did not have you by my side. You have helped me to become a more confident and happier person. I'm proud to be with you and hope that our love never ends.

TABLE OF CONTENTS

LIST OF TABLES

LIST OF FIGURES

ABSTRACT

Author: Alfaro, Clint, M. PhD
Institution: Purdue University
Degree Received: May 2019
Title: Development of Ambient Ionization Mass Spectrometry for Intraoperative Cancer Diagnostics and Surgical Margin Assessment
Committee Chair: R. Graham Cooks

Advancements in cancer treatments have increased rapidly in recent years, but cures remain elusive. Surgical tumor resection is a central treatment for many solid malignancies. Residual tumor at surgical margins leads to tumor recurrence. Novel tools for assessing residual tumor at surgical margins could improve surgical outcomes by helping to maximize the extent of resection. Ambient ionization-mass spectrometry (MS) methods generate and analyze ions from minimally prepared samples in near-real-time (e.g. seconds to minutes). These methods leverage the high sensitivity and specificity of mass spectrometry for analyzing gas phase ions and generating those ions quickly and with minimal sample preparation. Recent work has shown that differential profiles of ions, corresponding to phospholipids and small metabolites, are detected from cancerous and their respective normal tissue with ambient ionization-MS methods. When properly implemented, ambient ionization-MS could be used to assess for tumor at surgical margins and provide a molecular diagnosis during surgery.

The research herein reports efforts in developing rapid intraoperative ambient ionization-MS methods for the molecular assessment of cancerous tissues. Touch spray (TS) ionization and desorption electrospray ionization (DESI) were utilized to analyze kidney cancer and brain cancer.

As a demonstration of the applicability of TS-MS to provide diagnostic information from fresh surgical tissues, TS-MS was used to rapidly analyze renal cell carcinoma and healthy renal tissue biopsies obtained from human subjects undergoing nephrectomy surgery. Differential phospholipid profiles were identified using principal component analysis (PCA), and the significant ions were characterized using multiple stages of mass spectrometry and high resolution/exact mass MS. The same TS-MS analyzed renal tissues were subsequently analyzed with DESI-MS imaging to corroborate the TS-MS results, and the significant DESI-MS ions were also characterized with MS.

Significant efforts were made in developing and evaluating a standalone intraoperative DESI-MS system for analyzing brain tissue biopsies during brain tumor surgery. The intraoperative DESI-MS system consists of a linear trap quadrupole mass spectrometer placed on a custom-machined cart that contains all hardware for operating the mass spectrometer. This instrument was operated in the neurosurgical suites at Indiana University School of Medicine to rapidly analyze brain tissue biopsies obtained from glioma resection surgeries. A DESI-MS library of normal brain tissue and glioma was used to statistically classify the brain tissue biopsies collected in the operating room. Multivariate statistical methodologies were employed to predict the disease state and tumor cell percentage of the samples. A DESI-MS assay for detecting 2-hydroxyglutarate (2HG), the oncometabolic product of the isocitrate dehydrogenase (IDH) mutation (a key glioma prognostic marker), was developed and applied to determine the IDH mutation status during the surgical resection. The strengths, weaknesses, and areas of future work in this field are discussed.

CHAPTER 1.   INTRODUCTION

1.1   Research Objectives

My PhD research has focused on the development of ambient ionization mass spectrometry (MS) methods for diagnosing human tissue biopsies during cancer removal surgery. Our goal has been to acquire rapid chemical information from the tissue that correlates with the tissue disease state and, using informatics and statistical approaches, effectively translate the acquired data into actionable knowledge that can be used by clinicians to improve patient care and outcome. Diagnostic information that can assess the amount of residual tumor present in biopsies from the suspected tumor margin could allow for the surgeon to approach complete removal of the tumor, which corresponds to better patient survival. Current intraoperative cancer diagnosis and margin assessment is performed with histopathological evaluation of hematoxylin and eosin (H&E) stained tissue sections. The relatively low accuracy of this approach, poor relationship between tissue morphology and prognosis, and low throughput, makes it inappropriate for margin assessment in some cancers (e.g. glioma, a type of brain cancer). A significant gap in intraoperative diagnostics could be filled by a rapid molecular assessment of tissue biopsies during surgical resection. I've investigated three types of cancers during my PhD work: renal cell carcinoma (a kidney cancer), oral squamous cell carcinoma (a head and neck cancer) and glioma. Most of my research has focused on gliomas, and several dissertation chapters (3-5) are dedicated to these works. The following introductory sections discuss pertinent background information.

1.2   Ambient Ionization Mass Spectrometry

Mass spectrometry is a highly sensitive technique for detecting and quantifying molecules present in complex samples. In MS, molecules present in a sample are ionized and transferred to the gas phase and analyzed in the low-pressure regions ($< 10^{-5}$ Torr) of the mass analyzer to determine the ion mass-to-charge ratio (*m/z*). The dynamic range of conventional MS systems is typically 10^3 to 10^6, reported limits of detection in biological samples can be sub-parts-per-billion, over 10^3 chemical features can be detected in a single analysis, and the analysis time of the MS is remarkably short (typically milliseconds/scan). A significant limitation to the speed of the MS is

the time required for sample preparation, and whether an online chemical separation technique (e.g. high-performance liquid chromatography) is performed.

Ambient ionization methods generate gas phase ions for MS analysis under normal conditions of atmospheric pressure and temperature, and with little to no sample preparation. Generally, these methods provide rapid molecular information, and many have surface analysis capabilities, permitting the design and execution of novel experiments that could not be performed with conventional ionization methods.(1) The first of these methods was desorption electrospray ionization (DESI), invented and reported in 2004 by Prof. Cooks' group at Purdue University.(2) In DESI, a stream of charged (~5kV) solvent microdroplets are sprayed onto a sample surface. The droplets form a thin liquid film on the sample surface, extracting molecules that are then splashed by subsequent droplet impacts, ionized via electrospray-like mechanisms, and analyzed by the mass spectrometer (Figure 1).
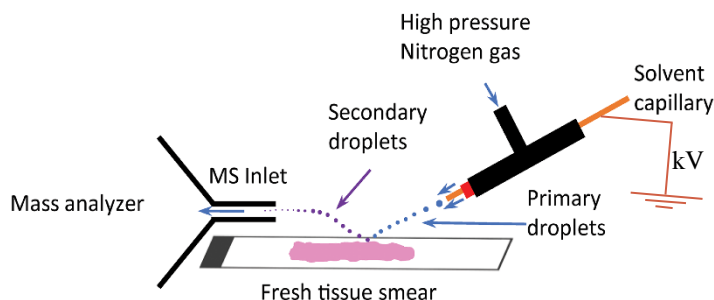
Figure 1.1 Illustration of desorption electrospray ionization. Modified from Alfaro et al. 2019 with permission.(2)

DESI-MS has been used by many investigators for qualitative and quantitative analyses. Representative analytes of interest include explosives, illicit drugs, food contaminants, metabolites, lipids, and proteins.(3-5) The wide range of detectable analytes, and the relative simplicity of the experiment, make DESI a powerful method for rapid chemical analysis. DESI has been used to do chemical imaging by moving the sample underneath the DESI spray with a precision moving stage. Correlating the raster speed of the moving stage with the MS acquisition time allows for the collection of discrete mass spectra from specific sample positions. The MS data is combined to generate an image, containing two dimensions of spatial coordinates (x,y) and a dimension of m/z variables and corresponding MS intensities that can contain thousands of elements.(6)

An additional ambient ionization method utilized in my work is touch-spray ionization (TS).(7) In this method, a solid or porous probe is used to contact and collect a small amount of sample (on the order of 1mg or less). The probe is then directed towards the interface of the mass spectrometer; solvent and high-voltage are applied to generate a Taylor cone and associated electrospray plume. With solid metal probes, the spray phenomenon lasts for only a few seconds during which MS signals can be detected.(8) With porous probes, such as medical swabs, the spray plume may last for several minutes over which MS signals can be detected.(9) TS is rapid, and the small sample requirement is amenable to *in vivo* sampling.

There are many other ambient ionization methods, developed in a range of laboratories, and widely cited examples include direct analysis in real time (DART),(10) laser ablation electrospray ionization (LAESI),(11) rapid evaporative ionization (REIMS),(12) and probe electrospray ionization (PESI).(13)

1.3   Metabolomics and Lipidomics for Disease Diagnosis

In biological systems, the flow of genetic information into phenotype proceeds from DNA, which is transcribed into RNA; RNA, which is translated into proteins; and proteins, specifically enzymes, catalyze the myriad biochemical transformations required to maintain organism homeostasis, and support growth, development, and reproduction. Mutations in DNA are propagated into altered RNA transcripts, and if in a protein coding region, lead to altered proteins that may produce altered profiles of metabolic pathway intermediates.

So called omics approaches aim to profile the complete population of a given class of molecular entities. Genomics seeks to profile all nucleic acids and proteomics covers the realm of proteins. The omics approaches of interest in my research are metabolomics and lipidomics, which encompass the small molecule and hydrophobic moiety bearing, respectively, complements of biochemistry.(14)

Metabolomics and lipidomics, a sub-field of metabolomics, are emerging fields that have been largely enabled by improvements in mass spectrometry instrumentation and expertise. These approaches have been applied to characterize many diseases, especially cancer.(15) Cancer cells adopt a unique metabolic phenotype due to the genetic alterations accumulated through mutations in key cell pathways involved in cell division, angiogenesis, and cell differentiation, among others.(16) The increased demand for energy for cell division, the lack of cell specialization to

perform normal functions, and the generally lower oxygen concentrations, all alter molecular fluxes in key metabolic pathways. Lipid synthesis and degradation is integral to many of these key metabolic pathways. Also, new cells require phospholipids, ceramides, cholesterol, and other complex lipids to create new lipid membranes. It has been hypothesized that metabolomic and lipidomic approaches applied to the study of disease could provide new insight into disease processes, diagnostics, prognostics, and response to treatment.(17) While DNA sequencing provides insight into genotype, it does not accurately reflect the phenotype. Metabolites and lipids are more directly involved in generating phenotypic effects, and their accurate profiling by mass spectrometry should provide a more accurate assessment of phenotype that would complement genotypic and other phenotypic measurements.(17)

Typical mass spectrometry-based metabolomics experiments measure the intensity of thousands of ions derived from the molecules present in a large set of samples. Samples that cover the relevant healthy condition as well as the diseased condition(s) must be analyzed and then compared. These experiments result in large amounts of data that must be handled with informatics techniques and analyzed using statistical approaches. Some of these statistical approaches will be discussed in the next section.

1.4   Statistical Approaches for Interpreting Metabolomic and Lipidomic Data

Typical metabolomic datasets from a single sample contain thousands of mass spectra, and each mass spectrum can be represented as a [2 x n] matrix, where n is $> 10^3$, one row corresponding to m/z values and the other row corresponding to detected intensities. Informatics approaches are utilized to compile the raw data into structures and matrices that can be analyzed subsequently with statistical methods. Metabolomic and lipidomic data are analyzed statistically in order to draw conclusions about the relationship between the intensity of specific detected m/z and the nature (e.g. disease state, age, drug treatment) of the analyzed samples. To increase statistical validity, large numbers of samples must be analyzed to obtain meaningful results. Further, the choice of statistical analysis must be matched with the experiment conducted and the research goals.

Multivariate procedures are predominant in this field to capitalize on the high number of responses (the MS intensities detected at specific m/z values) that can be reliably detected by mass spectrometry. More sophisticated conclusions regarding the relationship between the samples and the pattern of responses can be deduced and inferred with multivariate methods. Most multivariate

procedures require pre-processing of the data, such as normalization and mean-column centering (subtracting the mean value of each variable from each observation), in order to provide valid results.(18) Parametric procedures (e.g. simple linear regression) require further assumptions regarding the underlying distributions of the data, the homoscedasticity of the residuals (residuals are constant for all values of the independent variable), low multicollinearity of the variables (model variables are not highly correlated), and variance distributions (usually normally distributed) to be met for the statistical results to be reliable.

Unsupervised multivariate methods are used to explore the datasets in an unbiased way, without informing the algorithm to what classes the samples belong (e.g. normal or diseased). In contrast, supervised methods inform the algorithm the classifications of the samples, and they attempt to find differences between the known classes within the dataset. Unsupervised and supervised methods are often combined to learn something about a set of data, and then apply that knowledge to predict the classes of new samples in a more robust way.

The primary unsupervised multivariate approach utilized in my research is principal component analysis (PCA). PCA is a dimensionality reduction technique and provides easy to interpret visual outputs on how groups of samples cluster or separate in high-dimensional space (e.g. visualize similarities and differences). The objective of PCA is to find the eigenvalues and eigenvectors of the data covariance matrix. The data is arranged in a [i x j] matrix; each row i is a sample, and each column j is a different variable. In our case, the variables are each of the *m/z* values and associated MS intensities detected in the metabolomics experiment. PCA shifts the origin of the data set to the response hyperplane having the highest variation (covariance), referred to as a principal component (PC) 1, and each additional axis, PC 2 to PC n, is orthogonal and uncorrelated with the previous axis. The calculated eigenvectors are linear combinations of the original variables, referred to as the loadings. The eigenvalues represent the length of the eigenvectors, which describes the variance explained by that eigenvector (or PC). When the loading matrix, composed of eigenvectors, is multiplied by the data, the resulting matrix is referred to as the scores (the projection of the original data on the new PC coordinate system).(18)

Each sample will result with one score for each calculated PC; typically, only a few PCs are needed to explain most of the variation in the data. The fact that most of the variance in the dataset can be recapitulated with only a few PC variables is the basis of the variable reduction properties of PCA. The calculated PCs with low eigenvalues have low variance, can usually be excluded

without sacrificing much information content present in the dataset. This is advantageous in metabolomics experiments in which thousands of variables are measured, but only a few may be significantly different between sample groups. This reduces the number of variables in the data, from thousands of *m/z* to just a few useful principal components, that can be used in subsequent statistical procedures. The output of PCA, the loading matrix, can be used to project new samples into the calculated PC space.(18)

The primary supervised multivariate approach utilized in my research is linear discriminant analysis (LDA). LDA differs from PCA in that the classifications of the samples are input into the algorithm, and the analysis finds linear combinations of the input variables that maximize the difference between known groups of samples. This contrasts with PCA in which the largest variances in the data are found without prioritizing differences between the sample classes. The linear combinations of variables correspond to eigenvalues of the input data and are referred to as linear discriminants (LD). Several LDs can be utilized to separate the samples and maximally discriminate between them. Due to this aspect of the method, LDA is more prone to overfitting than PCA. Overfitting refers to statistical models that perform very well on one data set but perform poorly on new data sets.(18) Overfit models include effects derived from noise and factors other than the main effects of interest, which introduces bias. Performing PCA on a dataset first and using the PC scores as variables for LDA instead of the raw data, reduces the chance of model overfitting(64).

Other statistical strategies are used in certain chapters and will be discussed there in more detail.

1.5   Molecular Cancer Diagnostics and Surgical Margin Assessment

Cancer diagnosis increasingly relies on molecular factors to adequately predict disease prognosis.(19) Genetic subtyping of cancers has increased the accuracy with which clinicians can predict patient response to treatment and survival times. Growing bodies of research show that the molecular subtyping of malignant tumors provide a much greater ability to predict patient outcome than just the location of the tumor (e.g. organ) or the morphology of the cells.(19) Personalized medicine initiatives are on the rise in matching specific patient's tumors to treatment strategies that would most likely produce the largest survival benefit.(20) However, these predictions are still limited and often patient response to treatment is still guided by clinical experience.

Medical imaging, such as magnetic resonance imaging (MRI) and computed tomography (CT), are key in identifying the location of tumors and guiding interventions and treatments. In order to definitively diagnose a malignancy, analysis of a tissue biopsy must be performed. The biopsy procedure can be minimally invasive, such as a fine needle aspirate from a lymph node, or may be more complicated and require open surgery, such as a biopsy for a brain tumor inside the skull. With either approach, molecular diagnostics are typically not performed while the tissue biopsy is being taken. In some cases, an intraoperative frozen section is prepared from the biopsied tissue, H&E stained, and analyzed by a histopathologist for tumor content.(21) However, morphology alone does not provide enough evidence for a final diagnosis or prognosis. Molecular techniques, such as genetic sequencing, immunohistochemistry, and fluorescence in-situ hybridization, are all performed on biopsied tissue post-operatively, as they are time consuming procedures that must be performed in controlled laboratory environments.

The capability to provide a complete molecular diagnosis during the biopsy procedure could improve patient treatment. Mass spectrometry-based assays are heavily applied to analyze biopsied tissue in research laboratories, but there are no FDA approved MS-based clinical tests for cancer tissue diagnostics. Research on these applications has been ongoing since 2005, with the frequency of publications increasing significantly in recent years (Table 1.1).

Many types of cancers are treated with surgical tumor resection. In most cases, gross total resection provides a significant survival benefit to the patient.(22) The capability to cure localized malignancies is contingent on complete microscopic removal of the tumor. Currently, assessments of microscopic tumor removal are performed using serial frozen section histology, a cumbersome and at times inaccurate approach. Ambient ionization-MS approaches, the focus of my dissertation research, provide an innovative approach to assessing residual tumor in biopsied tissue obtained from surgical margins. If reliable molecular signatures of tumors can be rapidly profiled with ambient ionization-MS and accurately classified with multivariate statistical approaches, then molecular tissue diagnostics could be offered during the tumor biopsy procedure. The advanced development of these technologies could significantly improve patient care and management.

1.6 Applications of Ambient Ionization-MS in Point-of-Care Cancer Diagnostics

Point-of-care diagnostics refers to performing rapid laboratory tests at the clinic with the patient present, rather than sending a patient sample to a centralized laboratory for analysis (which

takes hours to days).(23) Point-of-care tests have several advantages, such as rapid results for more informed treatments, reduction in backlog created from centralized laboratories, and improved patient care. They also permit development of *in vivo* diagnostics, which are performed directly on the patient, which is in stark contrast to conventional lab tests which are inherently *in vitro*, analyzing samples obtained from the patient in a laboratory at a distant location.

Table 1.1 Chronology of ambient ionization-MS applications to cancerous tissues.

Year	Abbreviated Title	Year	Abbreviated Title
2005	DESI-MS analysis of liver adenocarcinoma(24)	2016	Lipid and metabolite profiles of human brain tumors by DESI-MS(25)
2009	DESI-MS analysis of cancerous breast tissue(6)	2016	Ambient ionization MS analysis of fresh surgical renal tissues(8)
2009	Lipid profiling of canine bladder carcinoma by DESI-MS(26)	2016	RIR-LA for human ovarian cancer(27)
2010	Tissue analysis by REIMS(12)	2016	Human ovarian tumors by REIMS (iKnife)(28)
2010	Human astrocytomas by DESI-MS(29)	2016	Human pancreatic cancer margins by DESI-MS(30)
2010	Renal cell carcinomas by DESI-MS(31)	2017	Human lung tumors by DAPCI-MS(32)
2010	DESI-MS imaging of cholesterol sulfate in prostate cancer(33)	2017	Human colorectal cancer with REIMS (iKnife)(34)
2011	Germ-cell cancer by DESI-MS lipid profiling(35)	2017	Human breast cancer with REIMS (iKnife)(36)
2011	Multivariate statistics and DESI-MS lipid profiling of human bladder cancer(37)	2017	Metastatic breast and thyroid cancer in lymph nodes by DESI-MS(38)
2012	Human brain tumors by DESI-MS imaging(39)	2017	Serous ovarian cancer aggressiveness by DESI-MS(40)
2012	Colorectal tumors by DESI-MS(41)	2017	Human breast, lung, thyroid and ovary cancer by MasSpec Pen(42)
2013	DESI-MS imaging of human brain tumors(43)	2017	Intraoperative DESI-MS of brain tumor margins during glioma resection(44)
2013	Intraoperative tissue analysis by REIMS(45)	2017	Human gliomas by swab touch spray-MS(46)
2014	Lipid profiles of lymphoma subtypes by DESI-MS(47)	2017	Human oral cancer by DESI-MS imaging(48)
2014	Human meningiomas by DESI-MS(49)	2018	DESI-MS for bladder cancer in canines(50)
2014	Breast cancer margins by DESI-MS(51)	2018	Human ovarian cancer with REIMS (iKnife)(52)
2014	Oncometabolite, 2HG, detection by DESI-MS(53)	2018	Multi-center DESI-MS for breast cancer diagnosis(54)
2014	Human gastric cancer margins by DESI-MS(55)	2019	Point of care tissue analysis with mini-MS(56)
2014	Lipid profiling of lymphoma by DESI-MS(57)	2019	MasSpec Pen for human ovarian cancer(58)
2015	Prostate cancer by DESI-MS(59)	2019	Intraoperative IDH status in gliomas with DESI-MS(60)
2015	Gastrointestinal cancer by REIMS(61)	2019	IDH status in gliomas on mini-MS(62)

A significant limitation in current point-of-care diagnostics is the loss in analytical (e.g. detection limits) and clinical (e.g. diagnostic sensitivity and specificity) performance compared to conventional laboratory tests. Ambient ionization-MS methods provide opportunities for point-of-care testing due to the speed and accuracy of the methods. The capability to diagnose pathologies at the clinic using MS based methods could improve patient care.

The research presented in this dissertation was focused on developing ambient ionization mass spectrometry-based methods that could be utilized in the operating room for cancer diagnosis and surgical margin assessment. Implementation of cancer diagnostics during surgery could improve surgical outcomes, extent of resection, reduce surgery time, and increase treatment efficiency.(63) The research reported in Chapters 2-5 was performed on conventional benchtop mass spectrometers, which are large (approx. 4 ft^3) and heavy (approx. 300 lbs). Recent advances in miniature mass spectrometers could reduce the footprint and ease of implementation, if the instruments retain adequate analytical and clinical performance.

1.7   References

1. Venter A, Nefliu M, Cooks RG. Ambient desorption ionization mass spectrometry. TrAC Trends in Analytical Chemistry. 2008;27(4):284-90.

2. Takats Z, Wiseman JM, Gologan B, Cooks RG. Mass Spectrometry Sampling Under Ambient Conditions with Desorption Electrospray Ionization. Science. 2004;306:471-3.

3. Talaty N, Mulligan CC, Justes DR, Jackson AU, Noll RJ, Cooks RG. Fabric analysis by ambient mass spectrometry for explosives and drugs. Analyst. 2008;133(11):1532-40.

4. Garza KY, Feider CL, Klein DR, Rosenberg JA, Brodbelt JS, Eberlin LS. Desorption Electrospray Ionization Mass Spectrometry Imaging of Proteins Directly from Biological Tissue Sections. Anal Chem. 2018;90(13):7785-9.

5. Eberlin LS, Ferreira CR, Dill AL, Ifa DR, Cooks RG. Desorption electrospray ionization mass spectrometry for lipid characterization and biological tissue imaging. Biochimica et Biophysica Acta (BBA)-Molecular and Cell Biology of Lipids. 2011;1811(11):946-60.

6. Dill AL, Ifa DR, Manicke NE, Ouyang Z, Cooks RG. Mass spectrometric imaging of lipids using desorption electrospray ionization. Journal of chromatography B, Analytical technologies in the biomedical and life sciences. 2009;877(26):2883-9.

7. Kerian KS, Jarmusch AK, Cooks RG. Touch spray mass spectrometry for in situ analysis of complex samples. Analyst. 2014;139:2714-20.

8. Alfaro CM, Jarmusch AK, Pirro V, Kerian KS, Masterson TA, Cheng L, et al. Ambient ionization mass spectrometric analysis of human surgical specimens to distinguish renal cell carcinoma from healthy renal tissue. Analytical and bioanalytical chemistry. 2016;408(20):5407-14.

9. Pirro V, Llor RS, Jarmusch AK, Alfaro CM, Cohen-Gadol AA, Hattab EM, et al. Analysis of human gliomas by swab touch spray-mass spectrometry: applications to intraoperative assessment of surgical margins and presence of oncometabolites. Analyst. 2017.

10. Cody RB, Laramee JA, Durst HD. Versatile new ion source for the analysis of materials in open air under ambient conditions. Anal Chem. 2005;77(8):2297-302.

11. Nemes P, Vertes A. Laser ablation electrospray ionization for atmospheric pressure molecular imaging mass spectrometry. Methods in molecular biology (Clifton, NJ). 2010;656:159-71.

12. Balog J, Szaniszlo T, Schaefer KC, Denes J, Lopata A, Godorhazy L, et al. Identification of biological tissues by rapid evaporative ionization mass spectrometry. Anal Chem. 2010;82(17):7343-50.

13. Hiraoka K, Nishidate K, Mori K, Asakawa D, Suzuki S. Development of probe electrospray using a solid needle. Rapid Communications in Mass Spectrometry. 2007;21(18):3139-44.

14. Schneider MV, Orchard S. Omics technologies, data and bioinformatics principles. Methods in molecular biology (Clifton, NJ). 2011;719:3-30.

15. Warburg O. On the Origin of Cancer cells. Science. 1956;123(3191):309-14.

16. Collins RRJ, Patel K, Putnam WC, Kapur P, Rakheja D. Oncometabolites: A New Paradigm for Oncology, Metabolism, and the Clinical Laboratory. Clin Chem. 2017.

17. Fiehn O. Metabolomics - the link between genotypes and phenotypes. Plant Molecular Biology. 2002;48(1-2):155-71.

18. Bro R, Smilde AK. Principal component analysis. Anal Methods. 2014;6:2812-31.

19. Louis DN, Perry A, Reifenberger G, von Deimling A, Figarella-Branger D, Cavenee WK, et al. The 2016 World Health Organization Classification of Tumors of the Central Nervous System: a summary. Acta Neuropathol. 2016;131(6):803-20.

20. Hamburg MA, Collins FS. The Path to Personalized Medicine. New England Journal of Medicine. 2010;363(4):301-4.

21. Babshet M, Nandimath K, Pervatikar S, Naikmasur V. Efficacy of oral brush cytology in the evaluation of the oral premalignant and malignant lesions. J Cytol. 282011. p. 165-72.

22. D'Amico RS, Englander ZK, Canoll P, Bruce JN. Extent of Resection in Glioma-A Review of the Cutting Edge. World neurosurgery. 2017;103:538-49.

23. Ferreira CR, Yannell KE, Jarmusch AK, Pirro V, Ouyang Z, Cooks RG. Ambient Ionization Mass Spectrometry for Point-of-Care Diagnostics and Other Clinical Measurements. Clin Chem. 2015;62(1):99-110.

24. Wiseman JM, Puolitaival SM, Takáts Z, Cooks RG, Caprioli RM. Mass spectrometric profiling of intact biological tissue by using desorption electrospray ionization. Angewandte Chemie. 2005;117(43):7256-9.

25. Jarmusch AK, Pirro V, Baird Z, Hattab EM, Cohen-Gadol AA, Cooks RG. Lipid and metabolite profiles of human brain tumors by desorption electrospray ionization-MS. Proc Natl Acad Sci U S A. 2016;113(6):1486-91.

26. Dill AL, Ifa DR, Manicke NE, Costa AB, Ramos-Vara JA, Knapp DW, et al. Lipid Profiles of Canine Invasive Transitional Cell Carcinoma of the Urinary Bladder and Adjacent Normal Tissue by Desorption Electrospray Ionization Imaging Mass Spectrometry. Anal Chem. 2009;81(21):8758-64.

27. Fatou B, Saudemont P, Leblanc E, Vinatier D, Mesdag V, Wisztorski M, et al. In vivo Real-Time Mass Spectrometry for Guided Surgery Application. Sci Rep. 2016;6:25919.

28. Phelps D, Balog J, El-Bahrawy M, Speller A, Brown R, Takats Z, et al. Diagnosis of borderline ovarian tumours by rapid evaporative ionisation mass spectrometry (REIMS) using the surgical intelligent knife (iKnife). Bjog-an International Journal of Obstetrics and Gynaecology. 2016;123(13):E4-E.

29. Eberlin LS, Dill AL, Golby AJ, Ligon KL, M. WJ, Cooks RG, et al. Discrimination of Human Astrocytoma Subtypes by Lipid Analysis Using Desorption Electrospray Ionization Imaging Mass Spectrometry. Angew Chem Int Ed. 2010;122(34):6089-92.

30. Eberlin LS, Margulis K, Planell-Mendez I, Zare RN, Tibshirani R, Longacre TA, et al. Pancreatic Cancer Surgical Resection Margins: Molecular Assessment by Mass Spectrometry Imaging. Plos Medicine. 2016;13(8).

31. Dill AL, Eberlin LS, Zheng C, Costa AB, Ifa DR, Cheng L, et al. Multivariate statistical differentiation of renal cell carcinomas based on lipidomic analysis by ambient ionization imaging mass spectrometry. Analytical and bioanalytical chemistry. 2010;398(7-8):2969-78.

32. Ouyang YZ, Liu JW, Nie BH, Dong NP, Chen X, Chen LF, et al. Differential diagnosis of human lung tumors using surface desorption atmospheric pressure chemical ionization imaging mass spectrometry. Rsc Advances. 2017;7(88):56044-53.

33. Eberlin LS, Dill AL, Costa AB, Ifa DR, Cheng L, Masterson T, et al. Cholesterol sulfate imaging in human prostate cancer tissue by desorption electrospray ionization mass spectrometry. Anal Chem. 2010;82(9):3430-4.

34. Alexander J, Gildea L, Balog J, Speller A, McKenzie J, Muirhead L, et al. A novel methodology for in vivo endoscopic phenotyping of colorectal cancer based on real-time analysis of the mucosal lipidome: a prospective observational study of the iKnife. Surgical Endoscopy and Other Interventional Techniques. 2017;31(3):1361-70.

35. Masterson TA, Dill AL, Eberlin LS, Mattarozzi M, Cheng L, Beck SD, et al. Distinctive glycerophospholipid profiles of human seminoma and adjacent normal tissues by desorption electrospray ionization imaging mass spectrometry. J Am Soc Mass Spectrom. 2011;22(8):1326-33.

36. St John ER, Balog J, McKenzie JS, Rossi M, Covington A, Muirhead L, et al. Rapid evaporative ionisation mass spectrometry of electrosurgical vapours for the identification of breast pathology: towards an intelligent knife for breast cancer surgery. Breast Cancer Research. 2017;19.

37. Dill AL, Eberlin LS, Costa AB, Zheng C, Ifa DR, Cheng L, et al. Multivariate statistical identification of human bladder carcinomas using ambient ionization imaging mass spectrometry. Chemistry-a European Journal. 2011;17(10):2897-902.

38. Zhang JL, Feider CL, Nagi C, Yu WD, Carter SA, Suliburk J, et al. Detection of Metastatic Breast and Thyroid Cancer in Lymph Nodes by Desorption Electrospray Ionization Mass Spectrometry Imaging. Journal of the American Society for Mass Spectrometry. 2017;28(6):1166-74.

39. Eberlin LS, Norton I, Dill AL, Golby AJ, Ligon KL, Santagata S, et al. Classifying human brain tumors by lipid imaging with mass spectrometry. Cancer research. 2012;72(3):645-54.

40. Sans M, Gharpure K, Tibshirani R, Zhang JL, Liang L, Liu JS, et al. Metabolic Markers and Statistical Prediction of Serous Ovarian Cancer Aggressiveness by Ambient Ionization Mass Spectrometry Imaging. Cancer Research. 2017;77(11):2903-13.

41. Gerbig S, Golf O, Balog J, Denes J, Baranyai Z, Zarand A, et al. Analysis of colorectal adenocarcinoma tissue by desorption electrospray ionization mass spectrometric imaging. Analytical and bioanalytical chemistry. 2012;403(8):2315-25.

42. Zhang JL, Rector J, Lin JQ, Young JH, Sans M, Katta N, et al. Nondestructive tissue analysis for ex vivo and in vivo cancer diagnosis using a handheld mass spectrometry system. Science Translational Medicine. 2017;9(406).

43. Eberlin LS, Norton I, Orringer D, Dunn IF, Liu X, Ide JL, et al. Ambient mass spectrometry for the intraoperative moleucular diagnosis of human brain tumors. PNAS. 2013;110(5):1611-6.

44. Pirro V, Alfaro CM, Jarmusch AK, Hattab EM, Cohen-Gadol AA, Cooks RG. Intraoperative assessment of tumor margins during glioma resection by desorption electrospray ionization-mass spectrometry. Proceedings of the National Academy of Sciences of the United States of America. 2017;114(26):6700-5.

45. Balog J, Sasi-Szabo L, Kinross J, Lewis MR, Muirhead LJ, Veselkov K, et al. Intraoperative tissue identification using rapid evaporative ionization mass spectrometry. Sci Transl Med. 2013;5(194):194ra93.

46. Pirro V, Llor RS, Jarmusch AK, Alfaro CM, Cohen-Gadol AA, Hattabd EM, et al. Analysis of human gliomas by swab touch spray-mass spectrometry: applications to intraoperative assessment of surgical margins and presence of oncometabolites. Analyst. 2017;142(21):4058-66.

47. Eberlin LS, Gabay M, Fan AC, Gouw AM, Tibshirani RJ, Felsher DW, et al. Alteration of the lipid profile in lymphomas induced by MYC overexpression. Proceedings of the National Academy of Sciences of the United States of America. 2014;111(29):10450-5.

48. D'Hue C, Moore M, Summerlin DJ, Jarmusch A, Alfaro C, Mantravadi A, et al. Feasibility of desorption electrospray ionization mass spectrometry for diagnosis of oral tongue squamous cell carcinoma. Rapid communications in mass spectrometry : RCM. 2017;32(2):133-41.

49. Calligaris D, Feldman DR, Norton I, Brastianos PK, Dunn IF, Santagata S, et al. Molecular typing of meningiomas by desorption electrospray ionization mass spectrometry imaging for surgical decision-making. International Journal of Mass Spectrometry. 2014;377:690-8.

50. D'Hue CA, Dhawan D, Peat T, Ramos-Vara J, Jarmusch A, Knapp DW, et al. Fatty Acid Patterns Detected By Ambient Ionization Mass Spectrometry in Canine Invasive Urothelial Carcinoma From Dogs of Different Breeds. Bladder Cancer. 2018;4(3):283-91.

51. Calligaris D, Caragacianu D, Liu X, Norton I, Thompson CJ, Richardson AL, et al. Application of desorption electrospray ionization mass spectrometry imaging in breast cancer margin analysis. Proceedings of the National Academy of Sciences of the United States of America. 2014;111(42):15184-9.

52. Phelps DL, Balog J, Gildea LF, Bodai Z, Savage A, El-Bahrawy MA, et al. The surgical intelligent knife distinguishes normal, borderline and malignant gynaecological tissues using rapid evaporative ionisation mass spectrometry (REIMS). British Journal of Cancer. 2018;118(10):1349-58.

53. Santagata S, Eberlin LS, Norton I, Calligaris D, Feldman DR, Ide JL, et al. Intraoperative mass spectrometry mapping of an onco-metabolite to guide brain tumor surgery. Proc Natl Acad Sci U S A. 2014;111(30):11121-6.

54. Porcari AM, Zhang JL, Garza KY, Rodrigues-Peres RM, Lin JQ, Young JH, et al. Multicenter Study Using Desorption-Electrospray-Ionization-Mass-Spectrometry Imaging for Breast-Cancer Diagnosis. Analytical Chemistry. 2018;90(19):11324-32.

55. Eberlin LS, Tibshirani RJ, Zhang J, Longacre TA, Berry GJ, Bingham DB, et al. Molecular assessment of surgical-resection margins of gastric cancer by mass-spectrometric imaging. Proceedings of the National Academy of Sciences. 2014;111(7):2436-41.

56. Zou R, Cao WB, Chong L, Hua W, Xu H, Mao Y, et al. Point-of-Care Tissue Analysis Using Miniature Mass Spectrometer. Analytical Chemistry. 2019;91(1):1157-63.

57. Jarmusch AK, Kerian KS, Pirro V, Peat T, Thompson CA, Ramos-Vara JA, et al. Characteristic lipid profiles of canine non-Hodgkin's lymphoma from surgical biopsy tissue sections and fine needle aspirate smears by desorption electrospray ionization–mass spectrometry. Analyst. 2015;140:6321-9.

58. Sans M, Zhang J, Lin JQ, Feider CL, Giese N, Breen MT, et al. Performance of the MasSpec Pen for Rapid Diagnosis of Ovarian Cancer. Clin Chem. 2019.

59. Kerian KS, Jarmusch AK, Pirro V, Koch MO, Masterson TA, Cheng L, et al. Differentiation of prostate cancer from normal tissue in radical prostatectomy specimens by desorption electrospray ionization and touch spray ionization mass spectrometry. Analyst. 2015;140(4):1090-8.

60. Alfaro CM, Pirro V, Keating MF, Hattab EM, Cooks RG, Cohen-Gadol AA. Intraoperative assessment of isocitrate dehydrogenase mutation status in human gliomas using desorption electrospray ionization-mass spectrometry. J Neurosurg. 2019:1-8.

61. Balog J, Kumar S, Alexander J, Golf O, Huang J, Wiggins T, et al. In Vivo Endoscopic Tissue Identification by Rapid Evaporative Ionization Mass Spectrometry (REIMS). Angew Chem Int Ed Engl. 2015;54(38):11059-62.

62. Pu F, Alfaro CM, Pirro V, Xie Z, Ouyang Z, Cooks RG. Rapid determination of isocitrate dehydrogenase mutation status of human gliomas by extraction nanoelectrospray using a miniature mass spectrometer. Analytical and bioanalytical chemistry. 2019.

63. Ifa DR, Eberlin LS. Ambient Ionization Mass Spectrometry for Cancer Diagnosis and Surgical Margin Evaluation. Clinical chemistry. 2016;62(1):111-23.

64. Martinez AM, Kak AC. PCA versus LDA. Ieee Transactions on Pattern Analysis and Machine Intelligence. 2001;23(2):228-33.

CHAPTER 2.   AMBIENT IONIZATION MASS SPECTROMETRIC ANALYSIS OF HUMAN SURGICAL SPECIMENS TO DISTINGUISH RENAL CELL CARCINOMA FROM HEALTHY RENAL TISSUE

2.1   Abstract

Touch spray - mass spectrometry (TS-MS) is an ambient ionization technique (ionization of unprocessed samples in the open air) that may find intraoperative applications in quickly identifying the disease state of cancerous tissues and in defining surgical margins. In this study, TS-MS was performed on fresh kidney tissue ($\sim$1-5 cm^3), within one hour of resection, from 21 human subjects afflicted by renal cell carcinoma (RCC). The preliminary diagnostic value of TS-MS data taken from freshly resected tissue was evaluated. Principal component analysis (PCA) of the negative ion mode (*m/z* 700-1000) data provided separation between RCC (16 samples) and healthy renal tissue (13 samples). Linear discriminant analysis (LDA) on the PCA compressed data estimated sensitivity (true positive rate) and specificity (true negative rate) of 98% and 95%, respectively, based on histopathological evaluation. The results indicate that TS-MS might provide rapid diagnostic information despite the complexity of unprocessed kidney tissue and the presence of interferences such as urine and blood. Desorption electrospray ionization imaging (DESI-MSI) in the negative ionization mode was performed on the tissue specimens after TS-MS analysis as a reference method. The DESI imaging experiments provided phospholipid profiles (*m/z* 700-1000) that also separated RCC and healthy tissue in the PCA space, with PCA-LDA sensitivity and specificity of 100% and 89%, respectively. The TS and DESI loading plots indicated that different ions contributed most to the separation of RCC from healthy renal tissue (*m/z* 794 [PC 34:1+Cl]$^-$ and 844 [PC 38:4+Cl]$^-$ for TS vs. *m/z* 788 [PS 36:1-H]$^-$ and 810 [PS 38:4-H]$^-$ for DESI), while

m/z 885 ([PI 38:4-H]⁻) was important in both TS and DESI. The prospect, remaining hurdles, and future work required for translating TS-MS into a method of intraoperative tissue diagnosis is discussed.

2.2 Introduction

Kidney cancers cause a significant fraction of cancer related fatalities in the United States, with 14,080 deaths and 61,560 new cases estimated in 2015. (1, 2) Approximately 90% of kidney cancers arise from the renal parenchyma and are termed renal cell carcinomas (RCC)(2). RCC has been differentiated from normal tissue based on epigenetic, (3, 4) genetic, (5) proteomic, (6-8) metabolomic, (9, 10) and lipidomic markers. (11, 12) While these techniques are highly informative, analysis time is generally incompatible with intraoperative application, which is the long-term objective of this study. Ambient ionization mass spectrometry (MS), the MS analysis of samples in their native environment with little or no sample preparation, may improve surgical outcomes by providing surgeons with information that helps determine tissue disease state and identifies the tumor margin on the time scale of surgery. Previous intraoperative and/or ex vivo results from several investigators for brain, (13-16) colon, lung, and liver (17, 18) cancers support this expectation. Moreover, it is known in several cancers that phospholipid profiles differ between tumor and normal tissues. (19-21) Lipids have been explored for recognizing cancerous tissue using a variety of ambient ionization techniques such as touch spray (TS), (22) probe electrospray ionization (PESI),(23) rapid evaporative ionization (REIMS),(17) and desorption electrospray ionization (DESI)-MS.(24) Lipids are of interest because of their roles in cell signaling, cell-cell recognition, immune response, energy metabolism, the malignant transformation of cells,(25-27) and are expected to be reflective of disease state.

TS-MS involves the physical sampling of tissue using a metallic probe with subsequent ionization occurring directly from the probe upon the addition of solvent (1-2μL) and high voltage (4 - 5kV) (Figure 2.1). (22, 28) Free fatty acids and glycerophospholipids, including phosphatidylcholines (PCs) and phosphatidylinositols (PIs), are typically detected when performing TS-MS on frozen tissue sections. (28) TS-MS was previously used to analyze frozen sections of prostate cancer specimens from 18 human subjects, differentiating between normal prostate and prostate cancer. (22) However, TS-MS has not been used to study fresh *in vitro* tissue in a way that emulates possible intraoperative use.
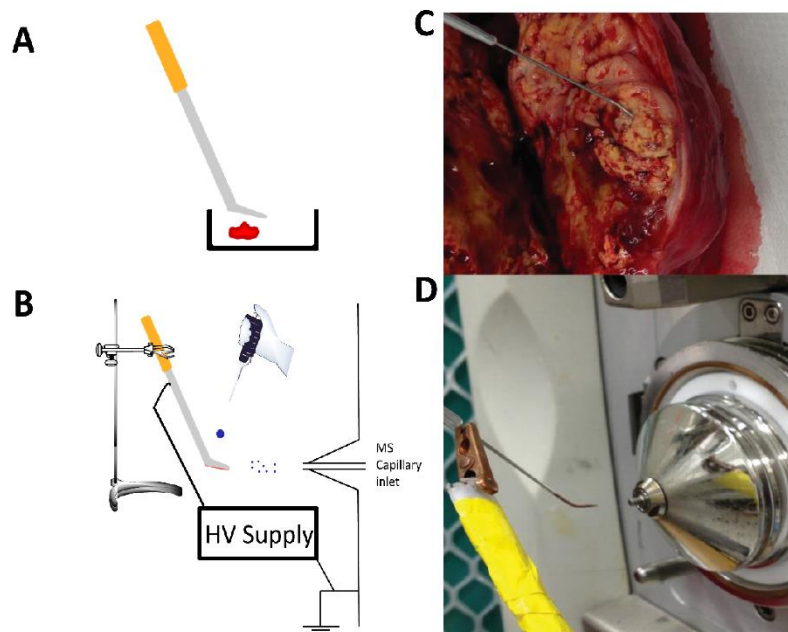
Figure 2.1 Schematic of the TS-MS experiment performed on a piece of biopsied tissue. A) The metal teasing needle (yellow handle, silver shaft) is used to touch the surface of the tissue (red) and transfer small amounts of cells, fluids, and extracellular matrix to the surface of the teasing needle. B) The probe is fixed to a ring stand with a clamp and positioned with the tip a few mm from the entrance of the mass spectrometer. A small aliquot (1-2 μL) of solvent is added manually and then high voltage (3-5kV) is applied to the teasing needle to initiate spray-based ionization from the tip of the needle. C) Photograph of the TS-MS probe in contact with a specimen obtained from a radical nephrectomy. Samples of this type were not typical and is shown for illustrative purposes. D) The TS-MS probe placed in front of the mass spectrometer after sampling the radical nephrectomy RCC specimen. The displayed probe contains an excess of sample; a minute quantity of tissue is required to generate mass spectra.

Like TS-MS, PESI-MS is an ambient ionization technique that uses a conductive metallic probe to sample tissue by puncturing it and then creating ions directly from the probe by application of high voltage. (23, 29)

Yoshimura et al. analyzed fresh human RCC specimens with PESI in the positive ion mode, and observed differences from normal tissue in phosphatidylcholine and triacylglycerol profiles. (11) PESI has also been used to analyze chemically induced hepatocellular carcinoma in a live mouse mounted on a sampling stage positioned in front of a mass spectrometer. (30) PESI and TS are both invasive techniques, but only small amounts of material (10-100 micrograms) are required to generate data. Both these techniques balance speed of analysis, degree of invasiveness, and amount of sample preparation such that they are amenable to intraoperative applications. An alternative technique, REIMS, samples ions directly from the surgical smoke produced by

electrocauterization. (17, 18, 31) REIMS is a fast method because the surgical removal of tissue and mass spectrometric sampling are performed nearly simultaneously; however, the data are harder to correlate with traditional histopathology, the gold standard for diagnosis.

DESI-MS is a microprobe experiment in which a charged aerosol is sprayed onto a sample (e.g. a tissue section or smear) with a spot size of around 200μm. The resulting thin liquid film formed on the sample surface dissolves some compounds, and subsequent droplet impacts produce splashes of charged, analyte containing microdroplets. Gas-phase ions are generated via electrospray like processes when the secondary microdroplets are sampled by the mass spectrometer. (32) DESI-MS imaging (DESI-MSI) experiments are performed by rastering the spot across the sample in a controlled fashion. An advantage of DESI-MSI when using an appropriate solvent is that the analyzed tissue can be stained with haematoxylin and eosin (H&E) subsequent to MS analysis and evaluated by histopathology, enabling direct correlations to be drawn between molecular and morphological information. (33) DESI-MSI has been applied to analyze several malignancies, (20, 21, 34, 35) including kidney cancers, (12, 36) and demonstrated that the detected ions were reliably indicative of disease state (viz. distinction between tumor and normal) via multivariate statistics. Finally, although not an ambient ionization technique, matrix assisted laser desorption ionization (MALDI) mass spectrometry has been performed in an imaging format and it can also be used to profile tissue specimens, but the technique requires additional sample manipulation and it takes longer to analyze biopsy specimens. (37-39)

In this study, TS-MS was used to analyze fresh healthy renal tissue and RCC specimens. As a reference method, DESI-MSI was performed following TS-MS analysis because DESI has been studied in more detail (DESI was first used to analyze tissue sections in 2005, (24) and TS was developed in 2014), (28) and because measured DESI-MS lipid profiles can be precisely correlated with histopathological information by staining the analyzed tissue after DESI-MSI. Previous DESI-MSI studies of RCC in the negative ionization mode indicated the ability to differentiate RCC and healthy renal tissue with multivariate statistics, including the ability to differentiate clear cell renal cell carcinoma (ccRCC) and papillary RCC. (12) Based on this previous work, we chose to perform the data acquisition in the negative ionization mode. This study focuses on the rapid analysis of fresh renal tissue using TS-MS with supporting DESI-MSI analysis.

2.3   Materials and Methods

2.3.1   Tissue Handling

All tissues samples were acquired from patients undergoing nephrectomy (partial or radical) for the treatment of RCC and were handled in accordance with approved Institutional Review Board (IRB) protocols at Indiana University School of Medicine (1205008669) and Purdue University (1203011967). A small portion (approximately 3 x 3 x 3 mm) of tumor and adjacent normal kidney tissue was taken from the biopsy in the pathology lab (University Hospital, Indianapolis) and analyzed on site using TS-MS. TS-MS analysis was performed while the tissue was fresh (not frozen or fixed). Subsequent to TS-MS analysis, the biopsy specimens were snap frozen in liquid N_2 and transported back to Purdue University on dry ice for DESI-MSI analysis. Tissue samples were obtained from 21 subjects over the period of one year. Of the 21 cancer subjects, there were 15 clear cell RCC, two papillary RCC, and three unclassified RCC, as well as one oncocytoma (Table 2.1).

2.3.2   TS-MS Analysis of Freshly Resected Kidney Tissue

On each day of surgery, the pathology laboratory at University Hospital notified the Purdue researchers when tissue was acquired from the operating room. The researchers transported the tissue specimens from the pathology laboratory to the LTQ mass spectrometer (Thermo Scientific, San Jose, CA) located in an adjacent research building. TS-MS was performed on the fresh (not frozen or fixed) tissue specimens using a metal teasing needle purchased from Fisher Scientific (Pittsburgh, PA, USA) to scrape small amounts of cellular material from the bulk tissue (22). The probe was positioned in front of the mass spectrometer with the metal tip pointing at the inlet (~5-8 mm) a high voltage (4 kV) was applied and a 1 µL aliquot of methanol was added to initiate ionization. Data were collected over the range *m/z* 200-1000 in the negative ionization mode. A chronogram showing the time dependence of a typical TS-MS signal recorded from a single solvent addition is shown in Figure 2.2. After TS-MS analysis at IUSM, the tissue specimens were snap frozen in liquid nitrogen to preserve morphology and halt biochemical processes. The samples were then transported to Purdue for subsequent cryosectioning and DESI-MSI analysis.

The teasing needle has an insulating plastic handle, metallic shaft (aluminum alloy) and roughened sharp metal tip. For data acquisition, the LTQ ion trap was set to scan *m/z* 200-1000 in the negative mode and automatic gain control (AGC) was utilized. A typical spray from a single

solvent application lasts for around five seconds. The tissue specimens were gently blotted with paper towels prior to TS sampling to remove macroscopic amounts of biofluids (e.g. blood). After data collection, the tip of the teasing needle was washed with nanopure water (EMD Millipore, Darmstadt, Germany) and 70% aqueous ethanol (Sigma-Aldrich, St. Louis, MO). The cleaned probe was then used to sample the tissue again to make replicate measurements, with washes after each data collection event. Significant carryover was not observed in the spectra. Future work should utilize a single use TS sampling probe that is discarded after a single data collection event.

Several scans (3-5) indicative of signal from ionizing the tissue (e.g. ion counts for previously observed ions in *m/z* 700-1000 with absolute intensities greater than $1x10^4$ compared to baseline noise of less than $1x10^2$ counts) were averaged for each data collection event to generate a representative mass spectrum. Each replicate sampling event was processed in a similar fashion. The data collection process was performed on both tumor and normal specimens when available. The entire process of obtaining the tissue from the frozen pathology lab and performing replicate TS-MS measurements took less than 20 minutes for each case; analysis was performed within one hour after resection from the patient. Ideally, the TS-MS analysis would take place on an instrument that is much closer to the patient.

MS/MS experiments were performed using a LTQ mass spectrometer on a select group of specimens after data was collected for all of the cases.

Parameters for MS/MS were: isolation width 1.1 Da, q = 0.25, collision energy = 30 arbitrary units, one microscan, and 500 ms maximum injection time. High-resolution MS data was obtained from an Orbitrap mass spectrometer (Thermo Exactive, San Jose, CA) for several specimens to aid in lipid attribution. The Exactive was calibrated in both polarities prior to analysis. Exactive parameters were as follows: resolution was set to Ultrahigh, AGC was set to ultimate mass accuracy, max injection time was 500 ms, and higher-energy collisional induced dissociation (HCD) gas was off.

2.3.3 DESI-MS Analysis of Frozen Tissue Sections

At Purdue, samples from each case were embedded in Optimal Cutting Temperature polymer (Sakura Finetek, Torrance, CA) and sectioned on a cryotome FSE to 10 μm thickness and thaw mounted on glass slides (Gold Seal UltraFrost Frosted Slides, Thermo Scientific, San Jose, CA). Tumor and normal specimens (as determined by gross analysis performed in the pathology

lab at IUSM) from each case were thaw mounted adjacent to each other on the same glass slide. Samples were removed from the freezer and dried in an electronic vacuum desiccator prior to DESI-MS analysis. A custom-built DESI source, similar to the DESI 2D Source available from Prosolia Inc. (Indianapolis, IN), was used to image the tissue. (40) A DESI spray solvent of dimethylformamide (DMF)-acetonitrile (ACN) 1:1 was used to minimize alteration of tissue morphology. (33) The DESI sprayer was 2 mm from the tissue surface, incident spray angle was 52°, collection angle was 10°, spray voltage was 5 kV, nitrogen gas pressure was 180 PSI, and solvent flow rate was 0.8 µL/min. DESI-MS imaging resolution was 250 µm, defined by pixel size, by setting the moving stage to move horizontally at ~200 µm/s determined by the scan time of the mass spectrometer, and the use a 250 µm vertical step.

MS data were recorded over the range *m/z* 200-1000 in the negative ion mode, automatic gain control (AGC) was turned off, and data acquired in the profile mode. The DESI imaging data were compiled into a data cube using an in-house program. BioMap was used to extract mass spectra from regions of interest (ROIs) representing RCC and healthy renal tissue based on the histopathological examination (see Figure 2.11).

2.3.4   Histological and Pathological Data

The pathology lab at IUSM performed histopathologic analyses on the remaining tissue after providing the specimens to researchers as discussed. The pathologic status of the adjacent tissue, as well as the histologic subtype, both determined by the pathology lab at IUSM, was used to correlate disease status with TS-MS lipid profiles. De-identified clinical and pathological data are provided in Table 2.1. In addition, the tissue sections analyzed by DESI-MSI were subsequently stained with H&E and interpreted by a pathologist (L.C.) to determine regions of healthy tissue and RCC.

2.3.5   Statistical Analyses of Mass Spectrometry Data and Data Visualization

Principal component analysis (PCA), using the non-linear iterative partial least squares algorithm, on the TS-MS and DESI-MSI data was performed using MATLAB (MathWorks, Natick, MA) and in-house routines which were described in previous work. (41) Mass spectra were extracted from the manufacturer's software (.raw files) and saved in Microsoft Excel. For TS-MS data, the spectrum from the signal peak in each chronogram was extracted as a .csv file from

Xcalibur and compiled into a matrix in Excel. Data were normalized using standard normal variate transforms to correct for baseline shifts and global variation in signal intensities. While data were recorded over the range *m/z* 200-1000, only *m/z* 700-1000 was utilized for PCA and subsequent linear discriminant analysis (LDA), as this mass range provides better diagnostic information. (35) LDA on the PCA compressed data was performed in MATLAB to discriminate between healthy renal tissue and RCC. (42) PCA-LDA was used to calculate sensitivity (true positive rate) and specificity (true negative rate) by means of cross validation (using n=5 deletion groups). This is done by using a subset of the dataset as a training set to build a LDA classifier, and then using the remaining dataset as test samples to validate the model. The process is iterated *n* times so that each sample will be in the validation set once. The LDA model is used to predict the class of the remaining samples (validation set) and the prediction rate is calculated. This procedure is described in detail elsewhere. (43) The dispersion in relative ion intensity for a few ions was plotted as box and whisker plots using OriginPro 2016 (OriginLab, Northampton, MA). Unpaired two sample T-tests of unequal variance and Kruskal-Wallis non-parametric tests were performed in OriginPro 2016 using the raw, unnormalized signal intensities.

2.4   Results and Discussion

2.4.1   Touch Spray Ionization

Principal component analysis (PCA) was performed on TS-MS data after standard normal variate (SNV) normalization and mean-centering. The PCA score and loading plots are shown in Figure 2.3. Separation between RCC and healthy renal tissue is observed in the score plot.

As seen in the loading plot (Figure 2.3), healthy renal tissue is more abundant in *m/z* 794 and 792 (tentatively identified as chlorinated adducts of PC 34:1 and PC 34:2, respectively), and RCC is more abundant in *m/z* 844 and 885 (tentatively identified as chlorinated PC 38:4 and deprotonated PI 38:4, respectively).

Table 2.1 Deidentified clinical and pathology data from the surgical cases.

Specimen ID	Subject Age	Gender	Race	Side	Histologic Type	Pathology Status	Original Tumor H X D X W	Grade	Grade System	T	N	M	TS-MS Data included?	DESI-MSI Data included?
1	62	M	White	Right	CLEAR CELL RENAL CELL CARCINOMA	cancer-primary	11 x 11 x 7 cm	3 of 4	Fuhrman	T3a	N0-N1	MX	N	Y
2	54	M	African American	Right	CLEAR CELL RENAL CELL CARCINOMA	cancer-primary	2.8 x 2 x 1.5 cm	2 of 4	Fuhrman	T1a	NX	MX	N	Y
3	36	M	White	Left	CLEAR CELL RENAL CELL CARCINOMA	cancer-primary	9.9 x 7.5 x 7.5 cm	3 of 4	Fuhrman	T3a	N0	M1	Y	Y
4	63	M	White	Left	PAPILLARY RENAL CELL CARCINOMA	cancer-primary	4.5 x 4.2 x 3.5 cm	2 of 4	Fuhrman	T1b	NX	MX	Y	Y
5	54	M	White	Left	CLEAR CELL RENAL CELL CARCINOMA	cancer-primary	12 x 12 x 8cm	3 of 4	Fuhrman	T3a	N1	MX	Y	N
6	54	M	White	Left	NORMAL TISSUE	normal adjacent	13 x 12 x 8cm	N/A	N/A	N/A	N/A	N/A	Y	Y
7	30	M	White	Left	NORMAL TISSUE	normal adjacent	12 x 7.5 x 7.5 cm	N/A	N/A	N/A	N/A	N/A	Y	Y
8	30	M	White	Left	RENAL CELL CARCINOMA, UNCLASSIFIED	cancer-primary	12 x 7.5 x 7.5 cm	4 of 4	Fuhrman	T4	N1	M1	Y	Y
9	46	F	White	Right	CLEAR CELL RENAL CELL CARCINOMA	cancer-primary	12.4 x 9.3 x 7.4 cm	2 of 4	Fuhrman	T3a	NX	MX	Y	Y
10	46	F	White	Right	NORMAL TISSUE	normal adjacent	12.4 x 9.3 x 7.4 cm	N/A	N/A	N/A	N/A	N/A	Y	Y
11	74	M	White	Right	CLEAR CELL RENAL CELL CARCINOMA	cancer-primary	14 x 8 x 7 cm	3 of 4	Fuhrman	T3c	NX	MX	Y	N
12	45	F	White	Left	NORMAL TISSUE	normal adjacent	1.5 x 1.3 x 1.0 cm	N/A	N/A	N/A	N/A	N/A	Y	Y
13	45	F	White	Left	CLEAR CELL RENAL CELL CARCINOMA	cancer-primary	1.5 x 1.3 x 1.0 cm	2 of 4	Fuhrman	T1	NX	MX	Y	Y
14	67	M	White	Left	NORMAL TISSUE	normal adjacent	1.8 x 1.5 x 1.4 cm	N/A	N/A	N/A	N/A	N/A	Y	Y
15	67	M	White	Left	PAPILLARY RENAL CELL CARCINOMA	cancer-primary	1.8 x 1.5 x 1.4 cm	2 of 4	Fuhrman	T1a	NX	MX	Y	Y
16	38	F	African American	Left	NORMAL TISSUE	normal adjacent	2.4 x 2.2 x 2.2 cm	N/A	N/A	N/A	N/A	N/A	N	Y
17	38	F	African American	Left	RENAL CELL CARCINOMA, UNCLASSIFIED	cancer-primary	2.4 x 2.2 x 2.2 cm	2 of 4	Fuhrman	T1a	NX	MX	N	N
18	51	F	White	Left	NORMAL TISSUE	normal adjacent	2.6 x 2.5 x 2.0 cm	N/A	N/A	N/A	N/A	N/A	Y	Y
19	51	F	White	Left	CLEAR CELL RENAL CELL CARCINOMA	cancer-primary	2.6 x 2.5 x 2.0 cm	2 of 4	Fuhrman	T1a	NX	MX	Y	Y
20	41	M	White	Right	CLEAR CELL RENAL CELL CARCINOMA	cancer-primary	3.8 x 3.8 x 3.5 cm	2 of 4	Fuhrman	T1a	NX	MX	Y	Y
21	57	M	White	Left	NORMAL TISSUE	normal adjacent	4.4 x 3.9 x 3.8 cm	N/A	N/A	N/A	N/A	N/A	Y	Y
22	57	M	White	Left	CLEAR CELL RENAL CELL CARCINOMA	cancer-primary	4.4 x 3.9 x 3.8 cm	2 of 4	Fuhrman	T1b	NX	MX	Y	Y
23	51	M	White	Right	NORMAL TISSUE	normal adjacent	3.9 x 3.8 x 3.4 cm	N/A	N/A	N/A	N/A	N/A	Y	Y
24	51	M	White	Right	CLEAR CELL RENAL CELL CARCINOMA	cancer-primary	3.9 x 3.8 x 3.4 cm	2 of 4	Fuhrman	T1a	NX	MX	Y	Y
25	71	M	White	Left	NORMAL TISSUE	normal adjacent	2.7 x 1.8 x 1.3cm	N/A	N/A	N/A	N/A	N/A	Y	N
26	71	M	White	Left	ONCOCYTOMA, NOS	cancer-primary	2.7 x 1.8 x 1.3cm	N/A	N/A	N/A	N/A	N/A	N	N
27	60	M	White	Right	CLEAR CELL RENAL CELL CARCINOMA	cancer-primary	5 x 2.7 x 2.2 cm	3 of 4	Fuhrman	T1b	NX	MX	Y	Y
28	60	M	White	Right	NORMAL TISSUE	normal adjacent	5 x 2.7 x 2.2 cm	N/A	N/A	N/A	N/A	N/A	Y	Y
29	48	F	White	Left	CLEAR CELL RENAL CELL CARCINOMA	cancer-primary	1.9 x 1.7 x 1.6 cm	2 of 4	Fuhrman	T1a	NX	MX	Y	Y
30	27	F	African American	Right	RENAL CELL CARCINOMA, UNCLASSIFIED	cancer-primary	9 x 9 x 8 cm	2 of 4	Fuhrman	T3	N1	MX	Y	N
31	27	F	African American	Right	NORMAL TISSUE	normal adjacent	9 x 9 x 8 cm	N/A	N/A	N/A	N/A	N/A	Y	Y
32	67	F	White	Right	CLEAR CELL RENAL CELL CARCINOMA	cancer-primary	10 x 7 x 7 cm	3 of 4	Fuhrman	T4	N1	M1	N	N
33	67	F	White	Right	NORMAL TISSUE	normal adjacent	10 x 7 x 7 cm	N/A	N/A	N/A	N/A	N/A	Y	Y
34	66	F	White	Right	CLEAR CELL RENAL CELL CARCINOMA	cancer-primary	3.0 x 2.7 x 2.0 cm	3 of 4	Fuhrman	T1a	NX	MX	Y	Y
35	66	F	White	Right	NORMAL TISSUE	normal adjacent	3.0 x 2.7 x 2.0 cm	N/A	N/A	N/A	N/A	N/A	Y	Y
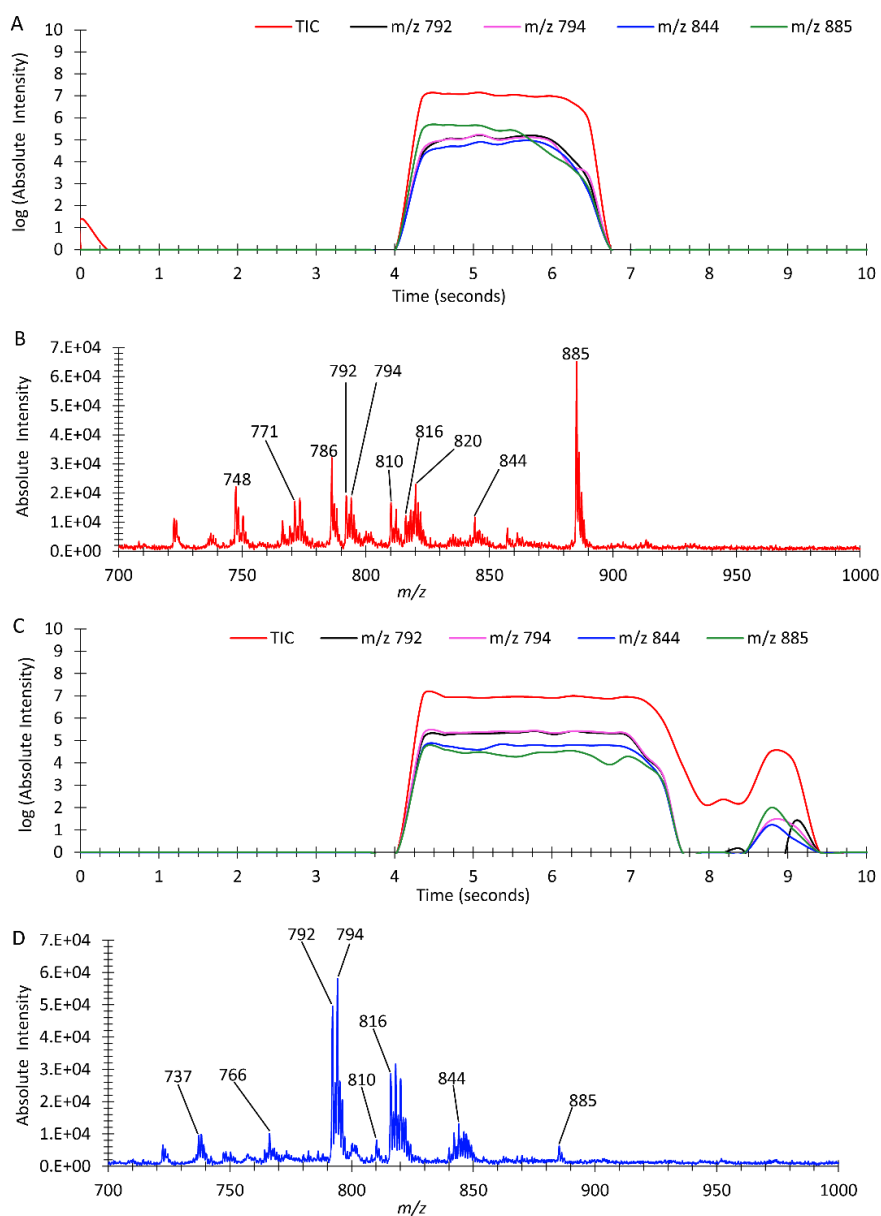
Figure 2.2 TS-MS chronograms and extracted mass spectra of the RCC (specimen 15, A&B) and healthy renal tissue (specimen 14, C&D) obtained from a single subject. A) The total ion current (red) as well as extracted ion chronograms (*m/z* 792, black; 794, pink; 844, blue; and 885, green) obtained from a single TS-MS experiment performed on RCC specimen 15. The log (absolute intensity) is plotted on the Y-axis. B) The mass spectrum extracted from the time interval t=4.2 to t=6 seconds from the chronogram shown in A; the absolute intensity is plotted on the Y-axis. C) Analogous to A, chronograms of the TIC and a set of XIC for a TS-MS experiment from specimen 14, healthy renal tissue. D) The mass spectrum extracted from the time interval t=4.8 to t=6.6 seconds from the chronogram shown in C for the healthy renal tissue.

These assignments are from MS/MS spectra of these ions, as well as exact mass data, which are shown in Figure 2.7 and Figure 2.8. The increased abundance of PI 38:4 in tumor cells is supported by biochemical studies from other laboratories which observed that altered inositol phospholipid metabolism as a common downstream effect due to the activation of several oncogenes including *src*, *met*, *trk*, *mos*, *raf*, and *ras*. (25, 44) Differences in *m/z* abundances are apparent in the average mass spectra of healthy renal tissue and RCC shown in Figure 2.3. Cross validation of a discriminant model, linear discriminant analysis (LDA) on the PCA compressed data, was performed. The average sensitivity (true positive rate) was 98.7% and specificity (true negative rate) was 94.6% using five deletion groups and five principal components. The preliminary sensitivity and specificity results are encouraging, and they warrant further investigations with larger sample sizes to establish and validate the method's diagnostic capabilities. Additional PCA score and loading plots are shown in Figure 2.4. The importance of additional ions in separating RCC from healthy renal tissue can be appreciated by examining the lower-order PCA score and loading plots shown in Figure 2.4; additional information on interpreting PCA score and loading plots can be found in Pirro et al. (41) The univariate statistical significance of several of these ions, including *m/z* 771, 788, 792, 794, 810, 816, 844, and 885, in differentiating tumor and normal was evaluated with an unpaired two sample T-test of unequal variance and a Kruskal-Wallis non-parametric test, as well as being visualized with box and whisker plots (Figure 2.5). Agreement was observed between the univariate tests for all tested *m/z* values. The p-value was < 0.05 for each of the eight ions except for *m/z* 844 in which the null hypothesis (the mean value of each dataset originates from the same distribution) failed to be rejected.

Histopathologic subtypes of the specimens were provided by the IUSM pathology lab, and additional PCA score and loading plot as well as average mass spectra are provided in Figure 2.6.

The number of samples in each subtype was too small to comment on the ability of TS-MS to delineate RCC subtypes. Subtyping is a topic worth exploring further but is beyond the scope of this communication.
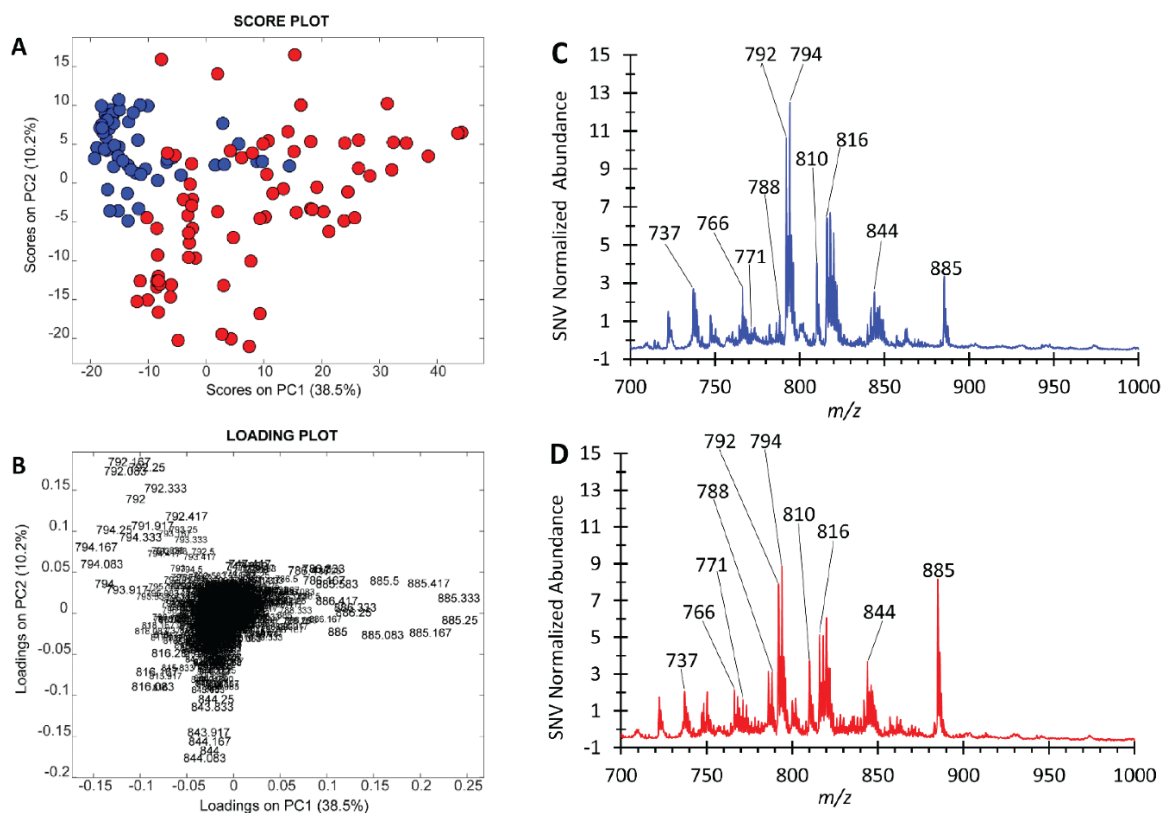
Figure 2.3 Negative ion mode TS-MS results from the kidney surgical cases. **A)** PCA score plot of the TS-MS data. Healthy renal tissue is blue, RCC is red. A total of 28 human subjects are represented, with 16 RCC and 13 healthy renal tissue specimens, respectively. **B)** PCA loading plot showing that *m/z* 792 ([PC 34:2 + Cl]⁻) , 794 ([PC 34:1 + Cl]⁻) , 844 ([PC 38:4 + Cl]⁻) , and 885 ([PI 38:4 - H]⁻) are the major contributors to the separation observed in A. **C and D)** Average mass spectra of the normal and tumor classes, respectively. The SNV normalized signal intensity is plotted in the average spectra.
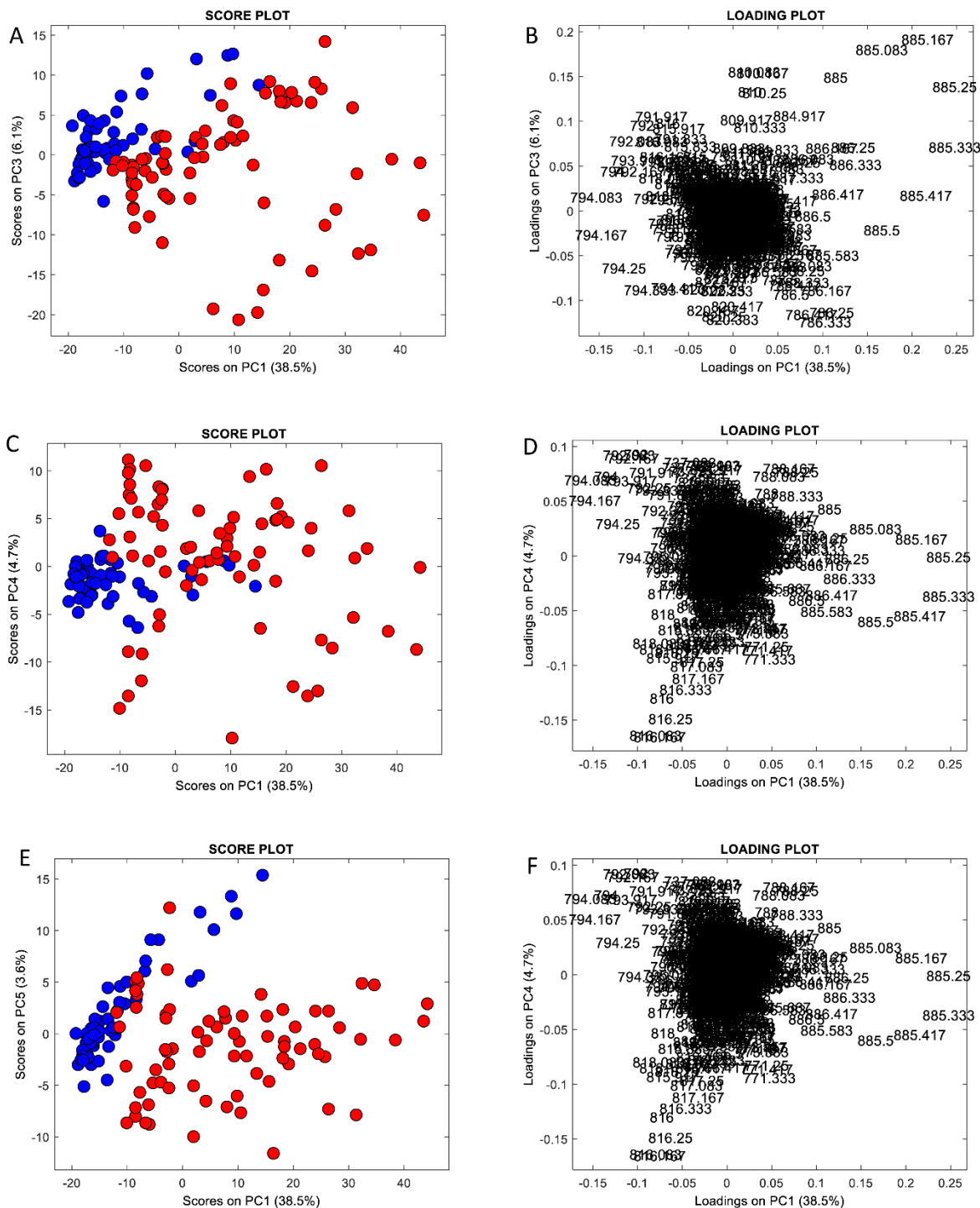
Figure 2.4 Principal component analysis results for PC3 vs. PC1, PC4 vs. PC1, and PC5 vs. PC1 for the TS-MS dataset. A&B) Score and loading plots for PC3 vs. PC1, respectively. C&D) Score and loading plots for PC4 vs. PC1, respectively. E&F) Score and loading plots for PC5 vs. PC1, respectively
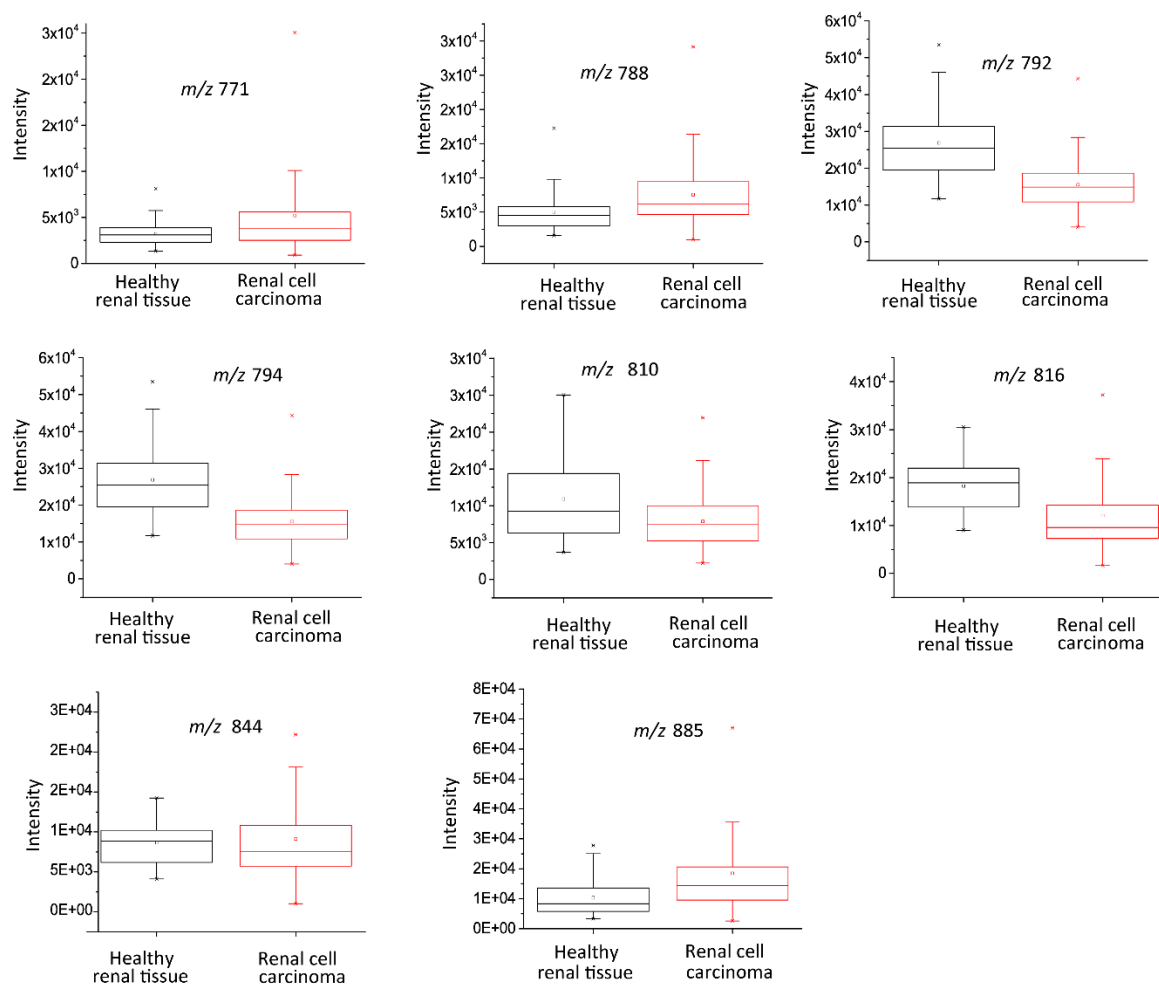
Figure 2.5 Box plots of selected ions observed in the average TS-MS mass spectra for healthy renal tissue and RCC using the raw/unnormalized signal intensities. T-tests and Kruskal-Wallis tests were performed on these data and all were significant at the $p < 0.05$ level except for m/z 844 in which the null hypothesis failed to reject.
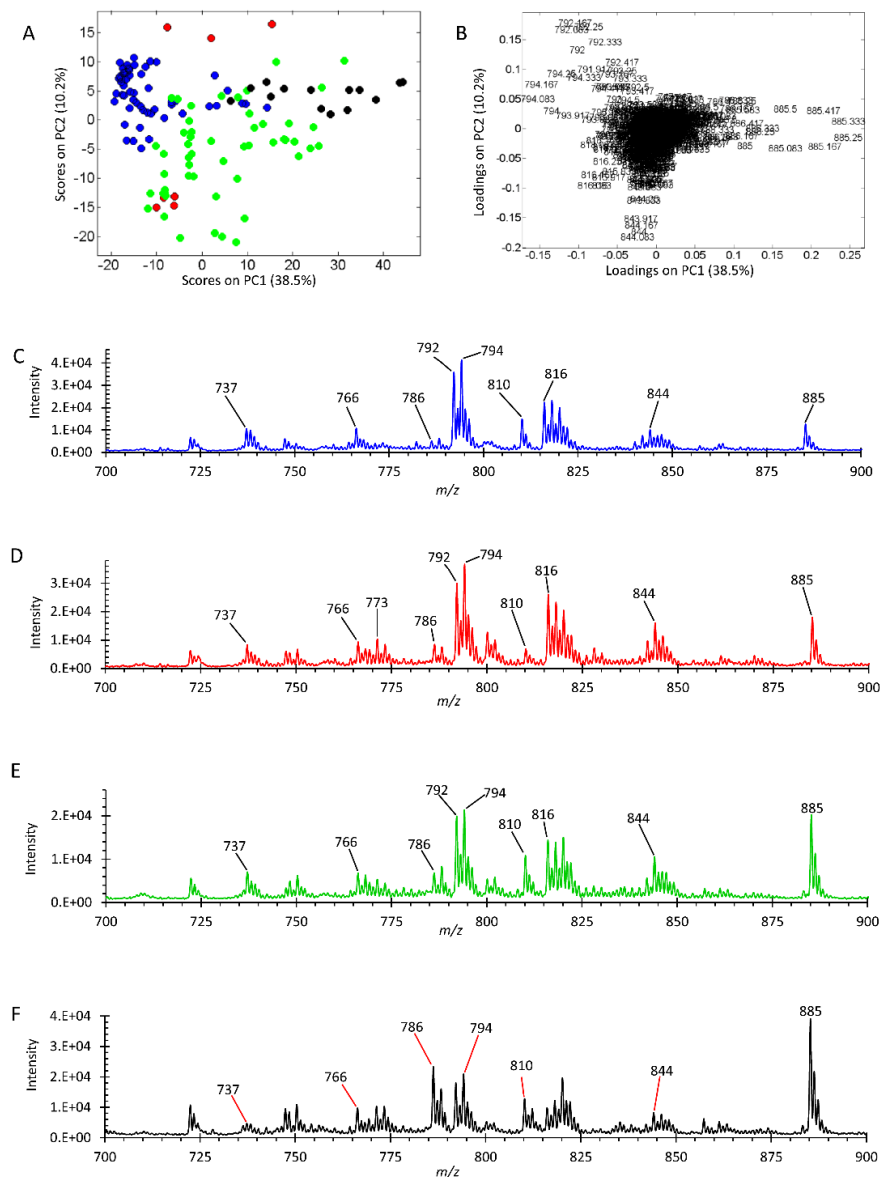
Figure 2.6 TS-MS results of the surgical specimens with the RCC class divided into the histological subtypes determined by the pathology lab at IUSM. Separations based on subtype need to be validated because the sampling size is too small. A) The PCA score plot showing separation of healthy renal tissue (blue) from clear cell (cc, green) RCC, and slight separation of papillary RCC (black) from ccRCC. One case of unclassified RCC (red) separated from all objects but a separate case grouped with ccRCC. Healthy renal tissue (n=13) is blue, unclassified RCC (n=2) is red, ccRCC (n=12) is green, and papillary RCC (n=2) is black.   B) The corresponding loading plot for the score plot shown in A. C-F) Average mass spectra of each of the tissue groups shown in the score plot in A. The raw, unnormalized signal intensities are plotted.
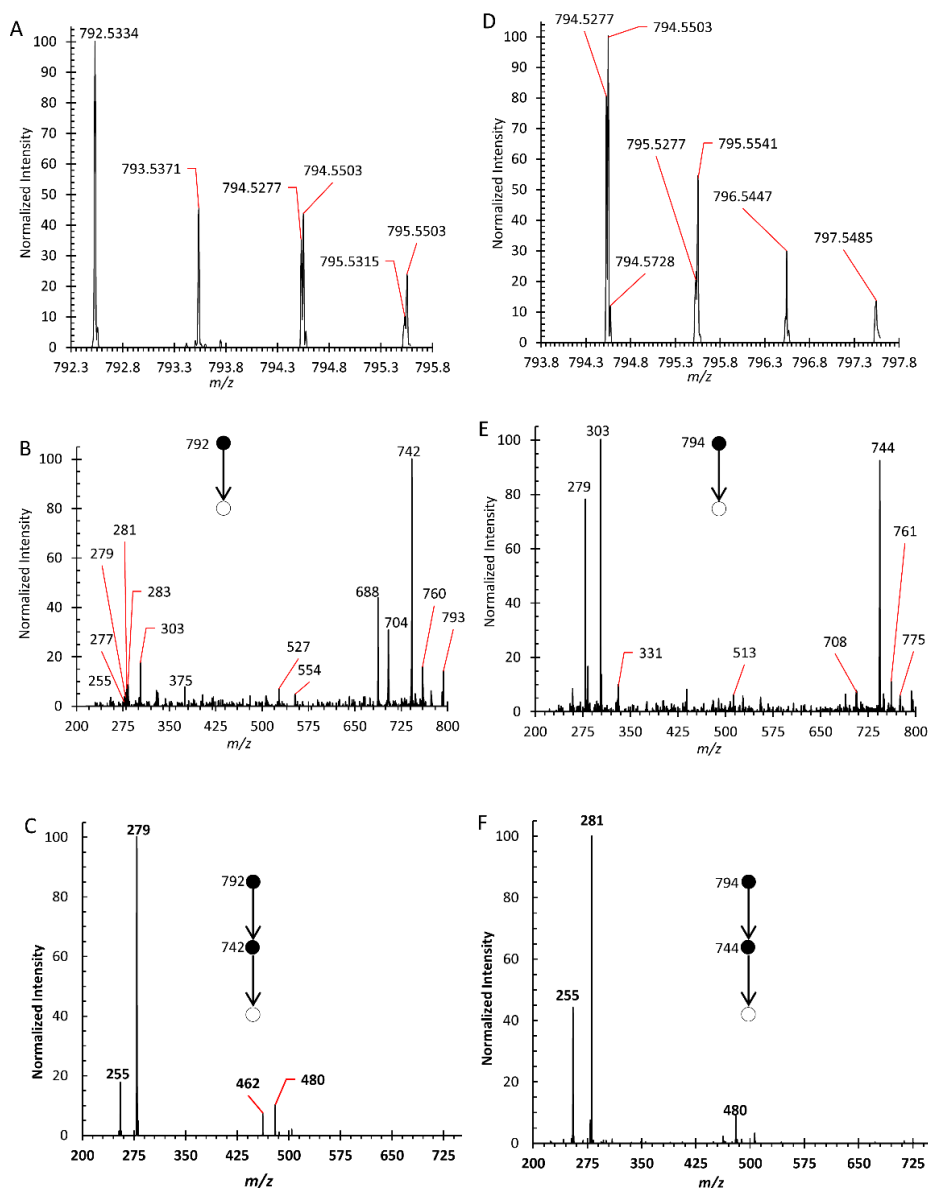
Figure 2.7 High resolution (A), MS² (B), and MS³ (C) spectra of *m/z* 792. High resolution (D), MS² (E), and MS³ (F) spectra of *m/z* 794. (A) Exact mass spectrum shows presence of isobars. The exact mass of the monoisotopic ion 792.5334 fits attribution of [PC 34:2 + Cl]⁻ . (B) The loss of 50 (ClCH³) from *m/z* 794 suggests that it is a chlorinated adduct. The mechanism of the ClCH³ fragmentation has been studied by Zhang et al.(6) C) MS³ of the [M-50] fragment shows that the 792 peak may be PC (16:0/18:2).(6) (D) The HRMS peak 794.5277 may be due to deprotonated PS(P-38:4). The peak at 794.5503 can be attributed to PC(34:1). (E) Product ion spectrum of *m/z* 794 shows loss of 50 which is likely ClCH³, suggesting 794 is the chloride adduct of a PC. (F) MS³ of the [M-50] fragment supports PC (16:0/18:1) as the structure of the PC (34:1).
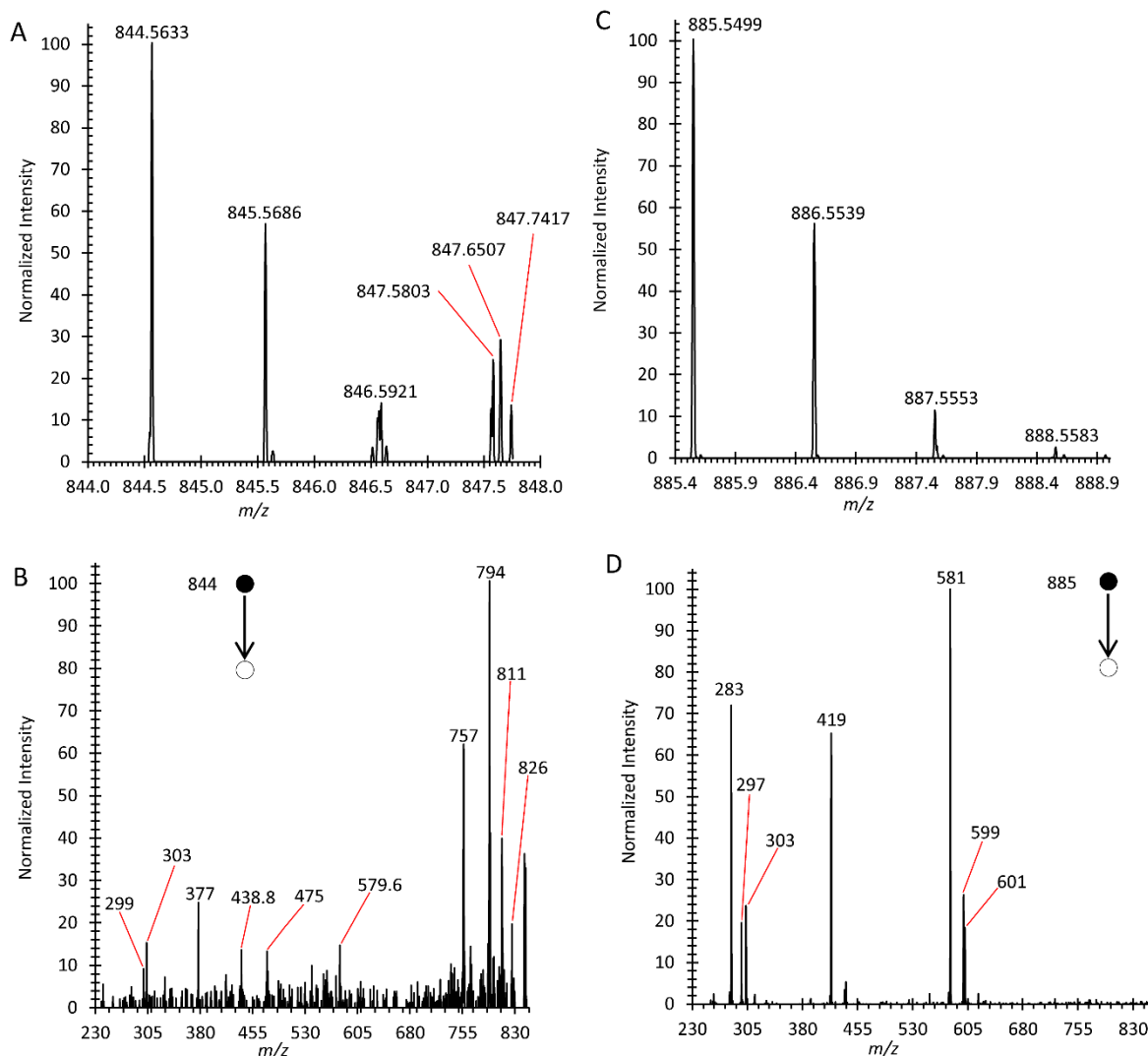
Figure 2.8 High resolution (A) and MS/MS (B) data for *m/z* 844. High resolution (C) and MS/MS (D) data for *m/z* 885. (A) Monoisotopic peak at 844.5633 supports attribution to [PC 38:4 + Cl]⁻ . Data was from one scan for high-resolution data which may explain the difference in expected isotopic pattern for a chlorinated PC adduct [PC 38:4 +Cl]⁻ . (B) Loss of 50 (likely ClCH₃) from *m/z* 844 in MS² spectrum supports the chlorinated adduct of a PC (6) and peak at *m/z* 303 indicates arachidonic acid as one of the fatty acid chains. (C) Experimental exact mass 885.5499 supports the chemical formula $C_{47}H_{82}O_{13}P$, consistent with [PI 38:4 – H]⁻. (D) MS/MS spectrum shows that fatty acids are likely arachidonate (*m/z* 303.25) and stearate (*m/z* 283.25), also the *m/z* 581 and 601 originate from the neutral losses of these fatty acids, respectively.

2.4.2   Desorption Electrospray Ionization

The results from the DESI-MSI experiments, used as a reference method to compare with the TS-MS results, are shown in Figure 2.9. Similar but better separation is observed in the DESI-MSI PCA score plot (Figure 2.9); however, the DESI loading plot (Figure 2.9) is characterized by

m/z 788 and 810 (tentatively deprotonated PS 36:1 and PS 38:4, respectively) and the same TS ion *m/z* 885 (deprotonated PI 38:4). These ions (*m/z* 788,810, and 885) are evident in the averaged spectra for RCC and healthy renal tissue shown in Figure 2.9.
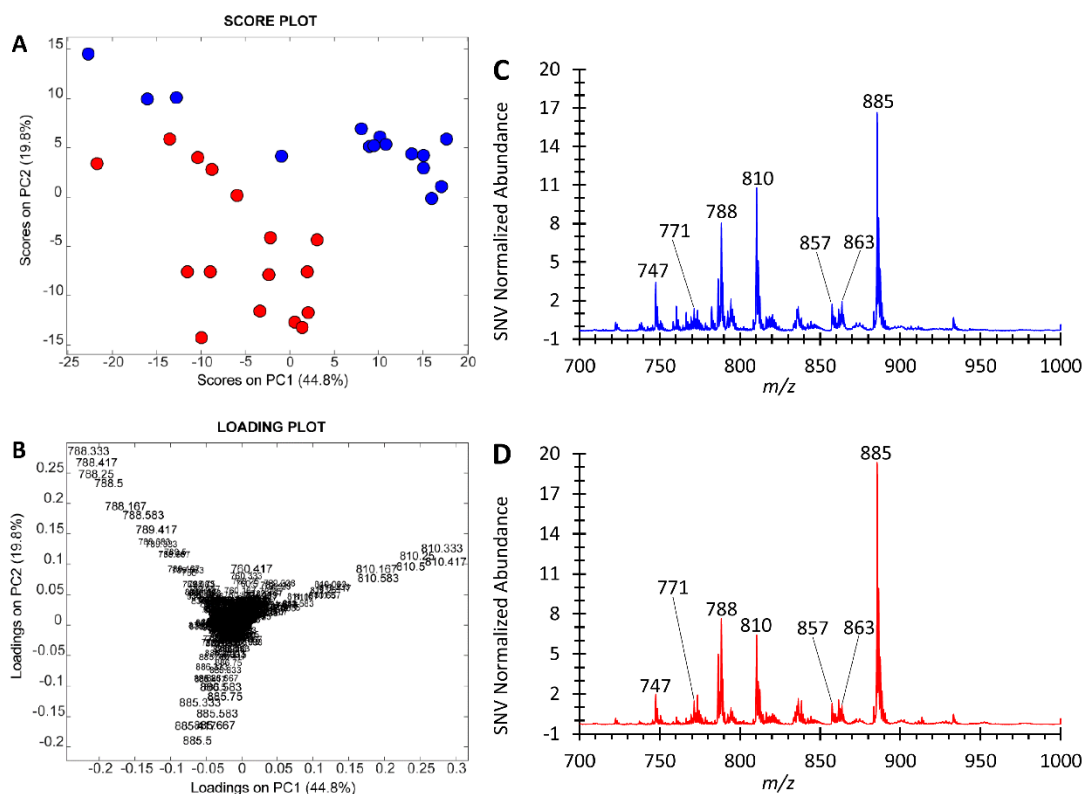
Figure 2.9 Negative ion mode DESI-MSI results from the surgical kidney specimens. A) The PCA score plot of the DESI-MSI data. Each object represents a mass spectrum obtained from a ROI of a single tissue specimen. Healthy renal tissue is blue, RCC is red. B) The corresponding loading plot for the score plot in A, showing contributions of *m/z* 788 ([PS 36:1-H]⁻), 810 ([PS 38:4-H]⁻), and 885 ([PI 38:4 - H]⁻) in the separation observed in the score plot. C & D) The SNV normalized average DESI mass spectra of the healthy renal tissue and RCC classes, respectively.
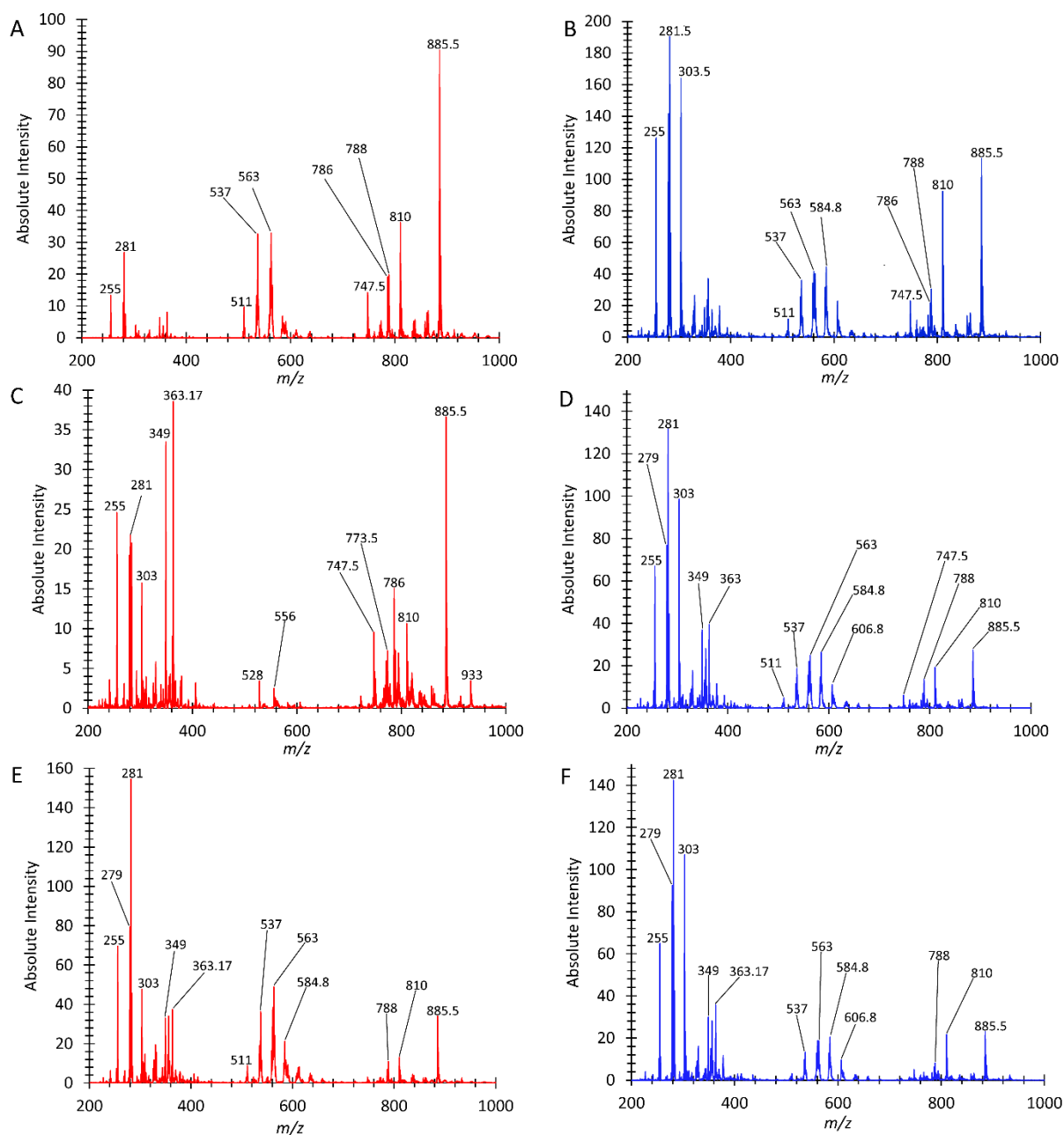
Figure 2.10 The mass spectra obtained by ROI selection from 3 sets of paired RCC and healthy renal tissue. ROI selection was guided by histopathological evaluation. Due to tissue homogeneity as determined by the pathologist, the entire tissue section was used for ROI selection. A) ROI from specimen 34. B) ROI from specimen 35. C) ROI from specimen 15. D) ROI from specimen 14. E) ROI from specimen 22. F) ROI from specimen 21.
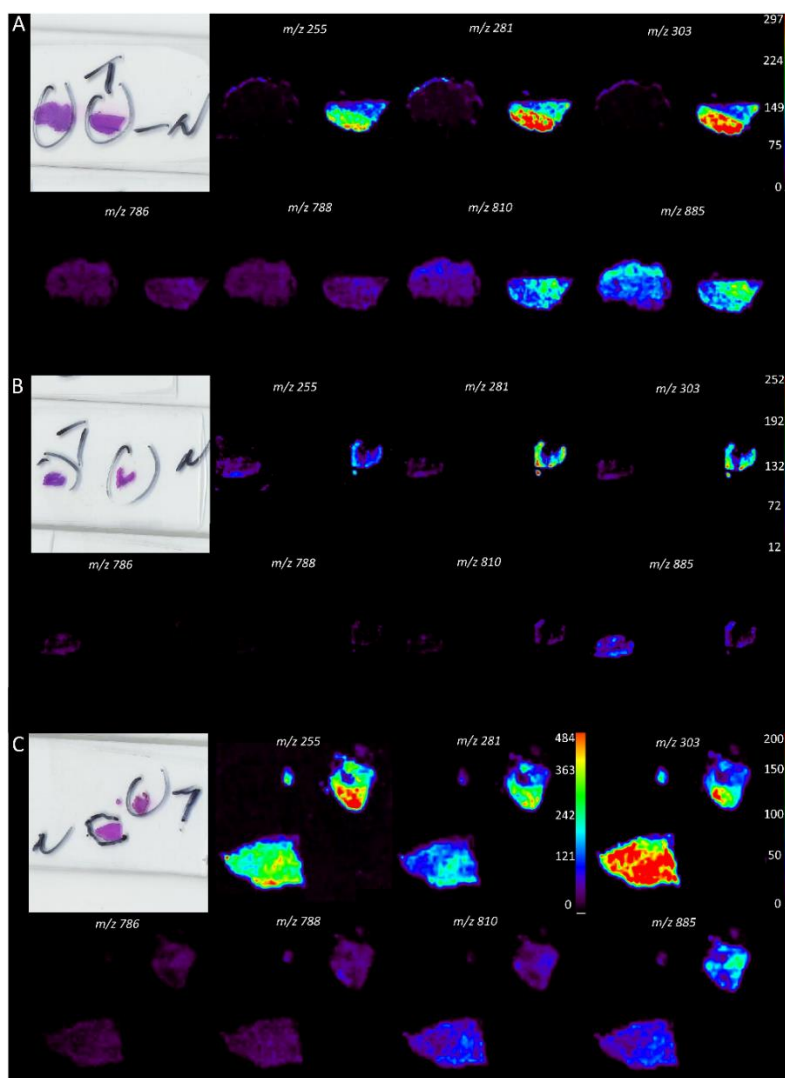
Figure 2.11 DESI-MS ion images of 3 paired normal and RCC specimens visualized as heat maps along with scanned images of the H&E stained tissues. The sets of images in A and B are all on the same heat-map scale. Scale bar corresponds to the absolute MS intensity. The ion *m/z* 281 in C is on a custom scale due to the high abundance of the ion in the tissues. Note that the scale between each set of paired specimens (e.g. A vs. B) is different. A) Specified ion images for specimens 34(left tissue) & 35 (right tissue), along with H&E stained tissue with histopathological evaluation. Scale bar is shown next to *m/z* 303. B) Specified ion images for specimens 15(left tissue) and 14(right tissue), with H&E stained tissue. C) Specified ion images for specimens 21(lower left tissue) and 22(upper right tissue) and H&E stained tissue. Scale bar next to *m/z* 281 is unique scale for that image. The scale bar for the rest of the ion images is shown next to *m/z* 303.
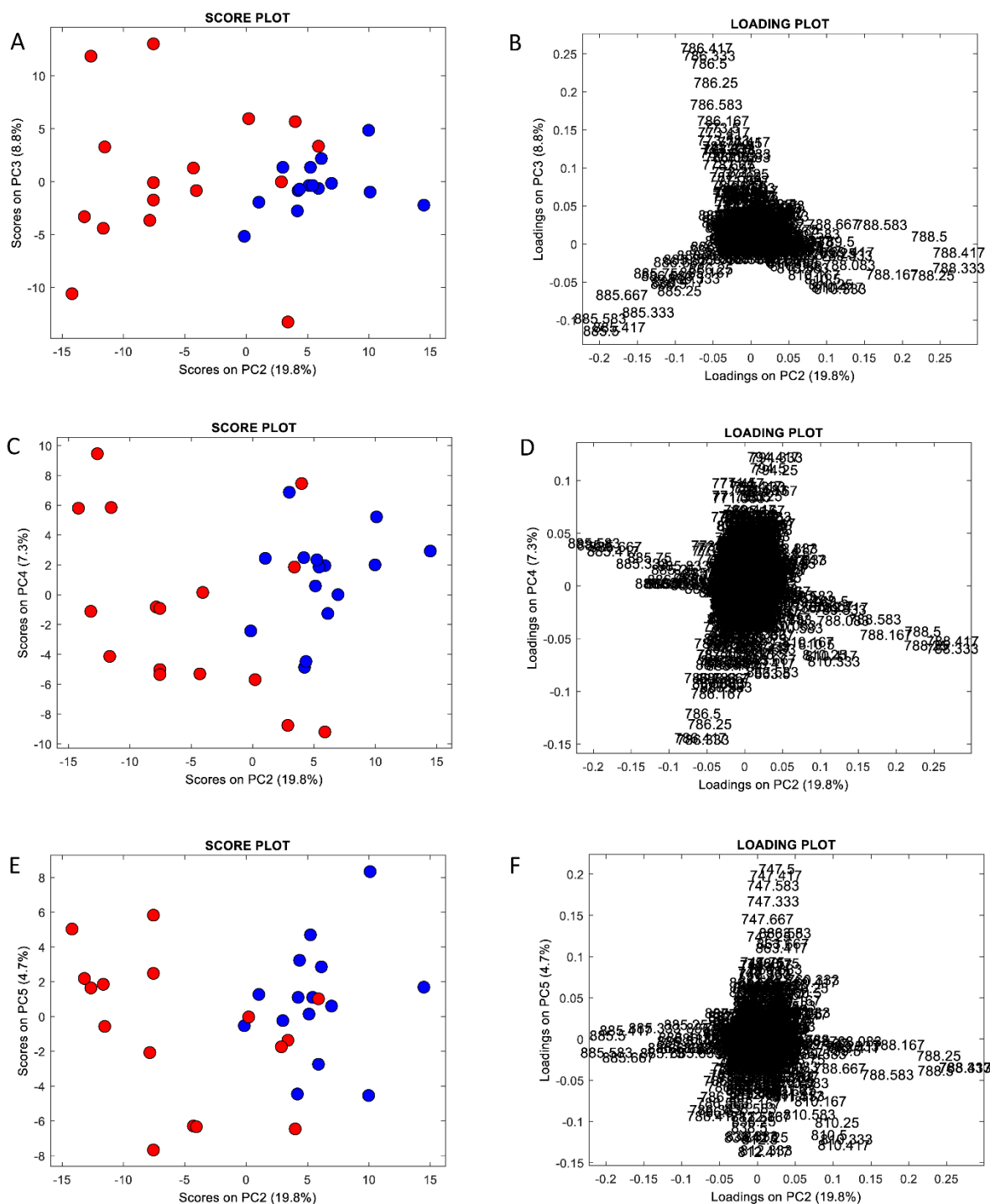
Figure 2.12 Principal component analysis results for PC3 vs. PC2, PC4, vs. PC2, and PC5 vs. PC2 for the DESI-MS dataset. A&B) Score and loading plots for PC3 vs. PC2, respectively. C&D) Score and loading plots for PC4 vs. PC2, respectively. E&F) Score and loading plots for PC5 vs. PC2, respectively.

The significant contribution of *m/z* 810 is also observed in the TS-MS data in PC5 (Figure 2.4). Examples of H&E stained tissue sections after DESI-MS analysis as well as a selection of DESI-MS ion images for specimens from three subjects are shown in Figure 2.11. Additional PCA score and loading plots for the DESI-MS data are shown in Figure 2.12. Cross validation was performed on the DESI PCA-LDA model in a fashion like the TS datasets. Using five deletion groups and three principal components, the average sensitivity was 100% and specificity was 88.9%.

The difference in abundance of the type of ion detected (i.e. chlorinated adduct vs. deprotonated molecule) between TS and DESI can be attributed simply to differences in ionization mechanisms, increased biofluid content in the fresh tissue analyzed by TS-MS, and perhaps to the use of different spray solvents (methanol for TS and 1:1 DMF-ACN for DESI).(28, 33) Relative to DESI, the greater contribution of chlorinated adducts in TS-MS is a previously reported phenomenon. (28) The difference between DESI and TS mass spectra suggest that future uses of TS as a diagnostic method will require the development of spectral databases (training sets) composed of TS-MS data.

2.4.3   Future Studies

The reported data suggest that TS-MS has the potential to yield diagnostic chemical information from fresh healthy renal tissue and RCC tissue. Prior to undertaking a large-scale study, a TS-MS ionization source equipped with microcontrollers for precise probe manipulation and an automated solvent delivery system should be designed and optimized to increase data quality and reproducibility. While the TS-MS experiments were conducted on tissue after resection from a human subject, the analysis occurred on the intraoperative timescale. The results support larger scale studies of ex vivo surgical tissue using TS-MS to generate a comprehensive database of RCC specimens.

Additional aspects worth investigating are tumor heterogeneity and tumor margins. Ideally, the short analysis time and minimal invasiveness of TS-MS suggest that it might be used to profile various regions within the tumor mass itself and in the surrounding parenchyma. It would be interesting to investigate how the TS-MS lipid profiles (e.g. molecular information) vary within the tumor, as it has been shown that the extent of tumor heterogeneity is underestimated because of limitations in the number of samples that can be obtained. (45, 46) Additionally, TS-MS may

aid in delineation of the tumor-parenchyma margin (i.e. tumor margin) in partial nephrectomies, as the utility of intraoperative frozen section analysis remains controversial.(47) This would be beneficial because negative parenchymal surgical margins of any size (e.g. less than 1mm) for localized, low grade (T1) RCC have been shown to result in virtually 0% recurrence of the disease. (48, 49)

2.5 Conclusions

This preliminary study demonstrated the feasibility of TS-MS analysis on a small number of fresh ex vivo surgical tissue specimens, as an intermediate step between frozen tissue analysis and intraoperative analysis. TS-MS differentiation of specimens using PCA and LDA was demonstrated, and the ions of greatest importance for separation were tentatively identified as complex membrane phospholipids *m/z* 794 (PC 16:0/18:1), 885 (PI 38:4), and 844 (PC 38:4). DESI-MS differentiation of RCC and normal specimens was readily achieved by TS-MS and DESI-MS although different ions were important for separation between the two methods. Future work aims to expand the number of specimens in order to validate diagnostic capabilities, and further study the analytical figures of merit of the TS-MS methodology. The applicability of the technique is likely not exclusive to renal cell carcinomas, and it would be fruitful to investigate TS-MS in other cancers. In addition, refinements to the TS-MS methodology should be pursued to increase the ruggedness, ease of use, accuracy, and reproducibility of the measurements.

2.6 Acknowledgements

2.7 References

1. Howlader N NA, Krapcho M, Garshell J, Miller D, Altekruse SF, Kosary CL, Yu M, Ruhl J, Tatalovich Z,Mariotto A, Lewis DR, Chen HS, Feuer EJ, Cronin KA. SEER Cancer Statistics Review, 1975-2012. National Cancer Institute. 2015.

2. Chow WH, Dong LM, Devesa SS. Epidemiology and risk factors for kidney cancer. Nat Rev Urol. 2010;7(5):245-57.

3. Lasseigne BN, Burwell TC, Patil MA, Absher DM, Brooks JD, Myers RM. DNA methylation profiling reveals novel diagnostic biomarkers in renal cell carcinoma. BMC Med. 2014;12:235.

4. Liao L, Testa JR, Yang H. The roles of chromatin-remodelers and epigenetic modifiers in kidney cancer. Cancer Genet. 2015;208(5):206-14.

5. Durinck S, Stawiski EW, Pavia-Jimenez A, Modrusan Z, Kapur P, Jaiswal BS, et al. Spectrum of diverse genomic alterations define non-clear cell renal carcinoma subtypes. Nat Genet. 2014;47(1):13-21.

6. Masui O, White NM, DeSouza LV, Krakovska O, Matta A, Metias S, et al. Quantitative proteomic analysis in metastatic renal cell carcinoma reveals a unique set of proteins with potential prognostic significance. Mol Cell Proteomics. 2012;12(1):132-44.

7. Morgan TM, Seeley EH, Fadare O, Caprioli RM, Clark PE. Imaging the clear cell renal cell carcinoma proteome. J Urol. 2012;189(3):1097-103.

8. Guo T, Kouvonen P, Koh CC, Gillet LC, Wolski WE, Rost HL, et al. Rapid mass spectrometric conversion of tissue biopsy samples into permanent quantitative digital proteome maps. Nat Med. 2015;21(4):407-13.

9. Ganti S, Weiss RH. Urine metabolomics for kidney cancer detection and biomarker discovery. Urol Oncol. 2011;29(5):551-7.

10. Monteiro MS, Carvalho M, Bastos ML, Pinho PG. Biomarkers in renal cell carcinoma: a metabolomics approach. Metabolomics. 2014;10:1210-22.

11. Yoshimura K, Chen LC, Mandal MK, Nakazawa T, Yu Z, Uchiyama T, et al. Analysis of renal cell carcinoma as a first step for developing mass spectrometry-based diagnostics. J Am Soc Mass Spectrom. 2012;23(10):1741-9.

12. Dill AL, Eberlin LS, Zheng C, Costa AB, Ifa DR, Cheng L, et al. Multivariate statistical differentiation of renal cell carcinomas based on lipidomic analysis by ambient ionization imaging mass spectrometry. Anal Bioanal Chem. 2010;398(7-8):2969-78.

13. Santagata S, Eberlin LS, Norton I, Calligaris D, Feldman DR, Ide JL, et al. Intraoperative mass spectrometry mapping of an onco-metabolite to guide brain tumor surgery. Proc Natl Acad Sci U S A. 2014;111(30):11121-6.

14. Eberlin LS, Norton I, Orringer D, Dunn IF, Liu X, Ide JL, et al. Ambient mass spectrometry for the intraoperative moleucular diagnosis of human brain tumors. Proc Natl Acad Sci U S A. 2013;110(5):1611-6.

15. Schafer KC, Balog J, Szaniszlo T, Szalay D, Mezey G, Denes J, et al. Real time analysis of brain tissue by direct combination of ultrasonic surgical aspiration and sonic spray mass spectrometry. Anal Chem. 2011;83(20):7729-35.

16. Agar NY, Golby AJ, Ligon KL, Norton I, Mohan V, Wiseman JM, et al. Development of stereotactic mass spectrometry for brain tumor surgery. Neurosurgery. 2011;68(2):280.

17. Balog J, Sasi-Szabo L, Kinross J, Lewis MR, Muirhead LJ, Veselkov K, et al. Intraoperative tissue identification using rapid evaporative ionization mass spectrometry. Sci Transl Med. 2013;5(194):194ra93.

18. Balog J, Kumar S, Alexander J, Golf O, Huang J, Wiggins T, et al. In Vivo Endoscopic Tissue Identification by Rapid Evaporative Ionization Mass Spectrometry (REIMS). Angewandte Chemie (International ed in English). 2015;54(38):11059-62.

19. Marien E, Meister M, Muley T, Fieuws S, Bordel S, Derua R, et al. Non-small cell lung cancer is characterized by dramatic changes in phospholipid profiles. Int J Cancer. 2015;137(7):1539-48.

20. Eberlin LS, Gabay M, Fan AC, Gouw AM, Tibshirani RJ, Felsher DW, et al. Alteration of the lipid profile in lymphomas induced by MYC overexpression. Proc Natl Acad Sci U S A. 2014;111(29):10450-5.

21. Ifa DR, Eberlin LS. Ambient Ionization Mass Spectrometry for Cancer Diagnosis and Surgical Margin Evaluation. Clin Chem. 2016;62(1):111-23.

22. Kerian KS, Jarmusch AK, Pirro V, Koch MO, Masterson TA, Cheng L, et al. Differentiation of prostate cancer from normal tissue in radical prostatectomy specimens by desorption electrospray ionization and touch spray ionization mass spectrometry. Analyst. 2015;140(4):1090-8.

23. Mandal MK, Saha S, Yoshimura K, Shida Y, Takeda S, Nonami H, et al. Biomolecular analysis and cancer diagnostics by negative mode probe electrospray ionization. Analyst. 2013;138(6):1682-8.

24. Wiseman JM, Puolitaival SM, Takáts Z, Cooks RG, Caprioli RM. Mass spectrometric profiling of intact biological tissue by using desorption electrospray ionization. Angewandte Chemie (International ed in English). 2005;117(43):7256-9.

25. Alonso T, Morgan RO, Marvizon JC, Zarbl H, Santos E. Malignant transformation by ras and other oncogenes produces common alterations in inositol phospholipid signaling pathways. Proc Natl Acad Sci U S A. 1988;85(12):4271-5.

26. Gaipl RC, Christina J, Luis M, Benjamin F, Martin H, Udo. Phospholipids: Key Players in Apoptosis and Immune Regulation. Molecules. 2009;14(12):4892-914.

27. Ackerman D, Simon MC. Hypoxia, lipids, and cancer: surviving the harsh tumor microenvironment. Trends Cell Biol. 2014;24(8):472-8.

28. Kerian KS, Jarmusch AK, Cooks RG. Touch spray mass spectrometry for in situ analysis of complex samples. Analyst. 2014;139:2714-20.

29. Mandal MK, Yoshimura K, Chen LC, Yu Z, Nakazawa T, Katoh R, et al. Application of probe electrospray ionization mass spectrometry (PESI-MS) to clinical diagnosis: solvent effect on lipid analysis. J Am Soc Mass Spectrom. 2012;23(11):2043-7.

30. Yoshimura K, Mandal MK, Hara M, Fujii H, Chen LC, Tanabe K, et al. Real-time diagnosis of chemically induced hepatocellular carcinoma using a novel mass spectrometry-based technique. Anal Biochem. 2013;441(1):32-7.

31. Balog J, Szaniszlo T, Schaefer KC, Denes J, Lopata A, Godorhazy L, et al. Identification of biological tissues by rapid evaporative ionization mass spectrometry. Anal Chem. 2010;82(17):7343-50.

32. Takats Z, Wiseman JM, Gologan B, Cooks RG. Mass Spectrometry Sampling Under Ambient Conditions with Desorption Electrospray Ionization. Science. 2004;306:471-3.

33. Eberlin LS, Ferreira CR, Dill AL, Ifa DR, Cheng L, Cooks RG. Nondestructive, histologically compatible tissue imaging by desorption electrospray ionization mass spectrometry. ChemBioChem. 2011;12(14):2129-32.

34. Eberlin LS, Tibshirani RJ, Zhang J, Longacre TA, Berry GJ, Bingham DB, et al. Molecular assessment of surgical-resection margins of gastric cancer by mass spectrometric imaging. Proc Natl Acad Sci U S A. 2014;111(7):2436-41.

35. Jarmusch AK, Pirro V, Baird Z, Hattab EM, Cohen-Gadol AA, Cooks RG. Lipid and metabolite profiles of human brain tumors by desorption electrospray ionization-MS. Proc Natl Acad Sci U S A 2016;113(6):1486-91.

36. Shroff EH, Eberlin LS, Dang VM, Gouw AM, Gabay M, Adam SJ, et al. MYC oncogene overexpression drives renal cell carcinoma in a mouse model through glutamine metabolism. Proc Natl Acad Sci U S A. 2015;112(21):6539-44.

37. Calligaris D, Feldman DR, Norton I, Olubiyi O, Changelian AN, Machaidze R, et al. MALDI mass spectrometry imaging analysis of pituitary adenomas for near-real-time tumor delineation. Proc Natl Acad Sci U S A 2015;112(32):9978-83.

38. Prentice BM, Chumbley CW, Caprioli RM. High-speed MALDI MS/MS imaging mass spectrometry using continuous raster sampling. J Mass Spectrom. 2015;50(4):703-10.

39. Spraggins JM, Caprioli RM. High-Speed MALDI-TOF Imaging Mass Spectrometry: Rapid Ion Image Acquisition and Considerations for Next Generation Instrumentation. J Am Soc Mass Spectrom. 2011;22(6):1022-31.

40. Bennet RV, Gamage CM, Fernandez FM. Imaging of biological tissues by desorption electrospray ionization mass spectrometry. J Visualized Exp. 2013(77):e50575.

41. Pirro V, Eberlin LS, Oliveri P, Cooks RG. Interactive hyperspectral approach for exploring and interpreting DESI-MS images of cancerous and normal tissue sections. Analyst. 2012;137(10):2374-80.

42. Pirro V, Oliveri P, Ferreira CR, Gonzalez-Serrano AF, Machaty Z, Cooks RG. Lipid characterization of individual porcine oocytes by dual mode DESI-MS and data fusion. Anal Chim Acta. 2014;848:51-60.

43. González-Serrano AF, Pirro V, Ferreira CR, Oliveri P, Eberlin LS, Heinzmann J, et al. Desorption electrospray ionization mass spectrometry reveals lipid metabolism of individual oocytes and embryos. PloS one. 2013;8(9):e74981.

44. Alonso T, Santos E. Increased intracellular glycerophosphoinositol is a biochemical marker for transformation by membrane-associated and cytoplasmic oncogenes. Biochem Biophys Res Commun. 1990;171(1):14-9.

45. Ricketts CJ, Linehan WM. Intratumoral heterogeneity in kidney cancer. Nat Genet. 2014;46(3):214-5.

46. Gerlinger M, Horswell S, Larkin J, Rowan AJ, Salm MP, Varela I, et al. Genomic architecture and evolution of clear cell renal cell carcinomas defined by multiregion sequencing. Nat Genet. 2014;46(3):225-33.

47. Sterious SN, Simhan J, Smaldone MC, Tsai KJ, Canter D, Wameedh E, et al. Is there a benefit to frozen section analysis at the time of partial nephrectomy? Can J Urol. 2013;20(3):6778-84.

48. Sutherland SE, Resnick MI, Maclennan GT, Goldman HB. Does the size of the surgical margin in partial nephrectomy for renal cell cancer really matter? J Urol. 2001;167(1):61-4.

49. Lam JS, Bergman J, Breda A, Schulam PG. Importance of surgical margins in the management of renal cell carcinoma. Nat Clin Pract Urol. 2008;5(6):308-17.

CHAPTER 3. INTRAOPERATIVE ASSESSMENT OF GLIOMA TUMOR MARGINS DURING SURGICAL RESECTION BY DESORPTION ELECTROSPRAY IONIZATION-MS

This chapter was adapted from the manuscript published in *Proceedings of the National Academy of Sciences of the United States of America:* Pirro V, Alfaro CM, Jarmusch AK, Hattab EM, Cohen-Gadol AA, Cooks RG. Intraoperative assessment of tumor margins during glioma resection by desorption electrospray ionization-mass spectrometry. Proc Natl Acad Sci USA 2017; 114(26): 6700-6705.

3.1   Abstract

Intraoperative desorption electrospray ionization-mass spectrometry (DESI-MS) is used to characterize tissue smears by comparison with a library of DESI mass spectra of pathologically-determined tissue types. Measurements are performed in the operating room within 3 minutes. These mass spectra provide direct information on tumor infiltration into white or grey brain matter based on N-acetylaspartate (NAA) and on membrane-derived complex lipids. The mass spectra also indicate the isocitrate dehydrogenase mutation status of the tumor via detection of 2-hydroxyglutarate, currently assessed postoperatively on biopsied tissue using immunohistochemistry. Intraoperative DESI-MS measurements made at surgeon-defined positions enable assessment of relevant disease state of tissue within the tumor mass and examination of the resection cavity walls for residual tumor. Results for 73 biopsies from 10 surgical resection cases show that DESI-MS allows detection of glioma and estimation of high tumor cell percentage (TCP) at surgical margins with 93% sensitivity and 83% specificity. TCP measurements from NAA are corroborated by indirect measurements based on lipid profiles. Notably, high percentages (>50%) of unresected tumor were found in one-half of the margin biopsy smears, even in cases where postoperative MRI suggested gross total tumor resection. Unresected tumor causes recurrence and malignant progression, as observed within a year in one case examined in this study. These results corroborate the utility of DESI-MS in assessing surgical margins for maximal safe tumor resection. Intraoperative DESI-MS analysis of tissue smears, ex

vivo, can be inserted into the current surgical workflow with no alterations. The data underscore the complexity of glioma infiltration.

3.2   Introduction

We describe the rapid analysis of neurological tissue smears by desorption electrospray ionization-mass spectrometry (DESI-MS) in the operating room (OR) from 10 subjects who underwent glioma resection. Biopsied tissue specimens from surgeon-defined positions in the tumor and the walls of the resection cavity were smeared onto glass microscope slides and sprayed with charged solvent droplets to extract molecules from the unprocessed tissue while the splashed secondary droplets were vacuumed into a customized ion trap mass spectrometer modified for use in the OR at Indianapolis IU (Indiana University) Health Methodist Hospital. Three separate items of information were sought from the DESI mass spectra: i) tissue type, specifically whether glioma, white brain matter, grey brain matter or mixtures of these types; ii) isocitrate dehydrogenase (IDH) status, i.e., whether or not this enzyme carries a characteristic mutation, the presence of which is associated with more favorable prognosis; and iii) the tumor cell percentage (TCP) in the sampled biopsy as a measure of tumor infiltration.

The infiltrative nature of most gliomas, as well as visual and textural similarities between infiltrative regions and normal brain parenchyma, poses a substantial challenge to the neurosurgeon during tumor resection. Microsurgical resection aims to maximize tumor excision while minimizing morbidity (1, 2) as the extent of resection affects both overall and progression-free survival. Improved survival and quality of life correlates with maximal resection of both low- and high-grade gliomas. (3) Importantly, tumor recurrence and malignant progression is likely to occur from residual tumor within 0.5 cm of the resection (i.e., surgical) margin, viz. the point at which resection ceases. (3) Stereotactic volumetric resection is usually based on preoperative structural and functional MRI used to determine tumor location, size, surgical approach, and to estimate the extent of resection achievable. Intraoperative MRI has been implemented to mitigate anatomical shifts and improve resection; however, MRI costs and technical hurdles, such as prolonged surgery time for image acquisition, limit its practical and routine implementation. (1)

The standard diagnostic approach of intraoperative consultation, pathology, provides information on tumor type and grade. Intraoperative histopathological evaluation of tissue resected from surgical margins to estimate residual tumor infiltration is uncommon, partly because

preparation and analysis of tissue sections or smears is laborious and time consuming, and partly due to the inherent difficulty in assessing the degree of infiltration in suboptimal preparations. Therefore, the amount of residual tumor near the resection margins is not usually measured during surgery and is only assessed postoperatively and indirectly by MRI.(1, 4)

Following the publication of the 2016 WHO classification of central nervous system tumors,(5) immunohistochemistry and molecular testing are also performed on sampled neurological tissue to evaluate several diagnostic and prognostic markers (e.g., IDH mutation and 1p/19q co-deletion) but results again are available only postoperatively. The need for near real-time assessment of tumor pathology, genetics, and margin status during surgical resection in predicting patient outcome would suggest advantages to a multimodal approach in which imaging and diagnostic technologies are coupled.

The analysis of neurological tissue smears using DESI-MS has the potential to become an ex vivo diagnostic strategy that can provide information on each of three points that we discuss in turn: i) Tissue type, specifically glioma, white brain matter, grey brain matter, or a mixture of these. The use of ambient ionization MS methods, specifically DESI (6) and rapid evaporative ionization mass spectrometry (REIMS),(7) to distinguish diseased from healthy tissue based on membrane derived phospholipid signatures is now well established. Note that an alternative method of molecular diagnosis of neurological tissue in the form of Raman spectroscopy is being developed concurrently.(8, 9) Both DESI-MS and REIMS have been applied to different organs,(7, 10-14) generally with excellent disease discrimination via comparison with spectra of pathology-defined reference material. REIMS requires the use of special surgical procedures but gives real-time information. DESI gives results in a few minutes but is applicable to any surgical method, with no alteration in procedures, and the same tissue smears can be stained after analysis and blindly evaluated by an expert pathologist for validation. While mass spectral profiles (i.e., chemical signatures) of tissue sections allow accurate differentiation between gliomas and normal brain parenchyma,(15-20) we emphasize in this intraoperative study the characterization of tissue smears, especially the recognition of those of mixed compositions. ii) IDH status. It has previously been shown that the presence of IDH mutation, a prognostic marker in gliomas,(21, 22) can be inferred by the MS detection of 2-hydroxyglutarate (2HG) in tissue sections.(20) The same discriminating information is sought here in tissue smears - which can be prepared and analyzed inside the OR more easily and rapidly than tissue sections (19, 23) - and this is the approach utilized

in this intraoperative study. iii) Percentage of tumor cells. Encouraging preliminary results on tissue sections indicated that it might be possible to estimate TCP in tissue via measurements of N-acetylaspartate (NAA). However, this highly important objective needed to be tested in the relevant intraoperative environment, especially on tissue resected near surgical margins for identification of residual tumor, and that is a significant aim of this study.
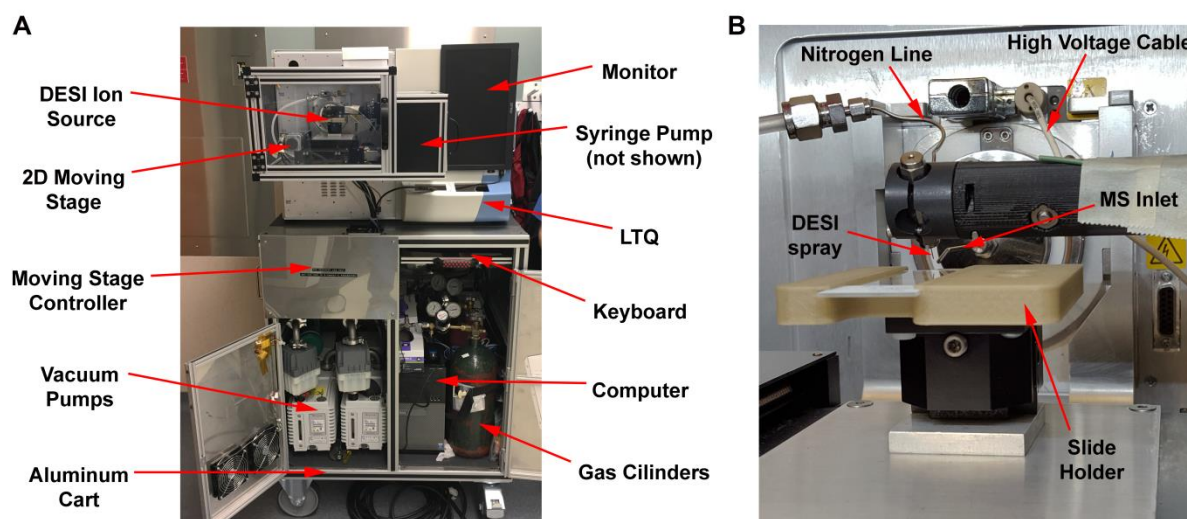
Figure 3.1**(A)** Intraoperative OR mass spectrometer for tissue smear analysis by DESI-MS. **(B)** Zoomed-in picture of the enclosed DESI-MS ion source.

3.3   Materials and Methods

3.3.1   Specimens

Ten patients who underwent glioma tumor resection at the Methodist Hospital in Indianapolis were recruited for the study. Written informed consent and HIPAA authorization were provided by all patients. The study was conducted in conformity with institutional protocols established at the Indiana University School of Medicine (IRB # 1410342262). Details of the patient cohort are reported in Table 3.3 and 3.4. Tissue biopsies resected during surgical glioma removal were provided to the Purdue researchers with no pretreatment and analyzed by DESI-MS inside the operating room (OR). DESI-MS measurements and off-line data acquisition had no effect on the surgical procedure. Tissue biopsies (5-50 mm^3) were used to prepare tissue smears on glass microscope slides.(1) Tissue specimens were smeared (a total of 80 smears, 73 usable) using a custom 3D-printed device.(1, 2) This disposable device was designed to smear the tissue

along the longer dimension of the glass slide, and confine it to the central area with an appropriate thickness, avoiding excessive dilution of the cellular material that would negatively impact the MS measurements. The act of smearing sufficiently homogenizes the tissue, mixing heterogeneous morphological features, so that there is no need to record mass spectra over more than a small fraction of the area of the smear to obtain representative MS data. The preparation of tissue smears is operator- and tissue-dependent (e.g. tumorous tissue does not smear evenly and tends to form clumps of tissue, whereas normal brain parenchyma tends to smear more homogeneously in thin layers). However, the intraoperative preparation of suboptimal smears does not affect the quality of mass spectral data obtained, as smearing disrupts tissue architecture but causes no alteration to the chemical content of the tissue, which is used as the diagnostic signature. As discussed elsewhere, variation in absolute signal intensity was noted and assigned to differences in smear cellularity and thickness, but relative spectral profiles (on which chemical diagnosis is based) were largely unaffected.(2, 3) Subsequently to DESI-MS analysis, all smears were sent to the Indiana University pathology laboratory for H&E staining using the pneumatic tube system of the hospital. Smears were evaluated by an expert pathologist, blindly. Pathological evaluation was used to validate molecular diagnosis by DESI-MS.

Seventy-three smears were included in the study. Seven of the original 80 were excluded for insufficient data quality. Three smears provided no MS signal (# 2, 56, 57, Table 3.4); two of which (# 56, 57) had acellular tissue as evaluated by post hoc pathology. Four smears (# 23, 30, 47, and 48) were of insufficient quality for pathological evaluation.

3.3.2 DESI-MS Instrumentation and Method

MS measurements were performed using a linear ion trap mass spectrometer (Finnigan LTQ, Thermo Scientific) coupled with a custom DESI source equipped with a precision 2D moving stage. The MS system (Figure 3.1) was modified for use in the OR as follows: (i) encasement of the entire MS system (vacuum pumps, computer, gases) into a transportable cart, (ii) additional vacuum pump noise reduction, (iii) integrated computer system with sealed keyboard, (iv) enclosed custom DESI ion source including an X-Y motion moving stage. The custom DESI interface was modified to fit a 3D printed holder for the microscope slide (Figure 3.1). The instrument was wheeled into the OR for each surgery and positioned following directions from the surgical team (typically, the furthest away from the head of the patient and sterile equipment). The

instrument was turned on before craniotomy began and pumped down for 30 min (on average) prior to analysis of tissue smears.

Table 3.1 DESI-MS Settings.

DESI		
Solvent flow rate	1.0 µL/min	
Pressure of nitrogen gas	170 PSI	
Applied high voltage	−5 kV	
Capillary temperature	275°	
Incident angle	52°	
Spray-to-surface distance	3 mm	
Spray-to-MS distance	7 mm	
Full Scan MS	**Lipid Profile**	**Metabolite Profile**
Mass range	*m/z* 700-1000	*m/z* 80-200
Injection time	250 ms	250 ms
Capillary voltage	−50 V	−50 V
Tube lenses potential	−118 V	−71 V
Tuned mass	*m/z* 786	*m/z* 174
Microscans	3	4
MS/MS CID* fragmentation	**NAA**	**2-HG**
Precursor ion	*m/z* 174	*m/z* 147
Tube lenses potential	−50 V	
Microscans	−71 V	
Microscans	2	
Injection time	500 ms	

DESI-MS was performed using dimethylformamide-acetonitrile (1:1 v/v) to preserve tissue morphology.(4) Both solvents were purchased from Sigma-Aldrich (anhydrous, >99.9% purity). MS measurements were made at four separate positions by coordinating the linear motion of the moving stage (speed, 12.5 mm/s) with the MS acquisition rate. Data were acquired by rastering the glass slide underneath the DESI sprayer in four separate operations. Per each acquisition, data were collected as rows (N=3, 12 mm in length along the X-dimension spanned 8-mm from each other in the Y-dimension). In the first acquisition, negative ions over the mass range *m/z* 700-1000 (which we will refer to as the lipid profile) were collected. The second acquisition collected negative ions over the range *m/z* 80-200 (the metabolite profile). The third and fourth acquisitions were used to record MS/MS product ions for NAA and 2HG by isolating and

fragmenting (collision-induced dissociation) the deprotonated ions *m/z* 174 and 147, respectively (Figure 3.5). The automatic gain control (AGC) was activated to minimize space charge effects in the linear ion trap that produces variable ion currents. Absolute intensities (arbitrary units) rather than relative ion intensities are shown in mass spectra to facilitate comparisons between samples. Total analysis time was 2.2 min for the four acquisitions. After each acquisition, the slide was translated 500 μm in the Y-dimension and the process was repeated. Additional instrument settings are reported in Table 3.1. Multiple MS measurements were acquired across the smear surface to compensate for any lack of tissue homogenization upon smearing. DESI-MS images of tissue smears showed that rastering the DESI spray a few times over the smear, orthogonally to the smearing direction, was sufficient to acquire representative diagnostic lipid and metabolite profiles, while holding the analysis time to a few minutes.(1)

3.3.3   Data Handling

MATLAB software (The MathWorks Inc. Natick, USA) was used to process all data unless otherwise specified. MS data were exported from XCalibur 2.0, converted into mzXML files using MSConverterGUI (http://proteowizard.sourceforge.net/index.shtml), and then imported into MATLAB using the mzxmlreal.mat function. MATLAB structures were comprised of all mass spectra acquired for the lipid profile, metabolite profile, and MS/MS product scans. The *m/z* domain was comprised of 3600 data points for the lipid profile (*m/z* 700-1000) and 1440 for the metabolite profile (*m/z* 80-200), and both used an acquisition step of *m/z* 0.0833. Average DESI-MS spectra of tissue smears were used to provide molecular diagnosis of the tissue using statistical methods for recognition of mass spectral patterns.(1, 2) MS scans from areas of the glass slide containing no smeared tissue were excluded by applying a cut-off to the absolute signal intensity (Figure 3.2). To establish an acceptable criterion for the lipid profile, the ion counts of ions *m/z* 768, 788, 794, 834, 885, and 888 (maximum peak intensity for each ion) – glycerophospholipids selectively present in brain tissue but absent in the glass slide – were summed in individual scans and plotted over the time of acquisition. Only scans with mass spectra having the summed ion counts > cut-off value were used for chemical predictions. Previous examination of DESI-MS images of tissue smears showed that this strategy could be used to identify and accurately remove areas of the glass slide containing no tissue.(1) For the metabolite profile, ions of *m/z* 89 and 175 (present in the tissue regardless of disease state, e.g. tumor) were summed and subtracted from the

intensity of ions *m/z* 119, 143, and 163 (detected on the glass slide). A cut-off in signal intensity was applied to select only scans with total ion count > cut-off. For each selected mass spectrum (both for lipid and metabolite profiles), the full width at half maximum (FWHM) was calculated for the base peak. All spectra with resolution < 1000 were disregarded to reduce the influence of peak broadening due to space charge on the pattern recognition algorithm (Figure 3.2). Space charge occurred occasionally in areas of the smear that were very dense in cellularity or had a large agglomeration of tissue. Irregularities in smear thickness, e.g. clumps of tissue, cause variance in the ion flux and peak broadening. The post hoc resolution filter is an additional countermeasure against peak broadening besides the AGC activation. The retained scans were averaged to obtain a representative mass spectrum of lipid and metabolite profiles respectively. Average product ion scans for NAA (*m/z* 174) and 2HG (*m/z* 147) were also extracted using MATLAB. Stereotactic biopsies were taken using the StealthStation S7 Surgical Navigation System (Medtronic, Minneapolis, USA). MRI volume reconstruction was done using the software InVesalius 3.0 (http://www.cti.gov.br/invesalius). Adobe Photoshop CC 2017 was used to produce publication-quality figures.
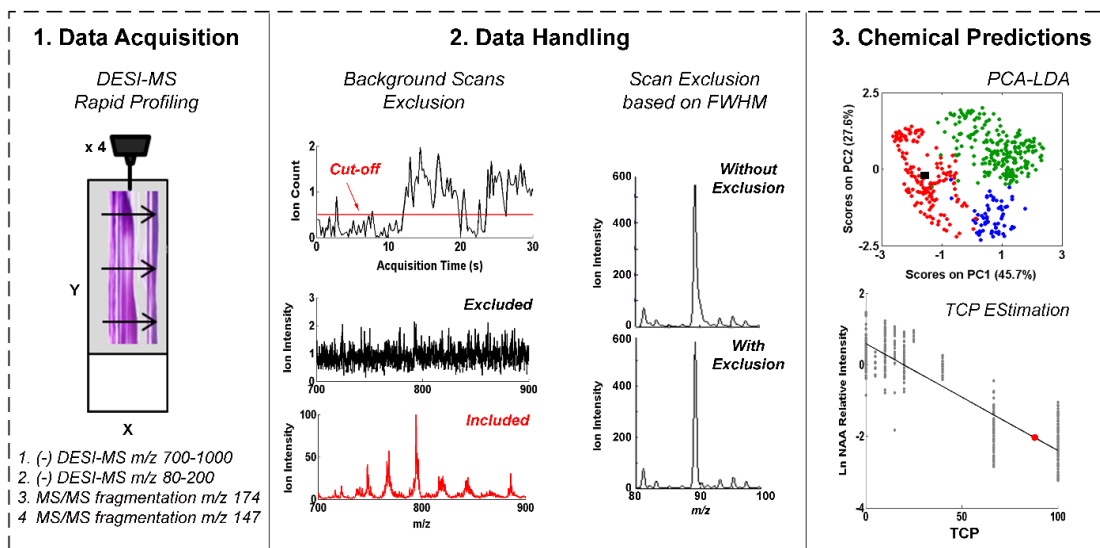
Figure 3.2 Scheme of the analytical method. 1. Data Acquisition: sequential negative-mode DESI-MS data are acquired by rastering 3 lines over the smeared tissue four times (total analysis time 2.2 min). Data acquired are 1: Full scan mass spectrum over the mass range *m/z* 700-1000 (the lipid profile); 2. full scan mass spectrum *m/z* 80-200 (the metabolite profile); 3. MS/MS CID fragmentation for the precursor ion *m/z* 174, NAA; 4. MS/MS CID fragmentation for the precursor ion *m/z* 147, 2-HG. MS instrument settings are reported in Table 3.1. Data Handling: based on the summed ion Intensity calculated as Isummed = I768 + I788 + I794 + I834 + I885 + I888, a cut-off of signal intensity is used to remove scans associated with the background of the glass slide where no tissue is smeared. Only scans with Isummed > cut-off are selected. The base peak resolution is calculated as M/ΔM for each selected scan. ΔM is calculated as full width at half maximum (FWHM). Scans with resolution < 1000 are disregarded to reduce bias due to peak broadening on the algorithm used for mass spectral pattern recognition. 3. Chemical Predictions: Average lipid and metabolite profiles are used to predict tissue state by mid-level fusion PCA-LDA.(1, 2) Tissue smear is predicted as grey matter, white matter or glioma. TCP is estimated via linear regression of the NAA intensity normalized to the total ion counts.(1, 2)

3.3.4   PCA-LDA Prediction of Brain Tumor

Tissue smears were chemically diagnosed as grey matter, white matter or glioma using linear discriminant analysis (LDA) with data compression by principal component analysis (PCA). Details can be found elsewhere.(1, 2) The mass spectral patterns detected for the tissue smears were tested against a reference library of spectra that was built using histologically-defined tissue sections analyzed by DESI-MS imaging (2). The average lipid and metabolite profiles were used for each smear. Projection of the PCA scores computed for each tested smear was graphically shown as black point onto the PCA score space of the reference library of DESI-MS spectra (Figure 3.3). The projection provides information about the similarity between the mass spectral signatures

of the smear and those of grey matter, white matter, and glioma. This similarity drives the LDA prediction into one of these three categories.(1) Pathology evaluation was given for the overall smear consistent with prior mixing of the tissue. The smear was either categorized as tumor, white matter, grey matter or infiltrated tissue not otherwise specified (IT nos).

3.3.5 Estimation of Tumor Cell Percentage Using NAA

The ion intensity of NAA (*m/z* 174) normalized to the total ion count (TIC) was used to estimate the percentage of tumor cells via linear regression. A least-squares first polynomial model used to predict TCP in tissue smears was built using histologically-defined tissue sections analyzed by DESI-MS imaging, as described elsewhere.(2) TCP was estimated using the logarithmic intensity of the TIC normalized NAA signal intensity in the average metabolite profile (Figure 3.7). Pathological evaluation was given for the overall smear consistent with prior tissue mixing. Values of 0% and 100% were assigned to all samples whose predictions exceeded those bounds (<0% and >100%).

3.3.6 Estimation of Tumor Cell Percentage Using Phospholipid Profiles

Representative lipid profiles of grey matter, white matter, and glioma were obtained by averaging spectra of histologically-defined tissue sections analyzed by DESI-MS imaging.(2) Infiltrated tissue with TCP< 15% was used for grey and white matter, high grade and high density tumor tissue (TCP > 90%) was used to represent gliomas. Lipid signature of all binary and tertiary mixtures of grey matter, white matter and gliomas were mathematically computed using the relationship $Y = b_1X_1 + b_2X_2 + b_3X_3$ where b_1, b_2, and b_3 represent the percentages of each component (grey matter, white matter and glioma) in mixture whose sum is constrained to 100%, and Y is the TIC normalized intensity of each *m/z* value (Figure 3.8). The mixed composition of grey matter, white matter, and glioma was estimated for tissue smears based on the minimum root-mean-square error (RMSE) between the experimental lipid profile spectrum and the theoretical ones.

3.4   Results and Discussion

3.4.1   General Observations

Intraoperative DESI-MS was performed in such a way as to mimic one foreseeable implementation in which a single mass spectrometer is moved into an OR setting just prior to surgery, powered on, and is ready for use within ~30 minutes. The chosen unit mass resolution linear ion trap mass spectrometer used (17-19) performed well without significant electronic, vacuum, or even mass calibration problems over the 15-month duration of the study. Fresh tissue samples were smeared and analyzed by DESI-MS within 3 minutes, a timeframe that addresses surgical needs. In the case of all surgeries, DESI-MS analysis of multiple biopsies was completed long before any intraoperative pathologic consultation findings were reported back to the neurosurgeon by the neuropathologist. The observed timing of in situ, quasi–real-time analysis by DESI-MS supports the fact that multiple measurements - made at discrete points selected by the neurosurgeon - are reliable and have the potential to provide the surgeon with additional information to guide resection maneuvers, particularly near critical anatomical structures.

3.4.2   Assessment of Disease State, Tumor Cell Percentage, and Isocitrate Dehydrogenase Mutation Status in Tumor Cores

In current practice, biopsies obtained from the tumor core, prepared either as frozen sections or as smears, are evaluated by the pathologist for tumor type, grade, and assessment of IDH mutation. Information on tumor type and grade (i.e., low vs. high) is supplied to the neurosurgeon via telephone - ideally in less than 20 minutes while IDH assessment requires more time and is only available post-surgery. Intraoperative DESI-MS was designed to predict disease state (i.e., glioma, grey matter, white matter, or mixed states) and TCP (i.e., tumor cell percentage relative to normal cells). The results of earlier DESI-MS studies suggested also the ability to predict tumor grade and subtype.(15) DESI-MS predictions of disease state from tumor core margin smears were compared with data from a library of MS spectra of known tissue types. The comparison was made using principal component (PC1, PC2) representations of the mass spectrum in a fashion analogous to that used earlier for tissue sections.(17) Representative data are shown in Figure 3.3. The results of these and many other such assignments matched one-to-one those of pathology (Table 3.4).
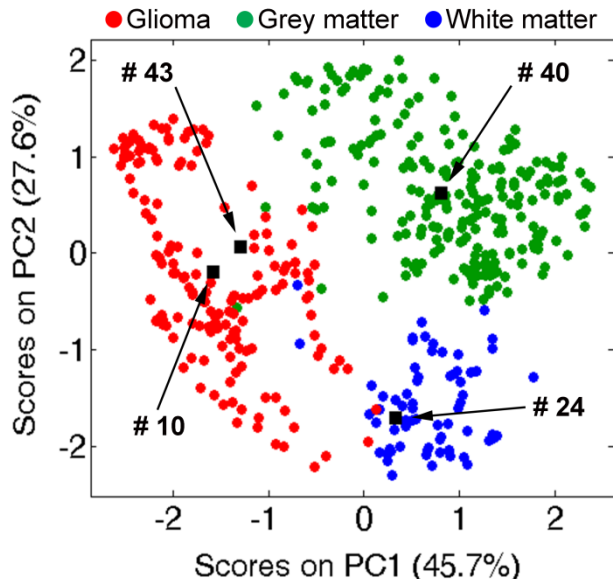
Figure 3.3 Chemical predictions of disease state for smears # 10 (glioma, 99% TCP), # 24 (white matter, 37% TCP), # 40 (grey matter, 15% TCP), and # 43 (glioma, 69% TCP). Projections of the tissue smears (black objects) are imposed on the principal component analysis (PCA) score space created from a reference DESI-MS spectral library (17); green, grey matter; blue, white matter; red, glioma.

TCP prediction by DESI-MS supplements the disease state information. Many tumor core biopsy smears have high (>67%) TCP, matching pathology and expectations given that high-grade gliomas tend to be hypercellular. Exceptionally, smear # 24 from case 3 (astrocytoma WHO grade III; Table 3.4) was infiltrated tissue with low TCP by pathology and was predicted by DESI-MS as white matter with 37% TCP (Table 3.4). Figure 3.4 depicts the chemical diversity of smear # 24 in comparison with another tumor core biopsy (smear # 43) from a WHO grade IV tumor with high TCP. Two smears were prepared from nine tumor core biopsies by splitting the tissue in half. Encouragingly, the disease state was the same and the NAA-based predicted TCP agreed to within 15% (Table 3.4).
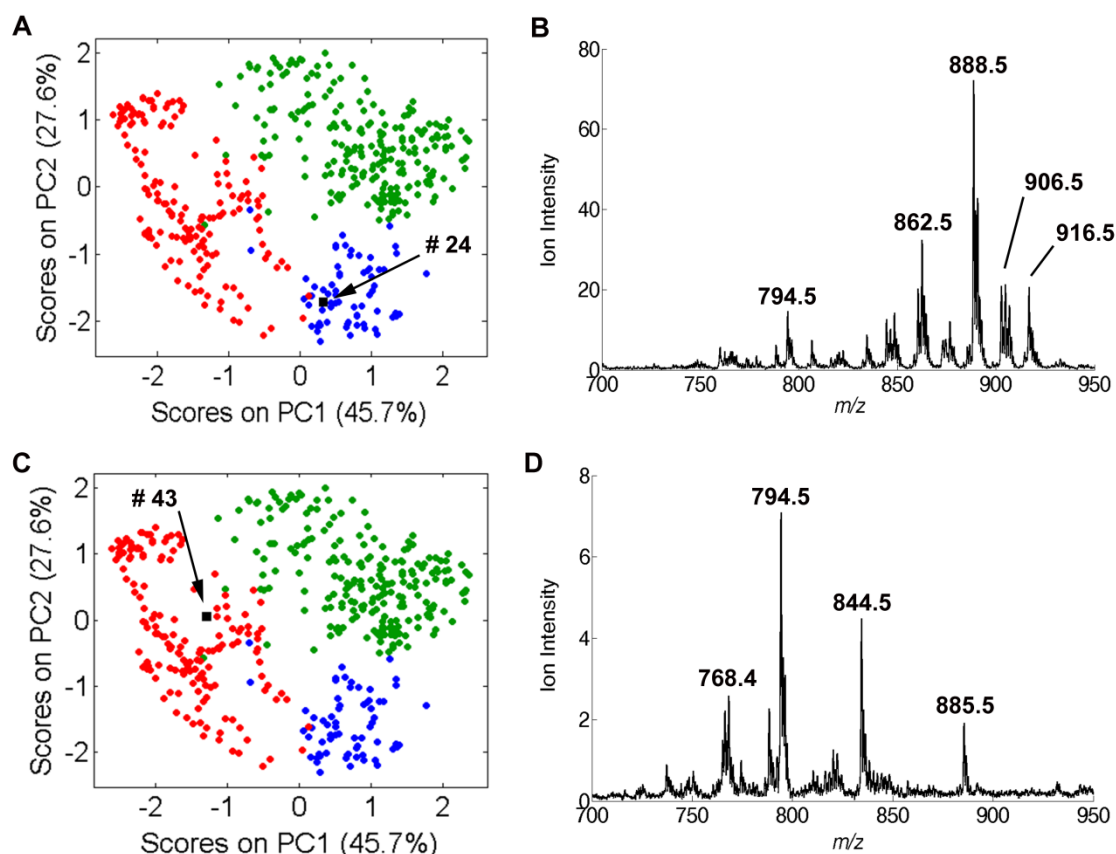
Figure 3.4 (A) Chemical predictions for smear # 24 (case 4). Smear identified as white matter with 37% TCP by DESI-MS and as infiltrated tissue (not otherwise specified) with 15% TCP by pathology. Projection of the tissue smear (black object) is imposed on the PCA score space of the brain reference dataset (1); green, grey matter; blue, white matter; red, glioma. (B) (–) DESI-MS lipid profile spectrum of smear # 24 (case 4). (C) Chemical predictions for smear # 43 (case 6). Smear identified as glioma with 69% TCP by DESI-MS and pathologically assigned as glioma with 80% TCP. (D) (–) DESI-MS lipid profile spectrum of smear # 43 (case 6).

IDH mutation status was assessed intraoperatively via negative ion DESI-MS detection of 2HG (m/z 147) followed by fragmentation using collision-induced dissociation for structural confirmation. IDH mutation status is currently only determined via immunohistochemistry and genetic testing postoperatively, even though its intraoperative assessment could have surgical utility. More aggressive resection of IDH-mutant tumors, which are associated with better prognosis,(21, 22) significantly improves overall and progression-free survival, while more aggressive resection of wild-type tumors does not result in such benefits.(24) 2HG was detected in the tumor core biopsies from cases # 1, 3, 5, 7, and 9, these were determined postoperatively to be IDH-mutant (Table 3.3). In the mutant tumors, the 2HG signal intensity varied between smears,

grossly correlating with the degree of tumor infiltration (Figure 3.5), as previously observed by DESI-MS for tissue sections.(20) Independent studies confirmed a positive correlation between 2HG concentration and tumor cellularity but showed no significant differences between tumor types and grades.(24) No 2HG was detected for wild-type tumors (Figure 3.6).
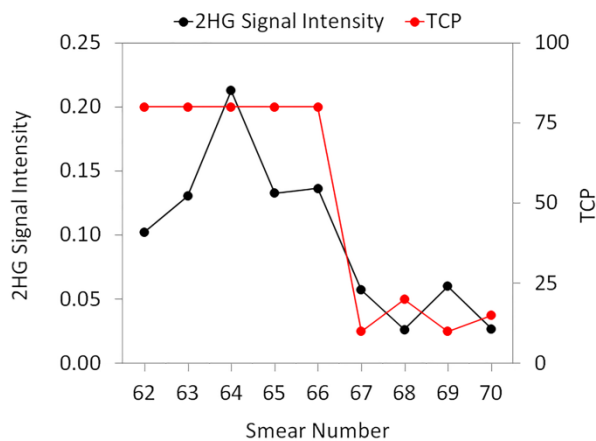
Figure 3.5 Signal intensity of 2HG (m/z 147) normalized to the total ion counts in smears # 62-70 for case 9. Secondary axis shows TCP as estimated by pathology in the same smears.

3.4.1 Assessment of Disease State and Tumor Cell Percentage at Discrete Points Near Resection Margins

Forty-four of 80 biopsies were obtained near surgical margins (within 0.5 cm from where tumor resection ceased). The visualization of the pseudo margin of gliomas and their margin status can be difficult and unreliable. It is also highly unusual and inefficient to use intraoperative pathologic consultation to determine where to cease resection. Postoperative MRI normally assesses the approximate volume of residual tumor. The absence of residual contrast enhancement around the resection cavity is interpreted as macroscopic or gross total resection.(4) We have developed two models for estimating residual tumor at discrete points resected at the discretion of the surgeon. One is based on NAA signal intensity while the other is a more indirect measure based on the lipid profile of the tissue. Note, although we provide prediction of disease state from smears of margin biopsies, the pathologist does not routinely or exclusively use such samples for the determination of tumor type, grade (such metrics are determined using tumor core biopsies), or margin status when applicable.
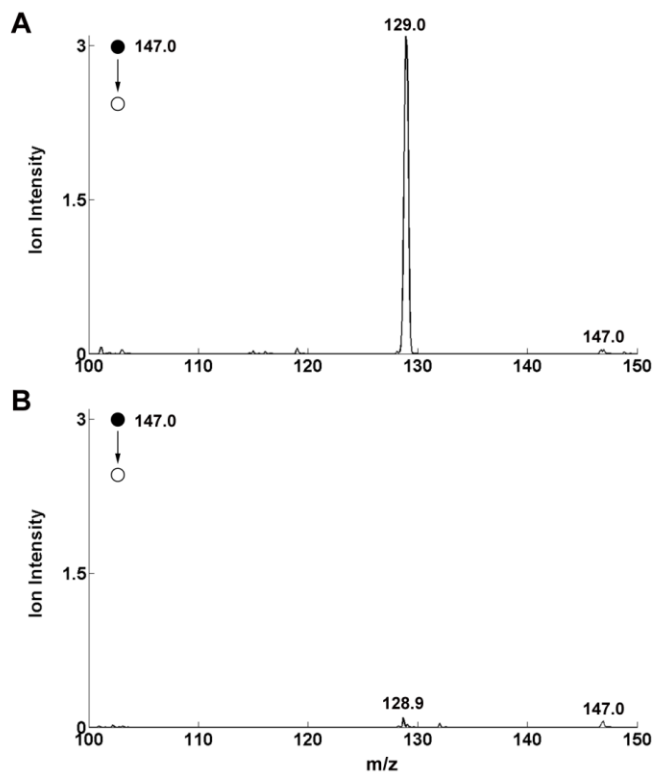
Figure 3.6 Collision-induced dissociation (CID) MS/MS fragmentation pattern obtained for 2HG (precursor ion *m/z* 147) from **(A)** case 8 in smear # 59 (pathology assignment: glioblastoma, IDH-mutant, WHO grade IV), **(B)** case 9 in smear # 66 (pathology assignment following WHO 2007 terminology: oligodendroglioma, wild-type, WHO grade II). Fragmentation *m/z* 147>129 corresponds to a neutral loss of *m/z* 18.

3.4.1.1   Simple Linear Regression for Predicting Tumor Cell Percentage from N-acetylaspartate

A roughly exponential decrease of NAA signal intensity was observed vs. pathologically measured increase in TCP in tissue sections. This observation has now been extended and confirmed in tissue smears analyzed intraoperatively (Figure 3.7). TCP predictions based on NAA of biopsied tissue from near surgical margins ranged between 0% and 100%. Notably, about one-half of the margin tissue smears were infiltrated with more than 50% tumor cells. Figure 3.6 shows the frequency of low, medium, and high TCP, as well as of the disease state predictions, both compared with histopathological results. Agreement is good. The absence of a signal for NAA in tissue - when a distinct glioma lipid profile is present - is specific for high-density gliomas (Table 3.4). Sensitivity is also high as just three smears (# 69, 77-79) showed low NAA signal (TCP estimates between 73–74%; Table 3.4) when pathology determined less than 10% tumor cells. The presence of vascular proliferation was noted in these smears.
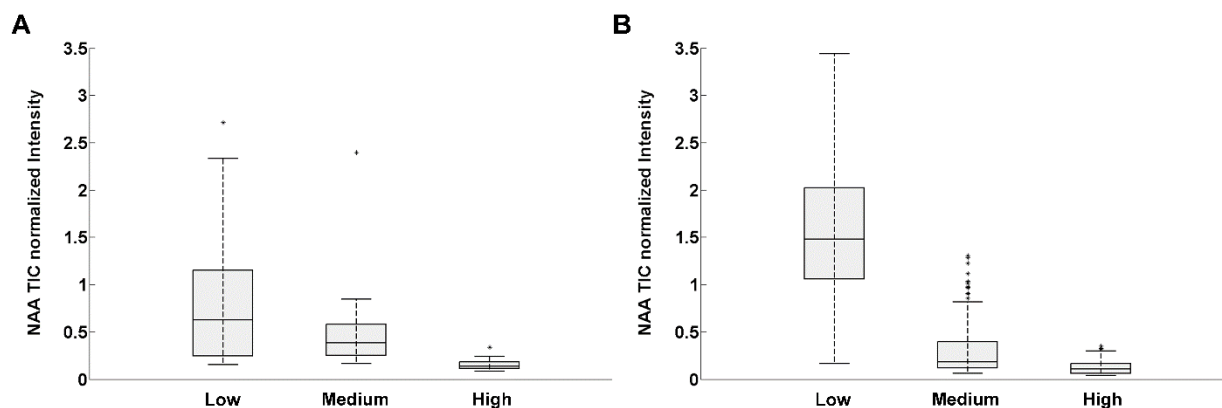
Figure 3.7(A) Box and whisker plot for the signal intensity of *m/z* 174 (normalized to the total ion counts) in tissue smears analyzed using DESI-MS intraoperatively (N=73). (B) Box and whisker plot for normalized intensity of *m/z* 174 in tissue sections analyzed using DESI-MS imaging (N=437). The box represents the interquartile range with a median line and whiskers at ±1.5 SD. Outliers are represented by asterisks. Data for tissue sections constitute part of the reference DESI-MS spectral library described in Jarmusch et al. (1). Copyright (2016) National Academy of Sciences.

Table 3.2 Association between chemical predictions of disease state and TCP vs. pathology for tumor cores

	Chemical Evaluation of Disease State		
Pathological evaluation	Grey matter	White matter	Glioma
Infiltrated tissue	0	3	1
Glioma	0	2	22
	Chemical Evaluation of Tumor Cell Percentage		
	Low (<33%)	Medium (34-67%)	High (>67%)
Low	0	2	2
Medium	0	2	1
High	0	0	21

Table 3.3 Patient Cohort. Radiology, operative, and pathology information.

Case	Gender	Age	Race	F[b]	Final Diagnosis[d]	Molecular markers[a]					
						IDH	1p-19q	GFAP	ATRX	p-53	Ki67
1[c]	M	30	White	N	Oligodendroglioma WHO grade II	1	0	1	0	1 (20%)	1 (1%)
2	M	23	Black	N	Dysembryoplastic neuroepitelial tumor WHO grade I	0	n/a	1	n/a	n/a	1 (1-5%)
3	M	24	White	N	Astrocytoma WHO grade III	1	0	1	0	1 (80%)	1 (4%)
4	M	65	White	N	Glioblastoma WHO grade IV	0	n/a	1	1	1 (3%)	1 (4%)
5	F	44	White	N	Oligodendroglioma WHO grade II	1	n/a	1	1	1	1 (5%)
6	M	47	White	Y	Glioblastoma WHO grade IV	0	n/a	1	n/a	n/a	1 (20%)
7[c]	M	30	White	N	Glioblastoma WHO grade IV	1	0	1	0	n/a	1
8	F	52	White	Y	Glioblastoma WHO grade IV	0	n/a	1	n/a	1 (40%)	1 (30%)
9	F	33	White	N	Oligodendroglioma WHO grade II	1	n/a	1	1	1	1 (<5%)
10	F	73	White	Y	Glioblastoma WHO grade IV	0	n/a	1	1	1	1 -30%

The availability of an intraoperative tool for Identification of high (>50%) residual tumor infiltration at surgical margins is essential for neurosurgeons to refine surgical maneuvers. Safe removal of high tumor infiltration is a primary goal of neurosurgery while areas of low infiltration are more likely the target of coadjuvant postsurgical therapies. Our current qualitative methodology is less accurate in differentiating between medium and low TCP (Table 3.4). The literature suggests that NAA varies with age, gender, and other biological factors (25) that were not controlled in this small study. Biological variability affecting agreement between chemical and pathological estimations manifests itself when NAA is present in the tissue; i.e., in low- and medium-infiltrated tissue.

3.4.1.2 Lipid Profile Deconvolution for Evaluation of Tumor Cell Percentage

The lipid profile detected by DESI-MS can show the presence of tumor in tissue and distinguishes the background into which the tumor infiltrates; i.e., grey or white brain matter.(17) The dynamic changes of DESI-MS lipid profiles acquired from tissue sections were previously interpreted in terms of three-component mixtures of glioma, white, and grey matter (Figure 3.8). The dynamics are reflective of the infiltrative nature of gliomas into the surrounding brain parenchyma. A linear regression model was developed to determine composition of grey matter, white matter, and glioma based on a reference spectral library (see Section 3.3.6). We further speculate that the deconvolution of lipid profiles into fractions of white matter, grey matter, and glioma can indicate tumor density and corroborate NAA predictions. In the 44 margin smears analyzed, the lipid deconvolution underscored the complexity of gliomas identifying tumor infiltration into white (e.g., smear # 18) or grey matter (e.g., smear # 44), into a mixture of those (e.g., smear # 49), or even identifying mixtures of grey and white matter with no detectable presence of tumor cells (e.g., smear # 68). Figure 3.9 depicts the dynamic of the lipid profiles reflecting such complexity. This determination is made even more difficult during pathological evaluation by the fact that tumor effaces normal parenchyma resulting in identification of infiltrated tissue not otherwise specified (IT nos; Figure 3.9). Most tumors infiltrate into white matter, so their lipid signatures express high abundances of sulfatides related to myelination of neurons.(17) Only a few smears showed infiltration into grey matter (# 20, 26, 40, 42, 44, 45, 55, 67, and 68; Table 3.4). In these cases, pathological evaluation confirmed the presence of grey

matter infiltrated with tumor cells or mixed with white matter. As was the case for NAA, tissue near surgical margins showed high heterogeneity in lipid expression.

The deconvolution of lipid profiles of the smears into their constituent tissue types accurately identified low- (14 smears of 18) and high-density gliomas (10 smears of 14), while less accuracy was obtained for medium-infiltrated tissue (Table 3.4). A larger cohort of patients is necessary to develop a more accurate multifactorial regression model based on experimental results rather than using the assumption of linear combination with no interactions.

3.4.1.3 Residual Tumor Near Surgical Margins

Tumor infiltration varied greatly not only in biopsied tissue resected near surgical margins but also within the epicenter of the tumor. The peculiar behavior of gliomas to infiltrate irregularly into brain matter, mostly following white matter tracts, was observed in the multiple measurements performed by DESI-MS. We found high TCP near the margins in both high- and low-grade gliomas, with only a weak relationship between TCP and biopsy location within the tumor volume (i.e., decreasing TCP moving from tumor core to margins). Marginal points sometimes showed TCP higher than those measured inside the tumor.

As extreme examples, we detail cases 2 and 4. For case 4, glioblastoma WHO grade IV, two biopsies (smears # 25 and 26) obtained near surgical margins had TCP (predicted using NAA) of 75% and 0%, respectively, matching pathology (high and low TCP). Two biopsies resected inside the tumor mass showed TCP of about 40% (Table 3.4). For case 2, dysembryoplastic neuroepitelial tumor WHO grade I, discrete biopsied tissue resected near the surgical margins showed TCP from 65% to 93% (Figure 3.11). Again, marginal points showed TCP higher than discrete locations inside the tumor mass (Table 3.4).
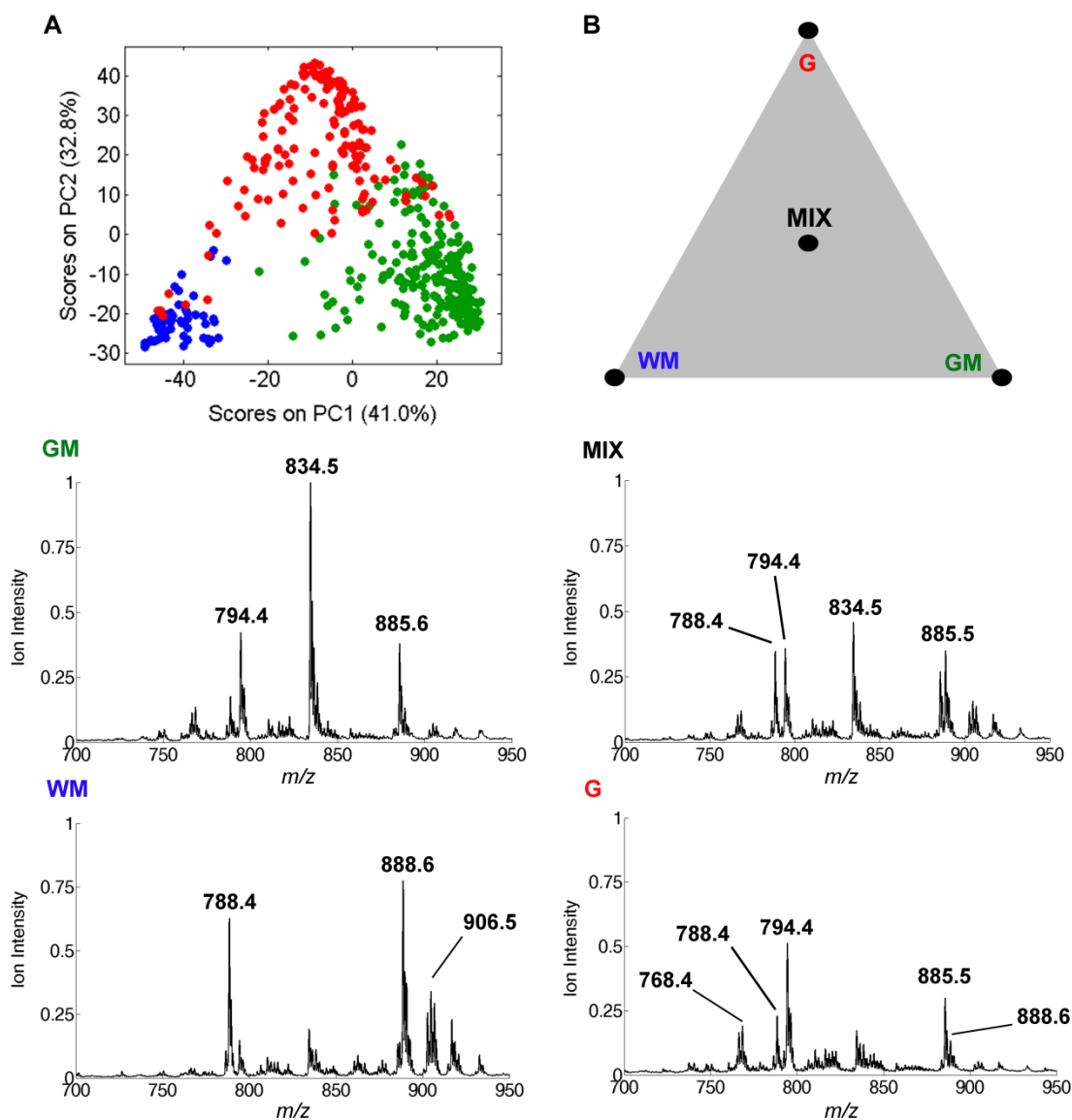
Figure 3.8 (A) PCA score plot using lipid profile information for histologically-defined tissue sections analyzed by DESI-MS imaging (specimens constituting the reference DESI-MS spectral library) (1). Green, grey matter; blue, white matter; red, glioma. (B) Three-mixture component surface. Vertices represent pure components (WM = white matter; GM = grey matter; G = glioma). Edges represent binary mixtures. Face represents tertiary mixture. (GM) (–) DESI-MS lipid signature of grey matter. (WM) (–) DESI-MS lipid signature of white matter. (MIX) Theoretical lipid signature of tissue equally mixed with grey matter (33.3%), white matter (33.3%), and tumor cells (33.3%). (G) (–) DESI-MS lipid signature of gliomas. DESI-MS spectra are normalized for ease of comparison.
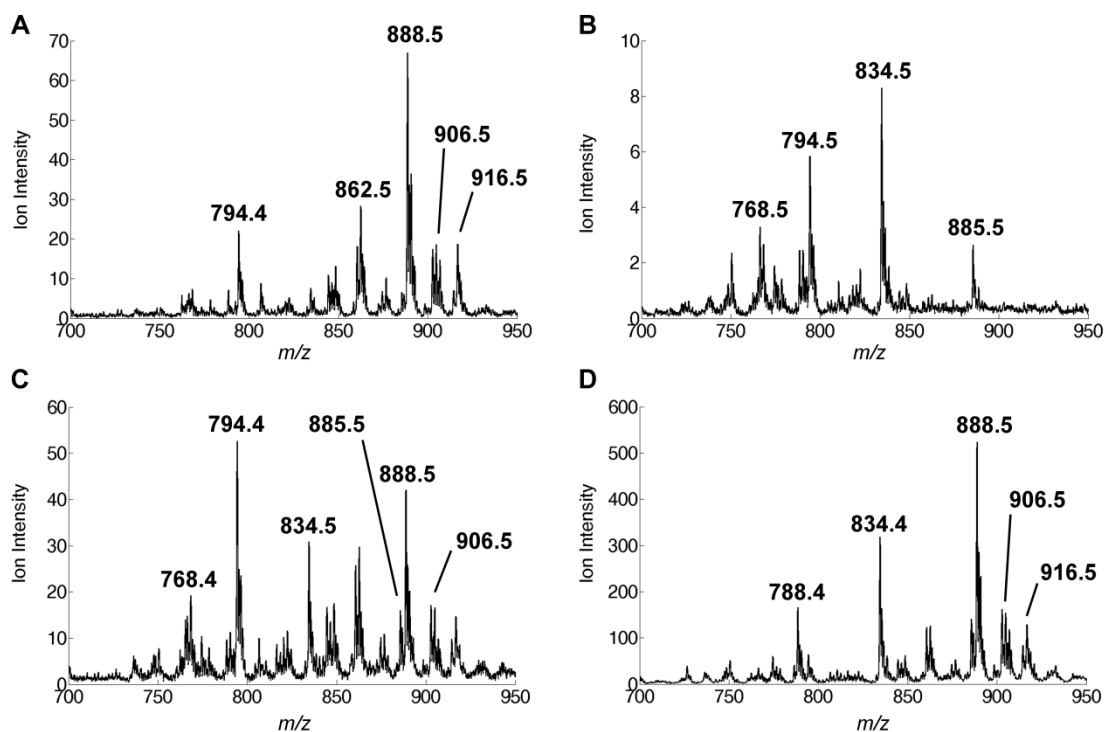
Figure 3.9 (A) (–) DESI-MS lipid profile spectrum of smear # 18. Lipid deconvolution [GM WM G]: [0 54 46]; DESI-MS assignment: G with 80% TCP. (B) (–) DESI-MS lipid profile spectrum of smear # 44. Lipid deconvolution [GM WM G]: [35 0 65]; DESI-MS assignment: G with 42% TCP. (C) (–) DESI-MS lipid profile spectrum of smear # 49. Lipid deconvolution [GM WM G]: [3 23 74]; DESI-MS assignment: G with 51% TCP. (D) (–) DESI-MS lipid profile spectrum of smear # 68. Lipid deconvolution [GM WM G]: [27 73 0]; DESI-MS assignment: WM with 2% TCP.
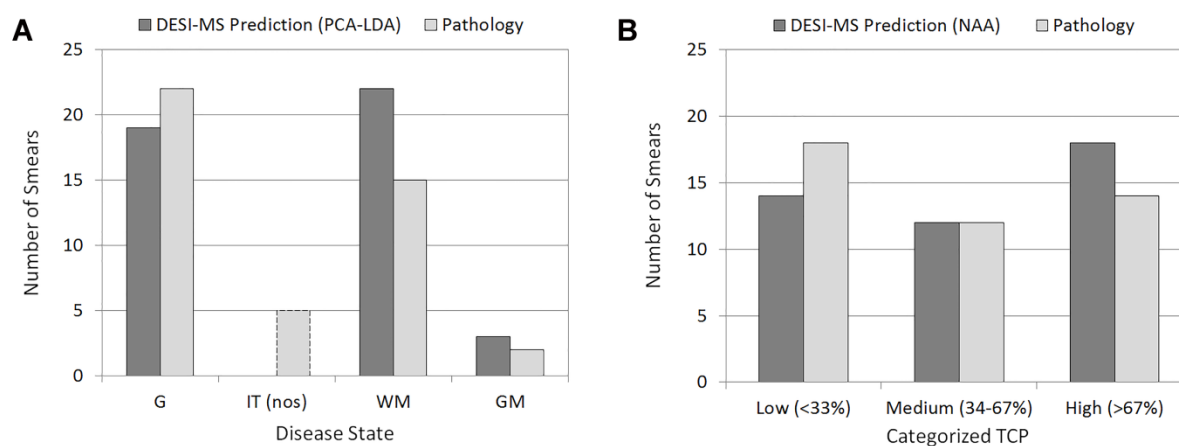
Figure 3.10 Margin smears (N=44). (A) Frequency of DESI-MS prediction of disease state vs. pathology. G, glioma; IT (nos), infiltrated tissue (not otherwise specified); WM, white matter; GM, grey matter. DESI-MS has no IT (nos) assignments as all smears were assigned. (B) Frequency of DESI-MS prediction of TCP using NAA vs. pathology. Percentages of tumor cells are categorized as low (<33%), medium (34–67%), and high (>67%).
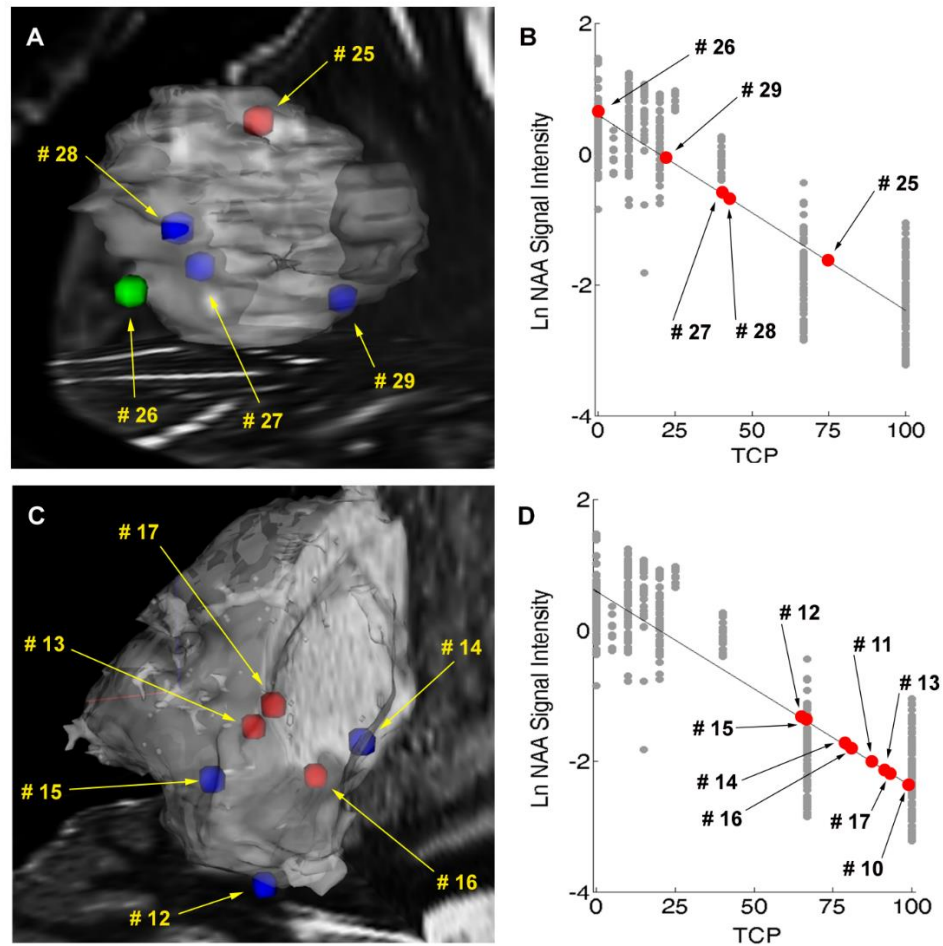
Figure 3.11 Chemical predictions of disease state and tumor cell percentage. (A) Three-dimensional mapping of chemical predictions over MRI volume reconstruction for case 4 with overlaid stereotactic positions of smears # 25–29. Stereotactic positions were registered digitally to the preoperative MRI using neuronavigation in the OR. Stereotactic positions are color coded by PCA-LDA classification: green, grey matter; blue, white matter; red, glioma. (B) TCP predictions via linear regression using NAA for smears # 25–29. Grey objects, natural log of the NAA signal intensity (normalized to the total ion count) versus TCP for histologically-defined reference specimens with a line of regression (black line); red objects, predictions of tissue smears. The equation of the regression line was calculated as y = –0.03x + 0.59 with a Pearson correlation r of –0.89. (C) Three-dimensional mapping of chemical predictions over MRI volume reconstruction for case 2 with overlaid stereotactic positions of smears # 12–17. The stereotactic image for the biopsied tissue corresponding to smears # 10 and 11 was not recorded. (D) TCP predictions via linear regression using NAA for smears # 10–17.
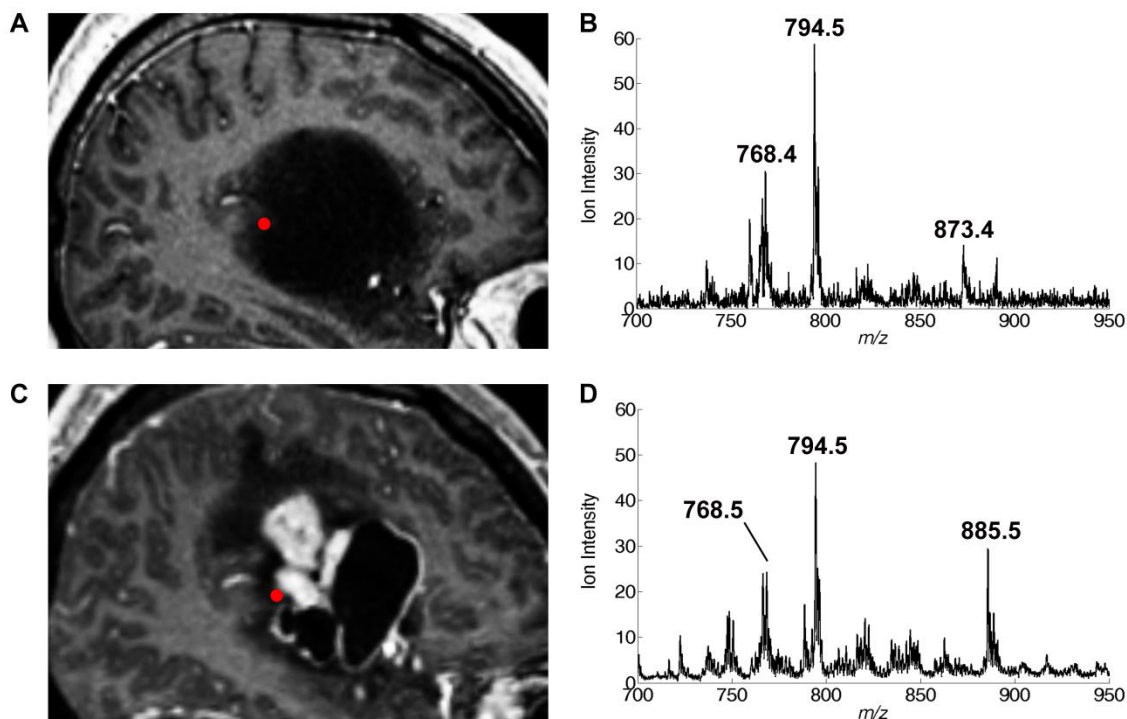
Figure 3.12 (A) Stereotactic position of the biopsied tissue for smear # 7 (case 1) mapped over the preoperative MRI of case 1. (B) (–) DESI-MS lipid profile (*m/z* 700-1000) for smear # 7 (case 1); pathological assignment: oligodendroglioma, IDH mutant, WHO grade II. (C) Stereotactic position of the biopsied tissue for smear # 7 (case 1) mapped over the preoperative MRI of case 7. (D) (–) DESI-MS lipid profile (*m/z* 700-1000) for smear # 50 (case 7); pathological assignment: glioblastoma, IDH mutant, WHO grade IV.

Similar trends were found in the other cases as well (Table 3.4). Remarkably, and unfortunately, postoperative MRI provided no evidence of residual tumor in any of the cases except 1 and 2. Limitations in estimating extent of resection by MRI exist and are largely due to lack of correlation between MRI contrast enhancement and histological composition of the tissue, difficulties in calculating tumor volume, and the occurrence of non-enhancing tumors. (4) Also, the volume of the resection cavity does not provide a true indication of the residual microscopic tumor burden. (3)

Unresected tumor is the primary cause of recurrence and malignant progression. This is shown in cases 1 and 7, which refer to the same subject who underwent glioma resection twice within one year. The primary tumor was diagnosed as oligodendroglioma WHO grade II (using WHO 2007 terminology) (Table 3.3). The tumor was adherent to medial structures and the lateral thalamus; only partial tumor resection was performed as total resection was determined to be

unsafe. Residual tumor was detected by DESI-MS in the posterior margin, with TCP ranging between 74% and 88% into the biopsied tissue (smears # 6–8, case 1). A secondary tumor mass recurred from the posterior margin and progressed into glioblastoma WHO grade IV (Figure 3.12). Notably, the lipid signature of the recurrent tumor showed higher intensity of phosphatidylinositol (38:4), *m/z* 885.5 (Figure 3.12), which has been noted as a discriminatory marker for glioblastoma in previous DESI-MS studies. (15) Also, DESI-MS identified the presence of 2HG in the primary oligodendroglioma, indicative of IDH mutation, confirmed postoperatively (Table 3.3). Progression of oligodendrogliomas into glioblastomas occurs predominantly in IDH-mutant tissue. (21, 22)

Table 3.4 Pathological and chemical prediction of tissue smears analyzed by DESI-MS intraoperatively.

Case	# Biopsy	Stereotactic Location	# Smear	Included	# in Main Text	Diagnosis[a]	TCP (%)	PCA-LDA Diagnosis	TCP (%) using NAA	GM	WM	G
1	1	Tumor	1	Y	1	G	>90	G	67	0	0	100
	2	Tumor	2	N	2	G	>90		Excluded			
	3	Tumor	3	Y	3	G	>90	G	99	0	0	100
	4	Tumor	4	Y	4	G	>90	G	75	0	0	100
	5	Margin	5	Y	5	G	>90	G	90	0	0	100
	6	Margin	6	Y	6	G	>90	G	88	0	0	100
	7	Margin	7	Y	7	G	>90	G	74	0	0	100
	8	Margin	8	Y	8	G	>90	G	80	0	0	100
	9	Margin	9	Y	9	G	40	G	40	0	0	100
2	1[b]	Tumor	1	Y	10	G	>90	G	99	0	0	100
			2	Y	11	G	>90	G	87	0	0	100
	2	Margin	3	Y	12	G	60	WM	65	0	49	51
	3	Tumor	4	Y	13	G	80	G	91	0	0	100
	4	Margin	5	Y	14	G	50	WM	79	0	38	62
	5	Margin	6	Y	15	G	60	WM	66	0	48	52
	6	Tumor	7	Y	16	G	80	G	80	0	4	96
	7	Margin	8	Y	17	G	80	G	93	0	0	100
3	1	Margin	1	Y	18	G	50	G	80	0	54	46
	2	Margin	2	Y	19	G	>90	G	98	0	0	100
	3	Margin	3	Y	20	IT	15	GM	25	22	0	78
	4	Tumor	4	Y	21	G	70	G	75	0	42	58
	5	Tumor	5	Y	22	G	50	G	75	0	37	63
			6	N	23	Excluded		G	72	0	68	32
	6	Tumor	7	Y	24	IT (nos)	15	WM	37	0	90	10
4	1	Margin	1	Y	25	G	>90	G	75	0	35	65
	2	Margin	2	Y	26	IT (nos)	10	GM	0	77	0	23
	3	Tumor	3	Y	27	G	50	WM	42	0	100	0
	4	Tumor	4	Y	28	G	50	WM	41	0	100	0
	5	Margin	5	Y	29	IT	10	WM	22	0	100	0
			6	N	30	Excluded		WM	2	0	100	0

Table 3.4 continued

5	1	Tumor	1	Y	31	G	90	G	77	0	32	68
			2	Y	32	G	90	G	68	0	21	79
	2	Margin	3	Y	33	IT	30	WM	0	0	100	0
	3	Margin	4	Y	34	IT	50	WM	0	0	100	0
	4	Margin	5	Y	35	G	65	WM	25	0	100	0
			6	Y	36	IT	30	WM	0	0	100	0
	5	Margin	7	Y	37	IT (nos)	15	WM	33	0	100	0
	6	Margin	8	Y	38	G	95	G	80	0	0	100
	7	Margin	9	Y	39	IT	<20	WM	0	0	100	0
6	1	Margin	1	Y	40	IT	30	GM	15	100	0	0
	2	Margin	2	Y	41	IT	20	WM	29	0	59	41
	3	Margin	3	Y	42	G	80	G	60	39	0	61
	4	Tumor	4	Y	43	G	80	G	69	0	0	100
	5	Margin	5	Y	44	G	67	G	42	35	0	65
	6	Margin	6	Y	45	G	60	G	48	15	0	85
			7	Y	46	IT	50	WM	27	0	55	45
7	1	Tumor	1	N	47	Excluded		G	91	0	0	100
			2	N	48	Excluded		G	100	0	0	100
	2	Tumor	3	Y	49	IT	15	G	51	3	23	74
	3	Tumor	4	Y	50	G	70	G	88	0	0	100
	4	Margin	5	Y	51	IT (nos)	40	G	51	0	8	92
	5	Margin	6	Y	52	G	80	WM	87	0	41	59
	6	Margin	7	Y	53	IT (nos)	50	WM	57	0	41	59
	7	Margin	8	Y	54	G	70	WM	83	0	71	29
8	1	Margin	1	Y	55	IT	30	WM	32	11	74	15
	2	Tumor	2	N	56	Excluded		*Excluded*				
			3	N	57	Excluded		*Excluded*				
	3	Margin	4	Y	58	G	70	G	98	4	0	96
	4	Tumor	5	Y	59	G	>90	G	100	0	0	100
	5	Margin	6	Y	60	G	>90	G	100	0	0	100
			7	Y	61	G	>90	G	93	0	0	100

Table 3.4 continued

9	1	Tumor	1	Y	62	G	80	G	76	13	7	80
			2	Y	63	G	80	G	91	0	7	93
	2	Tumor	3	Y	64	G	80	G	81	0	16	84
			4	Y	65	G	80	G	81	0	19	82
	3	Tumor	5	Y	66	G	80	G	78	0	15	85
	4	Margin	6	Y	67	IT	10	GM	41	17	30	53
			7	Y	68	IT	20	WM	2	27	73	0
	5	Margin	8	Y	69	IT (nos)	10	WM	73	0	74	26
	6	Margin	9	Y	70	IT	15	WM	44	0	100	0
10	1	Tumor	1	Y	71	G	>90	G	80	0	16	84
			2	Y	72	G	>90	G	93	0	6	94
	2	Tumor	3	Y	73	G	>90	G	89	0	2	98
			4	Y	74	G	>90	G	78	0	8	92
	3	Tumor	5	Y	75	IT	<5	WM	82	0	39	61
			6	Y	76	IT	<5	WM	74	0	62	38
	4	Margin	7	Y	77	IT	<5	WM	74	0	62	38
	5	Margin	8	Y	78	IT	<5	WM	73	0	81	19
	6	Margin	9	Y	79	IT	<5	WM	63	0	81	19
	7	Margin	10	Y	80	IT	<5	WM	39	0	100	0

[a]G = Glioma; GM = grey matter; WM = white matter; IT (nos) = infiltrated tissue (not otherwise specified).
[b]Nine biopsies were split in half to prepare two smears from adjacent tissue.

3.5 Conclusions

Rapid DESI-MS analysis of tissue smears was performed inside the OR during glioma resection for the first time. The results from the first 10 patients in a projected 50-patient study indicate that the DESI-MS methodology is simple, reliable, and can be inserted into the current surgical workflow without interference. Simplicity of the instrumentation, a low-resolution ion trap mass spectrometer, and the methodology is desirable for robustness and ruggedness. DESI-MS faithfully recapitulates basic diagnostic information (disease state and TCP) in less time than is needed for pathological evaluation. This enables multiple direct measurements on neurological tissue for examination of clinically relevant variants within the tumor and for the assessment of discrete points in the resection cavity for residual tumor. The remarkable finding that biopsies taken near each other and having

similar tumor types can show vastly different TCPs speaks to the complexity and known heterogeneity of glioma invasion into adjacent tissue. This heterogeneity partly accounts for failure of single treatment paradigms. High percentages of tumor cells were found near surgical margins, even in cases where postoperative MRI showed gross total resection, corroborating the utility of DESI-MS coupled with neuronavigation to assist in maximal tumor resection, an outcome associated with better patient survival. In situations where tumor is detected but cannot be safely removed, intraoperative measurement of residual tumor can serve to focus the delivery of adjuvant postsurgical therapies. Intraoperative DESI-MS can assess the presence of IDH mutation via detection of 2HG. Intraoperative assessment of IDH mutation could differentiate low-grade glioma from reactive tissue, potentially influencing surgical decision-making process and aggressiveness of resection, predominantly based on tumor location (24). The DESI-MS methodology can be improved to become more quantitative and relevant for detection of important markers such as 2HG and NAA. Prospective randomized clinical trials will be necessary to further validate these results and define how DESI-MS can be used to expedite clinical decision-making and improve the care of brain tumor patients.

3.6   Acknowledgements

3.7   References

1. Young RM, Jamshidi A, Davis G, & Sherman JH (2015) Current trends in the surgical management and treatment of adult glioblastoma. Ann Transl Med 3(9):121.

2. Orringer D, et al. (2012) Extent of resection in patients with glioblastoma: limiting factors, perception of resectability, and effect on survival. J Neurosurg 117(5):851-859.

3. Hervey-Jumper SL & Berger MS (2016) Maximizing safe resection of low- and high-grade glioma. J Neurooncol 130(2):269-282.

4. Eidel O, et al. (2017) Tumor infiltration in enhancing and non-enhancing parts of glioblastoma: a correlation with histopathology. PLoS One 12(1):e0169292.

5. Louis DN, et al. (2016) The 2016 World Health Organization Classification of Tumors of the Central Nervous System: a summary. Acta Neuropathol 131(6):803-820.

6. Cooks RG, Ouyang Z, Takats Z, & Wiseman JM (2006) Detection technologies. Ambient mass spectrometry. Science 311(5767):1566-1570.

7. Balog J, et al. (2013) Intraoperative tissue identification using rapid evaporative ionization mass spectrometry. Sci Transl Med 5(194):194ra193.

8. Orringer DA, et al. (2017) Rapid intraoperative histology of unprocessed surgical specimens via fibre-laser-based stimulated Raman scattering microscopy. Nature Biomedical Engineering 1:0027.

9. Jermyn M, et al. (2015) Intraoperative brain cancer detection with Raman spectroscopy in humans. Sci Transl Med 7(274):274ra219.

10. Eberlin LS, et al. (2014) Molecular assessment of surgical-resection margins of gastric cancer by mass-spectrometric imaging. Proc Natl Acad Sci U S A 111(7):2436-2441.

11. Eberlin LS, et al. (2016) Pancreatic cancer surgical resection margins: molecular assessment by mass spectrometry imaging. PLoS Med 13(8):e1002108.

12. Tata A, et al. (2016) Rapid detection of necrosis in breast cancer with desorption electrospray ionization mass spectrometry. Sci Rep 6:35374.

13. Calligaris D, et al. (2015) Molecular typing of meningiomas by desorption electrospray ionization mass spectrometry imaging for surgical decision-making. Int J Mass Spectrom 377:690-698.

14. Ifa DR & Eberlin LS (2016) Ambient ionization mass spectrometry for cancer diagnosis and surgical margin evaluation. Clin Chem 62(1):111-123.

15. Eberlin LS, et al. (2012) Classifying human brain tumors by lipid imaging with mass spectrometry. Cancer Res 72(3):645-654.

16. Eberlin LS, et al. (2013) Ambient mass spectrometry for the intraoperative molecular diagnosis of human brain tumors. Proc Natl Acad Sci U S A 110(5):1611-1616.

17. Jarmusch AK, et al. (2016) Lipid and metabolite profiles of human brain tumors by desorption electrospray ionization-MS. Proc Natl Acad Sci U S A 113(6):1486-1491.

18. Jarmusch AK, et al. (2016) Differential lipid profiles of normal human brain matter and gliomas by positive and negative mode desorption electrospray ionization - mass spectrometry imaging. PLoS One 11(9):e0163180.

19. Pirro V, et al. (2017) Utility of neurological smears for intrasurgical brain cancer diagnostics and tumour cell percentage by DESI-MS. Analyst 142(3):449-454.

20. Santagata S, et al. (2014) Intraoperative mass spectrometry mapping of an onco-metabolite to guide brain tumor surgery. Proc Natl Acad Sci U S A 111(30):11121-11126.

21. Tietze A, et al. (2017) Noninvasive assessment of isocitrate dehydrogenase mutation status in cerebral gliomas by magnetic resonance spectroscopy in a clinical setting. J Neurosurg:1-8.

22. Cohen AL, Holmen SL, & Colman H (2013) IDH1 and IDH2 mutations in gliomas. Curr Neurol Neurosci Rep 13(5):345.

23. Woolman M, et al. (2017) An assessment of the utility of tissue smears in rapid cancer profiling with desorption electrospray ionization mass spectrometry (DESI-MS). J Am Soc Mass Spectrom 28(1):145-153.

24. Beiko J, et al. (2014) IDH1 mutant malignant astrocytomas are more amenable to surgical resection and have a survival benefit associated with maximal surgical resection. Neuro Oncol 16(1):81-91.

25. Moffett JR, Ross B, Arun P, Madhavarao CN, & Namboodiri AM (2007) N-Acetylaspartate in the CNS: from neurodiagnostics to neurobiology. Prog Neurobiol 81(2):89-131.

26. Eberlin LS, et al. (2011) Nondestructive, histologically compatible tissue imaging by desorption electrospray ionization mass spectrometry. Chembiochem 12(14):2129-2132.

CHAPTER 4.   INTRAOPERATIVE ASSESSMENT OF ISOCITRATE DEHYDROGENASE MUTATION STATUS DURING GLIOMA RESECTION BY DESORPTION ELECTROSPRAY IONIZATION-MS

4.1   Abstract

Described is a rapid intraoperative ambient ionization mass spectrometry (MS) method for determining isocitrate dehydrogenase (IDH) mutation status from glioma tissue biopsies. This method offers new glioma management options and may impact extent of resection goals. Assessment of the IDH mutation is key for accurate glioma diagnosis, particularly for differentiating diffuse glioma from other neoplastic and reactive inflammatory conditions, a challenge for the standard intraoperative diagnostic consultation that relies solely on morphology. Banked glioma specimens (n = 37) were analyzed by desorption electrospray ionization–MS (DESI-MS) to develop a diagnostic method to detect the known altered oncometabolite in IDH-mutant gliomas, 2-hydroxyglutarate (2HG). The method was used intraoperatively to analyze tissue smears obtained from glioma patients undergoing resection and to rapidly diagnose IDH mutation status (< 5 minutes). Fifty-one tumor core biopsies from 25 patients (14 wild type [WT] and 11 mutant) were examined and data were analyzed using analysis of variance and receiver operating characteristic curve analysis. The optimized DESI-MS method discriminated between IDH-WT and IDH-mutant gliomas, with an average sensitivity and specificity of 100%. The average normalized DESI-MS 2HG signal was an order of magnitude higher in IDH-mutant glioma than in IDH-WT glioma. The DESI 2HG signal intensities correlated with independently measured 2HG concentrations ($R^2 = 0.98$). In 1 case, an IDH1 R132H–mutant glioma was misdiagnosed as a demyelinating condition by frozen section histology during the intraoperative consultation, and no resection was performed pending the final pathology report. A second

craniotomy and tumor resection was performed after the final pathology provided a diagnosis most consistent with an IDH-mutant glioblastoma. During the second craniotomy, high levels of 2HG in the tumor core biopsies were detected. This study demonstrates the capability to differentiate rapidly between IDH-mutant gliomas and IDH-WT conditions by DESI-MS during tumor resection. DESI-MS analysis of tissue smears is simple and can be easily integrated into the standard intraoperative pathology consultation. This approach may aid in solving differential diagnosis problems associated with low-grade gliomas and could influence intraoperative decisions regarding extent of resection, ultimately improving patient outcome. Research is ongoing to expand the patient cohort, systematically validate the DESI-MS method, and investigate the relationships between 2HG and tumor heterogeneity.

4.2   Introduction

The integrated diagnosis of gliomas includes morphological and grading criteria, but relies heavily on molecular characteristics.(1) A point mutation in the isocitrate dehydrogenase (IDH) 1 or 2 gene is a major diagnostic and prognostic factor that is now used to classify infiltrative gliomas into two major subgroups: IDH-wildtype or IDH-mutant.(2) The availability of such molecular information during glioma resection can improve diagnostic accuracy, personalize patient treatment, and might guide surgical decision making. Beiko et al.(3) found that gross total resection of IDH-mutant glioblastoma multiforme (GBM) can provide a better survival benefit compared to gross total resection of IDH-wildtype GBM.(3, 4) Patel et al.(5) showed that maximal extent of resection provided a better outcome for low-grade IDH-wildtype gliomas compared to low-grade IDH-mutant gliomas.(5)

Molecular testing for IDH mutations is typically performed postoperatively on a tissue biopsy sample collected during surgical tumor excision. Hence, patients still undergo neurosurgical procedures without the benefit of a molecular diagnosis. Immunohistochemistry (IHC) and genetic sequencing are the gold standard protocols. Several studies have reported more rapid IHC and genetic sequencing protocols with analysis times of approximately 30,(6) 60,(7, 8) or 90 minutes,(9) but they have not found routine implementation in the intraoperative consultations.

Magnetic resonance imaging spectroscopy (MRSI) provides a pre-operative and noninvasive means of assessing IDH mutation status by measuring 2-hydroxyglutarate (2HG), the

downstream oncometabolite that accumulates in IDH-mutant gliomas.(10-12) MRSI studies reported a cut-off 2HG concentration of 2mM (or approximately 300 ng/mg),(11) for optimal discrimination between IDH-mutant and IDH-wild-type gliomas. The diagnostic sensitivity and specificity of MRSI methods are typically ~85-88%,(11) which can be improved by using longer acquisition times and by acquiring more voxels from tumor areas. However, the high operational costs and long image acquisition time limit its routine implementation because the acquisition of MRI images needed for neuronavigation creates a preoperative backlog.

Alternatively, recent studies have shown that IDH mutation status can be assessed via the mass spectrometric (MS) measurement of 2HG from tissue biopsies. Several MS-based 2HG assays have been reported, based on ionization with matrix assisted laser desorption ionization (MALDI),(13) secondary ion mass spectrometry (SIMS),(14)liquid chromatography (LC),(15) and direct infusion electrospray ionization (ESI).(16) Each method demonstrates encouraging preliminary performance in terms of sensitivity and specificity. Lower cut-offs for discrimination between mutant and wildtype gliomas have been reported with accuracy of 100%.(16) However, the complexity of the instrumentation and sample preparation for these MS-based methods prevents the rapid turnaround times needed for intraoperative consultations.

Here we describe the use of desorption electrospray ionization (DESI) as a point-of-care diagnostic tool for IDH mutation status assessment. DESI is an ambient ionization method, generating ions for MS analysis from fresh tissue smears without the need for fixation, washing, or matrix deposition.(17) DESI uses a spray of charged organic solvent droplets to impact a 2D surface (e.g., tissue section or smear), extract molecules from the sample in real time, and introduce them into the mass spectrometer for mass analysis. DESI-MS is advantageous in its simplicity, robustness, short analysis time, and capability for deployment in the operating room (OR) or a pathology laboratory. Some spray solvent systems, such as those employed herein, preserve tissue morphology, permitting subsequent H&E and IHC staining of the same DESI-MS analyzed tissues for post-hoc histopathology.

In our recent work, a mobile DESI mass spectrometer was used to analyze brain tissue smears in the OR, and preliminary capability to assess the extent of residual tumor at surgical margins was demonstrated, as well as detection of 2HG in IDH-mutant gliomas,(18) first reported by Santagata et al.(19) Previous work focused on detection of membrane phospholipids(20, 21) and N-acetyl-aspartate(21) and their use in diagnosing tissue as normal brain or glioma and in

estimating tumor infiltration at surgical margins. An in-depth characterization of DESI-MS as an intraoperative diagnostic method for IDH mutation status has not been undertaken and there is significant need for such a development. Here, we present an optimized DESI-MS method for the diagnosis of IDH-mutation status via 2HG measurement from small tissue biopsies. The DESI-MS method was optimized in the laboratory using banked tissue sections and then applied in the OR to determine IDH mutation status on the timescale of a few minutes as proof of concept.

4.3   Materials and Methods

4.3.1   Laboratory Investigation

4.3.1.1   Banked Tissue Specimens

All human subject research reported herein was conducted in adherence to ethical guidelines established by the Institutional Review Boards (IRB) of Purdue University and Indiana University School of Medicine. For DESI-MS method optimization, banked, fresh-frozen human brain tissue (N=37) was obtained from the Methodist Research Institute Biorepository (Indianapolis) and used according to Purdue IRB protocol #1410015344.

4.3.1.2   Solvent System Optimization For Extracting 2HG From Brain Tissue

A set of nine solvent combinations were used to prepare tissue extracts from a IDH-mutant glioma specimen known from previous work to contain a high concentration of 2HG.44 Chromasolv acetonitrile, ethanol 200 proof, and 99.9% purity dimethylformamide were purchased from Sigma Aldrich (St. Louis, MO) and used as received. The solvent combinations used are shown as the black points in Figure 4.2. Each solvent system was spiked with deuterated stable isotope labelled internal standards 2HG-d3 (CDN Isotopes, Quebec, Canada), to provide a final concentration of 200 ng/mL. An approximately 40 mg piece of biopsied tissue was homogenized in a scintillation vial using forceps to create a tissue stock. An approximately 1 mg aliquot from the tissue stock was placed in a scintillation vial, weighed with an analytical balance, and a volume of solvent was added to make 1 mg tissue/mL solutions. Each sample was vortexed for one minute, centrifuged at 13000 rpm for 2 min, and then the solvent transferred to a centrifuge tube (Fisher Scientific, Chicago, IL) and placed in a -80 °C freezer until MS analysis. MS analysis was performed on a Thermo LTQ (ThermoFisher Scientific, Waltham, MA).

Each sample was nanoelectrosprayed using fire polished borosilicate glass capillaries (Sutter Instrument, Novato, CA) pulled to a 5 µm tip diameter using a model p-97 micropipette puller (Sutter Instrument, Novato, CA). An MS³ scan for 2HG and the deuterated internal standard was acquired for each sample in triplicate. The MS³ signal for 2HG was normalized by the 2HG-d3 internal standard signal. A linear regression model was fit to these data using JMP, and the global maximum was interpolated from the regression function (Figure 4.2).

4.3.1.3 DESI-MS Line Scanning Of Human Glioma Specimens Using The Optimized Solvent System

The optimized solvent system was used to collect DESI-MS data from a set of 37 de-identified human brain specimens (Purdue IRB 1410015344) and are shown in Table 4.5. The tissue specimens were cryosectioned on a cryotome (ThermoFisher Scientific, Waltham, MA) to 15-µm thickness and thaw-mounted on superfrost glass slides. The DESI source was custom built and is like a previously described apparatus.(22) Additional DESI source parameters are similar to those used in previous work.(15) For data collection, each sample was scanned under the DESI spray at a linear velocity of 300 µm/s in five equally spaced lines to collect negative ion mode data, the DESI spray was returned to the starting position, and then scanned with an additional five lines to collect positive ion data. The negative mode method consisted of five MS scan events that were repeated for the duration that the sample was scanned under the DESI spray. In the negative mode, scan 1 was a full mass scan over the *m/z* range 80-600, scans 2-5 were MS³ product scans targeting aspartate (*m/z* 132 -> 115 -> ○), 2HG (*m/z* 147 -> 129 -> ○), glutamate (*m/z* 146 -> 128 -> ○), and N-acetyl aspartate (*m/z* 174 -> 114 -> ○). The positive ion mode method consisted of two events, scan 1 was a full mass scan over *m/z* range 80-200, and scan 2 was an MS³ product scan (*m/z* 184 -> 86 -> ○) targeting phosphocholine. MS tuning and scan parameters are provided in Table 4.1 and 4.2, respectively. Analytical standards of aspartate, glutamate, N-acetyl-aspartate, 2HG, and phosphocholine were purchased from Sigma-Aldrich (St. Louis, MO) and used as to confirm structural attributions. After DESI-MS analysis, the analyzed tissue sections were stained with H&E, using a previously described procedure,(15) and blindly evaluated by an expert neuropathologist to provide information regarding disease status, relative percentage of tumor cells, and grade.

4.3.1.4 Processing of DESI-MS Data and Statistical Analysis

The raw Thermo MS data files were converted into mzXML files and assembled into datacubes in MATLAB. Scans corresponding to background of the glass slide were removed from each datacube. The remaining MS scans in the full mass scan (*m/z* 80-200) were summed and averaged to compute the total ion count (TIC) which was used to normalize all MS³ data by dividing each *m/z* intensity in each scan by the corresponding TIC. The normalized intensities for the peak maxima of 2HG, N-acetyl aspartate, aspartate, glutamate and phosphocholine in the full scan and respective MS³ scans were compiled in Excel and used for statistical analyses. ROC curve analysis was performed in JMP, with 2HG MS^3 fragment ion intensity as explanatory variable and IDH mutation status as the response variable. ANOVA and Tukey HSD tests were performed in JMP, using each ion as the response variable and IDH status, tumor cell percentage (TCP) category, and IDH*TCP interaction as explanatory variables. MATLAB, Adobe Photoshop, and Illustrator were used to regenerate the plots and compose publication quality figures.

4.3.1.5 ESI-MS Quantitation of 2HG in Brain Tissue Extracts

The concentration of 2HG was determined using methods described previously.[44] Briefly, the tissue samples were cryosectioned on a cryotome (ThermoFisher Scientific, Waltham, MA) to 15-µm thickness. Approximately five sections were placed in a Precellys tissue homogenization vial (Bertin Instruments, Rockville, MD). Vials were weighed on an analytical balance, solvent (3:2 methanol-water containing 2HG-d3 as internal standard) was then added to provide 2 mg/mL final concentration. Vials were homogenized for a few minutes using a Precellys tissue homogenizer (Bertin Instruments, Rockville, MD), centrifuged for 5 minutes at 13000 RPM, and the supernatant collected for direct analysis by ESI-MS/MS on a triple quadrupole mass spectrometer (TSQ Quantum, ThermoFisher Scientific, Waltham, MA). Adjacent tissue sections (each 15-µm thick) were collected and thaw-mounted on glass slides (Superfrost Plus, Electron Microscopy Services) for DESI-MS analysis and subsequent histopathology.

4.3.2 Intraoperative Investigation

The intraoperative study was conducted at the Methodist Hospital (Indianapolis) in adherence to the Indiana University IRB protocol #1410342262. Human subjects (N=25) under the care of neurosurgeons at the Indiana University Department of Neurosurgery and Goodman

Campbell Brain and Spine and undergoing tumor resection for a suspected glioma were recruited into the study (2017-2018) prospectively after providing written informed consent and Health Insurance Portability and Accountability Act authorization.

4.3.2.1 Intraoperative DESI-MS Detection of 2HG

The intraoperative mass spectrometry instrument has been previously described and is shown in Fig. 1A.(26) It consists of a Thermo LTQ linear ion trap mass spectrometer (ThermoFisher Scientific, Waltham, MA), a home-built DESI ion source enclosed to minimize escape of solvent vapors and provide electrical dissipation, a custom-built aluminum encasement that houses the roughing vacuum pumps (Edwards), compressed gas canisters of helium and nitrogen (Praxair), and a desktop computer. The DESI spray solvent used consisted of 25:37:38 % dimethylformamide-acetonitrile-ethanol. The tissue biopsy smears were analyzed using two scan events: a full mass scan in the negative ionization mode over m/z range 80-200, and a MS^3 product scan for 2HG (m/z 147→129→○). The MS method takes approximately 3.4 minutes to analyze a single tissue biopsy smear. The scans were acquired while the DESI spray rastered over the surface of the smeared tissue sampling about 300 µm (spray diameter) per second.

Table 4.1 DESI-MS Tuning Parameters for LTQ mass spectrometers used in the banked tissue and clinical studies. The tuning parameters are slightly different due to instrument specific differences.

Tune Parameter	Banked Tissue Analysis-Purdue LTQ		Clinical Study-IUSM LTQ
	Positive Ionization Mode	Negative Ionization Mode	Negative Ionization Mode
Capillary Temp (C):	300	300	275
Source Voltage (kV):	5	5	5
Capillary Voltage (V):	75.5	-1	-48.0
Tube Lens (V):	245	-40.32	-70.0
Skimmer Offset (V):	0	0	0
Multipole RF Amplifier (Vp-p):	780	400	400
Multipole 00 Offset (V):	-7	6	2.0
Lens 0 Voltage (V):	-7.2	6.0	2.50
Multipole 0 Offset (V):	-7.98	6.5	5.25
Lens 1 Voltage (V):	-11.3	9	31.0
Gate Lens Offset (V):	-58	42	14.0
Multipole 1 Offset (V):	-14.25	10	17.0
Front Lens (V):	-7.98	6.75	5.25

Table 4.2 MS/MS scan parameters used for the two LTQ instruments. In the scan column, the numbers indicate the precursor ions isolated and fragmented in each stage of MS/MS. The scan 132->115->O indicates the isolation and fragmentation of m/z 132 to produce m/z 115, and the subsequent isolation and fragmentation of m/z 115 and the detection of all resulting product ions within the mass range reported in the last column.

Scan	Ion Type	Collision Energy MS²	Collision Energy MS³	q-value (MS² and MS³)	Isolation width (MS² and MS³)	m/z range
Purdue University LTQ						
132→115→ O	[M-H]⁻	25	20	0.25	2	50-132
147→129→O	[M-H]⁻	20	20	0.25	2	50-129
146→128→O	[M-H]⁻	20	30	0.25	2	50-150
174→114→O	[M-H]⁻	25	25	0.25	2	50-180
184→86→O	[M]⁺	25	30	0.25	2	50-132
IUSM LTQ						
147→129→ O	[M-H]⁻	30	30	0.25	2	50-150

4.3.2.2 Data Processing and Statistical Analysis of Intraoperative MS Data

The raw MS data files were converted into mzXML files and analyzed in MATLAB. For each sample, the MS³ product scans, corresponding to the measurement of 2HG, were sorted based on the total ion current (sum of all ion intensities for each *m/z* value) in each scan. The TIC of each full MS scan over the *m/z* range 80-200 was computed and averaged and used to normalize the averaged MS³ scan. The peak intensities of *m/z* 85 and 101, corresponding to the MS³ product ions of 2HG, were extracted from the normalized MS³ spectra for each biopsy. The averaged, TIC normalized, and scaled 2HG MS³ product ion intensities were coded based on the patient's IDH mutation status as determined by Indiana University Health Molecular Pathology Lab (mutant or wildtype) and analyzed in JMP using ROC curve, box-plots, and ANOVA.

4.3.2.3 Assessment of IDH Mutation Status

DESI-MS assessment of IDH mutation status relied on detection of 2HG in tissue sections for the banked specimens (37 specimens, including 11 IDH-mutant and 26 IDH-wildtype gliomas) and for the intraoperative cases (51 biopsies from 25 human subjects, 11 IDH-mutant, 14 IDH-wildtype gliomas). Univariate analysis of variance (ANOVA) and receiver operating characteristic (ROC) curve analysis were performed using Mathworks MATLAB and JMP data analysis software to estimate the quality of diagnosis using 2HG signals measured by DESI-MS (i.e., to distinguish between IDH-mutant and IDH-wildtype gliomas as independently determined by IHC/genetic sequencing).

The IDH mutation status was obtained from the final pathology reports of each subject for post-hoc validation of the DESI-MS results. IDH1 R132H immunohistochemistry was initially performed; samples that provided a negative result were subjected to genetic sequencing of IDH1 and IDH2 genes according to the standard of care. Immunohistochemistry and genetic sequencing were performed at Indiana University Health Molecular Pathology Laboratory, certified under the Clinical Laboratory Improvement Amendments of 1988 to perform high-complexity clinical laboratory testing for clinical purposes.

4.4 Results

4.4.1 Correlation of 2HG DESI-MS Intensity with IDH Mutation Status in Banked Tissue Specimens

The optimized solvent system consisted of dimethylformamide-acetonitrile-ethanol 25:37:38 % v/v (Figure 4.2). This solvent system efficiently extracted 2HG from brain tissue, and it did not destroy or alter the tissue morphology, permitting H&E staining and post-hoc histopathology of the DESI-MS analyzed tissue sections.
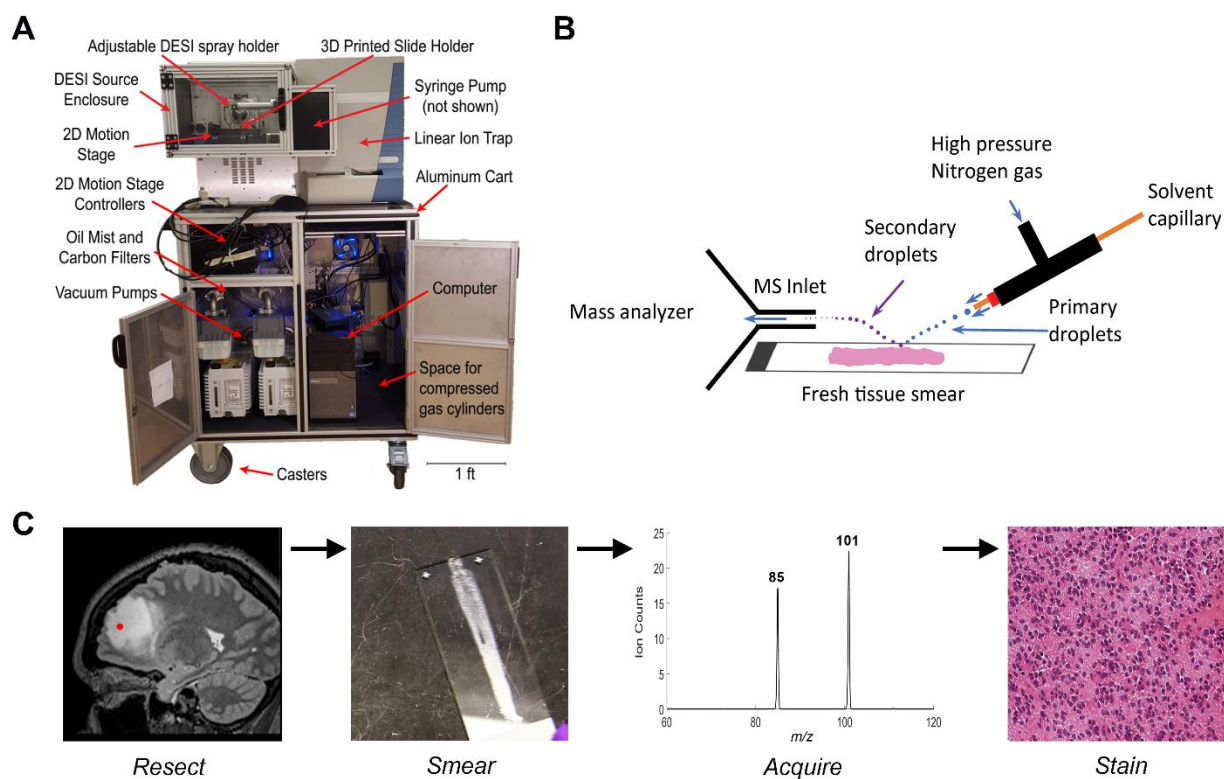
Figure 4.1 DESI-MS method overview. A) Image of the custom-made intraoperative DESI-MS system for intraoperative analysis of tissue biopsies. B) Diagram of the DESI process.(17) C) Workflow of intraoperative analysis protocol consisting of tissue collection (red spot) and smearing, DESI-MS analysis, and post-hoc histopathology
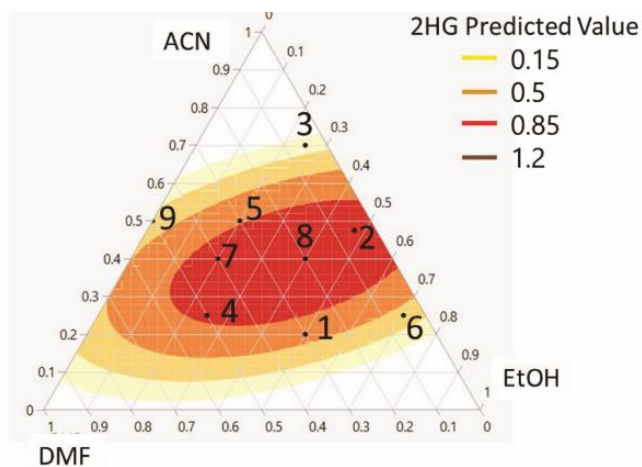
Figure 4.2 Ternary plot for extraction solvent optimization for detection of 2HG from brain tissue. The numbered black points are the solvent combinations tested in the study, the colored region is the value of the regression function fit to the experimental data. Theoretical maximum 2HG signal was obtained with the solvent combination of dimethylformamide-ethanol-acetonitrile 25:37:38 (% v/v).
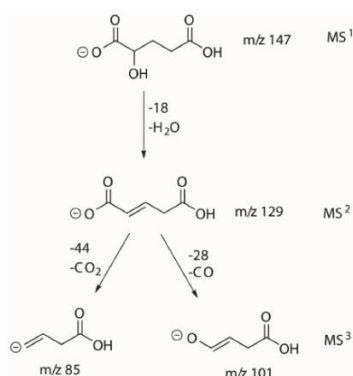
Figure 4.3 Proposed fragmentation pathway of 2HG using collision induced dissociation MS.

The 2HG was detected as a gaseous ion in the mass spectrometer at a specific mass-to-charge ratio (m/z) with an associated intensity. The 2HG ion was measured with high specificity by employing ion dissociation and detection of the resulting fragment ions; this procedure of isolation and fragmentation was performed twice. First, the precursor deprotonated ion, m/z 147 [M−H]⁻, was isolated in the ion trap mass spectrometer and fragmented with collision induced dissociation (CID) to produce a fragment ion peak at m/z 129, corresponding to a loss of 18 as H_2O from the intact 2HG precursor ion. The first product ion, m/z 129, was isolated and fragmented again, resulting in two additional product ions at m/z 85 and m/z 101.
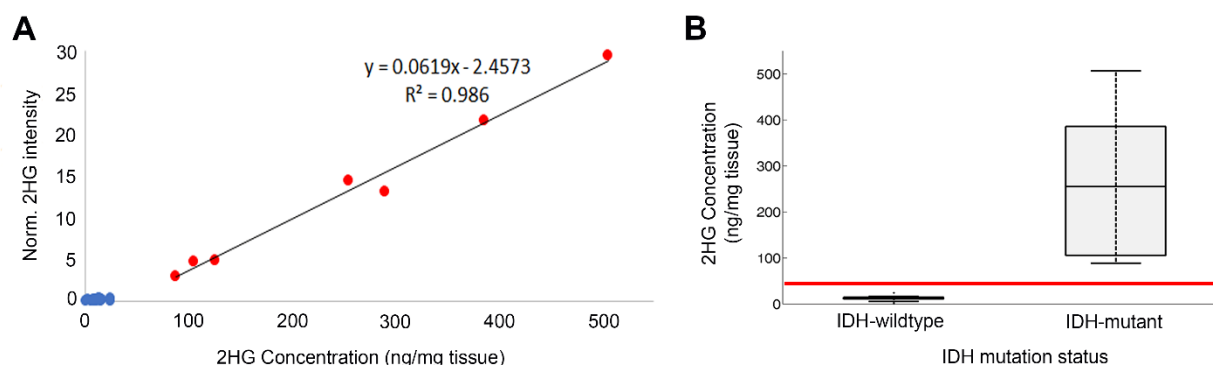
Figure 4.4 Correlation of 2HG DESI-MS signal with 2HG concentration in the banked tissue specimens. A) Correlation between 2HG DESI-MS signal (normalized relative to the full-scan total ion count), ion transition m/z 147→129→101, and 2HG concentration (ng/mg tissue). Adjacent tissue from the same specimens was used to perform both measurements. Only 28 of the 37 samples were used for the quantitative analysis. The remaining samples were excluded due to insufficient tissue quantity. Blue circles, IDH-wildtype samples, n=21; red circles, IDH-mutant samples, n=7. Quantitative data are described in reference 27. This figure was reproduced with permission of the American Association for Clinical Chemistry, Copyright 2018.(16) B) Box-and-whisker plot for 2HG concentrations (ng/mg tissue) in human glioma tissue specimens (N = 28) analyzed using direct infusion ESI-MS/MS.27 The box represents the interquartile range with a median line and whiskers are at ±1.5 standard deviation. Quantitative measurements were made using the MRM transitions m/z 147→129 for 2HG, and the signals were normalized by the MRM transition m/z 150->132 intensity of the added 2HG-d3 internal standard. Random numbers between 0 and the limit of detection were assigned to IDH-wildtype glioma specimens for which no 2HG was detected. Red line shows the cutoff of 45 ng/mg tissue determined from ROC curve analysis.

The peaks at m/z 85 and m/z 101 arose from structural losses of CO2 and CO from the m/z 129 product ion, respectively. This overall process is referred to as a MS³ product ion scan, and is shown schematically as 147->129->○, indicating that the m/z 147 ion is fragmented to produce m/z 129, and the m/z 129 ion is fragmented again and the fragments are detected. A proposed fragmentation pathway is shown in Figure 4.3.

We observed an approximately 40-fold change in m/z 101 signal intensity between IDH-mutant and IDH-wyldtype gliomas, which was statistically significant (p<0.0001). The absolute ion counts were normalized to the full-scan total ion counts (TIC) and scaled by $1x10^6$ (Table 4.5).

The signal of 2HG was significantly elevated in IDH-mutant glioma compared to IDH-wildtype specimens, despite differences in tumor density and smear cellularity (Figure 4.6), which was qualitatively assessed via post-hoc H&E histology. De-identified pathology information and DESI-MS data are provided for the banked tissue specimens in Table 4.5.
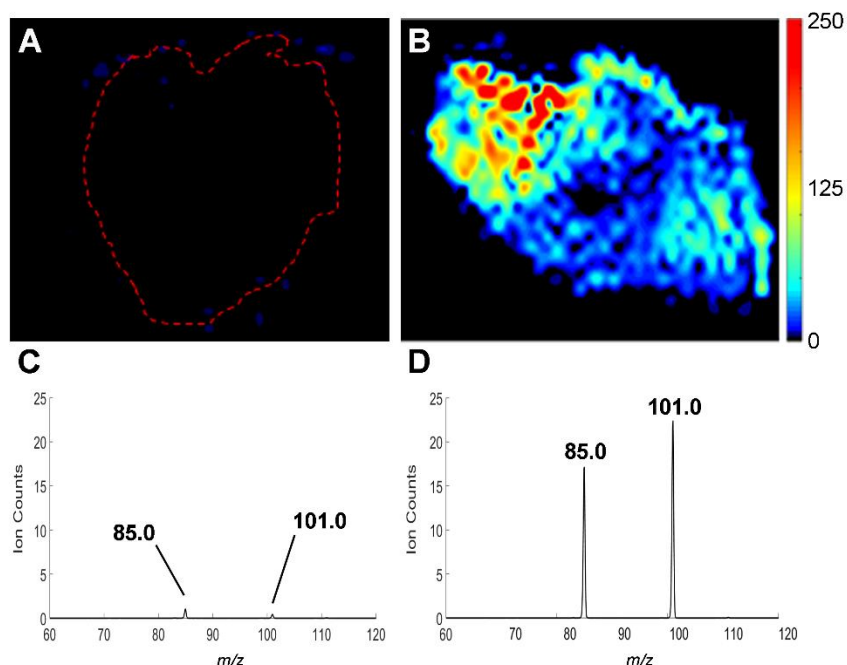
Figure 4.5 Diagnosis of isocitrate dehydrogenase mutation via DESI-MS monitoring of 2HG. A) DESI-MS ion map of ion transition m/z 147→129→101 for an IDH-wildtype tissue section, whose shape is shown in red (sample #11, Table 4.5). B) DESI-MS ion map of ion transition m/z 147→129→101 for an IDH-mutant tissue section (sample #2, Table 4.5). Absolute signal intensity is color-coded and normalized the same for both images. C) Average product ion spectra for m/z 147→129→○ of sample #11, IDH-wildtype. D) Average product ion spectra for m/z 147→129→○ of sample #2, IDH-mutant. See Table 4.5 for additional pathology information.

A representative set of DESI-MS ion images for an IDH-wildtype and IDH-mutant tissue section is shown in Figure 4.5, along with the average 2HG product ion scans recorded. In previous work, our laboratory quantified 2HG in human brain tissue extracts using MS,(16) and the concentration of 2HG was significantly elevated in IDH-mutant gliomas compared to wildtype (Figure 4.4). The tissue sections used for the optimization experiments reported herein were adjacent to the tissue used to prepare the tissue extracts used for quantitation,(16) and a high correlation (R^2=0.98) between the 2HG DESI signal and absolute concentration of 2HG was observed (Figure 4.4) which validates the effectiveness of DESI for real time extraction of 2HG from fresh tissue.
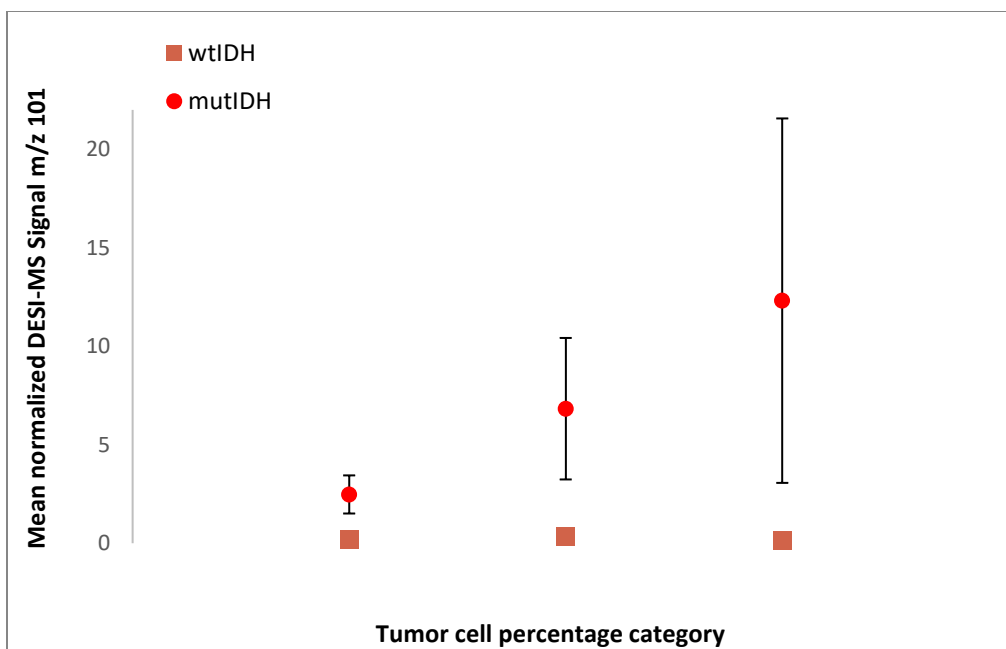
Figure 4.6 Interaction plot of normalized 2HG signal (as the MS³ fragment ion, *m/z* 101) as a function of tumor cell percentage category and IDH-mutation status from the study of banked tissue. Each point represents the mean normalized *m/z* 101 intensity for the respective IDH status and TCP category. The error bars are ± standard deviation.

In addition, we observed statistically significant differences in normalized aspartate (p=0.004) and phosphocholine (p=0.0008) intensities between IDH-wildtype and IDH-mutant samples using ANOVA (Table 4.3, Figure 4.7, Figure 4.8), consistent with recent studies showing significant alterations in the cellular metabolome due to the IDH mutation.(22) No statistically significant differences were measured in N-acetyl aspartate or glutamate signal intensity between IDH-wildtype and IDH-mutant gliomas.

4.4.1 IDH Mutation Status Determination During Glioma Surgery Using DESI-MS Monitoring of 2HG

In the intraoperative study, DESI-MS was used to monitor 2HG from tissue smears in near-real time during tumor resection. The optimized DESI-MS spray solvent (25-37-38 DMF-ACN-EtOH %v/v) was used, along with the same MS³ product ion scan for 2HG (147->129->○). Instrument specific parameters were optimized for the LTQ-MS employed for the clinical study, and optimal values differed slightly from the LTQ-MS used for the banked tissue study (see Tables 4.1 and 4.2).
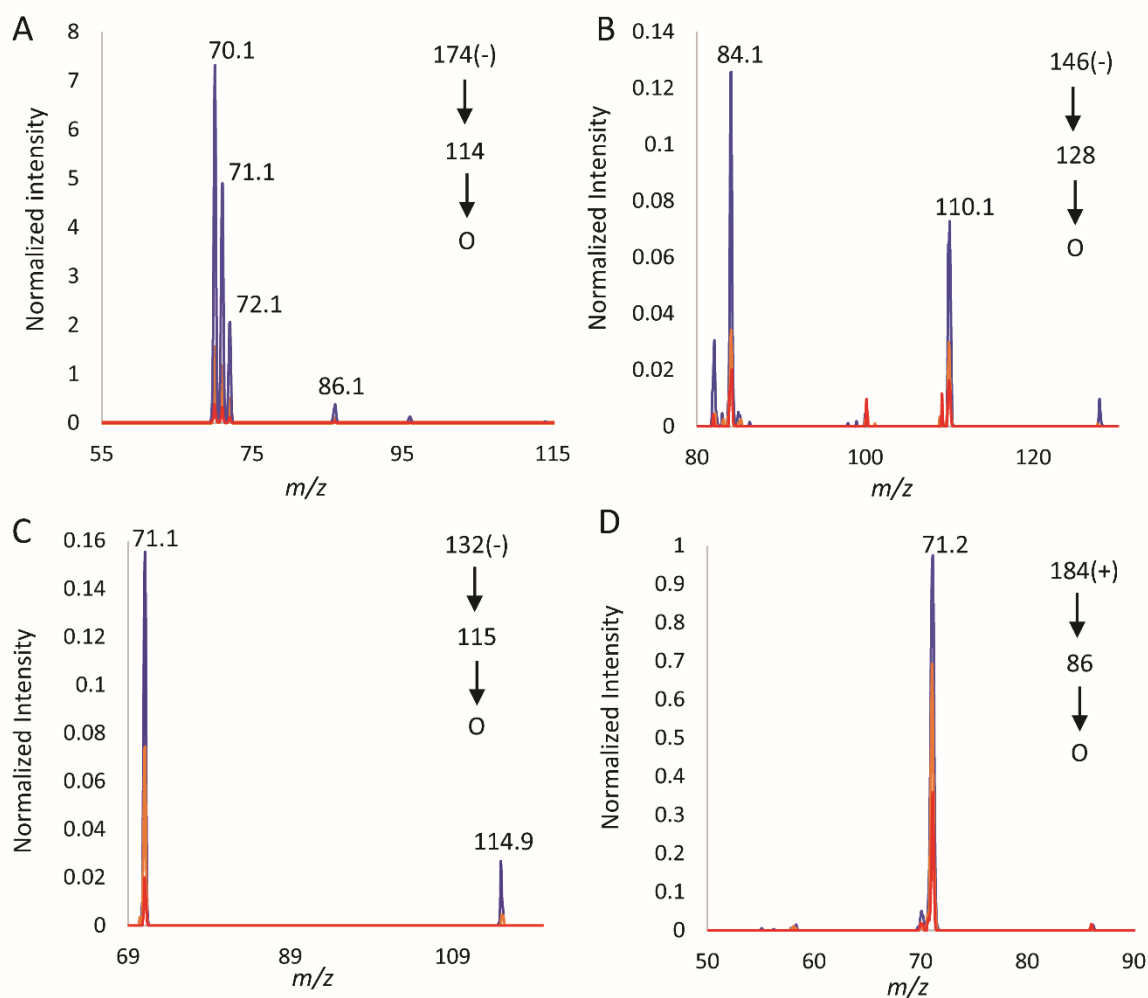
Figure 4.7 Average product ion spectra of metabolites of interest obtained by DESI-MS analysis of the banked tissue specimens. Additional sample data is shown in Table S1. A) Negative-mode MS³ scan 174->114->O, B) Negative-mode MS³ scan 146->128->O, C) Negative-mode MS³ scan 132->115->O, D) Positive-mode MS³ scan 184->86->O. In each figure, the blue trace are the Low TCP samples; Orange is medium TCP; Red is high TCP.
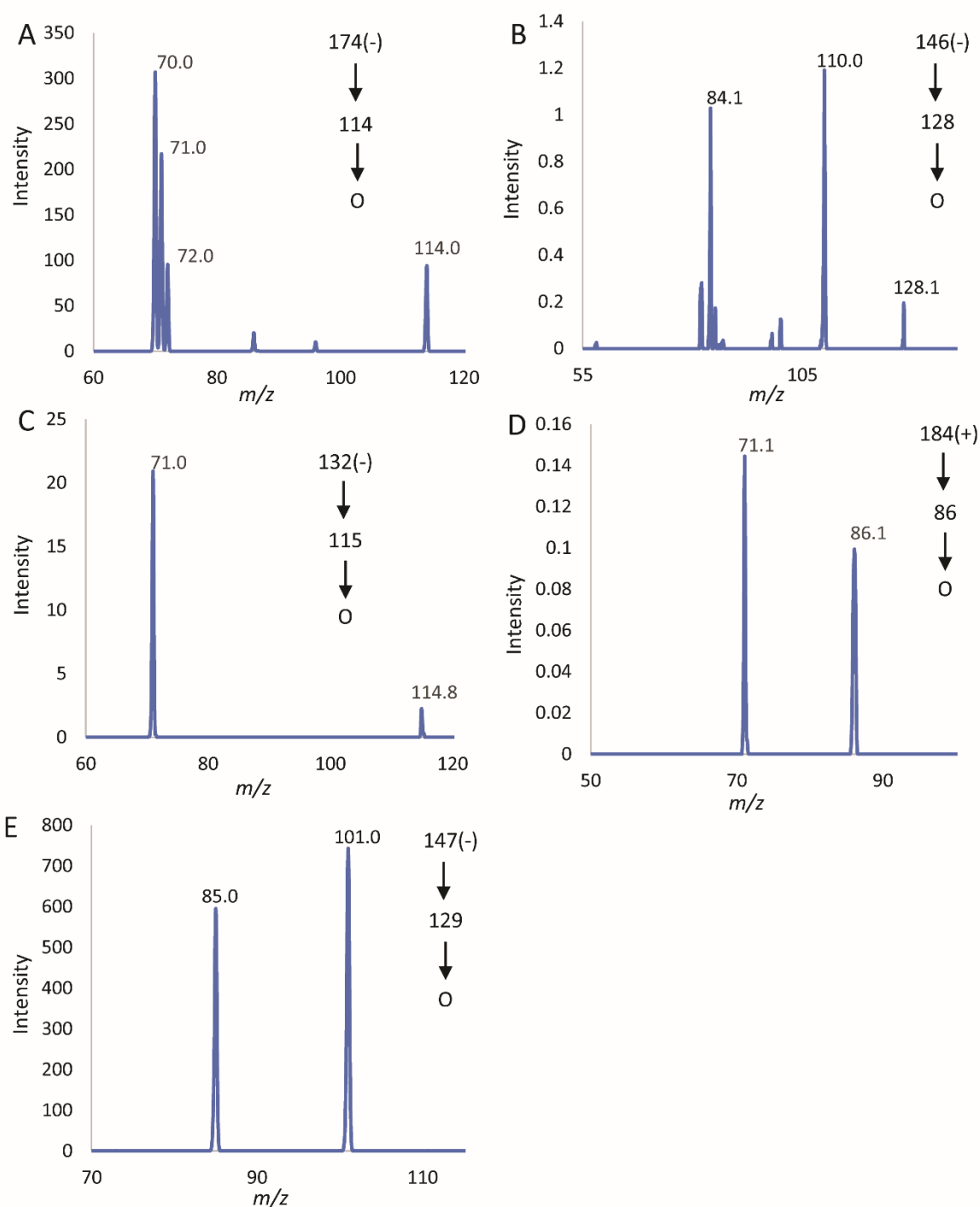
Figure 4.8 Product ion spectra obtained from standards of respective metabolites. A) N-acetyl aspartate, B) Glutamate, C)Aspartate, D)Phosphocholine, E) 2-hydroxyglutarate. Agreement with spectra obtained from the tissue supports tentative identifications of 174 as n-acetylaspartate, 146 as glutamate, 132 as aspartate, 184 as phosphocholine, and 147 as 2-hydroxyglutarate.

Table 4.3 F-test results from 2-way ANOVA for each metabolite, analyzed in the banked tissue specimens, using tumor cell percentage (TCP) and IDH status as factors. Small p-values (<0.05) indicate statistical significance of the respective factor in changing the measured intensity of the respective metabolite. The TCP*IDH interaction term tests whether the changes in the respective metabolite intensity for a given IDH status change differently as a function of TCP.

Metabolite	TCP p-value	IDH p-value	TCP*IDH p-value
2-hydroxyglutarate	0.0067	< 0.0001	< 0.0001
N-acetyl-aspartate	< 0.0001	0.967	< 0.0001
Aspartate	< 0.0001	0.0036	0.0114
Glutamate	0.0001	0.8236	0.87
Phosphocholine	0.0007	0.0008	0.0065
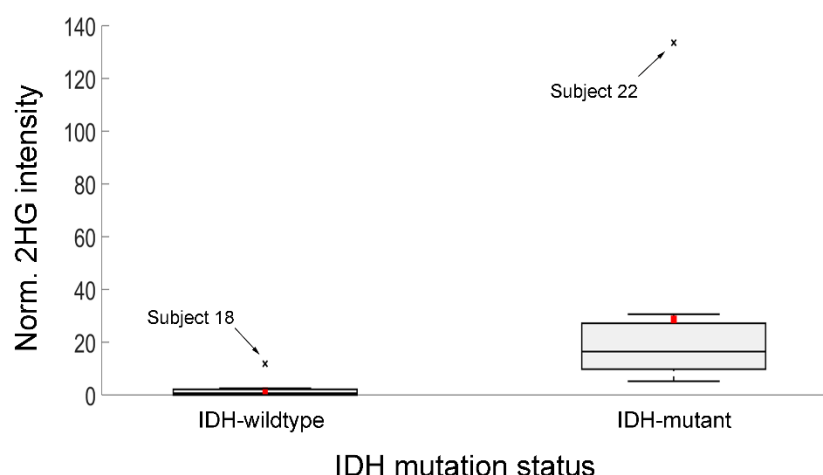
Figure 4.9 Intraoperative discrimination between IDH-wildtype and IDH-mutant gliomas via DESI-MS 2HG measurement. Box-and-whisker plot obtained from the patient cohort of the intraoperative study. IDH-wildtype subjects, n=14; IDH-mutant subjects, n=11. The average 2HG signal intensity, ion transition m/z 147→129→101 and normalized to the total ion count of the full scan, was plotted for each patient. The box represents the interquartile range with a median line and whiskers at ±1.5 standard deviation. Mean values are shown as red squares. Outliers are shown as black crosses. Signal intensities were statistically different (p<0.0001). Zeros were assigned to the wildtype glioma specimens for which no 2HG was detected.

The entire procedure, from tissue smearing to the end of data acquisition, took approximately five minutes per tissue biopsy. The number and size of the biopsies, as well as sampling areas, were decided at the discretion of the attending neurosurgeons. Typically, 2 biopsies were taken from the tumor core and 4 from the surgical margins. Only the tumor core biopsies were used in this study for the diagnosis of IDH mutation status. In total, 51 tumor core biopsies were provided by 25 human subjects (Table 4.4). The DESI process and the experimental

procedure are recapitulated in Figure 1B and 1C. De-identified clinical, pathologic, operative, and radiological data are provided in Table 4.4 for the 25 human subjects enrolled in this portion of the study. Intensities of 2HG were averaged for the multiple tumor core biopsies collected from each subject. The DESI-MS 2HG product ion intensities were compared to the IDH mutation status from the subject's final pathology reports.

We observed about a 20-fold change in the average 2HG m/z 101 product ion intensity between IDH-wildtype and IDH-mutant samples (Figure 4.9). Subject 22, a GBM WHO grade IV with IDH R132H mutation, had the highest signal detected for this patient cohort. Results were independent of the type of IDH mutation; nine subjects of eleven had IDH1 R132H mutation, one subject had IDH1 R132C, one had IDH1 R132X, and no subjects had IDH2 mutations (Table 4.4). The ROC AUC was equal to 1.0, indicating that no study subjects were misclassified. We observed large variance in 2HG intensity within and between the IDH-mutant samples. The intensity of 2HG is affected by differences in smear cellularity, thickness, and tumor density.(18, 19, 23) We observed a significant correlation between 2HG intensity and tumor cell percentage in the tissue smears (two-way ANOVA, p<0.001, Table 4.3). The IDH-mutant gliomas yielded higher 2HG intensity with increasing tumor cell percentage (TCP) which was roughly evaluated by histopathology and categorized in samples with low (<34%), medium (about 34-67%), and high (>67%) TCP (Figure 4.6). The IDH-mutant samples of low TCP were statistically distinguishable from IDH-wildtype gliomas.

4.4.2 Intraoperative Determination of IDH Status in an IDH-Mutated Granular Cell Astrocytoma

Subject 17, a 35-year-old woman, had a syncopal episode and underwent a brain MRI that indicated a right frontal brain tumor. The subject consented to our DESI-MS study and underwent an initial craniotomy and biopsy for frozen sectioning and standard clinical diagnostic tests. Frozen section histopathology during the intraoperative consultation indicated a possible demyelinating condition and no evidence of tumor. Therefore, no resection was performed, and no biopsies were provided for the DESI-MS study. Final pathologic examination performed on the biopsied tissue revealed a granular glioma based on the permanent section histology (formalin-fixed, paraffin-embedded H&E) as well as presence of IDH1 R132H and ATRX mutation (Figure 4.10, Table 4.4). The subject then opted to undergo a second craniotomy for tumor resection, exactly one week after the initial one. Three tissue biopsies were collected and analyzed intraoperatively using

DESI-MS. Our DESI-MS method detected high 2HG product ion signals in tissue, indicative of an IDH mutation, with an average m/z 101 TIC normalized 2HG fragment ion intensity of 30.6 for the three biopsies (Table 4.4). These results suggest that the DESI-MS method may have been able to confirm the glioma diagnosis during the initial craniotomy by providing intraoperative evidence of the presence of an IDH mutation.
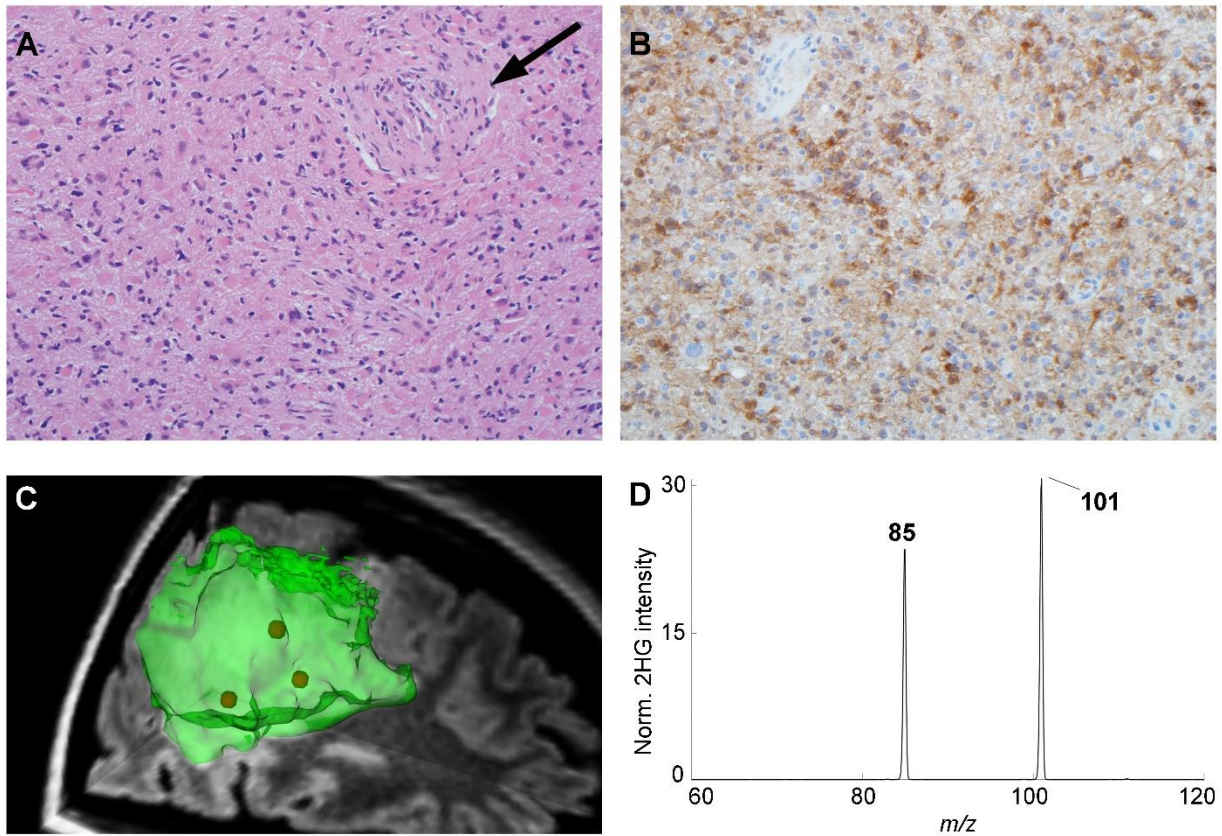
Figure 4.10 Subject 17, IDH-mutant diffuse glioma. A) H&E stained tissue. A diffusely infiltrative, moderately cellular glioma made up of abundant gemistocytic astrocytes with moderate atypia. Note the presence of vascular proliferation (arrow) indicating high-grade nature. B) Immunohistochemistry for IDH1 R132H (clone H09; Dianova, Hamburg, Germany) showing diffuse cytoplasmic immunoreactivity, indicating the present of IDH1 R132H mutation. C) Reconstruction of tumor volume (green volume) using the preoperative MRI scans (T2 weighted 3D Flair), showing the location of tumor core biopsies (in red) analyzed by DESI-MS. Sizes of the biopsies are not to scale. D) Average 2HG product ion scan m/z 147→129→◯ from the three biopsies analyzed.

Table 4.4 De-identified clinical, pathological, and MS data for subjects enrolled into the intraoperative study.

Pathology									MS	
Subject	Biopsies	Age	Gender	Final Diagnosis	IDH Mutation	1p/19q Codeletion	ATRX IHC	Ki67 Labeling Index	*m/z* 85 intensity[1]	*m/z* 101 intensity[1]
1	2	58	M	GBM[2], WHO grade IV, IDH-WT	WT[3]	N/A[4]	R[5]	40%	1.4	0.0
2	2	47	F	GBM, WHO grade IV, IDH WT	WT	N/A	R	40%	0.0	0.0
3	2	46	F	Anaplastic astrocytoma, WHO grade III, IDH-mutant	R132H	ND[6]	L[7]	5%	6.9	9.5
4	2	63	M	Gliosarcoma, WHO grade IV, IDH-WT	WT	ND	N/A	20%	0.3	2.3
5	2	53	F	Diffuse astrocytoma, WHO grade II, IDH-WT	WT	N/A	R	1-2%	0.0	0.0
6	2	38	M	Diffuse astrocytoma, WHO grade II, IDH-mutant	R132C	ND	L	1-2%	2.3	5.2
7	2	68	M	GBM, WHO grade IV, IDH WT	WT	N/A	R	50%	0.3	0.0
8	2	54	F	GBM, WHO grade IV, IDH-WT	WT	N/A	R	15-70%	0.0	0.0
9	2	20	M	Diffuse astrocytoma, WHO grade II, IDH-mutant	R132H	ND	R	10%	7.5	10.1
10	2	66	F	GBM, WHO grade IV, IDH WT	WT	ND	R	3-5%	0.2	0.7
11	2	46	M	GBM, WHO grade IV, IDH-WT	WT	N/A	R	30%	0.8	1.3
12	2	59	M	GBM, WHO grade IV, IDH-WT	WT	N/A	R	30%	0.0	0.0
13	2	28	M	Diffuse mixed glioma, not high grade, IDH-mutant	R132H	ND	L	5-10%	6.7	13.6
14	2	59	M	Recurrent GBM, WHO grade IV, IDH-WT	WT	N/A	N/A	N/A	1.7	2.1
15	2	57	F	GBM, WHO grade IV, IDH-WT	WT	N/A	L	20%	0.4	1.0
16	2	26	F	Diffuse glioma, not high grade, IDH-mutant	R132H	N/A	L	5%	5.7	10.4
17	3	35	F	GBM, WHO grade IV, IDH-mutant	R132H	N/A	R	5%	24.7	30.6
18	2	30	M	Residual/recurrent low-grade glioma	R132X	ND	L	3%	8.5	12.0
19	2	66	F	Diffuse glioma	WT	N/A	R	5-10%	2.0	1.1

Table 4.4 Continued

20	2	48	M	Residual/recurrent anaplastic astrocytoma, WHO grade III, IDH-mutant	R132H	ND	L	3-5%	16.0	25.6
21	2	68	M	GBM, WHO grade IV, IDH-WT	WT	N/A	R	10%	1.4	2.5
22	2	30	F	GBM, WHO grade IV, IDH-mutant	R132H	N/A	N/A	N/A	89.8	133.5
23	2	61	M	GBM, WHO grade IV, IDH-WT	WT	N/A	L	5-10%	3.2	0.0
24	2	27	M	Diffuse astrocytoma, WHO grade II, IDH-mutant	R132H	ND	N/A	3-4%	13.4	19.3
25	2	68	M	GBM, WHO grade IV, IDH-mutant	R132H	N/A	R	~10%	23.3	28.8

1. Normalized intensities
2. GBM = glioblastoma
3. WT = wildtype
4. N/A = not assessed
5. R = retained nuclear expression (i.e., no mutation detected)
6. ND = not detected
7. L = lost nuclear expression (i.e., mutation detected).

Table 4.5 De-identified pathology and DESI-MS data for banked tissue specimens.

	Pathology Data		DESI-MS normalized signal intensities				
Sample	Diagnosis[a]	IDH Status	Aspartate	NAA	Glutamate	2HG	Phosphocholine
1	No tumor (N)	WT	0.18	7.05	0.19	0.21	1.56
2	Oligoastrocytoma	Mutant	0.01	0.08	0.06	6.58	0.28
3	No tumor (N)	WT	0.11	7.44	0.16	0.20	2.22
4	GBM	WT	0.00	0.36	0.00	0.34	0.29
5	Oligoastrocytoma	Mutant	0.10	1.74	0.00	3.74	0.52
6	GBM	WT	0.06	0.51	0.06	0.15	0.91
7	Anaplastic astrocytoma	Mutant	0.07	1.16	0.16	6.59	1.40
8	No tumor (N)	WT	0.25	8.61	0.16	0.15	1.56
9	Oligodendroglioma	Mutant	0.04	0.49	0.03	17.99	0.07
10	No tumor (N)	WT	0.24	6.97	0.10	0.18	1.76
11	GBM	WT	0.00	0.10	0.16	0.16	0.98
12	No tumor (N)	WT	0.90	10.15	0.34	0.36	2.53
13	No tumor (N) from GBM pt.	WT	0.21	2.74	0.08	0.20	1.16
14	GBM	WT	0.01	0.08	0.00	0.09	0.22
15	Astrocytoma	WT	0.02	0.00	0.01	0.04	0.08
16	No tumor (N) from GBM pt.	WT	0.41	5.87	0.18	0.16	1.21
17	Oligoastrocytoma	Mutant	0.16	4.41	0.17	1.75	0.33
18	Oligoastrocytoma	Mutant	0.00	0.97	0.03	7.92	0.84
19	No tumor (N) from GBM pt.	WT	0.14	3.96	0.18	0.14	1.37
20	Oligodendroglioma	WT	0.54	5.74	0.05	0.83	1.50
21	Oligoastrocytoma	Mutant	0.16	1.44	0.00	9.35	0.72
22	No tumor (N)	WT	0.09	5.49	0.05	0.16	1.41
23	Oligodendroglioma	Mutant	0.52	6.96	0.64	3.21	0.30
24	No tumor (N)	WT	0.18	4.95	0.20	0.07	2.00
25	No tumor (N) from GBM pt.	WT	0.11	7.21	0.13	0.25	0.88
26	No tumor (N)	WT	0.18	8.64	0.19	0.20	1.19
27	GBM	WT	0.03	0.35	0.08	0.11	0.44
28	GBM	WT	0.13	2.96	0.05	0.18	1.12
29	No tumor (N)	WT	0.05	3.76	0.06	0.10	0.98
30	No tumor (N)	WT	0.64	12.55	0.33	0.09	1.60
31	No tumor (N)	WT	0.15	6.01	0.09	0.09	0.38
32	No tumor (N)	WT	0.10	8.00	0.35	0.22	1.21
33	No tumor (N) from GBM pt.	WT	0.15	18.90	0.07	0.24	1.42
34	No tumor (N) from GBM pt.	WT	0.35	7.65	0.19	0.22	1.47
35	Oligoastrocytoma	Mutant	0.26	0.24	0.00	13.22	0.40
36	Oligodendroglioma	Mutant	0.04	0.07	0.01	2.42	0.18
37	Oligodendroglioma	Mutant	0.00	0.14	0.03	15.21	0.84

4.5   Discussion

Several advantages are provided from intraoperative knowledge of IDH mutation status. First, the presence of an IDH mutation in a solid tumor is highly specific for glioma, regardless of other morphological or genetic characteristics. Second, a growing body of evidence shows that surgical strategies should be tailored based on IDH-mutation status, in addition to other clinical and oncological factors.(3, 5) Finally, decisions regarding patient management can be made with improved accuracy, especially in cases of IDH mutant gliomas that provide unremarkable morphological features on frozen section H&E during the intraoperative consultation. In the instance of Subject 17, misdiagnosis on frozen H&E-stained section during the first craniotomy was due to the granular subtype of glioma not being reliably differentiated from reactive macrophages.(24) This underlines the limitations of diagnosis based on cellular morphology from suboptimal preparations. A similar misdiagnosis on frozen section has been reported in the case of a 14-year-old boy.(25) Such cases clearly demonstrate a need for more rapid and reliable molecular diagnostic tests that can be used concurrently with histopathology for intraoperative consultations; our DESI-MS method for assessment of IDH mutation status is one example.

It is worth noting that the absence of IDH mutation does not rule out diffuse glioma; additional molecular information may aid in the differential diagnosis of IDH-wildtype intracranial lesions and increase the accuracy of the intraoperative consultation. Previous work in our laboratory showed the ability to discriminate between tumor subtypes,(21),(26) and we suggest that more extensive metabolic and lipidomic fingerprinting could allow differentiation of other primary CNS lesions as well. The incorporation of these additional molecular features has the potential to provide a significant contribution to intraoperative cancer diagnostics.

Lastly, the advantage of mass spectrometry for IDH mutation assessment is that all IDH1 132/IDH2 172 mutants produce 2HG.(12, 23, 27) MS has the same versatility as genetic sequencing but it provides a diagnosis in a much shorter timeframe. The tissue smear used for the DESI-MS 2HG assay could be H&E stained alongside the frozen tissue sections used for the standard intraoperative consultation, and the microscopic observation of the tissue can corroborate its viability and adequacy for molecular testing or otherwise call for resampling. The DESI-MS methodology for IDH mutation assessment could be implemented as a standalone pathology tool that can be used to supplement frozen section analysis for intraoperative consultations.
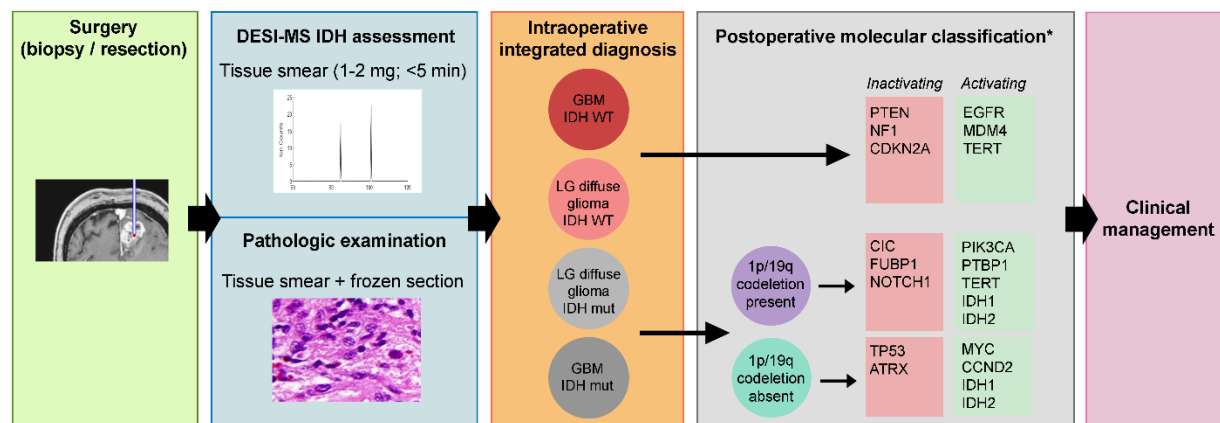
Figure 4.11 Proposed integrated intraoperative diagnosis workflow for infiltrative gliomas using frozen section H&E histopathology and DESI-MS IDH mutation assessment.(3) *Postoperative molecular classification was adapted from Brat et al. (2015) N Engl J Med 26:2481-98; with permission.(3)

4.6 Conclusions

This study reports diagnostic data and provides preliminary classification accuracy of a rapid DESI-MS method for intraoperative IDH assessment. This work goes beyond the mere detection of 2HG in IDH-mutant glioma and provides evidence that IDH mutation status can be accurately assessed from fresh tissue via DESI-MS detection of 2HG. The reported method is more sensitive, specific, and diagnostically accurate than previous DESI-MS methods. Further, the analysis time of our method is sufficiently short to be used in the intraoperative consultation to provide quasi real-time feedback on IDH status. The 25-subject cohort included herein is somewhat limited, but our preliminary results are encouraging and supported by the strong extant literature on the oncometabolite 2HG. Future studies should aim to conduct multicenter clinical trials and extensive multi-institution proficiency test studies.

4.7 Acknowledgements

4.8   References

1. Louis DN, Perry A, Reifenberger G, von Deimling A, Figarella-Branger D, Cavenee WK, et al. The 2016 World Health Organization Classification of Tumors of the Central Nervous System: a summary. Acta neuropathologica. 2016;131(6):803-20.

2. Pisapia DJ. The Updated World Health Organization Glioma Classification: Cellular and Molecular Origins of Adult Infiltrating Gliomas. Arch Pathol Lab Med. 2017;141(12):1633-45.

3. Beiko J, Suki D, Hess KR, Fox BD, Cheung V, Cabral M, et al. IDH1 mutant malignant astrocytomas are more amenable to surgical resection and have a survival benefit associated with maximal surgical resection. Neuro-Oncology. 2014;16(1):81-91.

4. Chen R, Ravindra VM, Cohen AL, Jensen RL, Salzman KL, Prescot AP, et al. Molecular features assisting in diagnosis, surgery, and treatment decision making in low-grade gliomas. Neurosurgical focus. 2015;38(3):E2.

5. Patel T, Bander ED, Venn RA, Powell T, Cederquist GY, Schaefer PM, et al. The Role of Extent of Resection in IDH1 Wild-Type or Mutant Low-Grade Gliomas. Neurosurgery. 2017;82(6):808-14.

6. Suzuki A, Maruyama T, Nitta M, Komori T, Ikuta S, Kawamata T, et al. Modified rapid immunohistochemical staining for intraoperative diagnosis of malignant brain tumors. Brain tumor pathology. 2017.

7. Kanamori M, Kikuchi A, Watanabe M, Shibahara I, Saito R, Yamashita Y, et al. Rapid and sensitive intraoperative detection of mutations in the isocitrate dehydrogenase 1 and 2 genes during surgery for glioma. J Neurosurg. 2014;120(6):1288-97.

8. Shankar GM, Francis JM, Rinne ML, Ramkissoon SH, Huang FW, Venteicher AS, et al. Rapid Intraoperative Molecular Characterization of Glioma. JAMA oncology. 2015;1(5):662-7.

9. Ohka F, Yamamichi A, Kurimoto M, Motomura K, Tanahashi K, Suzuki H, et al. A novel all-in-one intraoperative genotyping system for IDH1-mutant glioma. Brain tumor pathology. 2017;34(2):91-7.

10. Andronesi OC, Kim GS, Gerstner E, Batchelor T, Tzika AA, Fantin VR, et al. Detection of 2-hydroxyglutarate in IDH-mutated glioma patients by in vivo spectral-editing and 2D correlation magnetic resonance spectroscopy. Science translational medicine. 2012;4(116):116ra4.

11. Tietze A, Choi C, Mickey B, Maher EA, Parm Ulhoi B, Sangill R, et al. Noninvasive assessment of isocitrate dehydrogenase mutation status in cerebral gliomas by magnetic resonance spectroscopy in a clinical setting. J Neurosurg. 2017:1-8.

12. Choi C, Ganji SK, DeBerardinis RJ, Hatanpaa KJ, Rakheja D, Kovacs Z, et al. 2-hydroxyglutarate detection by magnetic resonance spectroscopy in IDH-mutated patients with gliomas. Nature medicine. 2012;18(4):624-9.

13. Longuespee R, Wefers AK, De Vita E, Miller AK, Reuss DE, Wick W, et al. Rapid detection of 2-hydroxyglutarate in frozen sections of IDH mutant tumors by MALDI-TOF mass spectrometry. Acta Neuropathol Commun. 2018;6(1):21.

14. Park J, Na HK, Shon HK, Son HY, Huh YM, Lee SW, et al. TOF-SIMS analysis of an isocitrate dehydrogenase 1 mutation-associated oncometabolite in cancer cells. Biointerphases. 2018;13(3):03b404.

15. Kanamori M, Maekawa M, Shibahara I, Saito R, Chonan M, Shimada M, et al. Rapid detection of mutation in isocitrate dehydrogenase 1 and 2 genes using mass spectrometry. Brain Tumor Pathol. 2018;35(2):90-6.

16. Yannell KE, Smith K, Alfaro CM, Jarmusch AK, Pirro V, Cooks RG. N-Acetylaspartate and 2-Hydroxyglutarate Assessed in Human Brain Tissue by Mass Spectrometry as Neuronal Markers of Oncogenesis. Clin Chem. 63. United States2017. p. 1766-7.

17. Takats Z, Wiseman JM, Gologan B, Cooks RG. Mass Spectrometry Sampling Under Ambient Conditions with Desorption Electrospray Ionization. Science. 2004;306:471-3.

18. Pirro V, Alfaro CM, Jarmusch AK, Hattab EM, Cohen-Gadol AA, Cooks RG. Intraoperative assessment of tumor margins during glioma resection by desorption electrospray ionization-mass spectrometry. Proc Natl Acad Sci U S A. 2017;114(26):6700-5.

19. Santagata S, Eberlin LS, Norton I, Calligaris D, Feldman DR, Ide JL, et al. Intraoperative mass spectrometry mapping of an onco-metabolite to guide brain tumor surgery. Proc Natl Acad Sci U S A. 2014;111(30):11121-6.

20. Eberlin LS, Norton I, Orringer D, Dunn IF, Liu X, Ide JL, et al. Ambient mass spectrometry for the intraoperative molecular diagnosis of human brain tumors. Proc Natl Acad Sci U S A. 2013;110(5):1611-6.

21. Jarmusch AK, Pirro V, Baird Z, Hattab EM, Cohen-Gadol AA, Cooks RG. Lipid and metabolite profiles of human brain tumors by desorption electrospray ionization-MS. Proc Natl Acad Sci U S A 2016;113(6):1486-91.

22. Reitman ZJ, Jin G, Karoly ED, Spasojevic I, Yang J, Kinzler KW, et al. Profiling the effects of isocitrate dehydrogenase 1 and 2 mutations on the cellular metabolome. Proceedings of the National Academy of Sciences of the United States of America. 2011;108(8):3270-5.

23. Choi C, Raisanen JM, Ganji SK, Zhang S, McNeil SS, An Z, et al. Prospective Longitudinal Analysis of 2-Hydroxyglutarate Magnetic Resonance Spectroscopy Identifies Broad Clinical Utility for the Management of Patients With IDH-Mutant Glioma. Journal of clinical oncology : official journal of the American Society of Clinical Oncology. 2017;34(33):4030-9.

24. Shi Y, Morgenstern N. Granular cell astrocytoma. Arch Pathol Lab Med. 2008;132(12):1946-50.

25. Sondergaard CB, Scheie D, Sehested AM, Skjoth-Rasmussen J. Finding of IDH1 R132H mutation in histologically non-neoplastic glial tissue changes surgical strategies, a case report. Child's nervous system : ChNS : official journal of the International Society for Pediatric Neurosurgery. 2017;33(7):1217-20.

26. Eberlin LS, Dill AL, Golby AJ, Ligon KL, Wiseman JM, Cooks RG, et al. Discrimination of human astrocytoma subtypes by lipid analysis using desorption electrospray ionization imaging mass spectrometry. Angew Chem Int Ed Engl. 2010;49(34):5953-6.

27. Catteau A, Girardi H, Monville F, Poggionovo C, Carpentier S, Frayssinet V, et al. A new sensitive PCR assay for one-step detection of 12 IDH1/2 mutations in glioma. Acta neuropathologica communications. 2014;2:58.

CHAPTER 5.   INTRAOPERATIVE-MS-BASED BIOPSY ANALYSIS PLATFORM FOR GLIOMA DIAGNOSIS, IDH SUBTYPING, AND ESTIMATION OF TUMOR CELL INFILTRATION

5.1   Abstract

5.1.1   Background

Surgical tumor resection is the primary treatment option for gliomas, the most common malignant brain cancer. The intraoperative diagnosis of gliomas can be improved by use of molecular diagnostics. Further, residual tumor is a primary cause of tumor recurrence and malignant progression. This study evaluates a desorption electrospray ionization-MS based system for glioma diagnosis, isocitrate dehydrogenase mutation assessment, and estimating tumor cell infiltration, which could improve outcomes from glioma resection and may guide post-surgical treatments.

5.1.2   Methods

A mobile DESI linear trap quadrupole mass spectrometer was modified and used inside neurosurgical operating rooms. A cohort of 49 human subjects undergoing craniotomy with tumor resection for suspected glioma was recruited into the study. Small tissue biopsies (n=272) from the tumor core and surgical margins were taken by neurosurgeons and provided to the DESI-MS operators, smeared on a glass slide, analyzed by DESI-MS in the operating room, and classified using multivariate and univariate statistics.

5.1.3   Results

For assessment of IDH mutation status, using 2HG fragment ion intensities as predictor variables and IDH mutation status determined by IHC as a response variable (n=158), an overall diagnostic accuracy of 92.4% was obtained. Using PCA-LDA and histopathology as a reference, the overall accuracy in differentiating glioma samples from infiltrative margins was 76.8% (n=272). Using lipid deconvolution based on a regression model, the sensitivities in detecting low and high tumor cell percentage were 73.0% and 74.1%, respectively (n =272).

5.1.4 Conclusions

The DESI-MS system provided good performance in assessing disease status, IDH mutation status, and TCP.

5.2 Introduction

Gliomas are high morbidity primary brain tumors. The five-year survival rate of patients with glioblastoma, the highest grade and most common form of glioma, is less than 5%.(1) Accurate diagnosis and prognosis of gliomas relies on molecular genetic information.(2) The primary treatment option for gliomas is gross total surgical resection.(3-6) However, the infiltrative nature of glioma and morbidity associated with neurological deficits often result in residual tumor at surgical margins, leading to recurrence and malignant progression.(7-9) Currently, brain surgical resections are typically performed without the aid of a molecular diagnosis as these slow assays must be performed post-operatively.(10) Most importantly, brain surgical margins are not assessed for residual tumor using pathology or analytical techniques.(9, 11)

Ambient ionization-mass spectrometry (MS) is a method for generating ions under normal atmospheric temperature and pressure, with little to no sample preparation, and then analyzing the ions sensitively and specifically using MS.(12) The capabilities of ambient ionization spectrometry-MS are being evaluated in their ability to assess molecular features of cancer, as well as in assessing surgical margins for residual tumor.(13) Probe-based methods such as probe electrospray ionization(14) and touch spray ionization(15, 16) have been demonstrated on fresh surgical tissue to yield pathologically relevant results. Rapid evaporative ionization mass spectrometry has been used intraoperatively in a variety of cancers(17, 18) Several laser ablation systems, based on picosecond-infrared and other optical regimes, have been shown to yield diagnostic MS signals and low tissue damage.(19-21) The recently developed MassSpec Pen has been used *in vivo* to assess residual tumor in a low-invasive approach.(22, 23)

Desorption electrospray ionization-mass spectrometry (DESI-MS) is an ambient ionization method in which charged microdroplets of a solvent are sprayed onto a sample surface, desorbing and ionizing molecules present in the sample and transporting them into a MS for mass analysis.(12) Under certain conditions, as used in this study, DESI-MS analyzed tissue samples

can be H&E stained and then interpreted by pathologists, allowing for correlations between tissue disease status as determined by these complementary methods.(24) Using this approach, DESI-MS has been applied to the recognition of cancerous and normal tissues in a variety of human organs.(13) Applications in brain cancer have shown the capability to differentiate gliomas, meningiomas, and pituitary tumors with high accuracy.(25) Importantly, each of these brain cancers could be distinguished from normal brain tissue. In a recent study, an intraoperative DESI-MS system was developed for analysis of glioma tissue during tumor resection surgery, and clinical data were shown for a set of 10 human subjects.(26) An intraoperative DESI-MS assay for the assessment of isocitrate dehydrogenase (IDH) mutation status via detection of the oncometabolite 2-hydroxyglutarate (2HG), a key glioma prognostic marker, has also been recently reported in a set of 51 glioma core biopsies obtained from 25 human subjects and analyzed intrasurgically.(27)

In this study, a DESI-MS system capable of rapidly analyzing brain tumor biopsies during glioma resection surgeries was evaluated in a cohort of 49 patients at a single medical institution. A dataset published in a previous study was used as a training set to statistically classify the brain tissue samples analyzed in this study which were used as a validation set.(25) Three categories of information were assessed: 1) IDH mutation status, 2) disease status, and 3) tumor cell percentage. The non-destructive nature of DESI-MS on cell and tissue morphology permitted the H&E staining of the analyzed tissue smears after MS analysis, providing a direct comparison between pathology and the DESI-MS results. No DESI-MS results were shared with neurosurgeons during the surgical resection so as not to affect the standard of care. The DESI-MS data was used to generate simple categorical outputs (e.g. low tumor cell percentage vs. high tumor cell percentage) for simple interpretation by the neurosurgeons. It is demonstrated that DESI-MS outputs could have provided pertinent molecular information that could have influenced surgical procedures and potentially improved patient care. An overall assessment of the current methodology is presented along with areas for future improvement.

5.3   Materials and Methods

5.3.1   Human Subjects

All human subjects research was performed in accordance with an Institutional Review Board approved study at the Indiana University School of Medicine (IRB #1410342262). Glioma patients undergoing craniotomy with tumor resection were prospectively enrolled in our study after providing written informed consent and Health Insurance Portability and Accountability Act authorization.

5.3.2   Intraoperative DESI-MS

All experiments were performed with a modified linear trap quadrupole mass spectrometer (Thermo LTQ) as previously described.(26, 27) The MS was placed on an aluminum cart with casters, permitting the facile movement of it in and out of operating rooms. The cart contained all equipment necessary to operate the instrument. For each surgery, the instrument was rolled into the OR and turned on. During tumor resection, small stereotactic tissue biopsies were provided by the neurosurgeon to the MS operators for tissue analysis. The number and location of the biopsies were made according to the surgeon's best medical judgement. Samples from the tumor core as well as surgical margins were typically provided for each case. The tissue biopsies were smeared on a glass microscope slide using a disposable 3D printed nylon tool. The tissue smears were then immediately analyzed with DESI using the intraoperative MS system. The DESI spray solvent consisted of 1:1 DMF-ACN, Nitrogen gas pressure of 180 psi, solvent flow rate of 1.2 µL / minute, spray voltage of 5kV, negative ion polarity was used. In order to obtain a high-quality average spectrum of the sample, the DESI spray was rastered across the tissue smear in a zigzag pattern using precision moving stage. Negative ion mode metabolite, lipid, and MS/MS data were collected as different segments in the MS over a total time of three minutes. The same smears were re-analyzed using a solvent consisting of 37:38:25 ACN-EtOH-DMF and using multiple-stage mass spectrometry for the detection of 2-hydroxyglutarate, for an additional three minutes of data acquisition.

5.3.3   Data Analysis

De-identified clinical data were obtained for each subject, consisting of radiology, surgical, pathology reports, and patient demographics, for correlation with the DESI-MS results (Tables 5.4-5.7). The DESI-MS analyzed tissue smears were H&E stained and interpreted by an expert neuropathologist (E.M.H.) to provide information on diagnosis (glioma or normal brain), relative percentage of tumor cells, and smear quality (Table 5.8). The DESI-MS data were analyzed in MATLAB using custom algorithms. To remove background scans (e.g. signal collected from bare glass slide containing no tissue), the collected lipid data were filtered using standard deviation thresholds of the absolute signal intensity compared to background spectra. The metabolite profiles were filtered by multivariate modeling of the background and selecting MS scans that were statistically different from the background. A reference library of mass spectra, published in a previous study, was used as a training set to classify the data collected in this study.(25) The samples in this study served as an external validation set for statistical classifications of disease state and tumor cell percentage.

Diagnosis was accomplished using principal component analysis-linear discriminant analysis (PCA-LDA). For this purpose, the lipid and metabolite data were combined using mid-level data fusion. The loading matrix eigenvectors calculated from the training set were used to calculate the PC scores of the new samples. The PC scores of the new samples were then used to classify their disease status using linear discriminant analysis (LDA) eigenvectors from the training set.

Principal component regression analysis was used to calculate the percentage of white matter, grey matter, and glioma contributing to the new sample based on a linear regression model. The lipid profiles were compressed using PCA, and the scores on PC1 and PC2 were used as the coefficients in the regression model.

The normalized intensity of *m/z* 174, corresponding to N-acetyl-aspartic acid (NAA), measured in the full scan MS metabolite profile was used to estimate (approximately) the tumor cell percentage, using a previously published data set as a training set.

For IDH mutation status, the normalized intensity of MS³ fragment ions (*m/z* 101 and 85) detected from sequential fragmentation of the 2HG precursor ion (*m/z* 147 in the negative mode) was used as a measure of IDH mutation status. The intensities of the two MS³ product ions were summed together to provide an IDH mutation score for each smear.

The disease diagnosis provided by PCA-LDA on the fused lipid and metabolite profiles obtained from DESI are glioma (G), grey matter (GM), or white matter (WM). G is indicative of diseased tissue; GM and WM are indicative of low infiltration brain tissue, referred to as infiltrative margins (I.M.). The tumor cell percentage is categorized as low (TCP 0-33%), medium (TCP 34-66%), or high (TCP 67-100%. The IDH mutation status is either mutant (IDH-M) or wild-type (IDH-WT).
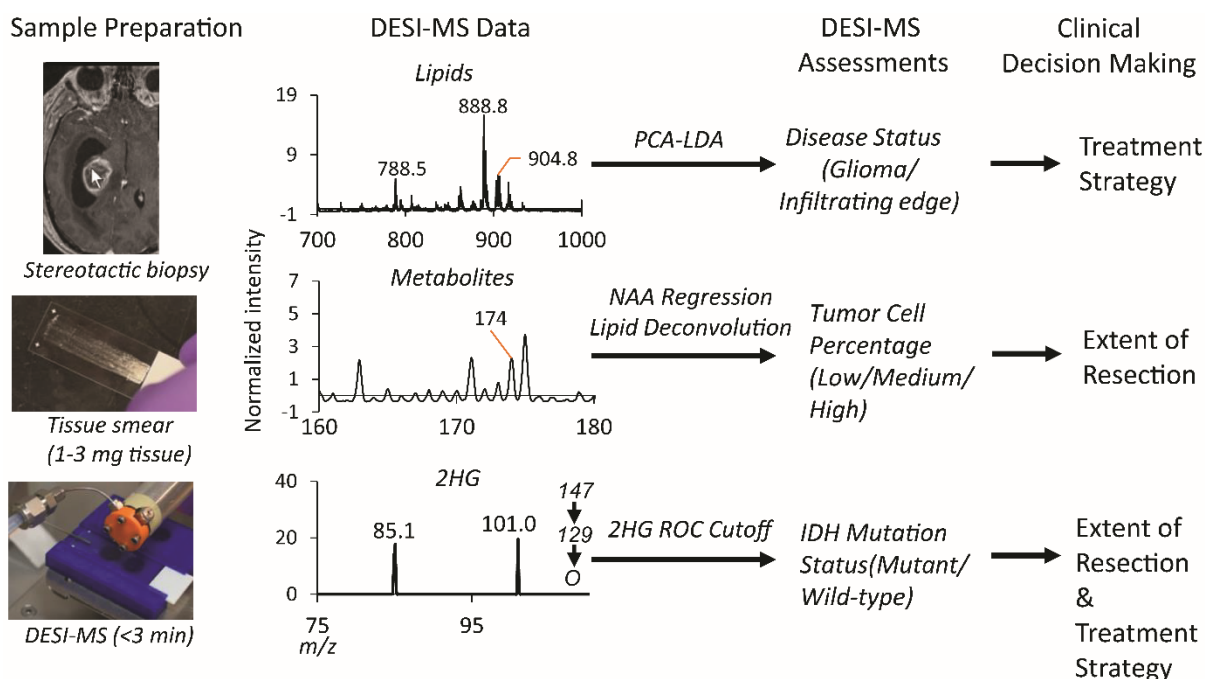
Figure 5.1 Summary of the experimental workflow. Stereotactic brain tissue biopsies are smeared on glass slides and analyzed by DESI-MS. Lipid and metabolite MS data is acquired and analyzed with statistical methods to provide categorical information regarding disease status, tumor cell percentage, and IDH mutation status that can be used to influence clinical decision making

5.4 Results

5.4.1 Summary of Patient Cohort and Tissue Samples

A total of 58 human subjects were enrolled in our study (Table 5.4). Of those, 6 subjects were clinical screenfails and subsequently excluded. Data from three subjects were excluded due to poor DESI signal. This resulted in 49 human subjects from whom tissue was collected and analyzed with DESI-MS.

A total of 247 biopsies were obtained; the average number of biopsies per subject was 5 (Table 5.4). Some biopsies were smeared multiple times when additional tissue was available, resulting in 334 total tissue smears. Of these smears, 62 were excluded due to poor DESI signal or inadequate quality for histopathology, resulting in 272 smears to be used for statistical analysis for disease status and tumor cell percentage and for comparison of DESI and histopathology

The method for IDH mutation status was developed during the study. Therefore, it could not be used for all subjects ,but it was used to analyze tissue smears (n = 158) obtained from 28 human subjects.
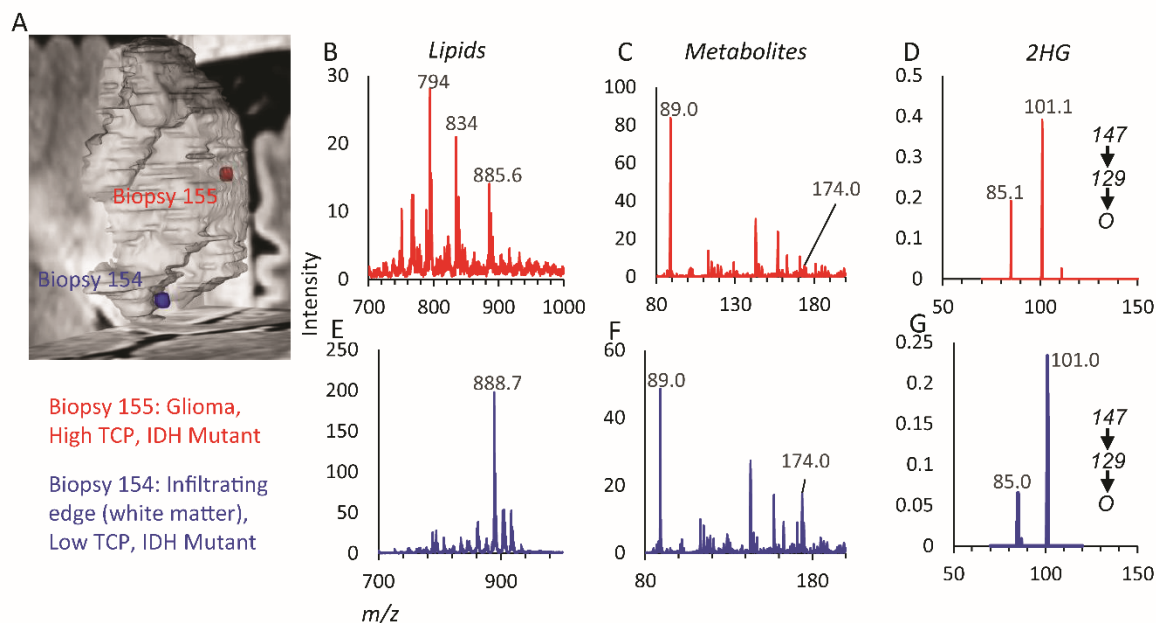
Figure 5.2 DESI-MS predictions of disease status, TCP, and IDH mutation status for a core and margin biopsy from case 26. A) Reconstruction of MRI tumor volume showing location of the two biopsies. B-D) The raw lipid, metabolite, and MS^3 product ion scan for biopsy 155. E-G) The raw lipid, metabolite, and MS^3 product ion scan for biopsy 154. Biopsy 155 was classified as glioma, high TCP, and IDH mutant; biopsy 154 was infiltrating edge (white matter), low TCP and IDH mutant.

The average patient age was 46 ± 16 years; 24 subjects were female and 25 subjects were male; the number of grade I, II, III, and IV gliomas were 1, 17, 6, and 25, respectively; 41 subjects had primary gliomas and 8 had recurrent gliomas; 23 subjects were IDH-M, 25 were IDH-WT, and one 1 subject had unknown IDH status (Table 5.5-5.6).

5.4.2 Simplified DESI-MS Outputs that Enable Surgical Decision Making

Each analyzed tissue smear was statistically analyzed to provide predictions of disease status, tumor cell percentage, and IDH mutation status. The experimental procedure is shown schematically in Figure 5.1. The statistical predictions for each of these categories of information are tabulated in Table 5.7. Each smear was analyzed by histopathology after DESI for validation, and the histopathology data is tabulated in Table 5.8.
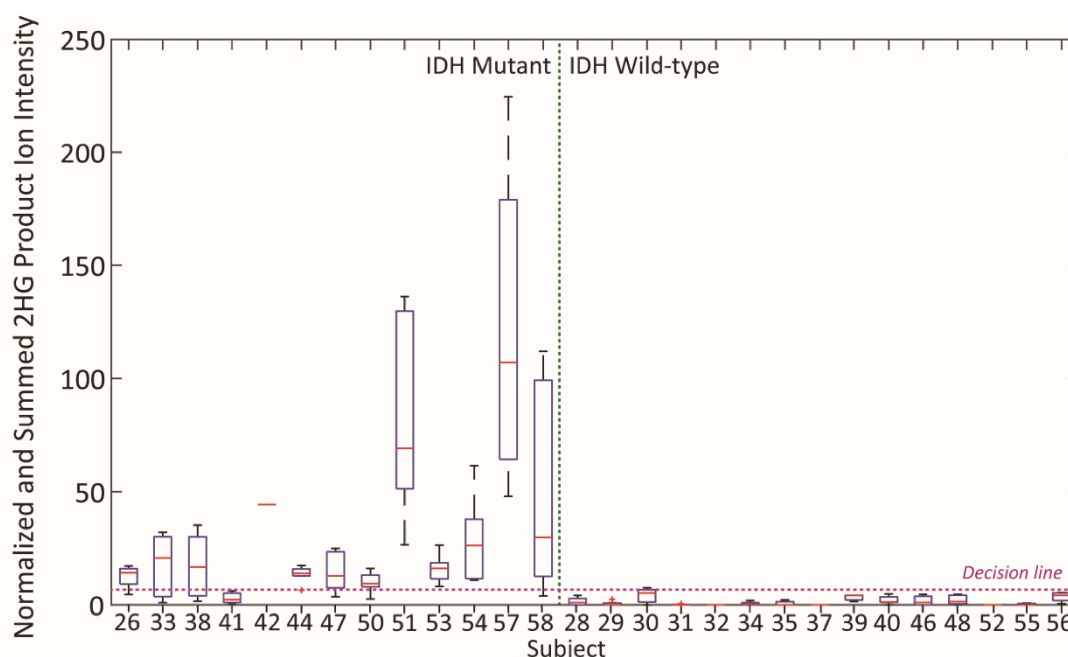
Figure 5.3 Intraoperative assessment of IDH mutation status. Data shown is from 158 biopsies from 29 human subjects. The summed MS³ fragment ion intensities (*m/z* 85 + *m/z* 101) produced by sequential dissociation of 2HG is plotted for each tissue biopsy from each human subject. The left half of the plot shows the IDH mutant subjects and right half shows the IDH wild-type subjects. The pink decision line was calculated from ROC curve analysis to maximally differentiate between the IDH-mutant and IDH-wild-type subjects.

For each smear, the high dimensional mass spectrometry data is reduced to categorical diagnostic information that could be provided to the surgeon. An example of this along with the stereotactic biopsy location is shown in Figure 5.2. With appropriate permissions this data could then influence treatment strategy, including the extent of resection.

5.4.3   Correlation Between Histopathology and DESI-MS Results

5.4.3.1   IDH Mutation Status

The methodology for IDH mutation status was developed midway through the study and was used to analyze tissue smears from 29 human subjects out of the 49 included in this study. These subjects all fell into the later stages of the study. All smears (n=158) for these 29 subjects were included in statistical analyses. In contrast to the methods for disease status and TCP, a different solvent system was best for detection of 2HG, as published previously.(1) This required that the smears be analyzed with DESI twice, first with the optimized solvent for lipids (1:1 DMF-ACN) then with the 2HG optimized solvent (25:37:38 DMF-ACN-EtOH). Two MS³ product ions

were detected from the sequential fragmentation of the 2HG [M-H]$^-$ precursor ion at *m/z* 85 and 101. A plot of the normalized and summed 2HG product ion intensities are shown as box plots in Figure 5.3 for each of the study subjects. The IDH mutation status of the subjects was obtained from the clinical pathology reports and was typically the result of IDH R132H immunohistochemistry. A clear increase in the 2HG signal is observed in the IDH-M subjects compared to the IDH-WT subjects. Using the pathology determined IDH status as the response variable and summed 2HG fragment ion intensities as explanatory variable, a receiver operating characteristic (ROC) curve model for these data provided an area under the curve (AUC) of 0.97. The summed 2HG product ion intensity cutoff of 6.18 resulted in the highest overall accuracy. Using the ROC determined cutoff, the sensitivity (correctly identifying IDH mutants when the IDH mutation was present) and specificity (correctly identifying IDH-wild-type when IDH mutation was absent) were 86.6% and 97.5%, respectively, with an overall accuracy of 92.4%.

5.4.3.2 Disease Status

The agreement between PCA-LDA classification of the DESI-MS data for each tissue smear and the disease status as given by histopathological assessment is shown in Table 5.1. The comparison is complicated by the fact that the PCA-LDA prediction of disease status uses as categories glioma (G), grey matter (GM), or white matter (WM); the histopathology assessment uses categories of G or infiltrative margin (I.M.), as the nature of the underlying normal brain tissue (specifically white or grey matter) could not be reliably determined from the tissue smears. The PCA-LDA classifications of GM and WM were recategorized into IM to match the histopathology categories. The overall accuracy in predicting disease status was 77%. The true positive rate for detecting glioma (the sensitivity) was 69%, and the true negative rate (specificity) was 85%. A significant portion of the glioma smears (n=36, 26%) by histopathology were classified as WM using PCA-LDA classification. These cases likely reflect mixed tissue smears which are challenging for histopathology assessment as well for our current DESI-MS system.
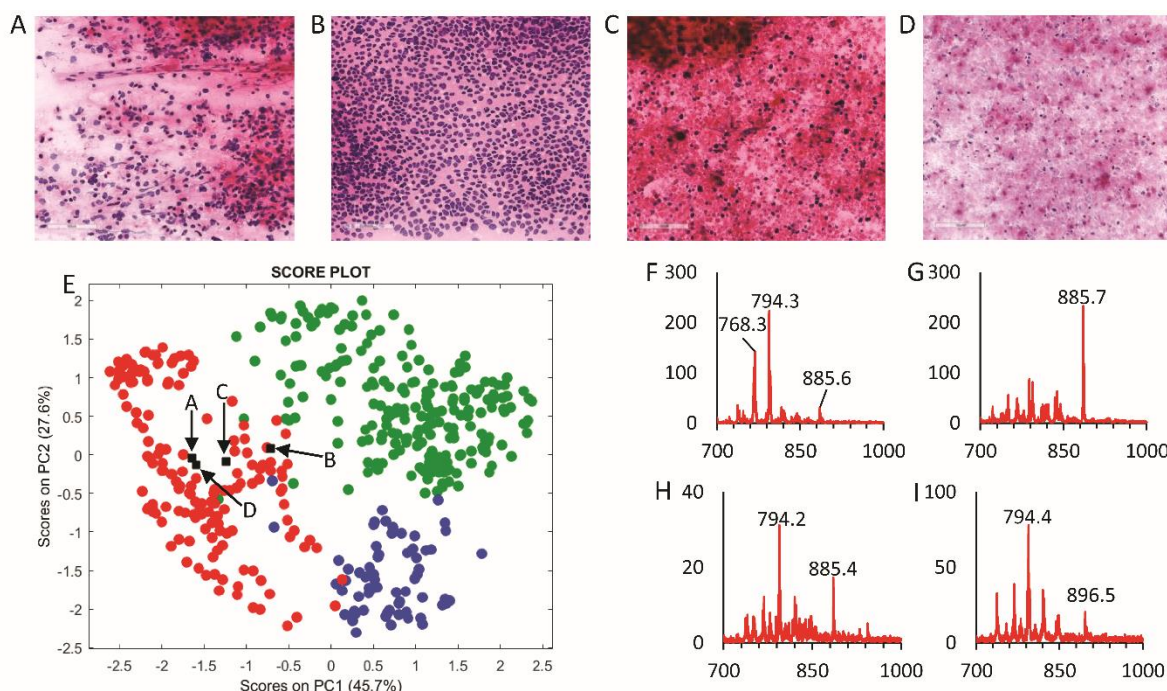
Figure 5.4 Heterogeneity of glioma tumor cores. A-D) Digital images of H&E smears for tumor core biopsies from subjects 47, 45, 51, and 40, respectively. E) Projection of the fused lipid and metabolite profiles recorded from these four subjects on the PCA score plot used as the training set. F-I) Raw lipid-MS profiles for subjects 47, 45, 51, and 40, respectively.

5.4.3.3   Estimating Glioma Content Using Lipid Profile Deconvolution

Principal component regression was used to calculate the relative proportions of G, WM, and GM contributing to the averaged lipid profiles collected for each tissue smear, also referred to as lipid profile deconvolution. The proportion of G contributing to the measured lipid profile was used to estimate the TCP. The average principal component scores obtained from a previous study(2) for GM, WM, and G were used to build the regression model based on the assumption that the lipid profiles of the unknown samples are based on contributions of GM, WM, and G, with each component contribution varying between 0 and 100%, and the total components summing to 100%. The loading matrix from the previous study was used to calculate the scores of the new samples. The percentage of glioma calculated for each unknown sample was used as an estimate of the tumor cell percentage. The confusion matrix comparing the lipid deconvolution estimates to histopathological evaluation is shown in Table 5.2. The overall accuracy for predicting TCP was low, just 67%. The true predictive rates for low (0-33% TCP), medium (34-66% TCP), and high (67-100% TCP) TCP were 73%, 24%, and 74%, respectively. As observed for disease status, the mixed tissue samples are challenging for our system, but higher sensitivity and specificity were

observed for the low and high TCP smears. Only 9% of the low TCP smears were misclassified as high TCP, and only 7% of the high TCP smears were misclassified as low TCP.

Table 5.1 Confusion matrix showing agreement between histopathology and PCA-LDA diagnosis of disease status.

| | | PCA-LDA Diagnosis from DESI-MS | | |
		G	I.M. (GM or WM)	Total
Histopathology Diagnosis	G	94	43	137
	I.M. (GM or WM)	20	115	135
	Total	114	158	272
	Sensitivity	68.61		
	Specificity	85.19		
	Accuracy	76.84		

Table 5.2 Confusion matrix showing agreement between histopathology and lipid deconvolution TCP category.

| | | Lipid Deconvolution TCP Category from DESI-MS | | | |
		Low	Medium	High	Total
Histopathology TCP Category	Low	92	23	11	126
	Medium	15	9	14	38
	High	8	20	80	108
	Total	115	52	105	272
	Sensitivity	73.02	23.68	74.07	
	Specificity	60.96	73.50	61.59	
	Accuracy	66.54			
	Average Sensitivity	56.92			
	Average Specificity	65.35			

5.4.3.4   Tumor Cell Percentage from NAA Regression

The SNV normalized intensity of NAA was used as an independent and approximate method to estimate the TCP of the tissue smears. A higher normalized abundance of NAA indicates lower TCP, and lower abundance indicates higher TCP, as previously published. The confusion matrix comparing TCP estimates based on NAA regression and histopathology are shown in Table 5.3. The overall accuracy for TCP using NAA was 58%. The true predictive rates for low, medium, and high TCP were 48%, 53%, and 71%, respectively. The NAA system works best for recognizing high TCP (high sensitivity or true positive rate) but is not proficient for the low or medium TCP smears (lower specificity or true negative rate).   The majority of the misclassifications for low TCP samples were predicted medium TCP by NAA intensity (43%), and only 9% of the low TCP smears were predicted to be high TCP. Similarly, only 5% of the high TCP smears were predicted to be low TCP.

Table 5.3 Confusion matrix showing agreement between histopathology and NAA regression TCP category.

		NAA TCP Category from DESI-MS			
		Low	Medium	High	Total
Histopathology TCP Category	Low	61	54	11	126
	Medium	11	20	7	38
	High	5	26	77	108
	Total	77	100	95	272
	Sensitivity	48.41	52.63	71.30	
	Specificity	66.44	58.97	49.39	
	Accuracy	58.09			
	Average Sensitivity	57.45			
	Average Specificity	58.27			

5.4.4   DESI-MS During Surgery can Improve Diagnostic Yield from the Intraoperative Consultation

5.4.4.1   Glioma Diagnosis Using Tumor Core Biopsies

As an intraoperative diagnostic tool to assist neurosurgery, the capability to recognize glioma when present would be useful. In some cases, a single biopsy of tumor area might be sufficient for this diagnostic information. When including a single stereotactic biopsy obtained

from a T2 weighted MRI enhancing area for each case, and histopathology assessed the tissue smear as glioma, the agreement between the PCA-LDA diagnosis and histopathology was 92% (n=38). Cases 30, 32, 39, 41, 50, 52, 53 were excluded due to histopathology assessment providing a diagnosis of I.M. for all tissue smears; cases 28, 29, and 35 excluded for lack of adequate DESI-MS signal obtained from smears for which histopathology provided a diagnosis of glioma; case 45 was excluded due to its histological diagnosis as tumor but not sufficient for diagnosis of glioma. These excluded cases are discussed in the next two subsections.

5.4.4.2 Heterogeneity of Tumor Core Biopsies

Several of the tumor core biopsies provided histopathological assessments indicating I.M. rather than G. The snapshots for these stereotactic biopsies from cases 30, 32, 39, 50, 52, and 53 are provided in the Supplemental Information, showing the biopsy location from tumor enhancing core areas. No samples from case 41 were taken from enhancing areas based on the MRI snapshots. The DESI-MS diagnosis for these smears agrees with the histopathological assessment (DESI predicted either WM or GM and histopathology found I.M.), except for smears from case 52 and 53, which DESI predicted G rather than I.M. These cases highlight the complexity and heterogeneity of gliomas, even in tumor cores. DESI-MS methods may be useful in assessing such heterogeneity during surgery.

5.4.4.3 Special Cases in Which DESI-MS Provided Potential Clinical Utility

Tissue smears containing large amounts of necrosis and necrotic tumor are indicative of a brain pathology but not specific for glioma in the absence of viable tumor cells. Smears from case 51 and 42 show significant necrosis and necrotic tumor. The DESI-MS diagnosis of these smears was consistent with glioma. For comparison, smears from case 47, which is a high TCP glioma smear, is shown. Case 45 was suspected for lymphoma during the frozen section consultation due to the high nuclear-to-cytoplasmic ratio and discohesive nature of the tumor cells. The biopsy from this case was analyzed by DESI and provided a PCA-LDA diagnosis of G, and histopathology identified tumor but could not confidently diagnose glioma due to the morphology of this subtype (Figure 5.4). The final pathology provided a diagnosis of glioblastoma based on molecular tests. These cases show that DESI-MS during surgery could provide diagnostic information during surgery that can assist in confirming a glioma diagnosis.

5.4.5 DESI-MS Assessment of Hetergeneity of Tumor Margins

In our study, 83 of the 247 biopsies were obtained from margins based on stereotactic location on the preoperative MRI and provided acceptable quality for histopathology and DESI-MS analysis. For the Grade I-III gliomas, 75.0% of the margin biopsies had low TCP and 7.5% had high TCP based on histopathology. Our agreement with histopathology assessment for the grade I-III margin samples was 72.3% overall using the lipid deconvolution approach. For the Grade IV gliomas, 53.5% of the margin biopsies were assessed to have low TCP and 37.2% had high TCP. Our agreement with the histopathology assessment for the grade IV gliomas was 74.4% overall using the lipid deconvolution approach. The difference in tendency for the margin biopsies to provide a histopathological assessment of high TCP was statistically significant using nominal logistic regression (p = 0.0033). This result corroborates literature reports showing that high TCP may extend beyond the ring enhancement of the tumor in grade IV gliomas.(9, 11, 28) A DESI-MS tool in addition to MRI for assessment of tumor burden would be particularly useful in these cases for maximizing extent of resection.

5.5 Discussion

The study results highlight the versatility and ruggedness of the intraoperative DESI-MS system developed and utilized over the 4-year period to analyze brain tissue biopsies from 49 human subjects. No significant safety issues, instrument failures or complications as a result of the instrument and operators being in the OR were encountered.

The IDH mutation assay performed with an overall accuracy of 92.4% using the summed 2HG product ion intensity cutoff of 6.18 determined from ROC curve analysis. The presence of an IDH mutation can be used to confirm the presence of glioma.(34) Utility of intraoperative IDH-mutation status is illustrated with case 42, which could not be diagnosed glioma morphologically but was a glioma molecularly from presence of the IDH mutation. 2HG intensity has been reported to fluctuate based on tumor grade, tumor density, and other factors.(27, 35) The 2HG signal is seen to fluctuate based on TCP in this and previous studies, and 2HG intensity could be used to assess TCP for IDH-mutant samples. IDH-WT tumors don't respond well to radiochemotherapy and benefit from maximal tumor resection and surgical strategy should be aggressive.(4, 36) IDH-Mut tumors respond better to radiochemotherapy, and the surgeon can afford to be less aggressive while

still producing significant survival benefit.(36, 37) IDH status, along with 1p/19q codeletion, are two molecular markers that can diagnose all major subtypes of glioma.(33) The development of diagnostic MS profiles that can assess 1p/19q codeletion status along with IDH mutation status should be pursued.

The current intraoperative consultation, based on tissue and cellular morphology analysis, is subjective and at times inconclusive. Tumor core biopsies are ideal samples for frozen section analysis because the observation of viable tumor cells is required.(38) Morphological analysis fails when the submitted tissue sample does not contain tumor, or the tumor cell morphology is not specific for glioma.(39, 40) The capability of DESI-MS to chemically recognize glioma, and provide some insight into prognosis, shows that it can be a useful surgical pathology tool. There were some cases in which the intraoperative frozen section was inconclusive and could not definitively provide a diagnosis (e.g. case 42 and 45). The DESI-MS results for biopsies from these cases show that DESI-MS could augment the intraoperative consultation and could significantly affect surgical decisions to resect the lesion or not.

The correlation of the DESI-MS results with a gold-standard diagnostic method was paramount for understanding the accuracy of the DESI-MS predictions of disease status and TCP. The results show that improvements are needed to increase the agreement between the DESI-MS predictions of disease status and TCP with the gold-standard method (H&E pathology). The low diagnostic sensitivity and specificity for the TCP predictions are likely due to the choice of statistical methods for making the predictions, the extent to which the DESI-MS results in the training set are precisely correlated with the tissue TCP as determined by TCP, and the lack of consistency in the DESI-MS data quality between the training set and the experimental set (samples analyzed in this study). These areas should be studied in future works seeking to improve the performance of DESI-MS assessments of surgical margins. The training set could be improved with a regression approach that allows for the TCP to be a continuous variable and collect DESI-MS data that directly correspond with each value of TCP. Future studies may seek comparisons with digital pathology evaluations, or immunohistochemical (IHC) or other molecular methods that are compatible with DESI and have higher precision and accuracy.(2, 33) Experimental factors for improvement include the tissue smear preparation, which was highly variable and unoptimized. Recent reports show that the choice of DESI substrate can significantly alter detected m/z intensities and reproducibility.(29) Substrates that do not transmit visible light, or that damage the

cellular morphology of the smeared tissue, could not be subsequently analyzed by H&E pathology, and may require preparation of adjacent samples on glass for pathology analysis. Finally, access to a fully functioning analytical laboratory near the surgical suite would enable better instrument maintenance (e.g. tuning and calibration) and troubleshooting.

The assessment of glioma margins is not routinely performed intraoperatively with pathology or molecular methods. Glioma infiltration is also known to be significant beyond contrast enhancement in MRI, especially in GBM,(9) and as observed in this study. The DESI-MS method is shown to provide some assessment on the residual tumor burden in these margin samples. In future studies, it would be interesting to evaluate whether DESI-MS assessment of these areas at the MRI tumor borders can increase extent of resection, and whether this reduces tumor recurrence and malignant progression.

5.6 Conclusions

DESI-MS is shown to provide utility in improving the differential diagnosis of glioma intraoperatively, and in assessing surgical margins for residual tumor, through molecular analysis of lipids and metabolites. The clinical accuracy of the IDH mutation assay was highest (92.4%), but the clinical accuracies of disease status and tumor cell percentage were relatively low (76.8 and 66.5%, respectively). Subtyping beyond IDH mutant/IDH wild-type (e.g. 1p/19q codeletion) would require the development of additional diagnostic models which can be studied using banked tissue samples and DESI-MS imaging.

5.7   Subject Data Tables

Table 5.4 Summary of subjects recruited, if excluded from study or analysis, and total biopsies/smears

Study subject number	Screenfail	Reason for Screenfail	Outlier	Reason for outlier	Total Biopsies	Total Smears
001	No		No	-	9	9
002	No		Yes	Poor DESI signal	0	0
003	Yes	Not glioma	No	-	0	0
004	No		Yes	Poor DESI signal	0	0
005	No		No	-	7	8
006	No		No	-	6	7
007	No		No	-	5	6
008	Yes (withdrawn)	Resection unsafe	No	-	0	0
009	No		No	-	7	9
010	No		No	-	6	7
011	No		Yes	Poor DESI signal	0	0
012	No		No	-	7	8
013	No		No	-	7	10
014	No		No	-	6	8
015	No		No	-	6	9
016	No		No	-	7	7
017	No		No	-	4	4
018	No		No	-	5	8
019	No		No	-	7	10
020	No		No	-	5	8
021	No		No	-	6	10
022	Yes	Not glioma	No	-	0	0
023	No		No	-	4	9
024	No		No	-	2	3
025	No		No	-	7	10
026	No		No	-	5	5
027	No		No	-	6	10
028	No		No	-	5	8
029	No		No	-	6	10
030	No		No	-	5	6
031	No		No	-	5	6
032	No		No	-	5	7
033	No		No	-	6	6
034	No		No	-	3	6

Table 5.4 Continued

035	No		No	-	6	6
036	Yes	Not glioma	No	-	0	0
037	No		No	-	4	5
038	No		No	-	6	6
039	No		No	-	3	3
040	No		No	-	3	6
041	No		No	-	5	5
042	No		No	-	3	3
043	Yes	Not glioma	No	-	0	0
044	No	-	No	-	6	10
045	No	-	No	-	1	1
046	No	-	No	-	6	9
047	No	-	No	-	4	8
048	No	-	No	-	3	7
049	Yes	Not glioma	No	-	0	0
050	No	-	No	-	6	6
051	No	-	No	-	6	6
052	No	-	No	-	3	4
053	No	-	No	-	6	9
054	No	-	No	-	3	7
055	No	-	No	-	4	4
056	No	-	No	-	2	4
057	No	-	No	-	2	4
058	No	-	No	-	6	7
Total Subjects Included	Total Screenfails (Subject)		Total Outliers (Subject)		Total Biopsies	Total Smears
49	6		3		247	334

	Avg Screenfail Rate	Avg Outlier rate (Subject)	Avg Biopsies/Sub	Avg Smears/Biopsy
	10.34482759	5.172414	5.0	1.4

Table 5.5 Study subject demographics, diagnosis, and treatment information.

Study subject number	Age	Gender	Race	Ethnicity	Tumor location	Integrated diagnosis	Primary/ Recurrent	F	Awake	Mapping	IMRI
001	30	M	W	N.H.	Left insula	Oligodendendrogliom a, IDH-M,WHO grade II	P	Y	N	Y	N
005	23	M	B	A.A.	Left frontal lobe	Dysembryoplastic neuroepithelial tumor, IDH-WT, WHO grade I	P	N	N	N	N
006	24	M	W	N.H.	Left frontal intra-axial	Astrocytoma, IDH-M, WHO grade III	P	N	N	N	N
007	65	M	W	N.H.	Right parietal lobe	GBM, IDH-WT, WHO grade IV	P	N	N	N	N
009	44	F	W	N.H.	Left parietal intra-axial	Oligodendrogliom a, IDH-M and 1p/19q codeleted,WHO grade II	P	N	N	Y	N
010	47	M	W	N.H.	Left frontotempor al	GBM, IDH-WT, WHO grade IV	R	Y	N	N	N
012	30	M	W	N.H.	Left insula	GBM, IDH-M, WHO grade IV	R	N	N	N	N
013	73	F	W	N.H.	Right temporoparie tal	GBM, IDH-WT, WHO grade IV	P	Y	N	N	N
014	52	F	W	N.H.	Left parietal lobe	GBM, IDH-WT, WHO grade IV	P	Y	N	N	N
015	33	F	W	N.H.	Right parietal lobe	Oligodendrogliom a, IDH-M,WHO grade II	P	N	N	N	N
016	68	M	W	N.H.	Right frontal intra-axial	Diffuse astrocytoma, IDH-M, WHO grade II	P	N	N	N	N
017	38	M	W	N.H.	Left posterior frontal	Diffuse glioma, IDH-M, WHO grade II	P	N	Y	Y	N
018	25	M	M.R.	N.H.	Left frontotempor al lobe	Diffuse glioma, IDH-WT, WHO grade II	P	N	N	N	N
019	39	F	W	N.H.	Left temporal lobe	Anaplastic glioma, IDH-M, WHO grade III	R	N	N	N	N
020	53	F	W	H.	Right parietal lobe; 2 nodules	GBM, IDH-WT, WHO grade IV	P	Y	N	N	N
021	45	F	W	N.H.	Left frontal lobe	Diffuse glioma, IDH-M, WHO grade II	P	N	N	N	N
023	63	F	W	N.H.	Left parietooccipi tal lobe	GBM, IDH-WT, WHO grade IV	P	N	N	N	Y
024	58	M	W	N.H.	Right temporal lobe	GBM and gliosarcoma, IDH wild-type, WHO grade IV	P	N	N	N	N

Table 5.5 Continued

025	47	F	W	N.H.	Right occipital lobe	GBM, IDH-WT, WHO grade IV	P	Y	N	N	N
026	46	F	W	N.H.	Right parietal lobe	Anaplastic astrocytoma, IDH-M, WHO grade III	P	N	N	Y	N
027	52	F	W	N.H.	Left frontoparietal lobe	Complex anaplastic astrocytoma, IDH-M, WHO grade III	P	N	Y	Y	N
028	63	M	W	N.H.	Right temporal lobe	Gliosarcoma,IDH-WT, WHO grade IV	R	N	N	N	N
029	53	F	W	N.H.	Right temporal lobe	Diffuse astrocytoma, IDH-WT, WHO grade II	P	N	N	N	N
030	38	F	W	N.H.	Right frontal lobe	Diffuse astrocytoma, IDH-WT, WHO grade II	P	N	N	N	Y
031	68	M	W	N.H.	Right parietal lobe	GBM, IDH-WT, WHO grade IV	P	N	N	N	N
032	54	F	W	N.H.	Left parietal lobe	GBM, IDH-WT, WHO grade IV	P	Y	Y	Y	N
033	20	M	W	N.H.	Left temporal lobe	Diffuse astrocytoma, IDH-M, WHO grade II	P	N	N	N	Y
034	66	F	W	N.H.	Right temporal lobe	GBM, IDH-WT, WHO grade IV	P	N	N	N	N
035	46	M	B	A.A.	Right posterior frontal periventricular	GBM, IDH-WT, WHO grade IV	P	Y	N	N	N
037	59	M	W	N.H.	Bifrontal	GBM, IDH-WT, WHO grade IV	P	N	N	N	N
038	23	M	W	N.H.	Left frontal lobe	Anaplastic astrocytoma, IDH-mutant, WHO grade III	P	N	N	N	N
039	59	M	W	N.H.	Left temporal lobe	GBM, IDH-WT, WHO grade IV	R	N	N	N	N
040	57	F	W	N.H.	Right frontal lobe	GBM, IDH-WT, WHO grade IV	P	N	N	N	N
041	26	F	W	N.H.	Right frontal lobe	Diffuse glioma, IDH-M	P	N	N	N	N
042	35	F	W	N.H.	Right frontal lobe	GBM, IDH-M, WHO grade IV	P	N	N	Y	N
044	30	M	W	N.H.	Left temporal lobe and insula	Diffuse astrocytoma, IDH-M,WHO grade II	R	N	N	N	N
045	62	F	W	N.H.	Right frontal lobe	GBM, IDH-WT, WHO grade IV	P	N	N	N	N
046	46	F	A	N.H.	Left temporal lobe	Diffuse glioma, IDH-WT	P	N	N	N	N
047	48	M	W	N.H.	Right frontal lobe	Anaplastic astrocytoma, IDH-mutant, WHO grade III	P	N	N	Y	N

Table 5.5 Continued

048	68	M	W	N.H.	Right frontal lobe	GBM with granular cell features, IDH-WT, WHO grade IV	P	Y	N	N	N
050	32	F	W	N.H.	Left insular and mesial temporal	Diffuse astrocytoma, IDH-M,WHO grade II	P	N	N	N	Y
051	30	F	A.A.	N.H.	Right frontal lobe	GBM, IDH-M, WHO grade IV	R	N	N	N	N
052	61	M	W	N.H.	Right temporal lobe	GBM, IDH-WT, WHO grade IV	P	Y	N	N	N
053	27	M	A	N.H.	Right temporal lobe and insula	Diffuse astrocytoma, IDH-M,WHO grade II	P	N	N	N	N
054	68	M	W	N.H.	Right parietal-occipital lobe	GBM, IDH-M, WHO grade IV	P	N	N	N	Y
055	73	M	W	N.H.	Right frontal lobe	GBM, IDH-WT, WHO grade IV	P	N	N	N	N
056	35	F	W	N.H.	Left parietal lobe	GBM, IDH-WT, WHO grade IV	P	N	N	N	N
057	56	F	W	N.H.	Left frontal lobe	Oligodendendroglioma, IDH-M and 1p/19q codeleted,WHO grade II	R	N	N	N	N
058	26	M	W	N.H.	Right frontoparietal region	Oligodendendroglioma, IDH-M and 1p/19q codeleted,WHO grade II	P	N	Y	Y	N

Race categories: W = White; N.H. = Non-Hispanic; B = Black; A = Asian; MR = multi-racial
Primary/Recurrent: P = Primary; R = Recurrent
F = Fluorescein
IMRI = Intraoperative MRI used (yes/no)
Mapping = Brain mapping used (yes/no)
Awake = Awake craniotomy (yes/no

Table 5.6 Additional pathology information for the study subjects

Study subject number	GFAP	ATRX	P53	Ki67	1p/19q	MGMT
001	1	0	1 (20%)	1 (1%)	0	--
002	-	-	-	-	-	-
003	-	-	-	-	-	-
004	-	-	-	-	-	-
005	1	--	--	1 (1-5%)	0	--
006	1	0	1 (80%)	1 (4%)	0	--
007	1	1	1 (3%)	1 (4%)	--	0
008	-	-	-	-	-	-
009	1	1	1 (<1%)	1 (5%)	1	--
010	1	--	--	1 (20%)	0	--
011	-	-	-	-	-	-
012	1	0	1	1	0	0
013	1 (large %)	0	1	1 (30%)	--	0
014	1	--	1 (40%)	1 (30%)	--	0
015	1	1	1	1 (< 5%)	0	--
016	1	0	1 (<1%)	1 (<1%)	0	--
017	1	0	1 (40%)	1 (3%)	--	--
018	1	0	1 (15%)	1 (1-2%)	--	--
019	1	0	1 (75%)	1 (40%)	--	--
020	1	1	1 (<10%)	1 (30%)	0	1
021	0	1	1 (rare cells)	1 (10%)	--	--
022	-	-	-	-	-	-
023	1	1	1 (80%)	1 (50%)	0	1
024	1	1	1 (scattered tumor cells) & 1 (<10% spindle cell and glial component)	1 (5% spindle cell component) & 1 (40% of glial component)	--	--
025	1	1	1 (<1%)	1 (40%)	--	1
026	1	0	1 (90%)	1 (5%)	0	1
027		1	1 (<1%)	1 (10% in anaplastic gliomatous component; <5% in remaining tumor)	0	--
028	1	--	--	1 (20%)	0	0
029	1	1	1 (<1%)	1 (1-2%)	--	--
030	1	2	1 (15-20%)	1 (1-2%)	0	--

Table 5.6 Continued

031	1	1	1 (<1%)	1 (approx. 50%)	--	--
032	1	1	1 (<5%)	1 (>60% in regions 1 ATRXl; as low as 10-15% in regions 0 ATRX)	--	1
033	1	2(partial loss of staining)	1 (20%)	1 (10%)	0	--
034	1	1	1 (10%)	1 (3-5%)	0	1
035	1	1	1 (10-15%) with faint staining	1 (30%)	--	1
036	-	-	-	-	-	-
037	1	1	1 (<5%)	1 (30%)	--	--
038	1	0	1 (>75%)	1 (up to 5-10%)	0	--
039	1	--	--	--	--	--
040	1	0	1 (25%)	1 (20%)	--	1
041	1	0	1 (positive in the majority of the tumor cells)	1 (approx. 5%)	--	--
042	1	0	1 (>80%)	1 (5%)	0	Ind.
043	-	-	-	-	-	-
044	1	0	1 (>95%)	1 (approx 3%)	0	--
045	1	0	0	1 (50-75%)	0	--
046	1	1	1 (<5%)	1 (5-10%) in most hypercellular regions	--	--
047	1	0	1 (>50%)	1 (approx. 3-5%)	0	--
048	1	1	1 (>50%)	1 (approx 10%)	--	0
049	-	-	-	-	-	-
050	1	0	1 (40-50%)	1 (<3%)	--	--
051	1	--	1 (>80%)	--	--	1
052	1	0	1 (<1%)	1 (5-10%)	--	--
053	1	--	1 (30%)	1 (3-4%)	0	--
054	--	1	1	--	--	0
055	1	1	1 (<5%)	1 (40-50%)	--	1
056	1	1	1 (20%)	1 (variably immunoreactive in up to 30% of tumor cells)	0	1
057	1	--	--	--	1	--
058	1	1	--	1(1%)	1	--

Table 5.7 DESI-MS predictions of disease status and TCP for the smears obtained for each subject

Sample Information				Selected Scans		PCA-LDA Diagnosis	NAA Prediction TCP		Lipid Prediction TCP	
Subject	Biopsy # (Subject)	Smear # (Subject)	Smear # (Overall)	# Lipid Scans	# Metabolite Scans	Classification	Mean Value	Category	Mean Value	Category
1	1	1	1	62	81	G	64	Medium	100	High
	2	2	2	-	120	-	91	High	-	-
	3	3	3	74	27	G	81	High	100	High
	4	4	4	72	110	G	72	High	100	High
	5	5	5	28	63	G	82	High	98	High
	6	6	6	64	95	G	80	High	100	High
	7	7	7	43	112	G	70	High	100	High
	8	8	8	55	106	G	74	High	100	High
	9	9	9	58	94	G	44	Medium	100	High
5	1	1	10	13	140	G	81	High	100	High
		2	11	24	115	G	72	High	100	High
	2	3	12	38	72	WM	55	Medium	32	Low
	3	4	13	23	60	G	72	High	100	High
	4	5	14	29	109	WM	66	Medium	52	Medium
	5	6	15	40	93	WM	57	Medium	40	Medium
	6	7	16	21	79	G	65	Medium	91	High
	7	8	17	30	137	G	79	High	100	High
6	1	1	18	40	78	WM	63	Medium	18	Low
	2	2	19	65	85	G	74	High	97	High
	3	3	20	78	60	WM	14	Low	77	High
	4	4	21	65	44	WM	63	Medium	48	Medium
	5	5	22	39	72	WM	58	Medium	52	Medium
		6	23	87	45	WM	55	Medium	30	Low
	6	7	24	99	53	WM	26	Low	0	Low
7	1	1	25	92	121	G	65	Medium	64	Medium
	2	2	26	125	127	GM	6	Low	21	Low
	3	3	27	125	120	WM	38	Low	0	Low
	4	4	28	80	86	WM	35	Low	0	Low
	5	5	29	87	91	WM	14	Low	0	Low
		6	30	98	93	WM	5	Low	0	Low

Table 5.7 Continued

9	1	1	31	9	34	G	57	High	74	High
		2	32	37	41	G	47	Medium	78	High
	2	3	33	124	127	WM	1	Low	0	Low
	3	4	34	111	120	WM	2	Low	0	Low
	4	5	35	92	65…….	WM	11	Low	0	Low
		6	36	105	90	WM	3	Low	0	Low
	5	7	37	117	109	WM	27	Low	0	Low
	6	8	38	61	84	G	58	Medium	99	High
	7	9	39	72	72	WM	0	Low	0	Low
10	1	1	40	48	109	GM	28	Low	0	Low
	2	2	41	120	106	G	25	Low	68	High
	3	3	42	55	93	G	49	Medium	98	High
	4	4	43	94	129	G	62	Medium	96	High
		5	44	70	96	G	40	Medium	74	High
	5	6	45	48	65	G	48	Medium	98	High
	6	7	46	104	127	WM	27	Low	38	Medium
12	1	1	47	42	83	G	76	High	100	High
		2	48	50	121	G	78	High	100	High
	2	3	49	52	87	G	48	Medium	65	Medium
	3	4	50	62	107	G	71	High	91	High
	4	5	51	45	92	G	48	Medium	82	High
	5	6	52	53	93	WM	66	Medium	50	Medium
	6	7	53	43	95	WM	58	Medium	50	Medium
	7	8	54	47	89	WM	63	Medium	26	Low
13	1	1	55	22	20	G	76	High	83	High
		2	56	12	22	G	85	High	87	High
	2	3	57	20	23	G	81	High	92	High
		4	58	24	25	G	80	High	87	High
	3	5	59	19	22	WM	78	High	47	Medium
		6	60	27	23	WM	65	Medium	32	Low
	4	7	61	12	-	-	-	-	21	Low
	5	8	62	11	-	-	-	-	8	Low
	6	9	63	18	-	-	-	-	1	Low
	7	10	64	4	25	WM	49	Medium	0	Low

Table 5.7 Continued

14	1	1	65	-	-	-	-	-	-	-
	2	2	66	24	17	WM	30	Low	21	Low
	3	3	67	-	-	-	-	-	-	-
		4	68	14	22	G	79	High	98	High
	4	5	69	9	24	G	88	High	97	High
	5	6	70	24	25	G	91	High	99	High
	6	7	71	5	24	G	88	High	100	High
		8	72	15	25	G	86	High	100	High
15	1	1	73	5	18	G	74	High	78	High
		2	74	7	24	G	79	High	100	High
	2	3	75	5	23	G	81	High	79	High
		4	76	14	22	G	75	High	80	High
	3	5	77	5	25	G	85	High	87	High
	4	6	78	33	21	G	40	Medium	87	High
		7	79	43	25	WM	7	Low	3	Low
	5	8	80	18	23	WM	69	Medium	13	Low
	6	9	81	28	24	WM	48	Medium	0	Low
16	1	1	82	14	15	WM	1	Low	0	Low
	2	2	83	9	22	G	21	Low	78	High
	3	3	84	26	25	WM	43	Low	29	Low
	4	4	85	24	18	WM	54	Medium	17	Low
	5	5	86	28	25	WM	41	Medium	17	Low
	6	6	87	25	21	WM	23	Low	0	Low
	7	7	88	21	-	-	-	-	33	Low
17	1	1	89	8	20	G	68	High	89	High
	2	2	90	15	25	WM	71	High	54	Medium
	3	3	91	32	25	WM	69	Medium	23	Low
	4	4	92	32	17	WM	52	Medium	28	Low
18	1	1	93	20	25	G	88	High	92	High
		2	94	23	23	G	88	High	91	High
	2	3	95	20	25	WM	84	High	58	Medium
	3	4	96	27	25	WM	89	High	68	High
	4	5	97	23	10	WM	11	Low	16	Low
		6	98	32	19	WM	26	Low	14	Low
	5	7	99	23	25	WM	80	High	33	Low
		8	100	28	25	WM	76	High	30	Low

Table 5.7 Continued

19	1	1	101	27	24	G	85	High	94	High
	2	2	102	24	25	WM	80	High	45	Medium
	3	3	103	-	25	-	88	High	-	-
		4	104	23	25	G	90	High	96	High
	4	5	105	14	25	G	89	High	92	High
	5	6	106	23	25	GM	26	Low	0	Low
		7	107	24	25	GM	26	Low	2	Low
	6	8	108	25	25	WM	52	Medium	0	Low
	7	9	109	13	25	WM	68	High	43	Medium
		10	110	28	25	WM	36	High	3	Low
20	1	1	111	13	25	WM	72	High	40	Medium
		2	112	30	25	WM	62	Medium	38	Medium
	2	3	113	30	25	WM	70	High	59	Medium
		4	114	31	25	WM	56	Medium	38	Medium
	3	5	115	32	25	WM	22	Low	0	Low
	4	6	116	33	25	G	72	High	83	High
	5	7	117	27	25	WM	31	Low	0	Low
		8	118	33	25	WM	12	Low	0	Low
21	1	1	119	8	25	G	32	Low	64	Medium
		2	120	18	25	G	24	Low	69	High
	2	3	121	30	22	GM	17	Low	57	Medium
		4	122	20	25	GM	12	Low	50	Medium
	3	5	123	26	25	GM	24	Low	70	High
		6	124	27	25	GM	25	Low	70	high
	4	7	125	29	22	WM	32	Low	40	Medium
		8	126	30	24	G	37	Low	68	High
	5	9	127	24	22	GM	18	Low	36	Medium
	6	10	128	30	21	WM	33	Low	11	Low
23	1	1	129	3	25	G	71	High	83	High
	2	2	130	2	25	WM	70	High	88	High
		3	131	32	25	WM	75	High	23	Low
	3	4	132	32	25	WM	69	High	47	Medium
		5	133	32	25	WM	76	High	54	Medium
	1	6	134	-	25	-	79	High	-	-
		7	135	-	25	-	83	High	-	-
	4	8	136	18	25	G	82	High	83	High
		9	137	10	25	G	80	High	81	High
24	1	1	138	17	25	G	75	High	84	High
		2	139	23	25	G	75	High	83	High
	2	3	140	26	25	G	79	High	85	High

Table 5.7 Continued

25	1	1	141	25	25	G	82	High	74	High
	2	2	142	21	21	GM	63	Medium	52	Medium
	3	3	143	21	25	GM	67	medium	59	Medium
		4	144	22	25	WM	58	Medium	19	Low
	4	5	145	-	25	-	79	High	-	-
	5	6	146	26	22	WM	33	Low	4	Low
	6	7	147	21	14	WM	44	Medium	0	Low
	7	8	148	30	18	WM	39	Medium	0	Low
	5	9	149	30	25	WM	22	Low	0	Low
	7	10	150	29	16	WM	33	Low	0	Low
26	1	1	151	15	9	G	64	Medium	76	High
	2	2	152	26	16	WM	7	Low	0	Low
	3	3	153	31	19	WM	22	Low	0	Low
	4	4	154	32	22	WM	16	Low	0	Low
	5	5	155	25	11	G	52	Medium	71	High
27	1	1	156	-	-	-	-	-	-	-
		2	157	2	6	G	81	High	100	High
	2	3	158	-	-	-	-	-	-	-
	3	4	159	-	-	-	-	-	-	-
		5	160	-	19	-	88	High	-	-
	4	6	161	-	23	-	87	High	-	-
		7	162	-	-	-	-	-	-	-
	5	8	163	-	13	-	83	High	-	-
	6	9	164	7	22	WM	76	High	31	Low
	5	10	165	14	9	WM	73	Medium	36	Medium
28	1	1	166	-	23	-	75	High	-	-
	2	2	167	-	-	-	-	-	-	-
	3	3	168	16	20	GM	34	Medium	0	Low
		4	169	25	15	GM	33	Low	0	Low
	4	5	170	-	-	-	-	-	-	-
		6	171	-	24	-	74	High	-	-
	5	7	172	24	25	GM	44	Medium	35	Medium
		8	173	-	-	-	-	-	-	-

Table 5.7 Continued

29	1	1	174	-	-	-	-	-	-	-
		2	175	-	-	-	-	-	-	-
	2	3	176	-	-	-	-	-	-	-
		4	177	-	-	-	-	-	-	-
	3	5	178	-	-	-	-	-	-	-
	4	6	179	30	26	WM	24	Low	0	Low
	5	7	180	30	25	WM	50	Medium	49	Medium
	6	8	181	19	25	WM	61	Medium	51	Medium
		9	182	29	25	WM	58	Medium	31	Low
		10	183	27	17	WM	46	Medium	35	Medium
30	1	1	184	28	26	WM	55	Medium	8	Low
		2	185	25	15	WM	60	Medium	46	Medium
	2	3	186	34	22	WM	1	Low	0	Low
	3	4	187	36	28	WM	1	Low	0	Low
	4	5	188	19	15	WM	7	Low	0	Low
	5	6	189	18	29	GM	1	Low	0	Low
31	1	1	190	14	29	G	79	High	72	High
		2	191	22	29	GM	80	High	66	Medium
	2	3	192	-	-	-	-	-	-	-
	3	4	193	27	29	WM	46	Medium	8	Low
	4	5	194	-	-	-	-	-	-	-
	5	6	195	12	12	WM	50	Medium	0	Low
32	1	1	196	18	25	WM	9	Low	0	Low
	2	2	197	20	26	WM	44	Medium	13	Low
		3	198	25	16	WM	31	Low	0	Low
	3	4	199	27	20	WM	48	Medium	0	Low
	4	5	200	20	19	WM	44	Medium	0	Low
	5	6	201	7	13	WM	37	Medium	0	Low
		7	202	17	8	WM	40	Medium	2	Low
33	1	1	203	7	21	WM	55	Medium	30	Low
	2	2	204	-	-	-	-	-	-	-
	3	3	205	-	-	-	-	-	-	-
	4	4	206	14	27	WM	77	High	21	Low
	5	5	207	-	-	-	-	-	-	-
	6	6	208	-	-	-	-	-	-	-

Table 5.7 Continued

34	1	1	209	21	19	GM	13	Low	0	Low
		2	210	29	23	GM	17	Low	0	Low
	2	3	211	24	24	WM	59	Medium	10	Low
		4	212	16	21	WM	59	Medium	1	Low
	3	5	213	9	22	WM	57	Medium	0	Low
		6	214	13	23	WM	52	Medium	0	Low
35	1	1	215	23	8	WM	29	Low	0	Low
	2	2	216	-	-	-	-	-	-	-
	3	3	217	12	-	-	-	-	11	Low
	4	4	218	20	-	-	-	-	0	Low
	5	5	219	9	-	-	-	-	9	Low
	6	6	220	-	-	-	-	-	-	-
37	1	1	221	10	16	G	84	High	71	High
		2	222	7	16	G	85	High	70	High
	2	3	223	9	22	G	85	High	99	High
	3	4	224	8	23	G	81	High	92	High
	4	5	225	12	7	G	77	High	73	High
38	1	1	226	6	29	G	87	High	100	High
	2	2	227	4	28	G	75	High	89	High
	3	3	228	28	27	WM	40	Medium	0	Low
	4	4	229	7	22	WM	65	Medium	56	Medium
	5	5	230	23	22	WM	78	High	36	Medium
	6	6	231	22	25	WM	84	High	54	Medium
39	1	1	232	50	46	WM	17	Low	6	Low
	2	2	233	62	64	WM	30	Low	0	Low
	3	3	234	67	66	WM	38	Low	0	Low
40	1	1	235	-	60	-	79	High	-	-
		2	236	-	60	-	82	High	-	-
	2	3	237	24	62	G	76	High	93	High
		4	238	33	65	G	65	Medium	84	High
	3	5	239	64	67	WM	19	Low	0	Low
		6	240	64	65	WM	22	Low	0	Low
41	1	1	241	49	64	WM	37	Medium	22	Low
	2	2	242	64	61	WM	7	Low	0	Low
	3	3	243	53	65	G	19	Low	71	High
	4	4	244	53	49	WM	20	Low	71	High
	5	5	245	38	37	WM	57	Medium	53	Medium
42	1	1	246	21	59	G	89	High	86	High
	2	2	247	20	64	WM	71	High	50	Medium
	3	3	248	37	64	WM	74	High	39	Medium

Table 5.7 Continued

44	1	1	249	20	64	G	95	High	94	High
		2	250	9	64	G	91	High	91	High
		3	251	22	63	G	96	High	88	High
	2	4	252	39	63	G	89	High	83	High
	3	5	253	26	63	G	80	High	93	High
		6	254	18	63	G	81	High	92	High
	4	7	255	60	64	G	97	High	83	High
	5	8	256	46	65	GM	8	Low	50	Medium
	6	9	257	36	65	G	66	Medium	89	High
		10	258	49	65	G	26	Low	78	High
45	1	1	259	59	65	G	83	High	89	high
46	1	1	260	36	64	G	70	High	75	High
		2	261	31	64	G	62	Medium	85	High
	2	3	262	33	65	G	68	High	68	High
	3	4	263	29	65	G	61	Medium	87	High
		5	264	31	66	G	62	Medium	83	High
		6	265	39	64	G	59	Medium	79	High
	4	7	266	38	62	G	56	Medium	49	Medium
	5	8	267	30	64	G	59	Medium	68	High
	6	9	268	60	65	WM	29	Low	10	Low
47	1	1	269	63	60	WM	45	Medium	33	Low
		2	270	66	62	WM	40	Medium	33	Low
	2	3	271	49	63	G	92	High	85	High
		4	272	52	61	G	79	High	73	High
	3	5	273	55	57	G	33	Low	56	Medium
		6	274	53	59	G	37	Medium	64	High
	4	7	275	57	61	G	57	Medium	38	Medium
		8	276	62	63	WM	46	Medium	28	Low
48	1	1	277	26	48	WM	43	Medium	25	Low
		2	278	18	58	G	30	Low	71	High
	2	3	279	19	63	WM	64	Medium	19	Low
		4	280	2	60	WM	81	High	11	Low
	3	5	281	62	64	WM	28	Low	16	Low
		6	282	60	63	WM	30	Low	10	Low
		7	283	63	65	WM	26	Low	6	Low

Table 5.7 Continued

50	1	1	284	70	75	WM	52	Medium	12	Low
	2	2	285	73	77	WM	4	Low	25	Low
	3	3	286	75	74	WM	51	Medium	9	Low
	4	4	287	62	74	G	17	Low	54	Medium
	5	5	288	41	72	WM	84	High	36	Medium
	6	6	289	69	73	WM	54	Medium	32	Low
51	1	1	290	6	71	G	100	High	72	High
	2	2	291	11	73	G	82	High	75	High
	3	3	292	2	72	G	83	High	89	High
	4	4	293	2	69	G	94	High	84	High
	5	5	294	9	72	G	71	High	83	High
	6	6	295	15	73	G	90	High	81	High
52	1	1	296	50	41	GM	43	Medium	27	Low
	2	2	297	61	42	WM	38	Medium	17	Low
	3	3	298	23	39	G	96	High	58	Medium
		4	299	60	41	G	96	High	35	Medium
53	1	1	300	60	41	WM	59	Medium	20	Low
	2	2	301	54	44	WM	36	Medium	25	Low
		3	302	68	41	WM	49	Medium	16	Low
	3	4	303	57	44	G	45	Medium	55	Medium
		5	304	37	44	G	46	Medium	76	High
	4	6	305	58	43	WM	65	Medium	20	Low
	5	7	306	55	43	WM	65	Medium	26	Low
	6	8	307	32	40	G	67	High	63	Medium
		9	308	40	43	G	52	Medium	49	Medium
54	1	1	309	-	-	-	-	-	-	-
		2	310	-	-	-	-	-	-	-
	2	3	311	16	75	WM	57	Medium	25	Low
		4	312	25	73	WM	51	Medium	11	Low
	3	5	313	16	74	G	85	High	78	High
		6	314	11	73	G	90	High	92	High
		7	315	15	75	G	87	High	90	High
55	1	1	316	25	75	G	83	High	42	Medium
	2	2	317	50	60	WM	38	Medium	7	Low
	3	3	318	22	67	G	86	High	63	Medium
	4	4	319	39	71	WM	72	High	27	Low

Table 5.7 Continued

56	1	1	320	4	74	G	100	High	67	High
	2	2	321	9	74	G	97	High	61	Medium
		3	322	37	76	G	91	High	52	Medium
		4	323	46	74	G	83	High	60	Medium
57	1	1	324	5	72	G	72	High	82	High
	2	2	325	15	74	G	57	High	76	High
		3	326	11	72	G	62	Medium	86	High
		4	327	9	73	G	77	High	91	High
58	1	1	328	14	74	G	39	Medium	87	High
		2	329	7	72	G	50	Medium	98	High
	2	3	330	5	74	WM	48	Medium	51	Medium
	3	4	331	24	74	WM	11	Low	9	Low
	4	5	332	19	74	WM	17	Low	16	Low
	5	6	333	33	73	WM	0	Low	5	Low
	6	7	334	23	73	WM	21	Low	16	Low

Cells with hyphens indicate that the signal to noise ratio was too low for the algorithms to select MS scans (from the lipid or metabolite profiles) to be used for statistical classification. These cells were excluded from subsequent correlations between the DESI-MS results and histopathology.

G = glioma
WM = White matter
GM = Grey Matter
Low = 0-33% TCP
Medium = 34-66% TCP
High = >66% TCP

Table 5.8 Pathological evaluation of the tissue smears obtained from each study subject

	Sample Information			Histopathology			
Subject	Biopsy # (Subject)	Smear # (Subject)	Smear # (Overall)	Diagnosis	TCP-Estimate	TCP-Cat	Smear Quality
1	1	1	1	G	100	High	--
	2	2	2	G	100	High	--
	3	3	3	G	100	High	--
	4	4	4	G	100	High	--
	5	5	5	G	100	High	--
	6	6	6	G	100	High	--
	7	7	7	G	100	High	--
	8	8	8	G	100	High	--
	9	9	9	I.M.	10	Low	BMA
5	1	1	10	G	90	High	--
		2	11	G	90	High	--
	2	3	12	G	60	Medium	--
	3	4	13	G	80	High	--
	4	5	14	G	50	Medium	--
	5	6	15	G	60	Medium	--
	6	7	16	G	80	High	--
	7	8	17	G	80	High	--
6	1	1	18	G	50	Medium	--
	2	2	19	G	90	High	--
	3	3	20	GM	0	Low	A
	4	4	21	G	70	High	--
	5	5	22	G	50	Medium	--
		6	23	I.M.	25	Low	MA
	6	7	24	I.M.	15	Low	--
7	1	1	25	G	90	High	--
	2	2	26	I.M.	10	Low	--
	3	3	27	G	50	Medium	--
	4	4	28	G	50	Medium	--
	5	5	29	I.M.	10	Low	--
		6	30	G	30	Low	--

Table 5.8 Continued

		1	31	G	90	High	--
	1	2	32	G	90	High	--
	2	3	33	I.M.	30	Low	--
	3	4	34	I.M.	50	Medium	--
9	4	5	35	G	60	Medium	--
		6	36	I.M.	30	Low	--
	5	7	37	I.M.	15	Low	--
	6	8	38	G	95	High	--
	7	9	39	I.M.	20	Low	--
	1	1	40	I.M.	30	Low	--
	2	2	41	GM	0	Low	MA
	3	3	42	G	80	High	--
10	4	4	43	G	80	High	--
		5	44	G	50	Medium	--
	5	6	45	G	60	Medium	--
	6	7	46	I.M.	50	Medium	--
	1	1	47	G	70	High	--
		2	48	G	70	High	--
	2	3	49	GM	0	Low	BMA
	3	4	50	G	70	High	--
12	4	5	51	I.M.	40	Medium	--
	5	6	52	G	80	High	--
	6	7	53	I.M.	50	Medium	--
	7	8	54	G	70	High	--
	1	1	55	G	90	High	--
		2	56	G	90	High	--
	2	3	57	G	90	High	--
		4	58	G	90	High	--
	3	5	59	WM	0	Low	BMA
13		6	60	WM	0	Low	MA
	4	7	61	WM	0	Low	BMA
	5	8	62	WM	0	Low	BMA
	6	9	63	I.M.	5	Low	--
	7	10	64	I.M.	5	Low	--

Table 5.8 Continued

14	1	1	65	--	--	--	IA
	2	2	66	I.M.	30	Low	--
	3	3	67	A.C.T.	100	High	--
		4	68	A.C.T.	100	High	--
	4	5	69	G	70	High	--
	5	6	70	G	90	High	--
	6	7	71	G	90	High	--
		8	72	G	90	High	--
15	1	1	73	G	75	High	--
		2	74	G	75	High	--
	2	3	75	G	75	High	--
		4	76	G	80	High	--
	3	5	77	G	80	High	--
	4	6	78	WM	10	Low	--
		7	79	GM	20	Low	--
	5	8	80	WM	10	Low	--
	6	9	81	WM	15	Low	--
16	1	1	82	I.M.	30	Low	--
	2	2	83	G	70	High	--
	3	3	84	G	75	High	MA
	4	4	85	I.M.	30	Low	MA
	5	5	86	I.M.	30	Low	--
	6	6	87	I.M.	40	Low	--
	7	7	88	I.M.	40	Low	MA
17	1	1	89	G	70	High	--
	2	2	90	G	80	High	--
	3	3	91	WM	0	Low	A
	4	4	92	G	50	Medium	--
18	1	1	93	G	50	Medium	BMA
		2	94	G	50	Medium	IA
	2	3	95	I.M.	10	Low	MA
	3	4	96	I.M.	10	Low	MA
	4	5	97	I.M.	20	Low	--
		6	98	I.M.	10	Low	--
	5	7	99	WM	0	Low	A
		8	100	WM	0	Low	MA

Table 5.8 Continued

19	1	1	101	G	90	High	--
	2	2	102	G	40	Medium	IA
	3	3	103	G	90	High	--
		4	104	G	90	High	--
	4	5	105	G	90	High	--
	5	6	106	WM	5	Low	--
		7	107	WM	5	Low	--
	6	8	108	WM	30	Low	--
	7	9	109	GM	5	Low	--
		10	110	GM	5	Low	--
20	1	1	111	G	70	High	--
		2	112	G	70	High	--
	2	3	113	G	70	High	--
		4	114	G	90	High	MA
	3	5	115	WM	5	Low	--
	4	6	116	G	70	High	--
	5	7	117	WM	5	Low	--
		8	118	WM	5	Low	--
21	1	1	119	I.M.	20	Low	MA
		2	120	G	50	Medium	--
	2	3	121	G	40	Low	--
		4	122	G	80	High	A
	3	5	123	G	60	Medium	--
		6	124	G	70	High	MA
	4	7	125	G	40	Low	--
		8	126	G	60	Medium	--
	5	9	127	I.M.	5	Low	--
	6	10	128	I.M.	5	Low	--
23	1	1	129	--	--	--	--
	2	2	130	G	90	High	--
		3	131	G	90	High	IA
	3	4	132	G	90	High	--
		5	133	G	90	High	--
	1	6	134	--	--	--	--
		7	135	--	--	--	--
	4	8	136	G	90	High	--
		9	137	G	90	High	--

Table 5.8 Continued

24	1	1	138	G	70	High	--
		2	139	G	80	High	--
	2	3	140	G	80	High	--
25	1	1	141	G	60	Medium	--
	2	2	142	G	70	High	--
	3	3	143	G	80	High	--
		4	144	G	50	Medium	--
	4	5	145	G	90	High	--
	5	6	146	WM	5	Low	--
	6	7	147	WM	5	Low	--
	7	8	148	WM	5	Low	--
	5	9	149	WM	5	Low	--
	7	10	150	WM	5	Low	--
26	1	1	151	G	80	High	--
	2	2	152	I.M.	10	Low	--
	3	3	153	WM	5	Low	--
	4	4	154	WM	10	Low	--
	5	5	155	G	60	Medium	--
27	1	1	156	G	90	High	MA
		2	157	G	90	High	MA
	2	3	158	G	90	High	MA
	3	4	159	G	90	High	MA
		5	160	G	90	High	A
	4	6	161	G	90	High	MA
		7	162	G	90	High	MA
	5	8	163	G	90	High	MA
	6	9	164	G	90	High	A
	5	10	165	G	90	High	A
28	1	1	166	G	90	High	A
	2	2	167	I.M.	0	Low	MA
	3	3	168	GM	10	Low	A
		4	169	GM	10	Low	A
	4	5	170	G	50	Medium	MA
		6	171	G	60	Medium	MA
	5	7	172	GM	20	Low	A
		8	173	GM	0	Low	A

Table 5.8 Continued

29	1	1	174	--	--	--	--
		2	175	G	60	Medium	MA
	2	3	176	I.M.	20	Low	MA
		4	177	I.M.	20	Low	BMA
	3	5	178	WM	0	Low	BMA
	4	6	179	WM	10	Low	MA
	5	7	180	WM	10	Low	MA
	6	8	181	WM	10	Low	A
		9	182	WM	10	Low	A
		10	183	WM	10	Low	MA
30	1	1	184	I.M.	30	Low	MA
		2	185	I.M.	15	Low	MA
	2	3	186	WM	5	Low	A
	3	4	187	WM	5	Low	A
	4	5	188	WM	5	Low	A
	5	6	189	GM	10	Low	A
31	1	1	190	G	90	High	A
		2	191	G	90	High	A
	2	3	192	G	90	High	MA
	3	4	193	WM	15	Low	MA
	4	5	194	--	--	--	--
	5	6	195	G	50	Medium	MA
32	1	1	196	GM	10	Low	A
	2	2	197	GM	10	Low	MA
		3	198	GM	10	Low	A
	3	4	199	WM	5	Low	A
	4	5	200	WM	5	Low	A
	5	6	201	I.M.	5	Low	MA
		7	202	I.M.	5	Low	MA
33	1	1	203	GM	10	Low	A
	2	2	204	GM	10	Low	A
	3	3	205	G	60	Medium	MA
	4	4	206	G	60	Medium	MA
	5	5	207	G	--	--	IA
	6	6	208	I.M.	30	Low	MA

Table 5.8 Continued

34	1	1	209	GM	10	Low	A
		2	210	GM	10	Low	A
	2	3	211	G	70	High	A
		4	212	G	70	High	MA
	3	5	213	G	70	High	MA
		6	214	G	70	High	MA
35	1	1	215	WM	10	Low	A
	2	2	216	G	90	High	A
	3	3	217	WM	10	Low	A
	4	4	218	WM	10	Low	A
	5	5	219	WM	0	Low	MA
	6	6	220	WM	0	Low	MA
37	1	1	221	G	90	High	MA
		2	222	G	70	High	MA
	2	3	223	G	80	High	A
	3	4	224	G	80	High	A
	4	5	225	G	80	High	A
38	1	1	226	G	80	High	MA
	2	2	227	G	80	High	A
	3	3	228	WM	30	Low	A
	4	4	229	GM	20	Low	MA
	5	5	230	WM	0	Low	MA
	6	6	231	I.M.	10	Low	MA
39	1	1	232	I.M.	0	Low	A
	2	2	233	WM	0	Low	A
	3	3	234	WM	0	Low	A
40	1	1	235	G	100	High	A
		2	236	G	100	High	A
	2	3	237	G	100	High	A
		4	238	G	100	High	A
	3	5	239	WM	20	Low	MA
		6	240	WM	20	Low	MA
41	1	1	241	WM	0	Low	A
	2	2	242	WM	0	Low	A
	3	3	243	GM	0	Low	A
	4	4	244	I.M.	5	Low	A
	5	5	245	I.M.	5	Low	MA
42	1	1	246	G	0	Low	A
	2	2	247	G	80	High	A
	3	3	248	--	--	--	IA

Table 5.8 Continued

		1	249	G	100	High	A
	1	2	250	G	100	High	A
		3	251	G	100	High	A
	2	4	252	G	100	High	A
	3	5	253	G	100	High	A
44		6	254	G	100	High	A
	4	7	255	G	100	High	A
	5	8	256	GM	0	Low	A
	6	9	257	GM	60	Medium	A
		10	258	GM	0	Low	A
45	1	1	259	T	100	High	A
	1	1	260	G	60	Medium	MA
		2	261	G	80	High	A
	2	3	262	G	80	High	A
		4	263	G	60	Medium	A
46	3	5	264	G	80	High	A
		6	265	G	80	High	A
	4	7	266	G	60	Medium	A
	5	8	267	I.M.	0	Low	A
	6	9	268	WM	5	Low	A
	1	1	269	WM	20	Low	MA
		2	270	WM	30	Low	A
	2	3	271	G	100	High	A
		4	272	G	100	High	A
47	3	5	273	I.M.	50	Medium	A
		6	274	I.M.	50	Medium	A
	4	7	275	WM	40	Low	A
		8	276	WM	40	Low	A
	1	1	277	GM	10	Low	A
		2	278	GM	0	Low	A
	2	3	279	WM	60	Medium	A
48		4	280	G	50	Medium	A
	3	5	281	GM	50	Medium	MA
		6	282	G	50	Medium	A
		7	283	G	70	High	A

Table 5.8 Continued

	1	1	284	WM	20	Low	MA
	2	2	285	GM	15	Low	A
50	3	3	286	WM	20	Low	MA
	4	4	287	GM	0	Low	A
	5	5	288	WM	50	Medium	MA
	6	6	289	WM	50	Medium	MA
	1	1	290	G	100	High	A
	2	2	291	T	100	High	A
51	3	3	292	T	100	High	A
	4	4	293	T	100	High	A
	5	5	294	T	100	High	A
	6	6	295	T	100	High	A
	1	1	296	GM	20	Low	MA
52	2	2	297	I.M.	30	Low	--
	3	3	298	WM	--	--	IA
		4	299	I.M.	40	Medium	MA
	1	1	300	WM	10	Low	MA
	2	2	301	GM	10	Low	MA
		3	302	GM	10	Low	A
	3	4	303	I.M.	20	Low	A
53		5	304	GM	40	Low	A
	4	6	305	WM	30	Low	MA
	5	7	306	WM	30	Low	MA
	6	8	307	GM	0	Low	MA
		9	308	GM	0	Low	A
	1	1	309	--	--	--	IA
		2	310	--	--	--	IA
	2	3	311	GM	10	Low	MA
54		4	312	GM	10	Low	MA
		5	313	WM	40	Low	MA
	3	6	314	G	60	Medium	MA
		7	315	G	70	High	MA
	1	1	316	G	100	High	A
55	2	2	317	WM	10	Low	A
	3	3	318	--	--	--	IA
	4	4	319	GM	30	Low	A
	1	1	320	G	100	High	MA
56		2	321	G	100	High	MA
	2	3	322	G	100	High	A
		4	323	G	100	High	A

Table 5.8 Continued

		1	324	G	80	High	A
57		2	325	G	80	High	A
	2	3	326	G	80	High	MA
		4	327	G	80	High	A
	1	1	328	G	80	High	A
		2	329	G	50	Medium	MA
	2	3	330	I.M.	10	Low	A
58	3	4	331	WM	0	Low	A
	4	5	332	WM	0	Low	A
	5	6	333	WM	0	Low	A
	6	7	334	WM	0	Low	A

G = glioma
WM = White matter
GM = Grey Matter
A = Adequate
MA = Marginally adequate
BMA = Barely marginally adequate
IA = Inadequate
Tissue smears with inadequate quality (IA) were not evaluated by EMH. The Smear Quality datapoint was not evaluated for all of the smears in the study; Smear Quality cells with hyphens indicate that smear was not evaluated for smear quality.

5.8   References

1.   D'Amico RS, Englander ZK, Canoll P, Bruce JN. Extent of Resection in Glioma-A Review of the Cutting Edge. World neurosurgery. 2017;103:538-49.

2.   Brat DJ, Verhaak RG, Aldape KD, Yung WK, Salama SR, Cooper LA, et al. Comprehensive, Integrative Genomic Analysis of Diffuse Lower-Grade Gliomas. N Engl J Med. 2015;372(26):2481-98.

3.   McGirt MJ, Chaichana KL, Gathinji M, Attenello FJ, Than K, Olivi A, et al. Independent association of extent of resection with survival in patients with malignant brain astrocytoma. J Neurosurg. 2008;110(1):156-62.

4.   Patel T, Bander ED, Venn RA, Powell T, Cederquist GY, Schaefer PM, et al. The Role of Extent of Resection in IDH1 Wild-Type or Mutant Low-Grade Gliomas. Neurosurgery. 2017;82(6):808-14.

5.   Hervey-Jumper SL, Berger MS. Maximizing safe resection of low- and high-grade glioma. Journal of neuro-oncology. 2016;130(2):269-82.

6.   Orringer D, Lau D, Khatri S, Zamora-Berridi GJ, Zhang K, Wu C, et al. Extent of resection in patients with glioblastoma: limiting factors, perception of resectability, and effect on survival. J Neurosurg. 2012;117(5):851-9.

7. Eseonu CI, ReFaey K, Garcia O, Raghuraman G, Quinones-Hinojosa A. Volumetric Analysis of Extent of Resection, Survival, and Surgical Outcomes for Insular Gliomas. World neurosurgery. 2017;103:265-74.

8. Mampre D, Ehresman J, Pinilla-Monsalve G, Osorio MAG, Olivi A, Quinones-Hinojosa A, et al. Extending the resection beyond the contrast-enhancement for glioblastoma: feasibility, efficacy, and outcomes. British journal of neurosurgery. 2018;32(5):528-35.

9. Eidel O, Burth S, Neumann JO, Kieslich PJ, Sahm F, Jungk C, et al. Tumor Infiltration in Enhancing and Non-Enhancing Parts of Glioblastoma: A Correlation with Histopathology. Plos One. 2017;12(1):12.

10. Chen R, Ravindra VM, Cohen AL, Jensen RL, Salzman KL, Prescot AP, et al. Molecular features assisting in diagnosis, surgery, and treatment decision making in low-grade gliomas. Neurosurgical focus. 2015;38(3):E2.

11. Claes A, Idema AJ, Wesseling P. Diffuse glioma growth: a guerilla war. Acta Neuropathologica. 2007;114(5):443-58.

12. Takats Z, Wiseman JM, Gologan B, Cooks RG. Mass Spectrometry Sampling Under Ambient Conditions with Desorption Electrospray Ionization. Science. 2004;306:471-3.

13. Ifa DR, Eberlin LS. Ambient Ionization Mass Spectrometry for Cancer Diagnosis and Surgical Margin Evaluation. Clinical chemistry. 2016;62(1):111-23.

14. Yoshimura K, Mandal MK, Hara M, Fujii H, Chen LC, Tanabe K, et al. Real-time diagnosis of chemically induced hepatocellular carcinoma using a novel mass spectrometry-based technique. Anal Biochem. 2013;441(1):32-7.

15. Kerian KS, Jarmusch AK, Cooks RG. Touch spray mass spectrometry for in situ analysis of complex samples. Analyst. 2014;139:2714-20.

16. Alfaro CM, Jarmusch AK, Pirro V, Kerian KS, Masterson TA, Cheng L, et al. Ambient ionization mass spectrometric analysis of human surgical specimens to distinguish renal cell carcinoma from healthy renal tissue. Analytical and bioanalytical chemistry. 2016;408(20):5407-14.

17. Balog J, Sasi-Szabo L, Kinross J, Lewis MR, Muirhead LJ, Veselkov K, et al. Intraoperative tissue identification using rapid evaporative ionization mass spectrometry. Sci Transl Med. 2013;5(194):194ra93.

18. Balog J, Kumar S, Alexander J, Golf O, Huang J, Wiggins T, et al. In Vivo Endoscopic Tissue Identification by Rapid Evaporative Ionization Mass Spectrometry (REIMS). Angew Chem Int Ed Engl. 2015;54(38):11059-62.

19. Woolman M, Ferry I, Kuzan-Fischer CM, Wu MG, Zou J, Kiyota T, et al. Rapid determination of medulloblastoma subgroup affiliation with mass spectrometry using a handheld picosecond infrared laser desorption probe. Chemical Science. 2017;8(9):6508-19.

20. Fatou B, Ziskind M, Saudemont P, Quanico J, Focsa C, Salzet M, et al. Remote Atmospheric Pressure Infrared Matrix-Assisted Laser Desorption-Ionization Mass Spectrometry (Remote IR-MALDI MS) of Proteins. Mol Cell Proteomics. 2018;17(8):1637-49.

21. Fatou B, Saudemont P, Leblanc E, Vinatier D, Mesdag V, Wisztorski M, et al. In vivo Real-Time Mass Spectrometry for Guided Surgery Application. Sci Rep. 2016;6:25919.

22. Zhang JL, Rector J, Lin JQ, Young JH, Sans M, Katta N, et al. Nondestructive tissue analysis for ex vivo and in vivo cancer diagnosis using a handheld mass spectrometry system. Science Translational Medicine. 2017;9(406).

23. Sans M, Zhang J, Lin JQ, Feider CL, Giese N, Breen MT, et al. Performance of the MasSpec Pen for Rapid Diagnosis of Ovarian Cancer. Clin Chem. 2019.

24. Eberlin LS, Ferreira CR, Dill AL, Ifa DR, Cheng L, Cooks RG. Nondestructive, Histologically Compatible Tissue Imaging by Desorption Electrospray Ionization Mass Spectrometry. ChemBioChem. 2011;12(14):2129-32.

25. Jarmusch AK, Pirro V, Baird Z, Hattab EM, Cohen-Gadol AA, Cooks RG. Lipid and metabolite profiles of human brain tumors by desorption electrospray ionization-MS. Proc Natl Acad Sci U S A. 2016;113(6):1486-91.

26. Pirro V, Alfaro CM, Jarmusch AK, Hattab EM, Cohen-Gadol AA, Cooks RG. Intraoperative assessment of tumor margins during glioma resection by desorption electrospray ionization-mass spectrometry. Proceedings of the National Academy of Sciences of the United States of America. 2017;114(26):6700-5.

27. Alfaro CM, Pirro V, Keating MF, Hattab EM, Cooks RG, Cohen-Gadol AA. Intraoperative assessment of isocitrate dehydrogenase mutation status in human gliomas using desorption electrospray ionization-mass spectrometry. J Neurosurg. 2019:1-8.

28. Price SJ, Jena R, Burnet NG, Hutchinson PJ, Dean AF, Pena A, et al. Improved delineation of glioma margins and regions of infiltration with the use of diffusion tensor imaging: an image-guided biopsy study. AJNR American journal of neuroradiology. 2006;27(9):1969-74.

29. Woolman M, Tata A, Bluemke E, Dara D, Ginsberg HJ, Zarrine-Afsar A. An Assessment of the Utility of Tissue Smears in Rapid Cancer Profiling with Desorption Electrospray Ionization Mass Spectrometry (DESI-MS). J Am Soc Mass Spectrom. 2016;28(1):145-53.

30. Firlik KS, Martinez AJ, Lunsford LD. Use of cytological preparations for the intraoperative diagnosis of stereotactically obtained brain biopsies: a 19-year experience and survey of neuropathologists. Journal of Neurosurgery. 1999;91(3):454-8.

31. Tilgner J, Herr M, Ostertag C, Volk B. Validation of intraoperative diagnoses using smear preparations from stereotactic brain biopsies: intraoperative versus final diagnosis--influence of clinical factors. Neurosurgery. 2005;56(2):257-65; discussion -65.

32. Sharma S, Deb P. Intraoperative neurocytology of primary central nervous system neoplasia: A simplified and practical diagnostic approach. J Cytol. 282011. p. 147-58.

33. Eckel-Passow JE, Lachance DH, Molinaro AM, Walsh KM, Decker PA, Sicotte H, et al. Glioma Groups Based on 1p/19q, IDH, and TERT Promoter Mutations in Tumors. N Engl J Med. 2015;372(26):2499-508.

34. Kim BYS, Jiang W, Beiko J, Prabhu SS, DeMonte F, Gilbert MR, et al. Diagnostic discrepancies in malignant astrocytoma due to limited small pathological tumor sample can be overcome by IDH1 testing. Journal of neuro-oncology. 2014;118(2):405-12.

35. Choi C, Raisanen JM, Ganji SK, Zhang S, McNeil SS, An Z, et al. Prospective Longitudinal Analysis of 2-Hydroxyglutarate Magnetic Resonance Spectroscopy Identifies Broad Clinical Utility for the Management of Patients With IDH-Mutant Glioma. Journal of clinical oncology : official journal of the American Society of Clinical Oncology. 2017;34(33):4030-9.

36. Hartmann C, Hentschel B, Wick W, Capper D, Felsberg J, Simon M, et al. Patients with IDH1 wild type anaplastic astrocytomas exhibit worse prognosis than IDH1-mutated glioblastomas, and IDH1 mutation status accounts for the unfavorable prognostic effect of higher age: implications for classification of gliomas. Acta Neuropathol. 2010;120(6):707-18.

37. Mellinghoff IK, Penas-Prado M, Peters KB, Cloughesy TF, Burris HA, Maher EA. Phase 1 study of AG-881, an inhibitor of mutant IDH1/IDH2, in patients with advanced IDH-mutant solid tumors, including glioma. Journal of Clinical Oncology. 2018;36(15).

38. Brat DJ, Prayson RA, Ryken TC, Olson JJ. Diagnosis of malignant glioma: role of neuropathology. Journal of neuro-oncology. 2008;89(3):287-311.

39. Plesec TP, Prayson RA. Frozen section discrepancy in the evaluation of central nervous system tumors. Archives of Pathology & Laboratory Medicine. 2007;131(10):1532-40.

40. Choi J, Lee EY, Shin KJ, Minn YK, Kim J, Kim SH. IDH1 mutation analysis in low cellularity specimen: a limitation of diagnostic accuracy and a proposal for the diagnostic procedure. Pathology, research and practice. 2013;209(5):284-90.

CHAPTER 6.   FUTURE PERSPECTIVES ON USE OF AMBIENT IONIZATION MASS SPECTROMETRY IN INTRAOPERATIVE CANCER DIAGNOSTICS

6.1   Conclusions

The prospects of ambient mass spectrometry-based methods being used in clinical practice are much brighter than they were 15 years ago. However, ambient ionization-based diagnostic methods (e.g. DESI) have not entered any significant clinical trials. Recently, the Biotyper™, a MALDI-TOF based microorganism identification assay, has been FDA approved and is widely used in clinical laboratories to identify microorganisms.(1-4) Newborn screening for inborn errors in metabolism are also widely conducted with direct infusion tandem mass spectrometry. Recently, FDA approval for MS/MS based screening of lysosomal storage disorders in newborns has been granted and are now performed in clinical laboratories worldwide.(5-9) The translational pipeline for ambient ionization diagnostic methods relying on molecular profiling may follow a similar translation pipeline as the Biotyper™. More targeted ambient ionization-MS diagnostics (i.e. measuring 2HG to determine IDH mutation status) may follow pipelines like the metabolic screening of newborns which also rely on MS/MS.

Changes to medical institution infrastructure could facilitate further developments in the areas of point-of-care and intraoperative cancer diagnostics with ambient ionization-MS. The incorporation of analytical chemistry research laboratories housed within medical schools would be a significant step forward. Clinical and engineering support for these laboratories would be essential for development of new technologies and the thorough vetting of them in the relevant clinical environment. Such improvements to infrastructure would increase the ability to conduct point-of-care mass spectrometry research.

The isocitrate dehydrogenase (IDH) assay reported in Chapter 4 seems to be an excellent candidate point-of-care ambient ionization-MS method to develop further as an intraoperative molecular diagnostic. In our intraoperative DESI-MS study for IDH mutation status assessment, a high ability to predict the results of the gold-standard test (immunohistochemistry) using the 2-hydroxyglutarate (2HG) fragment ion intensities was observed (Chapters 4&5). The finding and development of additional diagnostic methods that can recapitulate key molecular cancer markers could follow the same translational pipeline that has been used for the intraoperative 2HG MS

assay. The capability to perform molecular cancer diagnostics during surgery would significantly improve patient management. The IDH mutation assay is a prime example of this and the future development of this method into a diagnostic test is an active area of research.

Further improvements in miniature mass spectrometers will also facilitate the increased translation of ambient ionization-MS methods into clinical practice. A key advantage of mini-MS systems is the lower infrastructure requirements to run small MS systems compared to larger benchtop mass spectrometers. The number of manufacturers producing mini-MS systems is increasing, and an extensive list of mini-MS systems is reported in a recent review article.(15) Mini-MS systems are becoming smaller, easier to use, and higher performing in terms of MS resolution and analytical sensitivity. Some recent work has shown that IDH mutation status can be assessed in a short timeframe using a commercialized miniature MS system to measure 2HG in tissue biopsies, and experiments with this methodology in the operating room are ongoing in Prof. Cooks' laboratory in collaboration with IU School of Medicine.(10) A key outstanding issue with miniature MS systems for diagnostic applications is whether their performance can meet regulatory standards of analytical and clinical performance.

As demonstrated in the touch spray (TS) ionization study of renal cell carcinoma, rapid diagnostic information indicative of tissue disease state can be obtained with minute sample quantities and with a simple procedure. It can be envisioned that a surgeon could use a TS probe to sample an area of tissue and hand it off to a technician for analysis.(11) Culture swabs are routinely used to sample areas of tissue, and devices for this purpose are approved by the FDA and could be coopted as a sample probe and ambient ionization source. Further development of TS-MS to improve the robustness and data quality are needed to ensure that the analytical and clinical accuracies of TS-MS methods can meet regulatory standards.

As evidenced in the tumor cell percentage classification results for the glioma studies reported in Chapter 5, there is still much work to do in improving the classification accuracies of our DESI-MS method for assessing glioma margins. Glioma margins are highly complex and heterogenous due to the infiltrative nature of the glioma. A complicating factor is also the high morbidity that the patient can suffer from removal of healthy brain tissue. An objective surgical margin evaluation tool for gliomas would likely reduce the tumor recurrence rates and reduce neurological deficits. Stereotactic registration of the DESI-MS results onto the preoperative MRI could facilitate the surgeon keeping track of the nature of the brain tissue at discrete points in the

resection cavity. Further integration of ambient ionization-MS based diagnostics with complementary imaging and pathology methods would increase the confidence and information content of the results.

The intrasurgical application of ambient ionization-MS is a rapidly evolving field. The first multi-center DESI-MS study, led by Prof. Livia Eberlin, has been recently reported.(12) Point-of-care cancer tissue analysis with miniature-MS systems is soon to be reported, with preliminary studies led by Prof. Zheng Ouyang(13) and Prof. R. Graham Cooks(14) reported in early 2019. It is my expectation that this field will make even more significant advancements in the next 15 years.

6.2   References

1. Seng P, Drancourt M, Gouriet F, La Scola B, Fournier PE, Rolain JM, et al. Ongoing revolution in bacteriology: routine identification of bacteria by matrix-assisted laser desorption ionization time-of-flight mass spectrometry. Clin Infect Dis. 2009;49(4):543-51.

2. Clark AE, Kaleta EJ, Arora A, Wolk DM. Matrix-Assisted Laser Desorption Ionization-Time of Flight Mass Spectrometry: a Fundamental Shift in the Routine Practice of Clinical Microbiology. Clinical microbiology reviews. 2013;26(3):547-603.

3. Demirev PA, Ho YP, Ryzhov V, Fenselau C. Microorganism identification by mass spectrometry and protein database searches. Analytical Chemistry. 1999;71(14):2732-8.

4. https://www.bruker.com/products/mass-spectrometry-and-separations/fda-cleared-maldi-biotyper-usa/overview.html

5. Wilcken B, Wiley V, Hammond J, Carpenter K. Screening newborns for inborn errors of metabolism by tandem mass spectrometry. New England Journal of Medicine. 2003;348(23):2304-12.

6. Chace DH, Kalas TA, Naylor EW. Use of tandem mass spectrometry for multianalyte screening of dried blood specimens from newborns. Clinical chemistry. 2003;49(11):1797-817.

7. Mechtler TP, Stary S, Metz TF, De Jesus VR, Greber-Platzer S, Pollak A, et al. Neonatal screening for lysosomal storage disorders: feasibility and incidence from a nationwide study in Austria. Lancet. 2012;379(9813):335-41.

8. Zhang XK, Elbin CS, Chuang WL, Cooper SK, Marashio CA, Beauregard C, et al. Multiplex enzyme assay screening of dried blood spots for lysosomal storage disorders by using tandem mass spectrometry. Clinical chemistry. 2008;54(10):1725-8.

9. https://www.fda.gov/newsevents/newsroom/pressannouncements/ucm539893.htm

10. Pu F, Alfaro CM, Pirro V, Xie Z, Ouyang Z, Cooks RG. Rapid determination of isocitrate dehydrogenase mutation status of human gliomas by extraction nanoelectrospray using a miniature mass spectrometer. Analytical and bioanalytical chemistry. 2019.

11. Pirro V, Llor RS, Jarmusch AK, Alfaro CM, Cohen-Gadol AA, Hattab EM, et al. Analysis of human gliomas by swab touch spray-mass spectrometry: applications to intraoperative assessment of surgical margins and presence of oncometabolites. Analyst. 2017.

12. Porcari AM, Zhang JL, Garza KY, Rodrigues-Peres RM, Lin JQ, Young JH, et al. Multicenter Study Using Desorption-Electrospray-Ionization-Mass-Spectrometry Imaging for Breast-Cancer Diagnosis. Analytical Chemistry. 2018;90(19):11324-32.

13. Zou R, Cao WB, Chong L, Hua W, Xu H, Mao Y, et al. Point-of-Care Tissue Analysis Using Miniature Mass Spectrometer. Analytical Chemistry. 2019;91(1):1157-63.

14. Pu F, Alfaro CM, Pirro V, Xie Z, Ouyang Z, Cooks RG. Rapid determination of isocitrate dehydrogenase mutation status of human gliomas by extraction nanoelectrospray using a miniature mass spectrometer. Analytical and bioanalytical chemistry. 2019.

15. Snyder DT, Pulliam CJ, Ouyang Z, Cooks RG. Miniature and Fieldable Mass Spectrometers: Recent Advances. Anal Chem. 2015;88(1):2-29.

VITA

Education

Current: Fifth year PhD Candidate in Analytical Chemistry, Purdue University. Advisor: Prof. R. Graham Cooks. Expected thesis completion: May 2019.

Previous: BS Biochemistry and Biology (2014), University of North Carolina at Greensboro. Advisor: Prof. Nadja B. Cech studying electrospray ionization fundamentals.

Skills

1. Metabolomic and lipidomic characterization of tissue sections using desorption electrospray ionization-mass spectrometry imaging.

2. Paper-spray, touch spray, and nano-electrospray ionization mass spectrometry for detection of lipids and oncometabolites from biological tissues.

3. Identification of lipids and metabolites using tandem and high resolution mass spectrometry on ion traps (Thermo LTQ), triple quadrupole (TSQ), and orbitrap (Exactive) mass spectrometers.

4. Multivariate (principal component analysis) and univariate (ANOVA, hypothesis testing, multiple regression) statistical data analysis of metabolomic and lipidomic mass spectrometry data in MATLAB, JMP, and SAS

Publications

1) Pu, F.; Alfaro, C.M.; Pirro, V.; Xie, Z.; Ouyang, Z.; Cooks, R. G. Rapid determination of isocitrate dehydrogenase mutation status of human gliomas by extraction nanoelectrospray using a miniature mass spectrometer. *Anal. Bioanal. Chem.* **2019**. *In Press.*

2) Alfaro, C.; Pirro, V.; Keating, M.; Hattab, E. M.; Cooks, R. G.; Cohen-Gadol, A. A. Intraoperative assessment of isocitrate dehydrogenase mutation status in human gliomas using desorption electrospray ionization-mass spectrometry. *J. Neurosurgery.* **2018**. *In Press.*

3) D'Hue, C.; Moore, M.; Summerlin, D. J.; Jarmusch, A. K.; Alfaro, C. M.; et al. Feasibility of Desorption Electrospray Ionization Mass Spectrometry for Diagnosis of Oral Tongue Squamous Cell Carcinoma. *Rapid Commun. Mass Spectrom.* **2017**. 32, 133-141.

4) Yannell, K. E.; Smith, K.; Alfaro, C. M.; Jarmusch, A. K.; Pirro, V.; Cooks, R. G. N-acetylaspartate and 2-hydroxyglutarate assessed in human brain tissue by mass spectrometry as neuronal markers of oncogenesis. *Clin. Chem.* **2017**, 63(11), 1766.

5) Pirro, V.; Alfaro, C.M.; Jarmusch, A. K.; Hattab, E. M.; Cohen-Gadol, A. A.; Cooks, R. G., Intraoperative assessment of tumor margins during glioma resection by desorption electrospray ionization-mass spectrometry. *PNAS* **2017**, 114(26), 6700-6705.

6) Pirro, V.; Jarmusch, A. K.; <u>Alfaro, C. M.</u>; Hattab, E. M.; Cohen-Gadol, A. A.; Cooks, R. G., Utility of neurological smears for intrasurgical brain cancer diagnostics and tumour cell percentage by DESI-MS. *Analyst* **2017**, 142, 449-454.

7) Pirro, V., Llor, R.S., Jarmusch, A.K., <u>Alfaro, C.M.</u>, Cohen-Gadol, A.A., Hattab, E.M., Cooks, R. G., Analysis of human gliomas by swab touch spray-mass spectrometry: applications to intraoperative assessment of surgical margins and presence of oncometabolites. *Analyst.* 2017. 142,4058-4066.

8) Jarmusch, A. K[*].; <u>Alfaro, C. M[*]</u>.; Pirro, V.; Hattab, E. M.; Cohen-Gadol, A. A.; Cooks, R. G., Differential Lipid Profiles of Normal Human Brain Matter and Gliomas by Positive and Negative Mode Desorption Electrospray Ionization-Mass Spectrometry Imaging. *PLOS ONE.* **2016**, 11(9), e0163180. *Authors contributed equally

9) <u>Alfaro, C. M</u>.; Jarmusch, A. K.; Pirro, V.; Kerian, K. S.; Masterson, T. A.; Cheng, L.; Cooks, R. G., Ambient ionization mass spectrometric analysis of human surgical specimens to distinguish renal cell carcinoma from healthy renal tissue. *Anal Bioanal Chem.* **2016,** *408* (20), 5407-14.

10) Ferreira, C. R.; Jarmusch, A. K.; Pirro, V.; <u>Alfaro, C. M.;</u> Gonzalez-Serrano, A. F.; Niemann, H.; Wheeler, M. B.; Rabel, R. A. C.; Hallett, J. E.; Houser, R.; Kaufman, A.; Cooks, R. G. "Ambient ionisation mass spectrometry for lipid profiling and structural analysis of mammalian oocytes, preimplantation embryos and stem cells." *Reproduction, Fertility and Development*. **2015**, 27(4), 621-637.

11) <u>Alfaro, C. M</u>.; Uwakweh, A.; Todd, D. A.; Ehrmann, B. M.; Cech, N. B. "Investigations of Analyte-Specific Response Saturation and Dynamic Range Limitations in Atmospheric Pressure Ionization Mass Spectrometry". *Analytical Chemistry*. **2014**, 86(21), 10639-10645.

Conferences and Presentations

Presentation	Conference
Poster: Intraoperative-MS based biopsy analysis platform for glioma diagnosis, extent of tumor cell infiltration estimation, and IDH subtyping	2019 Translational Science, Washington, DC
Poster: Development and Clinical Application of an Intraoperative Desorption Electrospray Ionization-Mass Spectrometry Surgical Margin Assessment Tool	2018 Turkey Run Analytical Chemistry Conference, Marshall, IN
	2018 Indiana CTSI University of Notre Dame Retreat, South Bend, IN
	2018 Indiana CTSI Annual Meeting, Indianapolis, IN
Poster: Intraoperative Assessment of Isocitrate Dehydrogenase Mutation Status in Human Gliomas Using Desorption Electrospray Ionization-Mass Spectrometry	2018 Translational Science, Washington, DC

Poster: Desorption electrospray mass spectrometric determination of isocitrate dehydrogenase mutation status and tumor cell percentage in human glioma biopsies during tumor resection	2017 Indiana CTSI Annual Meeting, Indianapolis, IN
Oral: Towards intrasurgical brain tumor diagnosis and surgical margin characterization by desorption electrospray ionization mass spectrometry	2016 Turkey Run Analytical Chemistry Conference, Marshall, IN
Poster: Towards intrasurgical brain tumor diagnosis and surgical margin characterization by desorption electrospray ionization mass spectrometry	2016 Indiana CTSI Annual Meeting, Indianapolis, IN
	2016 Purdue Cancer Research Day, West Lafayette, IN
	2016 Indiana Life Sciences Summit, Indianapolis, IN
	2016 Eli Lilly Grand Rounds Poster Session, Indianapolis, IN
Oral: Enhanced discrimination of healthy human brain tissue and glioma using positive and negative polarity desorption electrospray ionization with data fusion	2016 American Society for Mass Spectrometry Annual Conference, San Antonio, TX
Poster: Towards human cancer tissue diagnosis using ambient ionization mass spectrometry	2015 Turkey Run Analytical Chemistry Conference, Marshall, IN
Poster: Protonation and desolvation as limiting factors in the linear dynamic range of electrospray ionization mass spectrometry	2014 American Society for Mass Spectrometry Annual Conference, Baltimore, MD
Poster: Insights into factors that limit the linear dynamic range in electrospray ionization mass spectrometry analysis of flavonoids	2013 American Society for Mass Spectrometry Annual Conference, Minneapolis, MN
Poster: Synthesis of zirconocene amino alcohol frustrated lewis pairs	2013 South Eastern Regional Meeting of the American Chemical Society, 2013

Teaching Experience   **Date Range**

Purdue Teaching Assistant for Junior/Senior Chemistry Seminar (CHM 494)   Spring 2016

Purdue Teaching Assistant for Instrumental Analysis Lecture & Lab (CHM 424) Fall 2015

Purdue Teaching Assistant for General Chemistry Lab (CHM 115)   Spring 2015

Purdue Teaching Assistant for General Chemistry Lab (CHM 112)   Fall 2014

UNCG Teaching Assistant Triad Mass Spectrometry Facility   Fall 2013 and Spring 2013

UNCG Quantitative Analysis Teaching Assistant (CHE 331)   Fall 2012

UNCG General Chemistry I Lab Section Instructor (CHE 112)   Fall 2012

Grants/Awards   **Date Range**

Purdue
MSACL Young Investigator Travel Grant   March 2019
Indiana CTSI Predoctoral Training Award (TL1) funded in part by Summer 2017-Summer 2019

Grant # UL1TR002529 (A. Shekhar, PI) 5/18/2018 – 4/30/2023

[2016 Analytical and Bioanalytical Chemistry Best Paper Award](#)   January 2017

Purdue Center for Cancer Research Phase 1 Concept Award   Spring 2016-Spring 2017

Ross Fellowship from Purdue University Graduate School   Fall 2014-Spring 2015

UNCG

Office of Undergraduate Research Travel Grant   Fall 2013

Science, Technology and Math Preparation Scholarship   Fall 2013 and Spring 2014

Honors Travel Grant   Summer 2013

Undergraduate Research Assistantship   Summer 2013

2011/2012 Departmental American Chemical Society Analytical Chemistry Award   Spring 2013

First place 7th Annual Carolyn and Norwood Thomas Undergraduate Research Expo Spring 2013

Office of Undergraduate Research Travel Grant   Spring 2013

Service/Outreach

[GK-12 Volunteer Teaching and Service Learning at Tecumseh Junior High](#)   Fall 2018

Electroplating Demonstration for NISE NanoDays at Purdue's Discovery Park   April 2018

Judge for Purdue Undergraduate Research Conference Poster Symposium   April 2018

Judge for 2016 Lafayette Regional Science and Engineering Fair   March 2016

Annual National Chemistry Week Demonstrations for Elementary Students October 2014, 2015 & 2017

Completed Graduate School Courses

BIOL 602   Cellular Neurobiology

CHM 620   Spectrochemical Instrumentation

CHM 621   Advanced Analytical Chemistry

CHM 624   Particle Spectroscopy

CHM 635   Biochemistry: Dynamic Aspects

CHM 648   Bioinorganic Chemistry

STAT 512   Applied Regression Analysis

STAT 514   Design of Experiments

PUBLICATIONS

1) Pu, F.; Alfaro, C.M.; Pirro, V.; Xie, Z.; Ouyang, Z.; Cooks, R. G. Rapid determination of isocitrate dehydrogenase mutation status of human gliomas by extraction nanoelectrospray using a miniature mass spectrometer. Anal. Bioanal. Chem. 2019. In Press.

2) Alfaro, C.; Pirro, V.; Keating, M.; Hattab, E. M.; Cooks, R. G.; Cohen-Gadol, A. A. Intraoperative assessment of isocitrate dehydrogenase mutation status in human gliomas using desorption electrospray ionization-mass spectrometry. J. Neurosurgery. 2018. In Press.

3) D'Hue, C.; Moore, M.; Summerlin, D. J.; Jarmusch, A. K.; Alfaro, C. M.; et al. Feasibility of Desorption Electrospray Ionization Mass Spectrometry for Diagnosis of Oral Tongue Squamous Cell Carcinoma. Rapid Commun. Mass Spectrom. 2017. 32, 133-141.

4) Yannell, K. E.; Smith, K.; Alfaro, C. M.; Jarmusch, A. K.; Pirro, V.; Cooks, R. G. N-acetylaspartate and 2-hydroxyglutarate assessed in human brain tissue by mass spectrometry as neuronal markers of oncogenesis. Clin. Chem. 2017, 63(11), 1766.

5) Pirro, V.; Alfaro, C.M.; Jarmusch, A. K.; Hattab, E. M.; Cohen-Gadol, A. A.; Cooks, R. G., Intraoperative assessment of tumor margins during glioma resection by desorption electrospray ionization-mass spectrometry. PNAS 2017, 114(26), 6700-6705.

6) Pirro, V.; Jarmusch, A. K.; Alfaro, C. M.; Hattab, E. M.; Cohen-Gadol, A. A.; Cooks, R. G., Utility of neurological smears for intrasurgical brain cancer diagnostics and tumour cell percentage by DESI-MS. Analyst 2017, 142, 449-454.

7) Pirro, V., Llor, R.S., Jarmusch, A.K., Alfaro, C.M., Cohen-Gadol, A.A., Hattab, E.M., Cooks, R. G., Analysis of human gliomas by swab touch spray-mass spectrometry: applications to intraoperative assessment of surgical margins and presence of oncometabolites. Analyst. 2017. 142,4058-4066.

8) Jarmusch, A. K*.; Alfaro, C. M*.; Pirro, V.; Hattab, E. M.; Cohen-Gadol, A. A.; Cooks, R. G., Differential Lipid Profiles of Normal Human Brain Matter and Gliomas by Positive and Negative Mode Desorption Electrospray Ionization-Mass Spectrometry Imaging. PLOS ONE. 2016, 11(9), e0163180. *Authors contributed equally

9) Alfaro, C. M.; Jarmusch, A. K.; Pirro, V.; Kerian, K. S.; Masterson, T. A.; Cheng, L.; Cooks, R. G., Ambient ionization mass spectrometric analysis of human surgical specimens to distinguish renal cell carcinoma from healthy renal tissue. Anal Bioanal Chem. 2016, 408 (20), 5407-14.

10) Ferreira, C. R.; Jarmusch, A. K.; Pirro, V.; Alfaro, C. M.; Gonzalez-Serrano, A. F.; Niemann, H.; Wheeler, M. B.; Rabel, R. A. C.; Hallett, J. E.; Houser, R.; Kaufman, A.; Cooks, R. G. "Ambient ionisation mass spectrometry for lipid profiling and structural analysis of mammalian oocytes, preimplantation embryos and stem cells." Reproduction, Fertility and Development. 2015, 27(4), 621-637.

11) Alfaro, C. M.; Uwakweh, A.; Todd, D. A.; Ehrmann, B. M.; Cech, N. B. "Investigations of Analyte-Specific Response Saturation and Dynamic Range Limitations in Atmospheric Pressure Ionization Mass Spectrometry". Analytical Chemistry. 2014, 86(21), 10639-10645.

PLOS | ONE

RESEARCH ARTICLE

Differential Lipid Profiles of Normal Human Brain Matter and Gliomas by Positive and Negative Mode Desorption Electrospray Ionization – Mass Spectrometry Imaging

Alan K. Jarmusch[1]☯, Clint M. Alfaro[1]☯, Valentina Pirro[1], Eyas M. Hattab[2], Aaron A. Cohen-Gadol[3], R. Graham Cooks[1]*

1 Department of Chemistry and Center for Analytical Instrument Development, Purdue University, West Lafayette, Indiana, United States of America, 2 Department of Pathology and Laboratory Medicine, University of Louisville School of Medicine, Louisville, Kentucky, United States of America, 3 Department of Neurological Surgery, Indiana University School of Medicine, Indianapolis, Indiana, United States of America

☯ These authors contributed equally to this work.
* cooks@purdue.edu

Abstract

Desorption electrospray ionization—mass spectrometry (DESI-MS) imaging was used to analyze unmodified human brain tissue sections from 39 subjects sequentially in the positive and negative ionization modes. Acquisition of both MS polarities allowed more complete analysis of the human brain tumor lipidome as some phospholipids ionize preferentially in the positive and others in the negative ion mode. Normal brain parenchyma, comprised of grey matter and white matter, was differentiated from glioma using positive and negative ion mode DESI-MS lipid profiles with the aid of principal component analysis along with linear discriminant analysis. Principal component–linear discriminant analyses of the positive mode lipid profiles was able to distinguish grey matter, white matter, and glioma with an average sensitivity of 93.2% and specificity of 96.6%, while the negative mode lipid profiles had an average sensitivity of 94.1% and specificity of 97.4%. The positive and negative mode lipid profiles provided complementary information. Principal component–linear discriminant analysis of the combined positive and negative mode lipid profiles, via data fusion, resulted in approximately the same average sensitivity (94.7%) and specificity (97.6%) of the positive and negative modes when used individually. However, they complemented each other by improving the sensitivity and specificity of all classes (grey matter, white matter, and glioma) beyond 90% when used in combination. Further principal component analysis using the fused data resulted in the subgrouping of glioma into two groups associated with grey and white matter, respectively, a separation not apparent in the principal component analysis scores plots of the separate positive and negative mode data. The interrelationship of tumor cell percentage and the lipid profiles is discussed, and how such a measure could be used to measure residual tumor at surgical margins.

Introduction

Ambient ionization mass spectrometry (MS) has the potential to improve tissue diagnosis and influence outcomes in patients undergoing surgical removal of cancer. Ambient ionization MS provides the opportunity to study biopsied tissue rapidly (seconds to minutes) and with minimal sample preparation [1]. Currently, pathologic diagnosis of gliomas, the most common malignant brain tumor, is performed upon formalin-fixed surgical biopsies via histopathology. However, this cannot be done on a timescale amenable to surgical guidance. Frozen tissue histopathology is performed as an alternative to provide the surgeon information but can take upwards of 20 minutes per biopsy. Methodologies for rapid intraoperative molecular diagnosis are sparse, with noteworthy ongoing interest in Raman spectroscopy [2] and fluorescence [3]; mass spectrometry, too, may meet this need. Several versions of ambient ionization MS have been tested for clinical applications. They include rapid evaporative MS for in vivo analysis of liver, lung, and colorectal cancers [4], desorption electrospray ionization (DESI) for detection of MRI contrast agents within tumors [5] and for analysis of frozen tissue sections, and substrate-based ambient ionization analysis of cancerous tissues; e.g., probe electrospray ionization [6] and touch spray [7,8].

DESI-MS uses a spray of charged solvent droplets to impact a surface and form a thin film in which analyte molecules dissolve. Subsequent droplet impacts release charged microdroplets from the surface and produce gas phase ions in the mass spectrometer [9,10]. DESI-MS can be performed on surfaces in an imaging mode, providing chemical information across two spatial dimensions [11]. Imaging (DESI-MSI) is typically performed in a line-by-line fashion by continuously scanning the DESI impact spot laterally across the sample in the x-dimension, and then stepping a defined distance in the y-dimension, and repeating this process. When performed in the full scan mode, every pixel in an MS image contains a mass spectrum that spans a user defined m/z range for a particular ionization mode (e.g., positive or negative ion mode). DESI-MSI spectra of biological tissues commonly detect metabolites and fatty acids in the lower m/z range (~50–300) and membrane lipids (such as phospholipids and sphingomyelins) in the higher m/z range (~700–1000).

Lipids serve many physiological and structural functions and are increasingly being considered as disease markers in cancer. Previous studies of prostate [7], bladder [12], kidney [13], breast [14], lymphoma [15], and gastrointestinal cancer [16], amongst others, have demonstrated that DESI-MS lipid profiles (m/z values and corresponding relative ion abundances) in combination with multivariate statistics, allow differentiation of cancer from normal tissue as corroborated by traditional histopathologic diagnosis. Further, these lipid profiles are not prone to degradation in the native atmosphere over the timescale of analysis, and have so far proven to be sufficiently reproducible, provided the same DESI conditions and solvents are utilized [17]. Lipid profiles acquired by DESI-MS analysis of human brain tumors have been studied previously; in particular those acquired in the negative ionization mode have been exploited for differentiating normal tissue from diseased [18] as well as for exploring the chemical differences among glioma subtypes, grades, and tissues differing in tumor cell concentrations (i.e., relative percentage of tumor cells compared with normal cells) [19,20]. Differences in the positive ion mode DESI mass spectra between different glioma grades and subtypes were previously noted, but analysis of normal parenchyma and differentiation from diseased tissue using multivariate statistics was not undertaken [21].

Recent studies of oncometabolites in human brain tumors have demonstrated the usefulness of considering low molecular weight metabolites. Notable examples are 2-hydroxyglutaric acid (2-HG) [22] and N-acetyl-aspartic acid (NAA) [18]. When the negative mode lipid profiles and additional sources of chemical information were used together, via data fusion, improved

differentiation of cancer from normal brain parenchyma (i.e., grey and white matter) was obtained [18].

This study is founded on the hypothesis that the positive ion lipid profile obtained with DESI-MSI will provide complementary chemical information and, in combination with the negative ion lipid profile, improve differentiation of normal brain parenchyma and glioma. This manuscript reports sequentially acquired positive and negative ion mode DESI-MSI of tissue sections from 39 human subjects. Multivariate statistical analysis performed upon regions of interest (ROI) revealed that the positive and negative ion mode data contained differentiating information. Further, the information in the positive ion mode was nearly equivalent to the negative ion mode in regards to sensitivity and specificity. This work serves to establish the diagnostic potential of DESI-MS information in both the positive and negative ion modes, either or both of which can be transferred to intrasurgical measurements.

Material and Methods

Banked frozen tissue specimens from 39 human subjects, obtained from the Biorepository of Methodist Research Institute (Indianapolis, IN, USA), were studied in accordance with Purdue IRB protocol (#1410015344). Specimens were cryosectioned (15 μm thickness) and thaw mounted onto glass microscope slides. All tissue sections were stored at −80°C prior to analysis. DESI-MSI was performed using a linear ion trap mass spectrometer, LTQ (Thermo Fisher Scientific, San Jose, CA USA). Dimethylformamide-acetonitrile (1:1 *v/v*) was used for DESI-MSI to preserve tissue morphology for subsequent pathology [23]. MS images at a lateral spatial resolution of 250 μm were collected in a series of rows by coordinating linear motion of the moving stage with MS duty cycle. Each tissue section was imaged twice, initially in the positive ion mode and subsequently in the negative ion mode. The moving stage was reset to the origin position between images. Additional parameters of DESI-MSI, MS/MS, and high resolution MS (HRMS) can be found in the S1 File. After DESI-MSI, the tissue sections were stained (hematoxylin and eosin, H&E) and blindly evaluated by an expert pathologist. ROI were selected in MATLAB (MathWorks, Natick, MA USA) based on histopathologic review of the tissue after MS analysis; each ROI selection was the average spectrum of 1 mm (4 pixels) by 1 mm (4 pixels), which permitted accurate correlation of the spatial and chemical information. The set of tissue sections used provided 585 ROI; 32 selections were removed as they contained significant amounts of ions related to Optimal Cutting Temperature Polymer in the spectra (Figure A in S1 File). The remaining selections were examined by principal component analysis from m/z 700–1000; the exclusion of lower m/z values improved separation as the lower mass-to-charge signals (e.g., fatty acids) were more variable in intensity. Multivariate statistics was performed using MATLAB routines and is detailed in the S1 File. Tentative attributions of m/z values to specific lipid structures were made based on HRMS and MS/MS product ion scans. The statistical results are independent of lipid identification: only the full scan mass-to-charge value and corresponding MS abundance are considered.

Results and Discussion

Sequential Positive and Negative Ionization Mode DESI-MS Imaging

Lipid metabolism has been shown to be significantly different in cancerous and non-cancerous cells and tissues due to the roles of lipids in cell growth, membrane fluidity, cell adhesion, and energy production [24]. The analysis of biological specimens in both MS polarities provides greater coverage of the lipidome; i.e., the totality of lipids in a cell, tissue, or an organism. The lipids detected in this study are primarily membrane phospholipids including phosphatidyl-choline (PC), phosphatidylethanolamine (PE), sphingomyelin (SM), ceramide (Cer),

phosphatidylserine (PS), phosphatidylinositol (PI), and sulfatide (ST). Some classes of membrane lipids preferentially ionize in the positive ion mode (e.g., PC and SM) and others in the negative ion mode (e.g., phosphatidic acids, PI, and PS) depending largely on the functionality of the polar headgroup [25]. We hypothesize that it is advantageous to maximize the acquired lipid information by acquiring data in both polarities to characterize different disease states (e.g., cancer) in order to increase diagnostic accuracy.

Janfelt et al. recently demonstrated acquisition of positive and negative DESI-MS data from the same specimen by alternating MS polarity every other line in the imaging experiment [26]. Their solvent system (methanol-water 19:1) destroys tissue samples during analysis, precluding subsequent analysis or staining of the same tissue specimen. We modified their approach by using morphology preserving solvents (e.g., DMF-ACN [1:1]) which allowed the same tissue section to be imaged multiple times using DESI-MS and subsequently stained for histopathology. Further, the same tissue section was analyzed twice in succession, once in the positive and then in the negative ionization mode, with mass spectra from m/z 200–1000 being obtained from each MS image pixel. The acquisition of data in subsequent images, as opposed to line-by-line polarity switching [26], reduces problems that might arise from incomplete charge equilibration and thus spray stability is improved.

Representative DESI-MS ion images for an illustrative specimen, specimen 51, are reported in Fig 1. Specimen 51 is comprised of a glioma region near the bottom of the tissue section with adjacent grey and white matter regions, determined by histopathology, and marked approximately in Fig 1A. Particular ions were relatively more abundant in different histological regions; for example m/z 798 ([PC 34:1 + K]$^+$), 848 ([GalCer d32:2 + K]$^+$), and 772 ([PE P-38:5 + Na]$^+$) in the positive ion mode (Fig 1A) appear to be relatively more abundant in grey matter, white matter, and glioma, respectively. The selected ion images are a small sampling of the many ions that appear to be differentially abundant in the different histologic regions. Negative ions characteristic of grey matter (m/z 834, [PS 40:6 –H]$^-$), white matter (m/z 888, [(3'-sulfo)GalCer 24:1 – H]$^-$), and glioma (m/z 794, [PC 34:1 + Cl]$^-$) were also observed at different abundances (Fig 1B). The distributions of m/z 834 and m/z 888 in grey and white matter, respectively, agree with prior DESI-MSI studies of human [18] and other mammalian brains [27], as well as other ambient ionization methods such as scanning probe electrospray ionization [28]. The combination of the positive and negative mode ion images provided visually distinct regions which matched well with histopathologic evaluation.
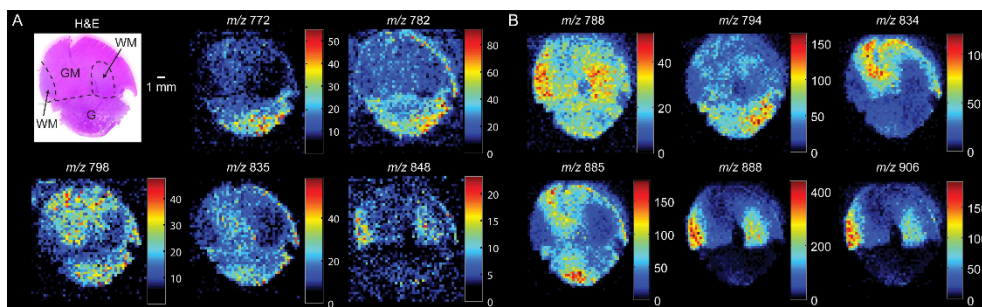
Fig 1. (A) Representative positive ionization mode ion images of specimen 51 and (B) representative negative mode ion images. The false-color ion images are scaled to the greatest intensity of the ion plotted in each image, the scale bar indicates the absolute MS abundance (counts) detected. Scanned H&E-stained tissue sections with regions of grey matter (GM), white matter (WM), and glioma (G) approximated based on histopathology.

doi:10.1371/journal.pone.0163180.g001

Positive ionization mode DESI-MS

The average positive mode lipid profiles for grey matter, white matter, and glioma are visually different (Fig 2A–2C, respectively). Grey matter is associated with a greater abundance of m/z 772 ([PC 32:0 + K]$^+$) and 798 ([PC 34:1 + K]$^+$). White matter appears to have greater abundances of m/z 750 ([GalCer d36:1 + K]$^+$ and [PE P-36:2 + Na]$^+$), 832 ([GalCer d32:2 + Na]$^+$), and 848 ([GalCer d32:2 + K]$^+$). Interestingly, gliomas appear to have greater abundances of m/z 754 ([PC 32:1 + Na]$^+$), 756 ([PC 32:0 + Na]$^+$), and 782 ([PC 34:1 + Na]$^+$). Tentative identifications based on HRMS and MS/MS experiments are shown in Table A in S1 File and Figure B—Figure H in S1 File. The data show that in some cases multiple lipid species are present in a single nominal mass peak (e.g., m/z 750, [PE P-36:2 + Na]$^+$), while other peaks are principally due to a single lipid species (e.g., m/z 754, [PC 32:1 + Na]$^+$). The measured profiles were consistent within classes given potential biological and analytical variation. The differences between classes were typically greater than the standard deviation of the average spectrum for ions important in distinguishing the class; e.g., m/z 848 (Figure I in S1 File). The observed increase in total PC abundance is consistent with magic angle spinning nuclear magnetic analysis of glioma tissue [29]. Other work has suggested a role of PCs in cell proliferation rate which is frequently increased in cancer [30]. A greater abundance of SMs and ceramides in white matter versus grey matter has also been reported [31]. Plasmalogens (e.g., 750) have been reported to compose approximately 50% and 85% of the PE fraction in grey and white matter, respectively [32,33]. In addition, multiple metal adducts of the same lipid (e.g., m/z 782 and 798) were detected (Figure J in S1 File) and are likely due to differences in the concentration of the adducting species (e.g., Na$^+$ and K$^+$) and that of the analyte (e.g., PC 34:1), matrix effects, and intrinsic ionization efficiency differences. Regardless, the differences in ion abundance are consistent between classes and appear to differentiate normal parenchyma from glioma.
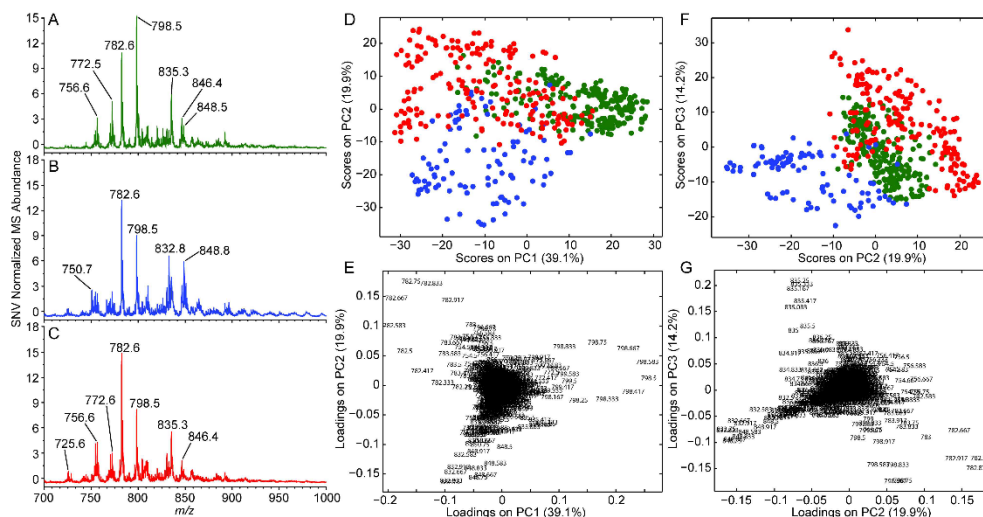

Fig 2. Average positive-mode DESI spectra (m/z 700–1000) for (A) grey matter, n = 223; (B) white matter, n = 98; and (C) gliomas, n = 185. (D and F) PCA score plots: grey matter (green), white matter (blue), and glioma (red). (E and G) PCA loading plots with ion m/z annotated.

doi:10.1371/journal.pone.0163180.g002

The positive ion mode data were analyzed by principal component analysis (PCA), an unsupervised multivariate statistical method, resulting in separation of grey matter (green points), white matter (blue points), and glioma (red points) (Fig 2). Separation of the groups in the PCA score plot of principal component 1 (PC1) vs PC2 (Fig 2D) was less clear than separation in the PCA score plot of PC2 vs PC3 (Fig 2F). The ions contributing to the observed separation in the PCA score plot are displayed in the corresponding PCA loading plots (Fig 2E and 2G). The ions displayed in the PCA loading plots recapitulate differences in the average mass spectra for grey matter, white matter, and gliomas (Fig 2A–2C, respectively). Linear discriminant analysis (LDA) was performed after compression of the variables by PCA to estimate the predictive ability of the positive ionization mode DESI-MSI data. PCA-LDA cross validation (six principal components, five deletion groups) resulted in an average sensitivity and specificity of all classes (grey matter, white matter, and glioma) of 93.2% and 96.6%, respectively. The sensitivity and specificity of each class is tabulated in Table B in S1 File. These values only provide an estimate of prediction performance; a study with a larger sample set is required for further validation but is beyond the scope of this paper.

Negative ionization mode DESI-MS

The presence of m/z 834 ([PS 40:6 –H]$^-$) and 888 ([(3′-sulfo)GalCer 24:1 –H]$^-$) are indicative of grey and white matter, respectively (Fig 3A and 3B). Additional predominant ions include m/z 788 ([PS 36:1 –H]$^-$), 794 ([PC 34:1 + Cl]$^-$), 885 ([PI 38:4 –H]$^-$), and 906 ([(3′-sulfo)GalCer 24:0(2OH)–H]$^-$). Gliomas appear to have suppressed levels of m/z 834 ([PS 40:6 –H]$^-$) and 888 ([(3′-sulfo)GalCer 24:1 –H]$^-$) relative to the grey and white matter average spectra, and therefore appear to have a visually distinct lipid profile (Fig 3C). Tentative identifications are based on previously published results [18,19]. PCA was performed on the negative ionization mode

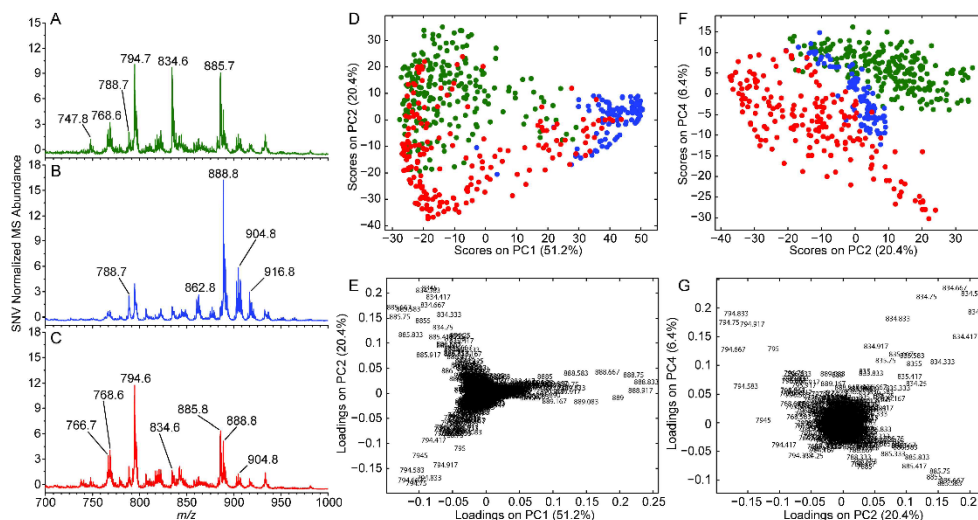**Fig 3.** Average negative-mode DESI spectra (m/z 700–1000) for (A) grey matter, n = 223; (B) white matter, n = 98; and (C) gliomas, n = 185. (D and F) PCA score plots and corresponding (E and G) PCA loading plots. Grey matter, white matter, and glioma are green, blue, and red in the PCA score plot, respectively. The m/z of each ion is annotated in the PCA loading plot.

doi:10.1371/journal.pone.0163180.g003

DESI-MSI data, and the resulting score and loading plots are displayed in Fig 3. The separation of grey matter (green points), white matter (blue points), and glioma (red points) as well as their lipid profiles are consistent with previous results [18] which utilized the same tissue specimens. The similarity of the results is encouraging because analyses were performed one year apart. The continuum of points observed between the main grey and white matter groupings in the PCA score plot of Fig 3D, reflect mixtures of grey and white matter that are present in normal neuroanatomy [34]. Similarly, the points which fall in between the normal parenchyma and glioma groupings represent glioma infiltration into adjacent matter which is well known [35,36]. Points (ROIs) falling in between the main groups had convoluted lipid profiles and support the presence of mixed compositions of grey, white matter, and glioma. For example, Figure K in S1 File shows the mass spectrum for a mixture of grey and white matter. In spite of the continuum between grey matter, white matter, and glioma, good separation is observed in additional PCA score plots; e.g., PC2 vs PC3 (Fig 3F). The PCA loading plots (Fig 3E and 3G) display the importance of specific ions in the separations seen in the PCA score plots.

Negative ionization mode PCA-LDA cross validation (six PCs, five deletion groups) resulted in an average sensitivity of 94.1% and specificity of 97.4%. The sensitivity and specificity of individual classes can be found in Table C in S1 File. The average values are consistent with unreported PCA-LDA results from our prior study which lie within ~5% [18]. Overall, the average positive and negative ionization mode sensitivity and specificity values are similar and appear to be equivalently useful in separating grey matter, white matter, and gliomas. The notable differences when comparing the classes individually are as follows: the sensitivity of gliomas in the positive mode was higher than the negative mode (93.0% versus 88.1%), respectively, while the sensitivity of white matter was lower (89.8%, positive mode, versus 95.9%, negative mode). The specificity of grey matter was greater in the negative mode than the positive mode (98.8% versus 92.2%); the specificity of white matter was higher in the positive mode, 99.7%, than in the negative mode, 93.9%. Comparison of the positive and negative mode cross validation results show that each mode provides complementary diagnostic information, while the average sensitivity and specificity of all classes are similar.

Positive and Negative Mode Data Fusion

Midlevel data fusion was applied considering the first six principal components. PCA of the fused data resulted in clearer separation of grey matter, white matter, and glioma, as shown in Fig 4A. The improved separation reduced overlap between the groupings (e.g., grey matter and
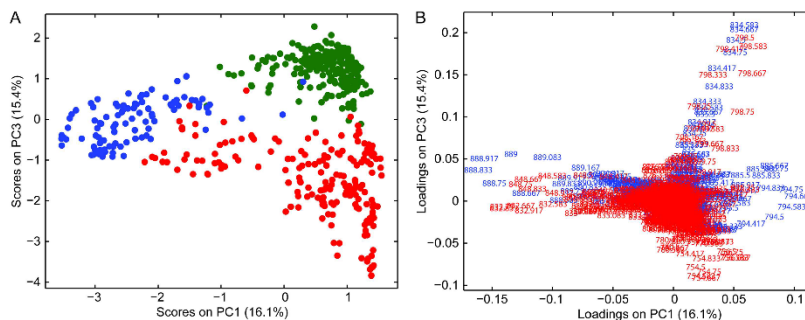

Fig 4. (A) Midlevel data fusion PCA score plot (*m/z* 700–1000) and (B) loading plots. Score plot symbols: Grey matter (green), n = 223; white matter (blue), n = 98; and glioma (red), n = 185. Loading plot values: negative mode (blue) and positive mode (red).

doi:10.1371/journal.pone.0163180.g004

glioma). Separation was also noted in additional PCA score plots (Figure L in S1 File). Interestingly, the glioma class was split into two subgroups, one closely associated with the white matter group and one more closely associated with the grey matter group (approximately delineated left-to-right at a PC1 score of 0 in Fig 4A). The glioma subgroups were not apparent in the positive or negative mode lipid profiles individually or in our prior study in which data for the lipids and metabolites in the negative ion mode were fused [18]. The ROIs of each glioma subgroup were averaged and are displayed in Figure M in S1 File. The negative mode lipid profile of the grey matter–associated glioma subgroup was similar to previously reported glioma profiles [18,20] and contained neither m/z 834 nor 888 at any appreciable abundance. The negative mode lipid profile of the white matter–associated glioma subgroup was similar to the negative mode white matter lipid profile. The positive mode lipid profiles for the two subgroups were visually different from those of normal grey and white matter. The PCA loading plot (Fig 4B) offers a basic understanding of the correlation between positive and negative ions; vectors of similar direction indicate a positive correlation; e.g., m/z 798 (positive mode) and 834 (negative mode) are important in separating grey matter. Similarly, m/z 832 (positive mode) and 888 (negative mode) are important in separating white matter. Additional detail as to the loading value of individual ions are shown in Figure N in S1 File. The loading plot does not reveal deeper relationships (e.g., biological reason) for the correlation between ions, only that they are correlated in separating the groups. A PCA score plot using the first three PCs (S1 Video) illustrates the separation of the classes in 3D space.

PCA-LDA was performed on the fused data (six principal components, five deletions groups) and resulted in the following cross validation results (Table 1). The average sensitivity and specificity of all classes was 94.7% and 97.6%, respectively. These values are not substantially different than the positive or negative mode separately. However, the sensitivity and specificity of individual classes was improved no value falling below 90%. Fusion of the data in some cases did slightly decrease the sensitivity or specificity of individual classes compared to the positive or negative mode results; e.g., specificity of white matter: fused (95.1%), positive mode (99.7%), and negative mode (93.9%). The PCA-LDA results support that information in the positive and negative lipid profiles are complementary and aid in more confidently distinguishing grey matter, white matter, and glioma.

DESI-MS Detection of Tumor Cell Percentage

Tumor cell percentage (TCP), previously dubbed tumor cell concentration, is a means by which to measure glioma infiltration. Its interrelationship with the lipid profiles is poorly understood except that it is partially responsible for the spread of points in the PCA score plots between groupings. The TCP, estimated via histopathology, was plotted (Figure O in S1 File); the PCA score plot indicated that the majority of the grey matter associated glioma subgroup was of medium to high TCP (regions defined as 33%< x <67% and >67%, respectively)

Table 1. Data fusion PCA-LDA confusion matrix with calculated sensitivity and specificity for grey matter, white matter, and glioma. The average sensitivity, 94.7%, and specificity, 97.6%, is the mean of the values for the individual classes.

		Histopathology		
		Grey matter	**White matter**	**Glioma**
DESI	Grey matter	216	2	1
	White matter	5	94	15
	Glioma	2	2	169
	Sensitivity (%)	96.9	95.9	91.4
	Specificity (%)	98.9	95.1	98.7

doi:10.1371/journal.pone.0163180.t001

whereas the white matter associated glioma subgroup was comprised of ROIs with low (<33%) to medium TCP. The grey matter associated glioma subgroup was better separated than the white matter associated glioma subgroup from their respective normal groupings, potentially the effect of a relatively higher TCP. Further, tumor grade and TCP are not completely independent as gliomas of higher grade (WHO III and IV) tend to have greater TCP; differences between tumor grades, plotted in Figure O in S1 File, cannot be commented upon in this study due to the low number of low grade gliomas (WHO I and II).

The complex nature of the molecular diagnosis of gliomas is illustrated in specimen 65 which contained regions of different TCP (40–60%). Illustrative ROI mass spectra are displayed in Figure P in S1 File. The positive and negative spectra of the ROI associated with 60% TCP is less reminiscent of white matter than the spectra from the 40% TCP region. The ROIs of specimen 65 were projected onto the fusion PCA score plot (Figure Q in S1 File) using a technique similar to that described in Bagnaso et al. [37] The ROIs associated with lower TCP in specimen 65 were projected within the white matter group while the ROIs associated with 60% TCP were projected within the white matter–associated glioma subgroup. Similarly, specimen 24, a heterogeneous tissue section, was comprised of a higher TCP glioma region (~80%) and a lower density tumor (10% TCP) in mostly grey matter (one small area of white matter was also present) (Figure R in S1 File). The ROI associated with the 80% TCP region of specimen 24 lay within the grey matter associated glioma subgroup, while the ROI associated with the 10% TCP grey matter region lay within the grey matter group. Note, ROI 13 lay between the grey matter and white matter groups and corresponds to a selection near a grey and white matter boundary.

Lipid changes associated with glioma, detected in the positive and negative mode lipid profiles, appear to be too attenuated to be a useful discriminator in areas of lower tumor cell percentage. Given that the future objective of this work is to assist in surgical resection, it is necessary to measure TCP levels at the surgical resection margin which may be in the 10–40% range, although no current information exists as to the actual proportion of tumor cells at the surgical margin. Current practice determines resection completeness via contrast enhanced MRI, which is an improvement over visual inspection [38]; however, this methodology relies on uptake of radiocontrast agent, can be confounded by intracranial volume changes, and cannot be used to interrogate specific regions that the neurosurgeon finds pathologically suspicious. For glioblastoma patients, there is controversy as to the effect of completeness of tumor resection and patient survival because the infiltrative nature of glioblastoma renders total surgical resection an impossible task with current surgical techniques [39]. Even in tissues that appear histologically normal, malignant glioma cells can be isolated and cultured. Indeed, the site of tumor recurrence is often within two centimeters of the resection margin from non-enhancing areas observed in MRI [40,41]. However, studies have shown that near-total tumor resection for low grade glioma patients significantly increases patient survival and time to malignant progression [42,43]. Optimization and evaluation of the DESI-MS methodology to assist the surgeon in checking discrete areas within the operative field for residual tumor, via the determination of TCP based on DESI-MS lipid profiles, is the subject of future work.

DESI-MS Analysis of Morphologically Effaced Tissue Sections

DESI-MSI could also be used to complement glioma diagnosis (particularly on frozen sections) as tumors commonly efface normal tissue morphology such that the background parenchyma cannot be definitively identified. For example, we found in specimen 70 that the DESI-MS data could be used to determine the background parenchyma when histopathology was inconclusive (Figure S in S1 File). Chemically, it was quite clear that the background parenchyma of

specimen 70 was white matter due to the presence of *m/z* 888. Such lipid information provided by DESI-MSI could be useful in clarifying current histopathologic evaluation and potentially enhance detection of glioma infiltration in tissue sections.

Conclusions

The serial acquisition of DESI-MS images in the positive and negative modes provided spatial and chemical information (i.e., lipid profiles) that differentiated human grey matter, white matter, and gliomas. The positive ion mode lipid profiles are reproducible and allow differentiation of grey matter, white matter, and gliomas with an average sensitivity and specificity of 93.2% and 96.6%, respectively. The inclusion of normal brain parenchyma samples and differentiation via multivariate statistics expand upon prior work which explored the differences in the positive mode lipid profile between different glioma grades and subtypes [21]. The positive ion mode lipid profiles yielded approximately the same differentiation ability as the negative ion lipid profiles. The repeatability of the acquired lipid profiles is illustrated by the similarity of the negative ion mode PCA, average mass spectra, and PCA-LDA cross validation results with that of a prior study [18]. Our hypothesis was supported as the complementary chemical information obtained from the positive and negative mode analyses slightly improved PCA separation of grey matter, white matter, and glioma when used together via data fusion. The fused data analyzed by PCA-LDA provided an average sensitivity of 94.7% and specificity of 97.6%, and the individual class values all exceeded 90%. Diagnosis of effaced glioma tissue specimens is complex, but DESI-MS lipid profiles were able to suggest, chemically, the background matter in such specimens. It is foreseeable that providing pathologists with supplemental DESI-MSI information would increase their diagnostic confidence. Regarding use in the surgical resection of gliomas, we observed the influence of glioma infiltration (assessed as TCP) on the lipid profiles and discussed the possible uses and limitations of this measurement. The limited ability of the lipid profiles to determine lower TCP emphasizes the need for further improvement to the current DESI-MS and multivariate statistical methods. One candidate solution is to combine the negative and positive ion mode lipid profiles with chemical measurements of oncometabolites, such as NAA, that distinguish normal and cancerous neural tissue with high sensitivity and specificity [44]. We envision that the intraoperative use of DESI-MS, collecting positive and negative mode lipid and metabolite data, will comprise an *ex vivo* tool to check discrete areas of tissue which are pathologically ambiguous by visual inspection, potentially augmenting current surgical practice.

Supporting Information

S1 File. Table A. HRMS and MS/MS data for selected ions detected in positive mode DESI-MSI of brain tissue and glioma specimens. Exact mass measurements were searched in the METLIN database (https://metlin.scripps.edu/metabo_search_alt2.php). MS/MS spectra were examined for expected losses from membrane lipid head groups such as 59 (trimethylamine) and 183 (phosphocholine) for PCs and SMs [45,46]; 162 (dehydrated C_6 sugar), 180 (C_6 sugar) for GalCer [47]; 43 and 141 (phosphoethanolamine) for PE [48,49]. Molecular species are consistent with previously published results in which lipid profiles from a small set of human astrocytoma specimens were obtained [21]. Plasmalogens were also detected at certain *m/z* values and supported with MS/MS experiments. **Table B.** Positive ion mode PCA-LDA confusion matrix (six principal components, five deletion groups) for grey matter, white matter, and glioma with calculated sensitivity and specificity for each class. **Table C.** Negative ion mode PCA-LDA confusion matrix (six principal components, five deletion groups) for grey matter, white matter, and glioma with calculated sensitivity and specificity for each class.

Figure A. (A) Negative-mode DESI-MS spectra of ROI removed due to OCT signal (B) detected in the positive-mode. OCT is a polymeric material, principally polyvinyl alcohol, which is readily ionized in the positive ion mode, easily recognized by polymeric peaks separated by 22 mass-to-charge units (e.g., m/z 708.7, 730.7, and 752.7; m/z 715.1 and 737.1; m/z 722.7 and 744.7). **Figure B.** High resolution mass spectrum obtained from specimen CGY, composed of normal white and grey matter, in the positive ion mode A) m/z range 748–811. B) m/z range 828–852. **Figure C.** (A) MS^2 product ion spectrum of m/z 750. (B) MS^3 product ion spectrum of m/z 588 ([GalCer(d36:1) + Na– 162]$^+$. (C) MS^3 product ion spectrum of m/z 707 ([PE(P-36:2) + Na– 43]$^+$. (D) MS^2 product ion spectrum of m/z 772. (E) MS^3 product ion spectrum of m/z 713 ([PC 32:0 + K– 59]$^+$. (F) MS^3 product ion spectrum of m/z 729 ([PE(P-38:5) + Na– 43]$^+$. **Figure D.** (A) MS^2 product ion spectrum of m/z 754. (B) MS^3 product ion spectrum of m/z 695 ([PC 32:1 + Na—59]$^+$). (C) MS^2 product ion spectrum of m/z 756. (D) MS^3 product ion spectrum of m/z 697 ([PC 32:0 + Na—59]$^+$). **Figure E.** (A) MS^2 product ion spectrum of m/z 782. (B) MS^3 product ion spectrum of m/z 723 ([PC 34:1 + Na– 59]$^+$). (C) MS^2 product ion spectrum of m/z 808. (D) MS^3 product ion spectrum of m/z 749 ([PC 36:2 + Na– 59]$^+$).
Figure F. (A) MS^2 product ion spectrum of m/z 798. (B) MS^3 product ion spectrum of m/z 739 ([PC 34:1 + K– 59]$^+$). (C) MS^3 product ion spectrum of m/z 755 ([PE(P-40:6) + Na—43]$^+$).
Figure G. (A) MS^2 product ion spectrum of m/z 832. (B) MS^3 product ion spectrum of m/z 670 ([GalCer(d32:2) + Na– 162]$^+$). (C) MS^2 product ion spectrum of m/z 835. (D) MS^3 product ion spectrum of m/z 776. **Figure H.** (A) MS^2 product ion spectrum of m/z 848. (B) MS^3 product ion spectrum of m/z 686 ([GalCer(d32:2) + K—162]$^+$). **Figure I.** (A–C) Selected m/z regions of the positive ion mode lipid profile displaying the mean (solid line) and standard deviation (dotted line and filled area) for grey matter (green), white matter (blue), and glioma (red). (D–E) Selected m/z regions of the negative ion mode lipid profile. The mean (solid line) and standard deviation (dotted line with filled area) are displayed for grey matter (green), white matter (blue), and glioma (red). **Figure J.** Bar graph of the SNV normalized MS abundance of (A) m/z 782, (B) m/z 798, and (C) m/z 794, associated with different adducts of PC 34:1 (sodium, potassium, and chloride respectively), displaying the mean and standard deviation per class: grey matter (N = 223), white matter (N = 98), and glioma (N = 200). Statistical significance indicated (Kruskal-Wallis, 95% CI) by a single asterisk (*). Overall, the differences in abundance were not predictive by themselves due to high variances, while differences in some mean values were statistically significant at 95% CI (e.g., m/z 782, grey matter and glioma) by Kruskal-Wallis. **Figure K.** Illustrative (A) negative and (B) positive ion mode DESI-MS spectra from a ROI of mixed grey and white matter composition. Both m/z 834 and 888 are abundant in the negative ion mode. Similarly, the positive mode lipid profile appears to be a combination of grey and white matter. **Figure L.** (A) Mid-level data fusion PCA score plot, PC2 vs PC3, and (B) loading plots. Score plot symbols: Grey matter (green), white matter (blue), and glioma (red). Loading plot values: negative mode (blue) and positive mode (red). **Figure M.** (A-B) Negative and positive mode average of the white matter associated glioma subgroup, respectively. (C) Negative mode average of the grey matter associated glioma subgroup. (D) Positive mode average of the grey matter associated glioma subgroup. Major ions are annotated. **Figure N.** Mid-level fusion PCA loading values of specific ions, negative mode (blue) and positive mode (red), on principal components 1–3 with m/z annotated. **Figure O.** (A) PCA score plot, PC1 vs PC3, for tumor cell percentage (TCP): n/a (yellow), normal grey or white matter; low (orange), <33%; medium (red), 33%< x <67%; high (dark red), >67%. (B) PCA score plot for glioma grade: n/a (blue heather), normal grey or white matter; low grade (light blue), glioma WHO grade I or II; high grade (dark blue), glioma WHO grade III or IV. **Figure P.** (A) Negative and (B) positive ion mode lipid profiles of ROI #1 with 40% TCP. (C) Negative and (D) positive ion mode lipid profiles of ROI #5 with 60% TCP. Note, that the 40% TCP spectra look more

reminiscent of normal white matter while the 60% TCP spectra appear more like the white matter associate glioma subgroup (e.g., altered ratio between m/z 794 and m/z 888 in the negative ion mode and altered ratio of m/z 798 and m/z 848 in the positive mode). **Figure Q.** (A) Mid-level data fusion PCA score plot, PC1 vs PC3, with ROI of specimen 65 projected (black squares). The points annotated correspond to specific ROIs indicated on the H&E stained tissue in (B). Score plot symbols: Grey matter (green), white matter (blue), and glioma (red). **Figure R.** (A) Midlevel data fusion PCA score plot, PC1 vs PC3, with ROI of specimen 24 projected (black squares). Score plot symbols: Grey matter (green), white matter (blue), and glioma (red). (B) ROI are annotated upon the H&E stained tissue section with accompanying selected ion images plotted in false-color with corresponding scale bar. Note, the regions of predominately normal grey (m/z 834) and white (m/z 888) contain approximately 10% tumor cells. **Figure S.** (A) Negative and (B) positive ion mode lipid profile from a specimen 70 that was effaced, morphologically. The spectra appear similar to that of white matter (via m/z 888 detection) and suggest the background parenchyma is white matter. (DOCX)

S1 Video. 3D PCA score plot of fused positive and negative mode spectra (m/z 700–1000) for grey matter (green), white matter (blue), and glioma (red). (AVI)

Acknowledgments

Author Contributions

Conceptualization: AKJ CMA VP RGC.

Data curation: VP.

Formal analysis: AKJ CMA VP.

Funding acquisition: RGC.

Investigation: AKJ CMA.

Methodology: AKJ CMA VP.

Project administration: RGC EMH AAC.

Resources: RGC.

Software: AKJ CMA VP.

Supervision: RGC EMH AAC.

Validation: AKJ CMA VP EMH AAC RGC.

Visualization: AKJ CMA VP.

Writing – original draft: AKJ CMA RGC.

Writing – review & editing: AKJ CMA VP EMH AAC RGC.

References

1. Ifa DR, Eberlin LS (2016) Ambient Ionization Mass Spectrometry for Cancer Diagnosis and Surgical Margin Evaluation. Clin Chem 62: 111–123. doi: 10.1373/clinchem.2014.237172 PMID: 26555455

2. Jermyn M, Mok K, Mercier J, Desroches J, Pichette J, et al. (2015) Intraoperative brain cancer detection with Raman spectroscopy in humans. Sci Transl Med 7: 274ra219.

3. Diaz RJ, Dios RR, Hattab EM, Burrell K, Rakopoulos P, et al. (2015) Study of the biodistribution of fluorescein in glioma-infiltrated mouse brain and histopathological correlation of intraoperative findings in high-grade gliomas resected under fluorescein fluorescence guidance. J Neurosurg 122: 1360–1369. doi: 10.3171/2015.2.JNS132507 PMID: 25839919

4. Balog J, Sasi-Szabo L, Kinross J, Lewis MR, Muirhead LJ, et al. (2013) Intraoperative tissue identification using rapid evaporative ionization mass spectrometry. Sci Transl Med 5: 194ra193.

5. Tata A, Zheng J, Ginsberg HJ, Jaffray DA, Ifa DR, et al. (2015) Contrast Agent Mass Spectrometry Imaging Reveals Tumor Heterogeneity. Anal Chem 87: 7683–7689. doi: 10.1021/acs.analchem.5b01992 PMID: 26138213

6. Mandal MK, Saha S, Yoshimura K, Shida Y, Takeda S, et al. (2013) Biomolecular analysis and cancer diagnostics by negative mode probe electrospray ionization. Analyst 138: 1682–1688. doi: 10.1039/c3an36554a PMID: 23348832

7. Kerian KS, Jarmusch AK, Pirro V, Koch MO, Masterson TA, et al. (2015) Differentiation of prostate cancer from normal tissue in radical prostatectomy specimens by desorption electrospray ionization and touch spray ionization mass spectrometry. Analyst 140: 1090–1098. doi: 10.1039/c4an02039a PMID: 25521825

8. Alfaro CM, Jarmusch AK, Pirro V, Kerian KS, Masterson TA, et al. (2016) Ambient ionization mass spectrometric analysis of human surgical specimens to distinguish renal cell carcinoma from healthy renal tissue. Anal Bioanal Chem: 1–8.

9. Costa AB, Cooks RG (2008) Simulated splashes: Elucidating the mechanism of desorption electrospray ionization mass spectrometry. Chemical Physics Letters 464: 1–8.

10. Venter A, Sojka PE, Cooks RG (2006) Droplet dynamics and ionization mechanisms in desorption electrospray ionization mass spectrometry. Anal Chem 78: 8549–8555. PMID: 17165852

11. Wiseman JM, Ifa DR, Venter A, Cooks RG (2008) Ambient molecular imaging by desorption electrospray ionization mass spectrometry. Nat Protoc 3: 517–524. doi: 10.1038/nprot.2008.11 PMID: 18323820

12. Dill AL, Eberlin LS, Costa AB, Zheng C, Ifa DR, et al. (2011) Multivariate statistical identification of human bladder carcinomas using ambient ionization imaging mass spectrometry. Chemistry 17: 2897–2902. doi: 10.1002/chem.201001692 PMID: 21284043

13. Dill AL, Eberlin LS, Zheng C, Costa AB, Ifa DR, et al. (2010) Multivariate statistical differentiation of renal cell carcinomas based on lipidomic analysis by ambient ionization imaging mass spectrometry. Anal Bioanal Chem 398: 2969–2978. doi: 10.1007/s00216-010-4259-6 PMID: 20953777

14. Calligaris D, Caragacianu D, Liu X, Norton I, Thompson CJ, et al. (2014) Application of desorption electrospray ionization mass spectrometry imaging in breast cancer margin analysis. Proc Natl Acad Sci U S A 111: 15184–15189. doi: 10.1073/pnas.1408129111 PMID: 25246570

15. Jarmusch AK, Kerian KS, Pirro V, Peat T, Thompson CA, et al. (2015) Characteristic lipid profiles of canine non-Hodgkin's lymphoma from surgical biopsy tissue sections and fine needle aspirate smears by desorption electrospray ionization—mass spectrometry. Analyst 140: 6321–6329. doi: 10.1039/c5an00825e PMID: 26236993

16. Eberlin LS, Tibshirani RJ, Zhang J, Longacre TA, Berry GJ, et al. (2014) Molecular assessment of surgical-resection margins of gastric cancer by mass-spectrometric imaging. Proc Natl Acad Sci U S A 111: 2436–2441. doi: 10.1073/pnas.1400274111 PMID: 24550265

17. Dill AL, Eberlin LS, Costa AB, Ifa DR, Cooks RG (2011) Data quality in tissue analysis using desorption electrospray ionization. Anal Bioanal Chem 401: 1949–1961. doi: 10.1007/s00216-011-5249-z PMID: 21789488

18. Jarmusch AK, Pirro V, Baird Z, Hattab EM, Cohen-Gadol AA, et al. (2016) Lipid and metabolite profiles of human brain tumors by desorption electrospray ionization-MS. Proc Natl Acad Sci U S A 113: 1486–1491. doi: 10.1073/pnas.1523306113 PMID: 26787885

19. Eberlin LS, Norton I, Dill AL, Golby AJ, Ligon KL, et al. (2012) Classifying human brain tumors by lipid imaging with mass spectrometry. Cancer Res 72: 645–654. doi: 10.1158/0008-5472.CAN-11-2465 PMID: 22139378

20. Eberlin LS, Norton I, Orringer D, Dunn IF, Liu X, et al. (2013) Ambient mass spectrometry for the intraoperative molecular diagnosis of human brain tumors. Proc Natl Acad Sci U S A 110: 1611–1616. doi: 10.1073/pnas.1215687110 PMID: 23300285

21. Eberlin LS, Dill AL, Golby AJ, Ligon KL, Wiseman JM, et al. (2010) Discrimination of human astrocytoma subtypes by lipid analysis using desorption electrospray ionization imaging mass spectrometry. Angew Chem Int Ed Engl 49: 5953–5956. doi: 10.1002/anie.201001452 PMID: 20602384

22. Santagata S, Eberlin LS, Norton I, Calligaris D, Feldman DR, et al. (2014) Intraoperative mass spectrometry mapping of an onco-metabolite to guide brain tumor surgery. Proc Natl Acad Sci U S A 111: 11121–11126. doi: 10.1073/pnas.1404724111 PMID: 24982150

23. Eberlin LS, Ferreira CR, Dill AL, Ifa DR, Cheng L, et al. (2011) Nondestructive, histologically compatible tissue imaging by desorption electrospray ionization mass spectrometry. Chembiochem 12: 2129–2132. doi: 10.1002/cbic.201100411 PMID: 21793152

24. Santos CR, Schulze A (2012) Lipid metabolism in cancer. FEBS J 279: 2610–2623. doi: 10.1111/j.1742-4658.2012.08644.x PMID: 22621751

25. Wang C, Wang M, Han X (2015) Applications of mass spectrometry for cellular lipid analysis. Mol Biosyst 11: 698–713. doi: 10.1039/c4mb00586d PMID: 25598407

26. Janfelt C, Wellner N, Hansen HS, Hansen SH (2013) Displaced dual-mode imaging with desorption electrospray ionization for simultaneous mass spectrometry imaging in both polarities and with several scan modes. J Mass Spectrom 48: 361–366. doi: 10.1002/jms.3166 PMID: 23494793

27. Eberlin LS, Ferreira CR, Dill AL, Ifa DR, Cooks RG (2011) Desorption electrospray ionization mass spectrometry for lipid characterization and biological tissue imaging. Biochim Biophys Acta 1811: 946–960. doi: 10.1016/j.bbalip.2011.05.006 PMID: 21645635

28. Otsuka Y, Naito J, Satoh S, Kyogaku M, Hashimoto H, et al. (2014) Imaging mass spectrometry of a mouse brain by tapping-mode scanning probe electrospray ionization. Analyst 139: 2336–2341. doi: 10.1039/c3an02340k PMID: 24683596

29. Righi V, Roda JM, Paz J, Mucci A, Tugnoli V, et al. (2009) 1H HR-MAS and genomic analysis of human tumor biopsies discriminate between high and low grade astrocytomas. NMR Biomed 22: 629–637. doi: 10.1002/nbm.1377 PMID: 19322812

30. Jain M, Nilsson R, Sharma S, Madhusudhan N, Kitami T, et al. (2012) Metabolite profiling identifies a key role for glycine in rapid cancer cell proliferation. Science 336: 1040–1044. doi: 10.1126/science.1218595 PMID: 22628656

31. O'Brien JS, Sampson EL (1965) Lipid composition of the normal human brain: gray matter, white matter, and myelin. J Lipid Res 6: 537–544. PMID: 5865382

32. Braverman NE, Moser AB (2012) Functions of plasmalogen lipids in health and disease. Biochim Biophys Acta 1822: 1442–1452. doi: 10.1016/j.bbadis.2012.05.008 PMID: 22627108

33. Han X, Holtzman DM, McKeel DW Jr (2001) Plasmalogen deficiency in early Alzheimer's disease subjects and in animal models: molecular characterization using electrospray ionization mass spectrometry. J Neurochem 77: 1168–1180. PMID: 11359882

34. Paus T, Collins DL, Evans AC, Leonard G, Pike B, et al. (2001) Maturation of white matter in the human brain: a review of magnetic resonance studies. Brain Res Bull 54: 255–266. PMID: 11287130

35. Swanson KR, Alvord EC Jr, Murray JD (2000) A quantitative model for differential motility of gliomas in grey and white matter. Cell Prolif 33: 317–329. PMID: 11063134

36. Claes A, Idema AJ, Wesseling P (2007) Diffuse glioma growth: a guerilla war. Acta Neuropathol 114: 443–458. PMID: 17805551

37. Bagnasco L, Zotti M, Sitta N, Oliveri P (2015) A PCA-based hyperspectral approach to detect infections by mycophilic fungi on dried porcini mushrooms (boletus edulis and allied species). Talanta 144: 1225–1230. doi: 10.1016/j.talanta.2015.07.071 PMID: 26452951

38. Senft C, Bink A, Franz K, Vatter H, Gasser T, et al. (2011) Intraoperative MRI guidance and extent of resection in glioma surgery: a randomised, controlled trial. The lancet oncology 12: 997–1003. doi: 10.1016/S1470-2045(11)70196-6 PMID: 21868284

39. Keles GE, Anderson B, Berger MS (1999) The effect of extent of resection on time to tumor progression and survival in patients with glioblastoma multiforme of the cerebral hemisphere. Surg Neurol 52: 371–379. PMID: 10555843

40. Giese A, Westphal M (2001) Treatment of malignant glioma: a problem beyond the margins of resection. J Cancer Res Clin Oncol 127: 217–225. PMID: 11315255

41. De Bonis P, Anile C, Pompucci A, Fiorentino A, Balducci M, et al. (2013) The influence of surgery on recurrence pattern of glioblastoma. Clin Neurol Neurosurg 115: 37–43. doi: 10.1016/j.clineuro.2012.04.005 PMID: 22537870

42. Smith JS, Chang EF, Lamborn KR, Chang SM, Prados MD, et al. (2008) Role of extent of resection in the long-term outcome of low-grade hemispheric gliomas. J Clin Oncol 26: 1338–1345. doi: 10.1200/JCO.2007.13.9337 PMID: 18323558

43. Berger MS, Deliganis AV, Dobbins J, Keles GE (1994) The effect of extent of resection on recurrence in patients with low grade cerebral hemisphere gliomas. Cancer 74: 1784–1791. PMID: 8082081

44. Moffett JR, Ross B, Arun P, Madhavarao CN, Namboodiri AM (2007) N-Acetylaspartate in the CNS: from neurodiagnostics to neurobiology. Prog Neurobiol 81: 89–131. PMID: 17275978

45. Manicke NE, Wiseman JM, Ifa DR, Cooks RG (2008) Desorption electrospray ionization (DESI) mass spectrometry and tandem mass spectrometry (MS/MS) of phospholipids and sphingolipids: ionization, adduct formation, and fragmentation. J Am Soc Mass Spectrom 19: 531–543. doi: 10.1016/j.jasms.2007.12.003 PMID: 18258448

46. Hsu FF, Turk J (2003) Electrospray ionization/tandem quadrupole mass spectrometric studies on phosphatidylcholines: the fragmentation processes. J Am Soc Mass Spectrom 14: 352–363. PMID: 12686482

47. Han X, Gross RW (2005) Shotgun lipidomics: electrospray ionization mass spectrometric analysis and quantitation of cellular lipidomes directly from crude extracts of biological samples. Mass Spectrom Rev 24: 367–412. PMID: 15389848

48. Hsu FF, Turk J (2000) Characterization of phosphatidylethanolamine as a lithiated adduct by triple quadrupole tandem mass spectrometry with electrospray ionization. J Mass Spectrom 35: 595–606. PMID: 10800048

49. Brugger B, Erben G, Sandhoff R, Wieland FT, Lehmann WD (1997) Quantitative analysis of biological membrane lipids at the low picomole level by nano-electrospray ionization tandem mass spectrometry. Proc Natl Acad Sci U S A 94: 2339–2344. PMID: 9122196

RAPID COMMUNICATION

Ambient ionization mass spectrometric analysis of human surgical specimens to distinguish renal cell carcinoma from healthy renal tissue

Clint M. Alfaro[1] · Alan K. Jarmusch[1] · Valentina Pirro[1] · Kevin S. Kerian[1] · Timothy A. Masterson[2] · Liang Cheng[3] · R. Graham Cooks[1]

Abstract Touch spray-mass spectrometry (TS-MS) is an ambient ionization technique (ionization of unprocessed samples in the open air) that may find intraoperative applications in quickly identifying the disease state of cancerous tissues and in defining surgical margins. In this study, TS-MS was performed on fresh kidney tissue (~1–5 cm^3), within 1 h of resection, from 21 human subjects afflicted by renal cell carcinoma (RCC). The preliminary diagnostic value of TS-MS data taken from freshly resected tissue was evaluated. Principal component analysis (PCA) of the negative ion mode (m/z 700–1000) data provided the separation between RCC (16 samples) and healthy renal tissue (13 samples). Linear discriminant analysis (LDA) on the PCA-compressed data estimated sensitivity (true positive rate) and specificity (true negative rate) of 98 and 95 %, respectively, based on histopathological evaluation. The results indicate that TS-MS might provide rapid diagnostic information in spite of the complexity of unprocessed kidney tissue and the presence of interferences such as urine and blood. Desorption electrospray ionization-MS imaging (DESI-MSI) in the negative ionization mode was performed on the tissue specimens after TS-MS analysis as a reference method. The DESI imaging experiments provided phospholipid profiles (m/z 700–1000) that also separated RCC and healthy tissue in the PCA space, with PCA-LDA sensitivity and specificity of 100 and 89 %, respectively. The TS and DESI loading plots indicated that different ions contributed most to the separation of RCC from healthy renal tissue (m/z 794 [PC 34:1 + Cl]$^-$ and 844 [PC 38:4 + Cl]$^-$ for TS vs. m/z 788 [PS 36:1 − H]$^-$ and 810 [PS 38:4 − H]$^-$ for DESI), while m/z 885 ([PI 38:4 − H]$^-$) was important in both TS and DESI. The prospect, remaining hurdles, and future work required for translating TS-MS into a method of intraoperative tissue diagnosis are discussed.

✉ R. Graham Cooks
   cooks@purdue.edu

[1]   Department of Chemistry, Center for Analytical Instrumentation Development and Purdue University Center for Cancer Research, Purdue University, West Lafayette, IN 47907, USA

[2]   Department of Urology, Indiana University School of Medicine, Indiana University Melvin and Bren Simon Cancer Center, Indianapolis, IN 46202, USA

[3]   Department of Pathology and Laboratory Medicine, Indiana University School of Medicine, Indiana University Melvin and Bren Simon Cancer Center, Indianapolis, IN 46202, USA

Introduction

Kidney cancers cause a significant fraction of cancer-related fatalities in the USA, with 14,080 deaths and 61,560 new cases estimated in 2015 [1, 2]. Approximately 90 % of kidney cancers arise from the renal parenchyma and are termed renal cell carcinomas (RCC) [2]. RCC has been differentiated from normal tissue based on epigenetic [3, 4], genetic [5], proteomic [6–8], metabolomic [9, 10], and lipidomic markers [11, 12]. While these techniques are highly informative, analysis time is generally incompatible with intraoperative application, which is the long-term objective of this study. Ambient ionization mass spectrometry (MS), the MS analysis of samples in their native environment with little or no sample preparation, may improve surgical

🖄 Springer

outcomes by providing surgeons with information that helps determine tissue disease state and identifies the tumor margin on the time scale of surgery. Previous intra-operative and/or ex vivo results from several investigators for brain cancer [13–16] and colon, lung, and liver cancers [17, 18] support this expectation. Moreover, it is known in several cancers that phospholipid profiles differ between tumor and normal tissues [19–21]. Lipids have been explored for recognizing cancerous tissue using a variety of ambient ionization techniques such as touch spray (TS) [22], probe electrospray ionization (PESI) [23], rapid evaporative ionization MS (REIMS) [17], and desorption electrospray ionization (DESI)-MS [24]. Lipids are of interest because of their roles in cell signaling, cell-cell recognition, immune response, energy metabolism, and malignant transformation of cells [25–27] and are expected to be reflective of disease state.

TS-MS involves the physical sampling of tissue using a metallic probe with subsequent ionization occurring directly from the probe upon the addition of solvent (1–2 μL) and high voltage (4–5 kV) (see Electronic Supplementary Material Fig. S1) [22, 28]. Free fatty acids and glycerophospholipids, including phosphatidylcholines (PCs) and phosphatidylinositols (PIs), are typically detected when performing TS-MS on frozen tissue sections [28]. TS-MS was previously used to analyze frozen sections of prostate cancer specimens from 18 human subjects, differentiating between normal prostate and prostate cancer [22]. However, TS-MS has not been used to study fresh in vitro tissue in a way that emulates possible intraoperative use. Like TS-MS, PESI-MS is an ambient ionization technique that uses a conductive metallic probe to sample tissue by puncturing it and then creating ions directly from the probe by application of high voltage [23, 29]. Yoshimura et al. analyzed fresh human RCC specimens with PESI in the positive ion mode and observed differences from normal tissue in phosphatidylcholine and triacylglycerol profiles [11]. PESI has also been used to analyze chemically induced hepatocellular carcinoma in a live mouse mounted on a sampling stage positioned in front of a mass spectrometer [30]. PESI and TS are both invasive techniques, but only small amounts of material (10–100 μg) are required to generate data. Both these techniques balance speed of analysis, degree of invasiveness, and amount of sample preparation such that they are amenable to intraoperative applications. An alternative technique, REIMS, samples ions directly from the surgical smoke produced by electrocauterization [17, 18, 31]. REIMS is a fast method because the surgical removal of tissue and mass spectrometric sampling are performed nearly simultaneously; however, the data are harder to correlate with traditional histopathology, the gold standard for diagnosis.

DESI-MS is a microprobe experiment in which a charged aerosol is sprayed onto a sample (e.g., a tissue section or smear) with a spot size of around 200 μm. The resulting thin liquid film formed on the sample surface dissolves some compounds, and subsequent droplet impacts produce splashes of charged analyte containing microdroplets. Gas-phase ions are generated via electrospray-like processes when the secondary microdroplets are sampled by the mass spectrometer [32]. DESI-MS imaging (DESI-MSI) experiments are performed by rastering the spot across the sample in a controlled fashion. An advantage of DESI-MSI when using an appropriate solvent is that the analyzed tissue can be stained with hematoxylin and eosin (H&E) subsequent to MS analysis and evaluated by histopathology, enabling direct correlations to be drawn between molecular and morphological information [33]. DESI-MSI has been applied to analyze several malignancies [20, 21, 34, 35], including kidney cancers [12, 36], and demonstrated that the detected ions were reliably indicative of disease state (viz., distinction between tumor and normal tissues) via multivariate statistics. Finally, although not an ambient ionization technique, matrix-assisted laser desorption ionization (MALDI)-mass spectrometry has been performed in an imaging format, and it can also be used to profile tissue specimens, but the technique requires additional sample manipulation and it takes longer to analyze biopsy specimens [37–39].

In this study, TS-MS was used to analyze fresh healthy renal tissue and RCC specimens. As a reference method, DESI-MSI was performed following TS-MS analysis because DESI has been studied in more detail (DESI was first used to analyze tissue sections in 2005 [24], and TS was developed in 2014 [28]) and because measured DESI-MS lipid profiles can be precisely correlated with histopathological information by staining the analyzed tissue after DESI-MSI. Previous DESI-MSI studies of RCC in the negative ionization mode indicated the ability to differentiate RCC and healthy renal tissue with multivariate statistics, including the ability to differentiate clear cell renal cell carcinoma (ccRCC) and papillary RCC [12]. Based on this previous work, we chose to perform the data acquisition in the negative ionization mode. This study focuses on the rapid analysis of fresh renal tissue using TS-MS with supporting DESI-MSI analysis.

Materials and methods

Tissue handling

All tissue samples were acquired from patients undergoing nephrectomy (partial or radical) for the treatment of RCC and were handled in accordance with approved Institutional Review Board (IRB) protocols at Indiana University School of Medicine (1205008669) and Purdue University (1203011967). A small portion (approximately 3 × 3 × 3 mm) of tumor and adjacent normal kidney tissue was taken from the biopsy in the pathology lab (University

Hospital, Indianapolis, IN) and analyzed on-site using TS-MS. TS-MS analysis was performed while the tissue was fresh (not frozen or fixed). Subsequent to TS-MS analysis, the biopsy specimens were snap frozen in liquid N_2 and transported back to Purdue University on dry ice for DESI-MSI analysis. Tissue samples were obtained from 21 subjects over the period of 1 year. Of the 21 cancer subjects, there were 15 with clear cell RCC, 2 with papillary RCC, 3 with unclassified RCC, and 1 with oncocytoma (see Table S1).

TS-MS analysis of freshly resected kidney tissue

On each day of surgery, the pathology laboratory at University Hospital notified the Purdue researchers when tissue was acquired from the operating room. The researchers transported the tissue specimens from the pathology laboratory to the linear trap quadrupole (LTQ) mass spectrometer (Thermo Scientific, San Jose, CA) located in an adjacent research building. TS-MS was performed on the fresh (not frozen or fixed) tissue specimens using a metal teasing needle purchased from Fisher Scientific (Pittsburgh, PA) to scrape small amounts of cellular material from the bulk tissue [22]. The probe was positioned in front of the mass spectrometer with the metal tip pointing at the inlet (~5–8 mm), a high voltage (4 kV) was applied, and a 1-μL aliquot of methanol was added to initiate ionization. Data were collected over the range m/z 200–1000 in the negative ionization mode. A chronogram showing the time dependence of a typical TS-MS signal recorded from a single solvent addition is shown in Electronic Supplementary Material Fig. S2. After TS-MS analysis at Indiana University School of Medicine (IUSM), the tissue specimens were snap frozen in liquid nitrogen to preserve morphology and halt biochemical processes. The samples were then transported to Purdue for subsequent cryosectioning and DESI-MSI analysis. Parameters for MS/MS experiments which used an LTQ mass spectrometer and exact mass measurements using an orbitrap (Thermo Exactive, San Jose, CA), as well as additional methods on data handling, are provided in the Electronic Supplementary Material.

DESI-MS analysis of frozen tissue sections

At Purdue, the samples from each case were embedded in an optimal cutting temperature polymer (Sakura Finetek, Torrance, CA) and sectioned on a cryotome FSE to 10 μm thickness and thaw mounted on glass slides (Gold Seal UltraFrost Frosted Glass Slides, Thermo Scientific, San Jose, CA). Tumor and normal specimens (as determined by gross analysis performed in the pathology lab at IUSM) from each case were thaw mounted adjacent to each other on the same glass slide. A custom-built DESI source, similar to the DESI 2D source available from Prosolia Inc. (Indianapolis, IN), was used to image the tissue [40]. DESI spray solvent of

dimethylformamide (DMF)-acetonitrile (ACN) 1:1 was used to minimize alteration of tissue morphology [33]. Additional DESI imaging and sample handling parameters are provided in the Electronic Supplementary Material. MS data were recorded over the range m/z 200–1000 in the negative ion mode, automatic gain control (AGC) was turned off, and data were acquired in the profile mode. The tissue sections were stained with H&E after DESI-MSI. A pathologist (L.C.) determined regions of healthy renal tissue and RCC. The DESI imaging data were compiled into a data cube using an in-house program. Data format was compatible with BioMap software (free to download at http://www.imzml.org/index.php?option=com_content&view=article&id=14&Itemid=32). BioMap and was used to extract mass spectra from regions of interest (ROIs) representing RCC and healthy renal tissue based on the histopathological examination (see Fig. S3).

Histological and pathological data

The pathology lab at IUSM performed histopathological analyses on the remaining tissue after providing the specimens to researchers as discussed. The pathological status of the adjacent tissue as well as the histological subtype, both determined by the pathology lab at IUSM, were used to correlate disease status with TS-MS lipid profiles. De-identified clinical and pathological data are provided in Electronic Supplementary Material Table S1. In addition, the tissue sections analyzed by DESI-MSI were subsequently stained with H&E and interpreted by a pathologist (L.C.) to determine regions of healthy tissue and RCC.

Statistical analyses of mass spectrometry data and data visualization

Principal component analysis (PCA), using the non-linear iterative partial least squares algorithm, on the TS-MS and DESI-MSI data was performed using MATLAB (MathWorks, Natick, MA) and in-house routines which were described in previous work [41]. Data were normalized using standard normal variate transformations to correct for baseline shifts and global variation in signal intensities. While data were recorded over the range m/z 200–1000, only the range m/z 700–1000 was utilized for PCA and subsequent linear discriminant analysis (LDA), as this mass range provides better diagnostic information [35]. LDA on the PCA-compressed data was performed in MATLAB to discriminate between healthy renal tissue and RCC [42]. PCA-LDA was used to calculate sensitivity (true positive rate) and specificity (true negative rate) by means of cross validation (using $n = 5$ deletion groups, Table S2). This procedure is described in detail elsewhere [43]. The dispersion in relative ion intensity for a few ions was plotted as box and whisker plots using OriginPro 2016 (OriginLab, Northampton, MA). Unpaired two-sample t

tests of unequal variance and Kruskal-Wallis non-parametric tests were performed in OriginPro 2016 using the raw, unnormalized signal intensities (Table S3).

Results and discussion

PCA was performed on TS-MS data after standard normal variate (SNV) normalization and mean centering. The PCA score and loading plots are shown in Fig. 1A, B, respectively. The separation between RCC and healthy renal tissue is observed in the score plot. As seen in the loading plot (Fig. 1B), healthy renal tissue is more abundant in m/z 794 and 792 (tentatively identified as chlorinated adducts of PC 34:1 and PC 34:2, respectively) and RCC is more abundant in m/z 844 and 885 (tentatively identified as chlorinated PC 38:4 and deprotonated PI 38:4, respectively). These assignments are from MS/MS spectra of these ions, as well as exact mass data, which are shown in Electronic Supplementary Material Figs. S4 and S5. The increased abundance of PI 38:4 in tumor cells is supported by biochemical studies from other laboratories which observed the altered inositol phospholipid metabolism as a common downstream effect due to the activation of several oncogenes including *src, met, trk, mos, raf*, and *ras* [25, 44]. Differences in m/z abundances are apparent in the average mass spectra of healthy renal tissue and RCC shown in Fig. 1C, D, respectively. Cross validation of a discriminant model, LDA on the PCA-compressed data, was performed. The average sensitivity (true positive rate) was 98.7 % and the specificity (true negative rate) was 94.6 % using five deletion groups and five principal components. The preliminary sensitivity and specificity results are encouraging, and they warrant further investigations with larger sample sizes to establish and validate the method's diagnostic capabilities. Additional PCA score and loading plots are shown in Fig. S6, and confusion matrices for the cross validation are shown in supplemental Table S2. The importance of additional ions in separating RCC from healthy renal tissue can be appreciated by examining the lower-order PCA score and loading plots shown in Fig. S6; additional information on interpreting PCA score
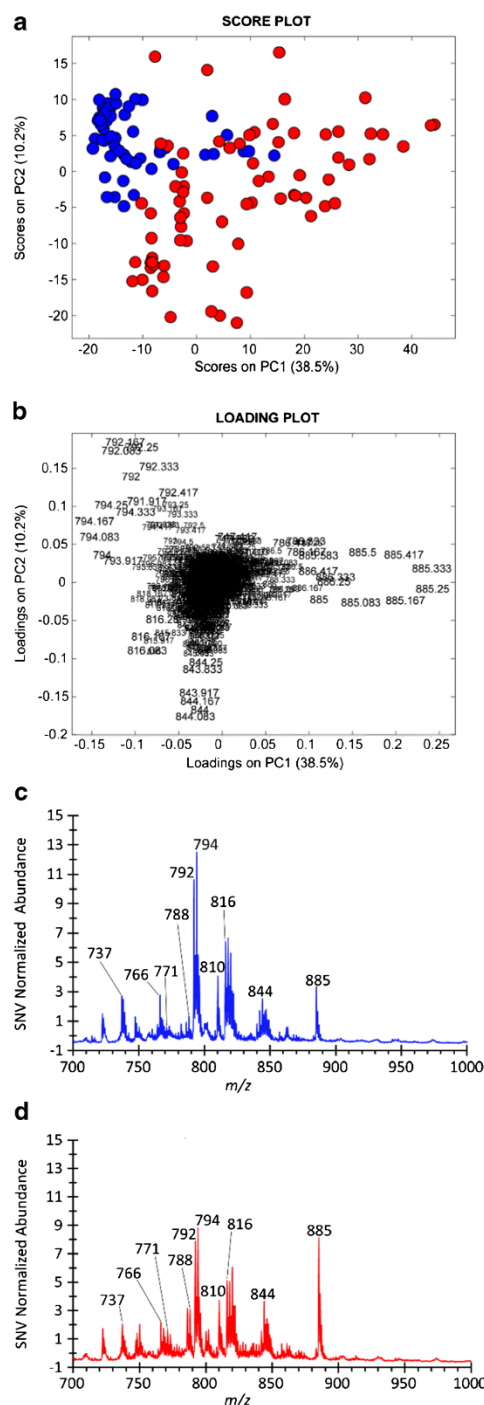
Fig. 1 Negative ion mode TS-MS results from the kidney surgical cases. A The PCA score plot of the TS-MS data. Each object represents a separate sampling ionization event from the freshly resected tissue. Healthy renal tissue is *blue*, and RCC is *red*. A total of 18 human subjects are represented, with 16 RCC and 13 healthy renal tissue specimens, respectively. The average sampling events per tissue is 5. B The corresponding PCA loading plot showing that m/z 792 ([PC 34:2 + Cl]⁻), 794 ([PC 34:1 + Cl]⁻), 844 ([PC 38:4 + Cl]⁻), and 885 ([PI 38:4 − H]⁻) are the major contributors to the separation observed in A. C, D Average mass spectra of the normal and tumor classes, respectively. The SNV-normalized signal intensity is plotted in the average spectra

Springer

and loading plots can be found in Pirro et al. [41]. The univariate statistical significance of several of these ions, including m/z 771, 788, 792, 794, 810, 816, 844, and 885, in differentiating tumor and normal tissues was evaluated with an unpaired two-sample t test of unequal variance and a Kruskal-Wallis non-parametric test (Table S3) and is being visualized with box and whisker plots (Fig. S7). An agreement was observed between the univariate tests for all tested m/z values. The p value was <0.05 for each of the eight ions except for m/z 844 in which the null hypothesis (the mean value of each dataset originates from the same distribution) failed to be rejected.

Histopathological subtypes of the specimens were provided by the IUSM pathology lab, and additional PCA score and loading plot as well as average mass spectra are provided in Electronic Supplementary Material Fig. S8. The number of samples in each subtype was too small to comment on the ability of TS-MS to delineate RCC subtypes. Subtyping is a topic worth exploring further but is beyond the scope of this communication.

The results from the DESI-MSI experiments, used as a reference method to compare with the TS-MS results, are shown in Fig. 2. Similar but better separation is observed in the DESI-MSI PCA score plot (Fig. 2A); however, the DESI loading plot (Fig. 2B) is characterized by m/z 788 and 810 (tentatively deprotonated PS 36:1 and PS 38:4, respectively) and the same TS ion by m/z 885 (deprotonated PI 38:4). These ions (m/z 788, 810, and 885) are evident in the averaged spectra for RCC and healthy renal tissue shown in Fig. 2C, D. The significant contribution of m/z 810 is also observed in the TS-MS data in PC5 (see Electronic Supplementary Material Fig. S6E and F). Examples of H&E-stained tissue sections after DESI-MS analysis as well as a selection of DESI-MS ion images for specimens from three subjects are shown in Fig. S9. Additional PCA score and loading plots for the DESI-MS data are shown in Fig. S10. Cross validation was performed on the DESI PCA-LDA model in a fashion similar to the TS datasets. Using five deletion groups and three principal components, the average sensitivity was 100 % and the specificity was 88.9 % (Table S2). The difference in abundance of the type of ion detected (i.e., chlorinated adduct vs. deprotonated molecule) between TS and DESI can be

Fig. 2 Negative ion mode DESI-MSI results from the surgical kidney specimens. DESI-MSI on cryosectioned tissue was conducted after the TS-MS analysis on the fresh tissue. Samples from 20 human subjects are presented, with 16 RCC and 15 healthy renal tissue specimens, respectively. **A** The PCA score plot of the DESI-MSI data. Each object represents a mass spectrum obtained from a ROI of a single tissue specimen. Healthy renal tissue is *blue*, and RCC is *red*. **B** The corresponding loading plot for the score plot in **A**, showing contributions of m/z 788 ([PS 36:1 − H]⁻), 810 ([PS 38:4 − H]⁻), and 885 ([PI 38:4 − H]⁻) in the separation observed in the score plot. **C, D** The average SNV-normalized DESI mass spectra of the healthy renal tissue and RCC classes, respectively
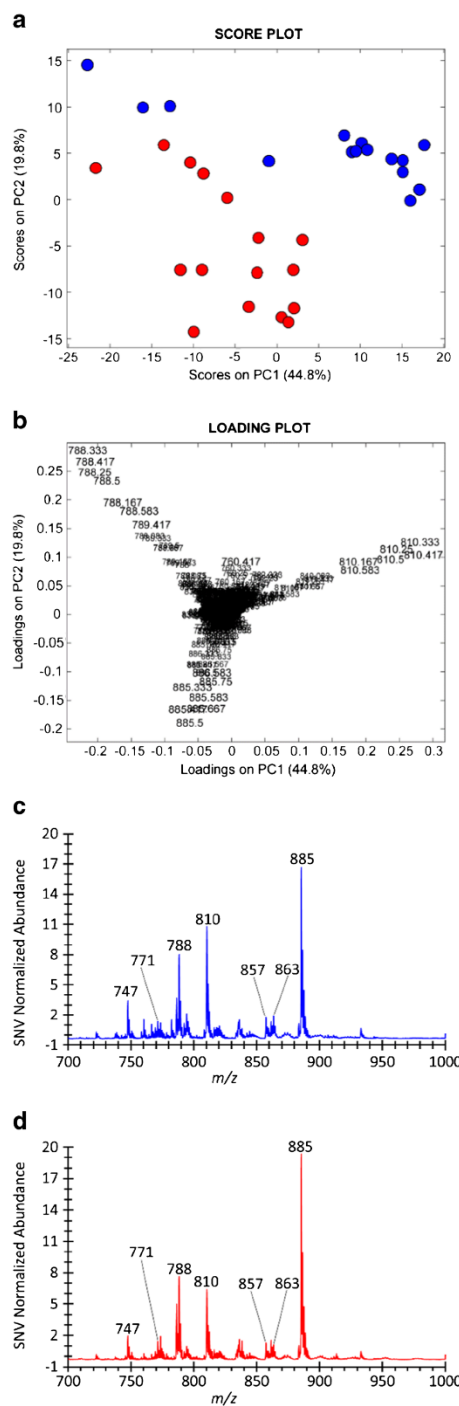
attributed simply to differences in ionization mechanisms, increased biofluid content in the fresh tissue analyzed by TS-MS, and perhaps to the use of different spray solvents (methanol for TS and 1:1 DMF-ACN for DESI) [28, 33]. Relative to DESI, the greater contribution of chlorinated adducts in TS-MS is a previously reported phenomenon [28]. The difference between DESI and TS mass spectra suggests that future uses of TS as a diagnostic method will require the development of spectral databases (training sets) composed of TS-MS data.

The reported data suggest that TS-MS has the potential to yield diagnostic chemical information from fresh healthy renal tissue and RCC tissue. Prior to undertaking a large-scale study, a TS-MS ionization source equipped with microcontrollers for precise probe manipulation and an automated solvent delivery system should be designed and optimized to increase data quality and reproducibility. While the TS-MS experiments were conducted on tissue after resection from a human subject, the analysis occurred on the intraoperative time scale. The results support larger-scale studies of ex vivo surgical tissue using TS-MS to generate a comprehensive database of RCC specimens.

Additional aspects worth investigating are tumor heterogeneity and tumor margins. Ideally, the short analysis time and minimal invasiveness of TS-MS suggest that it might be used to profile various regions within the tumor mass itself and in the surrounding parenchyma. It would be interesting to investigate how the TS-MS lipid profiles (e.g., molecular information) vary within the tumor, as it has been shown that the extent of tumor heterogeneity is underestimated because of limitations in the number of samples that can be obtained [45, 46]. Additionally, TS-MS may aid in delineation of the tumor-parenchyma margin (i.e., tumor margin) in partial nephrectomies, as the utility of intraoperative frozen section analysis remains controversial [47]. This would be beneficial because negative parenchymal surgical margins of any size (e.g., less than 1 mm) for localized, low-grade (T1) RCC have been shown to result in virtually 0 % recurrence of the disease [48, 49].

Conclusions

This preliminary study demonstrated the feasibility of TS-MS analysis on a small number of fresh ex vivo surgical tissue specimens, as an intermediate step between frozen tissue analysis and intraoperative analysis. TS-MS differentiation of specimens using PCA and LDA was demonstrated, and the ions of greatest importance for separation were tentatively identified as complex membrane phospholipids m/z 794 (PC 16:0–18:1), 885 (PI 38:4), and 844 (PC 38:4). Differentiation of RCC and normal specimens was readily achieved by TS-MS and DESI-MS, although different ions were important

for the separation between the two methods. Future work aims to expand the number of specimens in order to validate diagnostic capabilities, and further study the analytical figures of merit of the TS-MS methodology. The applicability of the technique is likely not exclusive to renal cell carcinomas, and it would be fruitful to investigate TS-MS in other cancers. In addition, refinements to the TS-MS methodology should be pursued to increase the ruggedness, ease of use, accuracy, and reproducibility of the measurements.

Compliance with ethical standards The research involving human subjects was conducted in compliance with the ethical guidelines of the approved Institutional Review Board protocols at the Indiana University School of Medicine (study # 1205008669R004) and Purdue University (study # 1203011967). The renal cell carcinoma samples were obtained from 21 human subjects after they provided written informed consent to participate in the research study.

Conflict of interest The authors declare that they have no conflict of interest.

References

1. Howlader N, Noone A, Krapcho M, Garshell J, Miller D, Altekruse SF, et al. SEER cancer statistics review, 1975–2012. Bethesda: National Cancer Institute; 2015.
2. Chow WH, Dong LM, Devesa SS. Epidemiology and risk factors for kidney cancer. Nat Rev Urol. 2010;7(5):245–57.
3. Lasseigne BN, Burwell TC, Patil MA, Absher DM, Brooks JD, Myers RM. DNA methylation profiling reveals novel diagnostic biomarkers in renal cell carcinoma. BMC Med. 2014;12:235.
4. Liao L, Testa JR, Yang H. The roles of chromatin-remodelers and epigenetic modifiers in kidney cancer. Cancer Genet. 2015;208(5): 206–14.
5. Durinck S, Stawiski EW, Pavia-Jimenez A, Modrusan Z, Kapur P, Jaiswal BS, et al. Spectrum of diverse genomic alterations define non-clear cell renal carcinoma subtypes. Nat Genet. 2014;47(1):13–21.
6. Masui O, White NM, DeSouza LV, Krakovska O, Matta A, Metias S, et al. Quantitative proteomic analysis in metastatic renal cell carcinoma reveals a unique set of proteins with potential prognostic significance. Mol Cell Proteomics. 2012;12(1):132–44.
7. Morgan TM, Seeley EH, Fadare O, Caprioli RM, Clark PE. Imaging the clear cell renal cell carcinoma proteome. J Urol. 2012;189(3):1097–103.
8. Guo T, Kouvonen P, Koh CC, Gillet LC, Wolski WE, Rost HL, et al. Rapid mass spectrometric conversion of tissue biopsy samples into permanent quantitative digital proteome maps. Nat Med. 2015;21(4):407–13.

9. Ganti S, Weiss RH. Urine metabolomics for kidney cancer detection and biomarker discovery. Urol Oncol. 2011;29(5):551–7.

10. Monteiro MS, Carvalho M, Bastos ML, Pinho PG. Biomarkers in renal cell carcinoma: a metabolomics approach. Metabolomics. 2014;10:1210–22.

11. Yoshimura K, Chen LC, Mandal MK, Nakazawa T, Yu Z, Uchiyama T, et al. Analysis of renal cell carcinoma as a first step for developing mass spectrometry-based diagnostics. J Am Soc Mass Spectrom. 2012;23(10):1741–9.

12. Dill AL, Eberlin LS, Zheng C, Costa AB, Ifa DR, Cheng L, et al. Multivariate statistical differentiation of renal cell carcinomas based on lipidomic analysis by ambient ionization imaging mass spectrometry. Anal Bioanal Chem. 2010;398(7–8):2969–78.

13. Santagata S, Eberlin LS, Norton I, Calligaris D, Feldman DR, Ide JL, et al. Intraoperative mass spectrometry mapping of an oncometabolite to guide brain tumor surgery. Proc Natl Acad Sci U S A. 2014;111(30):11121–6.

14. Eberlin LS, Norton I, Orringer D, Dunn IF, Liu X, Ide JL, et al. Ambient mass spectrometry for the intraoperative molecular diagnosis of human brain tumors. Proc Natl Acad Sci U S A. 2013;110(5):1611–6.

15. Schafer KC, Balog J, Szaniszlo T, Szalay D, Mezey G, Denes J, et al. Real time analysis of brain tissue by direct combination of ultrasonic surgical aspiration and sonic spray mass spectrometry. Anal Chem. 2011;83(20):7729–35.

16. Agar NY, Golby AJ, Ligon KL, Norton I, Mohan V, Wiseman JM, et al. Development of stereotactic mass spectrometry for brain tumor surgery. Neurosurgery. 2011;68(2):280.

17. Balog J, Sasi-Szabo L, Kinross J, Lewis MR, Muirhead LJ, Veselkov K, et al. Intraoperative tissue identification using rapid evaporative ionization mass spectrometry. Sci Transl Med. 2013;5(194):194ra93.

18. Balog J, Kumar S, Alexander J, Golf O, Huang J, Wiggins T, et al. In vivo endoscopic tissue identification by rapid evaporative ionization mass spectrometry (REIMS). Angew Chem Int Ed. 2015;54(38):11059–62.

19. Marien E, Meister M, Muley T, Fieuws S, Bordel S, Derua R, et al. Non-small cell lung cancer is characterized by dramatic changes in phospholipid profiles. Int J Cancer. 2015;137(7):1539–48.

20. Eberlin LS, Gabay M, Fan AC, Gouw AM, Tibshirani RJ, Felsher DW, et al. Alteration of the lipid profile in lymphomas induced by MYC overexpression. Proc Natl Acad Sci U S A. 2014;111(29):10450–5.

21. Ifa DR, Eberlin LS. Ambient ionization mass spectrometry for cancer diagnosis and surgical margin evaluation. Clin Chem. 2016;62(1):111–23.

22. Kerian KS, Jarmusch AK, Pirro V, Koch MO, Masterson TA, Cheng L, et al. Differentiation of prostate cancer from normal tissue in radical prostatectomy specimens by desorption electrospray ionization and touch spray ionization mass spectrometry. Analyst. 2015;140(4):1090–8.

23. Mandal MK, Saha S, Yoshimura K, Shida Y, Takeda S, Nonami H, et al. Biomolecular analysis and cancer diagnostics by negative mode probe electrospray ionization. Analyst. 2013;138(6):1682–8.

24. Wiseman JM, Puolitaival SM, Takáts Z, Cooks RG, Caprioli RM. Mass spectrometric profiling of intact biological tissue by using desorption electrospray ionization. Angew Chemie Int Ed. 2005;117(43):7256–9.

25. Alonso T, Morgan RO, Marvizon JC, Zarbl H, Santos E. Malignant transformation by ras and other oncogenes produces common alterations in inositol phospholipid signaling pathways. Proc Natl Acad Sci U S A. 1988;85(12):4271–5.

26. Chaurio RA, Janko C, Muñoz L, Frey B, Herrmann M, Gaipl U. Phospholipids: key players in apoptosis and immune regulation. Molecules. 2009;14(12):4892–914.

27. Ackerman D, Simon MC. Hypoxia, lipids, and cancer: surviving the harsh tumor microenvironment. Trends Cell Biol. 2014;24(8):472–8.

28. Kerian KS, Jarmusch AK, Cooks RG. Touch spray mass spectrometry for in situ analysis of complex samples. Analyst. 2014;139:2714–20.

29. Mandal MK, Yoshimura K, Chen LC, Yu Z, Nakazawa T, Katoh R, et al. Application of probe electrospray ionization mass spectrometry (PESI-MS) to clinical diagnosis: solvent effect on lipid analysis. J Am Soc Mass Spectrom. 2012;23(11):2043–7.

30. Yoshimura K, Mandal MK, Hara M, Fujii H, Chen LC, Tanabe K, et al. Real-time diagnosis of chemically induced hepatocellular carcinoma using a novel mass spectrometry-based technique. Anal Biochem. 2013;441(1):32–7.

31. Balog J, Szaniszlo T, Schaefer KC, Denes J, Lopata A, Godorhazy L, et al. Identification of biological tissues by rapid evaporative ionization mass spectrometry. Anal Chem. 2010;82(17):7343–50.

32. Takats Z, Wiseman JM, Gologan B, Cooks RG. Mass spectrometry sampling under ambient conditions with desorption electrospray ionization. Science. 2004;306:471–3.

33. Eberlin LS, Ferreira CR, Dill AL, Ifa DR, Cheng L, Cooks RG. Nondestructive, histologically compatible tissue imaging by desorption electrospray ionization mass spectrometry. Chembiochem. 2011;12(14):2129–32.

34. Eberlin LS, Tibshirani RJ, Zhang J, Longacre TA, Berry GJ, Bingham DB, et al. Molecular assessment of surgical-resection margins of gastric cancer by mass spectrometric imaging. Proc Natl Acad Sci U S A. 2014;111(7):2436–41.

35. Jarmusch AK, Pirro V, Baird Z, Hattab EM, Cohen-Gadol AA, Cooks RG. Lipid and metabolite profiles of human brain tumors by desorption electrospray ionization-MS. Proc Natl Acad Sci U S A. 2016;113(6):1486–91.

36. Shroff EH, Eberlin LS, Dang VM, Gouw AM, Gabay M, Adam SJ, et al. MYC oncogene overexpression drives renal cell carcinoma in a mouse model through glutamine metabolism. Proc Natl Acad Sci U S A. 2015;112(21):6539–44.

37. Calligaris D, Feldman DR, Norton I, Olubiyi O, Changelian AN, Machaidze R, et al. MALDI mass spectrometry imaging analysis of pituitary adenomas for near-real-time tumor delineation. Proc Natl Acad Sci U S A. 2015;112(32):9978–83.

38. Prentice BM, Chumbley CW, Caprioli RM. High-speed MALDI MS/MS imaging mass spectrometry using continuous raster sampling. J Mass Spectrom. 2015;50(4):703–10.

39. Spraggins JM, Caprioli RM. High-speed MALDI-TOF imaging mass spectrometry: rapid ion image acquisition and considerations for next generation instrumentation. J Am Soc Mass Spectrom. 2011;22(6):1022–31.

40. Bennet RV, Gamage CM, Fernandez FM. Imaging of biological tissues by desorption electrospray ionization mass spectrometry. J Vis Exp. 2013;77:e50575.

41. Pirro V, Eberlin LS, Oliveri P, Cooks RG. Interactive hyperspectral approach for exploring and interpreting DESI-MS images of cancerous and normal tissue sections. Analyst. 2012;137(10):2374–80.

42. Pirro V, Oliveri P, Ferreira CR, Gonzalez-Serrano AF, Machaty Z, Cooks RG. Lipid characterization of individual porcine oocytes by dual mode DESI-MS and data fusion. Anal Chim Acta. 2014;848:51–60.

43. González-Serrano AF, Pirro V, Ferreira CR, Oliveri P, Eberlin LS, Heinzmann J, et al. Desorption electrospray ionization mass spectrometry reveals lipid metabolism of individual oocytes and embryos. PLoS ONE. 2013;8(9):e74981.

44. Alonso T, Santos E. Increased intracellular glycerophosphoinositol is a biochemical marker for transformation by membrane-associated and cytoplasmic oncogenes. Biochem Biophys Res Commun. 1990;171(1):14–9.

45. Ricketts CJ, Linehan WM. Intratumoral heterogeneity in kidney cancer. Nat Genet. 2014;46(3):214–5.
46. Gerlinger M, Horswell S, Larkin J, Rowan AJ, Salm MP, Varela I, et al. Genomic architecture and evolution of clear cell renal cell carcinomas defined by multiregion sequencing. Nat Genet. 2014;46(3):225–33.
47. Sterious SN, Simhan J, Smaldone MC, Tsai KJ, Canter D, Wameedh E, et al. Is there a benefit to frozen section analysis at the time of partial nephrectomy? Can J Urol. 2013;20(3): 6778–84.
48. Sutherland SE, Resnick MI, Maclennan GT, Goldman HB. Does the size of the surgical margin in partial nephrectomy for renal cell cancer really matter? J Urol. 2001;167(1):61–4.
49. Lam JS, Bergman J, Breda A, Schulam PG. Importance of surgical margins in the management of renal cell carcinoma. Nat Clin Pract Urol. 2008;5(6):308–17.

JNS

Intraoperative assessment of isocitrate dehydrogenase mutation status in human gliomas using desorption electrospray ionization–mass spectrometry

Clint M. Alfaro, BS,[1] Valentina Pirro, PhD,[1] Michael F. Keating, BS,[1] Eyas M. Hattab, MD, MBA,[2] R. Graham Cooks, PhD,[1] and Aaron A. Cohen-Gadol, MD, MSc, MBA[3]

[1]Department of Chemistry, Purdue University, West Lafayette, Indiana; [2]Department of Pathology and Laboratory Medicine, University of Louisville, Kentucky; and [3]Department of Neurological Surgery, Indiana University School of Medicine, Goodman Campbell Brain and Spine, Indianapolis, Indiana

OBJECTIVE The authors describe a rapid intraoperative ambient ionization mass spectrometry (MS) method for determining isocitrate dehydrogenase (IDH) mutation status from glioma tissue biopsies. This method offers new glioma management options and may impact extent of resection goals. Assessment of the IDH mutation is key for accurate glioma diagnosis, particularly for differentiating diffuse glioma from other neoplastic and reactive inflammatory conditions, a challenge for the standard intraoperative diagnostic consultation that relies solely on morphology.

METHODS Banked glioma specimens (n = 37) were analyzed by desorption electrospray ionization–MS (DESI-MS) to develop a diagnostic method to detect the known altered oncometabolite in IDH-mutant gliomas, 2-hydroxyglutarate (2HG). The method was used intraoperatively to analyze tissue smears obtained from glioma patients undergoing resection and to rapidly diagnose IDH mutation status (< 5 minutes). Fifty-one tumor core biopsies from 25 patients (14 wild type [WT] and 11 mutant) were examined and data were analyzed using analysis of variance and receiver operating characteristic curve analysis.

RESULTS The optimized DESI-MS method discriminated between IDH-WT and IDH-mutant gliomas, with an average sensitivity and specificity of 100%. The average normalized DESI-MS 2HG signal was an order of magnitude higher in IDH-mutant glioma than in IDH-WT glioma. The DESI 2HG signal intensities correlated with independently measured 2HG concentrations (R^2 = 0.98). In 1 case, an IDH1 R132H–mutant glioma was misdiagnosed as a demyelinating condition by frozen section histology during the intraoperative consultation, and no resection was performed pending the final pathology report. A second craniotomy and tumor resection was performed after the final pathology provided a diagnosis most consistent with an IDH-mutant glioblastoma. During the second craniotomy, high levels of 2HG in the tumor core biopsies were detected.

CONCLUSIONS This study demonstrates the capability to differentiate rapidly between IDH-mutant gliomas and IDH-WT conditions by DESI-MS during tumor resection. DESI-MS analysis of tissue smears is simple and can be easily integrated into the standard intraoperative pathology consultation. This approach may aid in solving differential diagnosis problems associated with low-grade gliomas and could influence intraoperative decisions regarding extent of resection, ultimately improving patient outcome. Research is ongoing to expand the patient cohort, systematically validate the DESI-MS method, and investigate the relationships between 2HG and tumor heterogeneity.

https://thejns.org/doi/abs/10.3171/2018.8.JNS181207

KEYWORDS intraoperative diagnosis; glioma; isocitrate dehydrogenase; 2-hydroxyglutarate; mass spectrometry; oncometabolite; oncology

Alfaro et al.

THE integrated diagnosis of gliomas includes morphological and grading criteria but relies heavily on molecular characteristics.[13] A point mutation in the isocitrate dehydrogenase (*IDH*) 1 or 2 gene is a major diagnostic and prognostic factor that is now used to classify infiltrative gliomas into 2 major subgroups: wild type (IDH-WT) or mutant (IDH-mutant).[18] The availability of such molecular information during glioma resection can improve diagnostic accuracy, personalize patient treatment, and might guide surgical decision making. Beiko et al.[2] found that gross-total resection of IDH-mutant glioblastoma (GBM) can provide a better survival benefit than gross-total resection of IDH-WT GBM.[2,4] Patel et al.[16] showed that maximal extent of resection provided a better outcome for low-grade IDH-WT gliomas than for low-grade IDH-mutant gliomas.[16]

Molecular testing for IDH mutations is typically performed postoperatively on a tissue biopsy sample collected during tumor excision. Hence, patients still undergo neurosurgical procedures without the benefit of a molecular diagnosis. Immunohistochemical staining and genetic sequencing are the gold-standard protocols. Several studies have reported more rapid immunohistochemical staining and genetic sequencing protocols with analysis times of approximately 30,[24] 60,[10,21] or 90 minutes,[14] but they have not found routine implementation in the intraoperative consultations.

Magnetic resonance spectroscopy imaging (MRSI) provides a preoperative and noninvasive means of assessing IDH mutation status by measuring 2-hydroxyglutarate (2HG), the downstream oncometabolite that accumulates in IDH-mutant gliomas.[1,5,26] For optimal discrimination between IDH-mutant and IDH-WT gliomas, MRSI studies have reported a cutoff 2HG concentration of 2 mM (or approximately 300 ng/mg).[26] The diagnostic sensitivity and specificity of MRSI methods are typically approximately 85%–88%,[26] which can be improved by using longer acquisition times and by acquiring more voxels from tumor areas. However, the high operational costs and long image acquisition time limit its routine implementation because the acquisition of MR images needed for neuronavigation creates a preoperative backlog.

Alternatively, recent studies have shown that IDH mutation status can be assessed via the mass spectrometry (MS) measurement of 2HG from tissue biopsies. Several MS-based 2HG assays have been reported, based on ionization with matrix assisted laser desorption ionization,[12] secondary ion mass spectrometry,[15] liquid chromatography (LC),[11] and direct infusion electrospray ionization (ESI).[27] Each method demonstrates encouraging preliminary performance in terms of sensitivity and specificity. Lower cutoffs for discrimination between mutant and WT gliomas have been reported with an accuracy of 100%.[27] However, the complexity of the instrumentation and sample preparation for these MS-based methods prevents the rapid turnaround times needed for intraoperative consultations.

Here, we describe the use of desorption electrospray ionization (DESI) as a point-of-care diagnostic tool for IDH mutation status assessment. DESI is an ambient ionization method, generating ions for MS analysis from fresh tissue smears without the need for fixation, washing, or matrix deposition.[25] DESI uses a spray of charged organic solvent droplets to impact a 2D surface (e.g., tissue section or smear), extract molecules from the sample in real time, and introduce them into the mass spectrometer for mass analysis. DESI-MS is advantageous in its simplicity, robustness, short analysis time, and capability for deployment in the operating room or a pathology laboratory. Some spray solvent systems, such as those employed herein, preserve tissue morphology, permitting subsequent H & E and immunohistochemical staining of the same DESI-MS–analyzed tissues for post hoc histopathological analysis.

In our recent work, a mobile DESI mass spectrometer was used to analyze brain tissue smears in the operating room, and preliminary capability to assess the extent of residual tumor at surgical margins was demonstrated, as well as detection of 2HG in IDH-mutant gliomas,[17] first reported by Santagata et al.[20] Previous work focused on detection of membrane phospholipids[8,9] and N-acetyl-aspartate[9] and their use in diagnosing tissue as normal brain or glioma and in estimating tumor infiltration at the surgical margins. An in-depth characterization of DESI-MS as an intraoperative diagnostic method for IDH mutation status has not been undertaken, and there is significant need for such a development. Here, we present an optimized DESI-MS method for the diagnosis of IDH mutation status via 2HG measurement from small tissue biopsies. The DESI-MS method was optimized in the laboratory using banked tissue sections and then applied in the operating room to determine IDH mutation status on the timescale of a few minutes as proof of concept.

Methods

Banked Tissue Specimens

All human subject research was conducted in adherence to ethics guidelines established by the IRBs of Purdue University and Indiana University School of Medicine. For DESI-MS method optimization, banked, fresh-frozen human brain tissue (n = 37) was obtained from the Methodist Research Institute Biorepository (Indianapolis) and used according to Purdue IRB protocol.

DESI-MS Method Development and Optimization

Method development experiments with banked tissue were performed using a home-built DESI ionization source and a commercial Thermo linear trap quadrupole (LTQ) mass spectrometer located at Purdue University (ThermoFinnigan). Normal brain, IDH-WT, and IDH-mutant glioma specimens were analyzed using a range of DESI spray solvents that contained dimethylformamide (DMF), acetonitrile (ACN), and ethanol (EtOH) in different proportions (Fig. S1) and MS conditions to optimize the detection of 2HG.

Glutamate, aspartate, N-acetylaspartate, and phosphocholine were also monitored using the method optimized for 2HG to investigate differential distribution between IDH-mutant and IDH-WT gliomas, as previously reported in the literature.[19] Experimental details for the MS method, sample preparation protocol, and DESI-MS analysis of
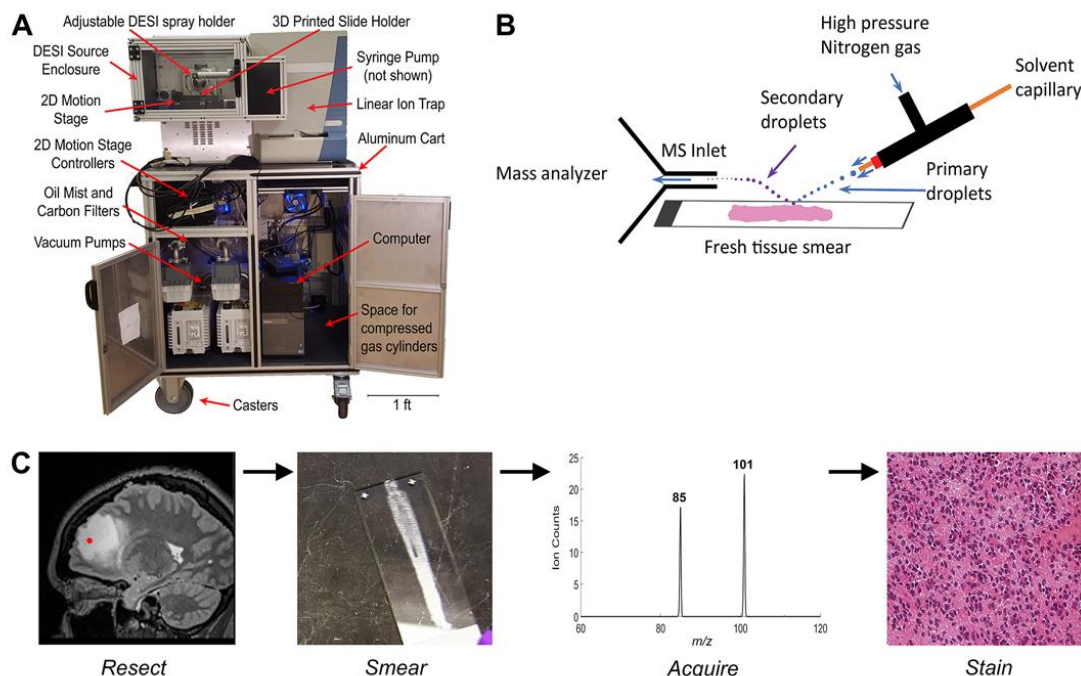
FIG. 1. DESI-MS method overview. **A:** Image of the custom-made intraoperative DESI-MS system for intraoperative analysis of tissue biopsies. **B:** Diagram of the DESI process as described by Takáts et al. **C:** Workflow of intraoperative analysis protocol consisting of tissue collection (*red spot*) and smearing, DESI-MS analysis, and post hoc histopathological staining. Original magnification ×20. Figure is available in color online only.

banked tissue specimens, are provided in the Supplemental Information.

Intraoperative Patient Cohort

The intraoperative study was conducted at the Methodist Hospital (Indianapolis) in adherence to the Indiana University IRB. Patients (n = 25) under the care of neurosurgeons at the Indiana University Department of Neurosurgery and Goodman Campbell Brain and Spine and undergoing tumor resection for a suspected glioma were recruited into the study (2017–2018) prospectively after providing written informed consent and Health Insurance Portability and Accountability Act authorization.

Intraoperative DESI-MS Detection of 2HG

The DESI-MS method optimized for detection of 2HG was adapted for rapid intraoperative analysis of tissue smears. A mobile stand-alone DESI mass spectrometer, previously built for use in the operating room, was used (Fig. 1A)[17] This instrument was the same model although a different physical unit from that used in the study of banked tissue; however, it was operated with the same DESI and MS conditions. The instrument was wheeled into the operating room for each surgical case, turned on and pumped down for 30 minutes, and used to analyze

multiple stereotactic tissue biopsies (tissue quantity < 3 mg) as they were resected within the standard-of-care workflow. Tissue smears were prepared inside the operating room using a custom 3D-printed device and a microscope glass slide, and they were immediately analyzed by DESI-MS. The data were analyzed using methods described in the Supplemental Information.

Assessment of IDH Mutation Status

DESI-MS assessment of IDH mutation status relied on detection of 2HG in tissue sections for the banked specimens (37 specimens, including 11 IDH-mutant and 26 IDH-WT gliomas) and for the intraoperative cases (51 biopsies from 25 patients; 11 IDH-mutant and 14 IDH-WT gliomas). Univariate ANOVA and receiver operating characteristic (ROC) curve analysis were performed using MATLAB (MathWorks) and JMP (SAS Institute, Inc.) data analysis software to estimate the quality of diagnosis using 2HG signals measured by DESI-MS (i.e., to distinguish between IDH-mutant and IDH-WT gliomas as independently determined by immunohistochemical staining/genetic sequencing).

The IDH mutation status was obtained from the final pathology reports of each patient for post hoc validation of the DESI-MS results. IDH1 R132H immunohistochemical

staining was initially performed; samples that provided a negative result were subjected to genetic sequencing of *IDH1* and *IDH2* genes according to the standard of care. Immunohistochemical analysis and genetic sequencing were performed at Indiana University Health Molecular Pathology Laboratory, certified under the Clinical Laboratory Improvement Amendments of 1988 to perform high-complexity clinical laboratory testing for clinical purposes.

Results

Correlation of 2HG DESI-MS Intensity With IDH Mutation Status in Banked Tissue Specimens

The optimized solvent system consisted of DMF-ACN-EtOH 25:37:38% vol/vol (Fig. S1). This solvent system efficiently extracted 2HG from brain tissue, and it did not destroy or alter the tissue morphology, permitting H & E staining and post hoc histopathology of the DESI-MS–analyzed tissue sections.

The 2HG was detected as a gaseous ion in the mass spectrometer at a specific mass-to-charge ratio (m/z) with an associated intensity. The 2HG ion was measured with high specificity by employing ion dissociation and detection of the resulting fragment ions; this procedure of isolation and fragmentation was performed twice. First, the precursor deprotonated ion, m/z 147 [M–H]$^-$, was isolated in the ion trap mass spectrometer and fragmented with collision-induced dissociation to produce a fragment ion peak at m/z 129, corresponding to a loss of 18 as H_2O from the intact 2HG precursor ion. The first product ion, m/z 129, was isolated and fragmented again, resulting in 2 additional product ions at m/z 85 and m/z 101. The peaks at m/z 85 and m/z 101 arose from structural losses of CO_2 and CO from the m/z 129 product ion, respectively. This overall process is referred to as an MS^3 product ion scan, and is shown schematically as 147→129→○, indicating that the m/z 147 ion is fragmented to produce m/z 129, and the m/z 129 ion is fragmented again and the fragments are detected. The fragmentation pathway is shown in Fig. S2.

We observed an approximately 40-fold change in m/z 101 signal intensity between IDH-mutant and IDH-WT gliomas, which was statistically significant (p < 0.0001). The absolute ion counts were normalized to the full-scan total ion counts and scaled by 1×10^6 (Table S1).

The signal of 2HG was significantly elevated in IDH-mutant glioma compared with IDH-WT specimens, despite differences in tumor density and smear cellularity, which was qualitatively assessed via post hoc H & E histology. De-identified pathology information and DESI-MS data for the banked tissue specimens are provided in Table S1. A representative set of DESI-MS ion images for an IDH-WT and an IDH-mutant tissue section is shown in Fig. S3A and S3B, respectively, along with the average 2HG product ion scans recorded (Fig. S3C and S3D).

In previous work, our laboratory quantified 2HG in human brain tissue extracts using MS,[27] and the concentration of 2HG was significantly elevated in IDH-mutant gliomas compared with WT (Fig. 2B). The tissue sections used for the optimization experiments reported herein were adjacent to the tissue used to prepare the tissue ex-

tracts used for quantitation,[27] and a high correlation (R^2 = 0.98) between the 2HG DESI signal and absolute concentration of 2HG was observed (Fig. 2A), which validates the effectiveness of DESI for real-time extraction of 2HG from fresh tissue.

In addition, we observed statistically significant differences in normalized aspartate (p = 0.004) and phosphocholine (p = 0.0008) intensities between IDH-WT and IDH-mutant samples using ANOVA (Table S2), consistent with that in recent studies showing significant alterations in the cellular metabolome due to the IDH mutation.[19] No statistically significant differences were measured in *N*-acetyl aspartate or glutamate signal intensity between IDH-WT and IDH-mutant gliomas.

IDH Mutation Status Determination During Glioma Surgery Using DESI-MS Monitoring of 2HG

In the intraoperative study, DESI-MS was used to monitor 2HG from tissue smears in near-real time during tumor resection. The optimized DESI-MS spray solvent (DMF-ACN-EtOH 25:37:38% vol/vol) was used, along with the same MS^3 product ion scan for 2HG (147→129→○). Instrument-specific parameters were optimized for the LTQ-MS used for the clinical study, and optimal values differed slightly from the LTQ-MS used for the banked tissue study (see Tables S3–S4).

The entire procedure, from tissue smearing to the end of data acquisition, took approximately 5 minutes per tissue biopsy. The number and size of the biopsy samples, as well as sampling areas, were decided at the discretion of the attending neurosurgeons. Typically, 2 biopsy samples were taken from the tumor core and 4 from the surgical margins. Only the tumor core biopsies were used in this study for the diagnosis of IDH mutation status. In total, 51 tumor core biopsies were provided by 25 patients (Table 1). The DESI process and the experimental procedure are recapitulated in Fig. 1B and 1C. De-identified clinical, pathological, operative, and radiological data are provided in Table 1 for the 25 patients enrolled in this portion of the study. Intensities of 2HG were averaged for the multiple tumor core biopsy samples collected from each patient. The DESI-MS 2HG product ion intensities were compared with the IDH mutation status from the patient's final pathology reports.

We observed about a 20-fold change in the average 2HG m/z 101 product ion intensity between IDH-WT and IDH-mutant samples (Fig. 2C, Table 1). Patient 22, a patient with GBM (WHO grade IV) with an IDH R132H mutation, had the highest signal detected for this patient cohort. Results were independent of the type of IDH mutation; 9 of 11 patients had IDH1 R132H mutation, 1 had an IDH1 R132C, 1 had an IDH1 R132X mutation, and no patient had IDH2 mutations (Table 1). The ROC area under the curve was equal to 1.0, indicating that no patients were misclassified. We observed large variance in 2HG intensity within and between the IDH-mutant samples. The intensity of 2HG is affected by differences in smear cellularity, thickness, and tumor density.[6,17,20] We observed a significant correlation between 2HG intensity and tumor cell percentage in the tissue smears (2-way ANOVA, p < 0.001; Table S2). The IDH-mutant gliomas yielded high-
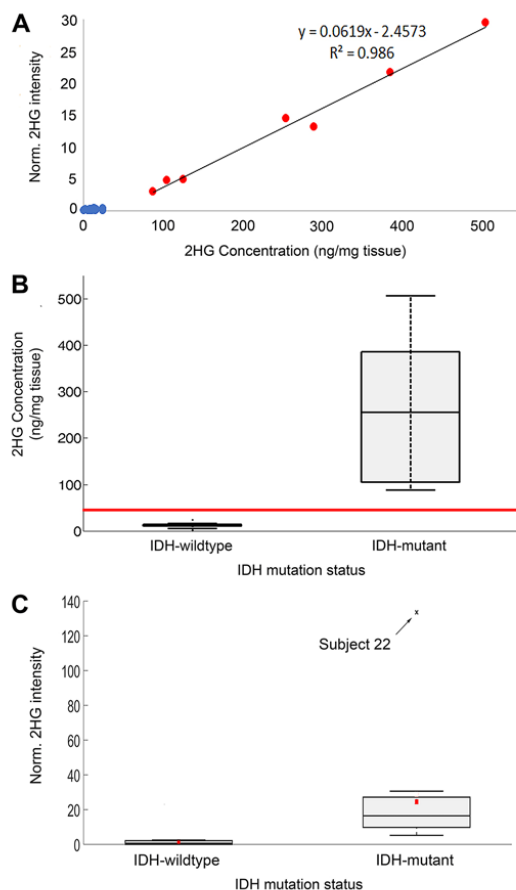
FIG. 2. C: Intraoperative discrimination between IDH-WT and IDH-mutant gliomas via DESI-MS 2HG measurement. Box-and-whisker plot obtained from the patient cohort of the intraoperative study. IDH-WT, n = 14; IDH-mutant, n = 11. The average 2HG signal intensity, ion transition m/z $147 \rightarrow 129 \rightarrow 101$, and normalized to the total ion count of the full scan, was plotted for each patient. The *box* represents the IQR with a median line and *whiskers* at ± 1.5 standard deviation. Mean values are shown as *red squares*. The outlier is shown as a *black x*. Signal intensities were significantly different (p < 0.0001). Zeros were assigned to the WT glioma specimens for which no 2HG was detected. Figure is available in color online only.

FIG. 2. Correlation of 2HG DESI-MS signal with 2HG concentration in the banked tissue specimens. **A:** Correlation between 2HG DESI-MS signal (normalized [norm.] relative to the full-scan total ion count), ion transition m/z $147 \rightarrow 129 \rightarrow 101$, and 2HG concentration (ng/mg tissue). Adjacent tissue from the same specimens was used to perform both measurements. Only 28 of the 37 samples were used for the quantitative analysis. The remaining samples were excluded due to insufficient tissue quantity. *Blue circles* indicate IDH-WT samples (n = 21); *red circles*, IDH-mutant samples (n = 7). Quantitative data are described by Yannell et al. and also appear in the Supplemental Information. **B:** Box-and-whisker plot for 2HG concentrations (ng/mg tissue) in human glioma tissue specimens (n = 28) analyzed using direct infusion ESI-MS/MS as described by Yannell et al.[27] The *box* represents the IQR with a median line and *whiskers* are at ± 1.5 standard deviation. Quantitative measurements were made using the MRM transitions m/z $147 \rightarrow 129$ for 2HG, and the signals were normalized by the MRM transition m/z $150 \rightarrow 132$ intensity of the added 2HG-d_3 deuterium isotope labelled internal standard. Random numbers between 0 and the limit of detection were assigned to IDH-WT glioma specimens for which no 2HG was detected. The *red line* shows the cutoff of 45 ng/mg tissue determined from ROC curve analysis. Reproduced with permission from Yannell KE, Smith K, Alfaro CM, Jarmusch AK, Pirro V, Cooks RG: N-acetylaspartate and 2-hydroxyglutarate assessed in human brain tissue by mass spectrometry as neuronal markers of oncogenesis. *Clin Chem* 63:1766–1767, 2017 ©American Association for Clinical Chemistry, 2018. **FIG. 2.** (*continued→*)

er 2HG intensity with increasing tumor cell percentage (TCP), which was roughly evaluated by histopathology and categorized in samples with low (< 34%), medium (about 34%–67%), and high (> 67%) TCPs (Fig. S4). The IDH-mutant samples of low TCP were statistically distinguishable from IDH-WT gliomas.

Intraoperative Determination of IDH Status in an IDH-Mutant Granular Cell Astrocytoma

Patient 17, a 35-year-old woman, had a syncopal episode and underwent brain MRI, which indicated a right frontal brain tumor. The patient provided consent for our DESI-MS study and underwent an initial craniotomy and biopsy for frozen sectioning and standard clinical diagnostic tests. Frozen-section histopathology during the intraoperative consultation indicated a possible demyelinating condition and no evidence of tumor. Therefore, no resection was performed, and no biopsies were provided for the DESI-MS study. Final pathological examination performed on the biopsied tissue revealed a granular glioma based on the permanent-section histology (formalin-fixed, paraffin-embedded H & E) as well as the presence of IDH1 R132H mutation and retention of ATRX nuclear expression (Fig. 3; Table 1). The patient then opted to undergo a second craniotomy for tumor resection exactly 1 week after the initial one. Three tissue biopsy samples were collected and analyzed intraoperatively using DESI-MS. Our DESI-MS method detected high 2HG product ion signals in tissue, indicative of an IDH mutation, with an average m/z 101 total ion count normalized 2HG fragment ion intensity of 30.6 for the 3 biopsy samples (Table 1). These results suggest that the DESI-MS method might have been able to confirm the glioma diagnosis during the initial craniotomy by providing intraoperative evidence of the presence of an IDH mutation.

Discussion

Several advantages are provided from intraoperative knowledge of IDH mutation status. First, the presence of an IDH mutation in a solid tumor is highly specific for glioma, regardless of other morphological or genetic characteristics. Second, a growing body of evidence shows that surgical strategies should be tailored based on IDH mutation status, in addition to other clinical and oncological factors.[2,16] Finally, decisions regarding patient management can be made with improved accuracy, especially in cases of IDH-mutant gliomas that provide unremarkable mor-

Alfaro et al.

TABLE 1. De-identified clinical, pathological, and MS data for patients enrolled in the intraoperative study

			Pathology					MS	
Patient No.	No. of Biopsies	Age (yrs), Sex	Final Diagnosis	IDH Mutation	1p/19q Codeletion	ATRX IHC	Ki-67 Labeling Index	m/z 85 Intensity*	m/z 101 Intensity*
1	2	58, M	GBM, WHO grade IV, IDH-WT	WT	NA	RNE	40%	1.4	0.0
2	2	47, F	GBM, WHO grade IV, IDH-WT	WT	NA	RNE	40%	0.0	0.0
3	2	46, F	Anaplastic astrocytoma, WHO grade III, IDH-mutant	R132H	ND	LNE	5%	6.9	9.5
4	2	63, M	Gliosarcoma, WHO grade IV, IDH-WT	WT	ND	NA	20%	0.3	2.3
5	2	53, F	Diffuse astrocytoma, WHO grade II, IDH-WT	WT	NA	RNE	1–2%	0.0	0.0
6	2	38, M	Diffuse astrocytoma, WHO grade II, IDH-mutant	R132C	ND	LNE	1–2%	2.3	5.2
7	2	68, M	GBM, WHO grade IV, IDH-WT	WT	NA	RNE	50%	0.3	0.0
8	2	54, F	GBM, WHO grade IV, IDH-WT	WT	NA	RNE	15–70%	0.0	0.0
9	2	20, M	Diffuse astrocytoma, WHO grade II, IDH-mutant	R132H	ND	RNE	10%	7.5	10.1
10	2	66, F	GBM, WHO grade IV, IDH-WT	WT	ND	RNE	3–5%	0.2	0.7
11	2	46, M	GBM, WHO grade IV, IDH-WT	WT	NA	RNE	30%	0.8	1.3
12	2	59, M	GBM, WHO grade IV, IDH-WT	WT	NA	RNE	30%	0.0	0.0
13	2	28, M	Diffuse mixed glioma, not high grade, IDH-mutant	R132H	ND	LNE	5–10%	6.7	13.6
14	2	59, M	Recurrent GBM, WHO grade IV, IDH-WT	WT	NA	NA	NA	1.7	2.1
15	2	57, F	GBM, WHO grade IV, IDH-WT	WT	NA	LNE	20%	0.4	1.0
16	2	26, F	Diffuse glioma, not high grade, IDH-mutant	R132H	NA	LNE	5%	5.7	10.4
17	3	35, F	GBM, WHO grade IV, IDH-mutant	R132H	NA	RNE	5%	24.7	30.6
18	2	30, M	Residual/recurrent low-grade glioma	R132X	ND	LNE	3%	8.5	12.0
19	2	66, F	Diffuse glioma	WT	NA	RNE	5–10%	2.0	1.1
20	2	48, M	Residual/recurrent anaplastic astrocytoma, WHO grade III, IDH-mutant	R132H	ND	LNE	3–5%	16.0	25.6
21	2	68, M	GBM, WHO grade IV, IDH-WT	WT	NA	RNE	10%	1.4	2.5
22	2	30, F	GBM, WHO grade IV, IDH-mutant	R132H	NA	NA	NA	89.8	133.5
23	2	61, M	GBM, WHO grade IV, IDH-WT	WT	NA	LNE	5–10%	3.2	0.0
24	2	27, M	Diffuse astrocytoma, WHO grade II, IDH-mutant	R132H	ND	NA	3–4%	13.4	19.3
25	2	68, M	GBM, WHO grade IV, IDH-mutant	R132H	NA	RNE	~10%	23.3	28.8

IHC = immunohistochemistry; LNE = lost nuclear expression (i.e., mutation detected); NA = not assessed; ND = not detected; RNE = retained nuclear expression (i.e., no mutation detected).
* Normalized intensities.

phological features on frozen-section H & E during the intraoperative consultation. In the instance of patient 17, misdiagnosis on frozen H & E–stained section during the first craniotomy was due to the granular subtype of glioma not being reliably differentiated from reactive macrophages.[22] This underlines the limitations of diagnosis based on cellular morphology from suboptimal preparations. A similar misdiagnosis on frozen section was reported in the case of a 14-year-old boy.[23] Such cases clearly demonstrate a need for more rapid and reliable molecular diagnostic tests that can be used concurrently with histopathology for intraoperative consultations; our DESI-MS method for assessment of IDH mutation status is one example.

It is worth noting that the absence of IDH mutation does not rule out diffuse glioma; additional molecular information may aid in the differential diagnosis of IDH-WT intracranial lesions and increase the accuracy of the intraoperative consultation. Previous work in our laboratory showed the ability to discriminate between tumor subtypes,[7,9] and we suggest that more extensive metabolic and lipidomic fingerprinting could allow differentiation of other primary CNS lesions as well. The incorporation of these additional molecular features has the potential to provide a significant contribution to intraoperative cancer diagnostics.

Lastly, the advantage of MS for IDH mutation assessment is that all IDH1 132/IDH2 172 mutants produce 2HG.[3,5,6] MS has the same versatility as genetic sequencing, but it provides a diagnosis in a much shorter timeframe. The tissue smear used for the DESI-MS 2HG assay could be stained with H & E alongside the frozen tissue sections used for the standard intraoperative consultation, and the microscopic observation of the tissue can corroborate its viability and adequacy for molecular testing or otherwise call for resampling. The DESI-MS methodology for IDH mutation assessment could be implemented as a standalone pathology tool that can be used to supplement frozen section analysis for intraoperative consultations.
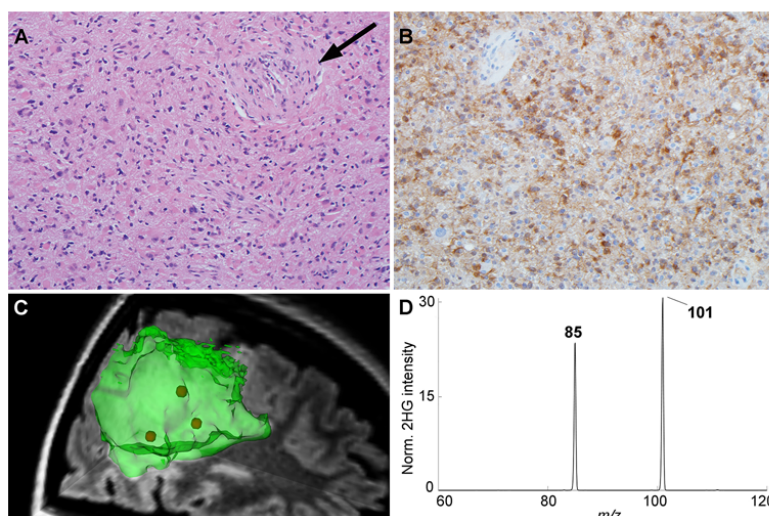
FIG. 3. Patient 17, who had an IDH-mutant glioblastoma. **A:** H & E–stained tissue. Original magnification ×200. A diffusely infiltrative, moderately cellular glioma made up of abundant gemistocytic astrocytes with moderate atypia. Note the presence of vascular proliferation (*arrow*) indicating high-grade nature. **B:** Immunohistochemistry for IDH1 R132H (clone H09; Dianova) showing diffuse cytoplasmic immunoreactivity, indicating the presence of IDH1 R132H mutation. Original magnification ×200. **C:** Reconstruction of tumor volume (*green*) using the preoperative MRI scans (T2-weighted 3D FLAIR), showing the location of tumor core biopsies (*dark objects*) analyzed by DESI-MS. Sizes of the biopsies are not to scale. **D:** Average 2HG product ion scan *m/z* 147→129→○ from the 3 analyzed biopsy samples. Figure is available in color online only.

Conclusions

This study reports diagnostic data and provides preliminary classification accuracy of a rapid DESI-MS method for intraoperative IDH assessment. This work goes beyond the mere detection of 2HG in IDH-mutant glioma and provides evidence that IDH mutation status can be accurately assessed from fresh tissue via DESI-MS detection of 2HG. The reported method is more sensitive, specific, and diagnostically accurate than previous DESI-MS methods. Furthermore, the analysis time of our method is sufficiently short to be used in the intraoperative consultation to provide quasi real-time feedback on IDH status. The 25-patient cohort included herein is somewhat limited, but our preliminary results are encouraging and supported by the strong extant literature on the oncometabolite 2HG. Future studies should aim to conduct multicenter clinical trials and extensive multi-institution proficiency test studies.

Acknowledgments

References

1. Andronesi OC, Kim GS, Gerstner E, Batchelor T, Tzika AA, Fantin VR, et al: Detection of 2-hydroxyglutarate in IDH-mutated glioma patients by in vivo spectral-editing and 2D correlation magnetic resonance spectroscopy. **Sci Transl Med 4:**116ra4, 2012
2. Beiko J, Suki D, Hess KR, Fox BD, Cheung V, Cabral M, et al: IDH1 mutant malignant astrocytomas are more amenable to surgical resection and have a survival benefit associated with maximal surgical resection. **Neuro Oncol 16:**81–91, 2014
3. Catteau A, Girardi H, Monville F, Poggionovo C, Carpentier S, Frayssinet V, et al: A new sensitive PCR assay for one-step detection of 12 IDH1/2 mutations in glioma. **Acta Neuropathol Commun 2:**58, 2014
4. Chen R, Ravindra VM, Cohen AL, Jensen RL, Salzman KL, Prescot AP, et al: Molecular features assisting in diagnosis, surgery, and treatment decision making in low-grade gliomas. **Neurosurg Focus 38(3):**E2, 2015
5. Choi C, Ganji SK, DeBerardinis RJ, Hatanpaa KJ, Rakheja D, Kovacs Z, et al: 2-Hydroxyglutarate detection by magnetic

resonance spectroscopy in IDH-mutated patients with gliomas. **Nat Med 18:**624–629, 2012

6. Choi C, Raisanen JM, Ganji SK, Zhang S, McNeil SS, An Z, et al: Prospective longitudinal analysis of 2-hydroxyglutarate magnetic resonance spectroscopy identifies broad clinical utility for the management of patients with IDH-mutant glioma. **J Clin Oncol 34:**4030–4039, 2016

7. Eberlin LS, Dill AL, Golby AJ, Ligon KL, Wiseman JM, Cooks RG, et al: Discrimination of human astrocytoma subtypes by lipid analysis using desorption electrospray ionization imaging mass spectrometry. **Angew Chem Int Ed Engl 49:**5953–5956, 2010

8. Eberlin LS, Norton I, Orringer D, Dunn IF, Liu X, Ide JL, et al: Ambient mass spectrometry for the intraoperative molecular diagnosis of human brain tumors. **Proc Natl Acad Sci U S A 110:**1611–1616, 2013

9. Jarmusch AK, Pirro V, Baird Z, Hattab EM, Cohen-Gadol AA, Cooks RG: Lipid and metabolite profiles of human brain tumors by desorption electrospray ionization-MS. **Proc Natl Acad Sci U S A 113:**1486–1491, 2016

10. Kanamori M, Kikuchi A, Watanabe M, Shibahara I, Saito R, Yamashita Y, et al: Rapid and sensitive intraoperative detection of mutations in the isocitrate dehydrogenase 1 and 2 genes during surgery for glioma. **J Neurosurg 120:**1288–1297, 2014

11. Kanamori M, Maekawa M, Shibahara I, Saito R, Chonan M, Shimada M, et al: Rapid detection of mutation in isocitrate dehydrogenase 1 and 2 genes using mass spectrometry. **Brain Tumor Pathol 35:**90–96, 2018

12. Longuespée R, Wefers AK, De Vita E, Miller AK, Reuss DE, Wick W, et al: Rapid detection of 2-hydroxyglutarate in frozen sections of IDH mutant tumors by MALDI-TOF mass spectrometry. **Acta Neuropathol Commun 6:**21, 2018

13. Louis DN, Perry A, Reifenberger G, von Deimling A, Figarella-Branger D, Cavenee WK, et al: The 2016 World Health Organization Classification of Tumors of the Central Nervous System: a summary. **Acta Neuropathol 131:**803–820, 2016

14. Ohka F, Yamamichi A, Kurimoto M, Motomura K, Tanahashi K, Suzuki H, et al: A novel all-in-one intraoperative genotyping system for IDH1-mutant glioma. **Brain Tumor Pathol 34:**91–97, 2017

15. Park J, Na HK, Shon HK, Son HY, Huh YM, Lee SW, et al: TOF-SIMS analysis of an isocitrate dehydrogenase 1 mutation-associated oncometabolite in cancer cells. **Biointerphases 13:**03B404, 2018

16. Patel T, Bander ED, Venn RA, Powell T, Cederquist GY, Schaefer PM, et al: The role of extent of resection in IDH1 wild-type or mutant low-grade gliomas. **Neurosurgery 82:**808–814, 2018

17. Pirro V, Alfaro CM, Jarmusch AK, Hattab EM, Cohen-Gadol AA, Cooks RG: Intraoperative assessment of tumor margins during glioma resection by desorption electrospray ionization-mass spectrometry. **Proc Natl Acad Sci U S A 114:**6700–6705, 2017

18. Pisapia DJ: The updated World Health Organization glioma classification: cellular and molecular origins of adult infiltrating gliomas. **Arch Pathol Lab Med 141:**1633–1645, 2017

19. Reitman ZJ, Jin G, Karoly ED, Spasojevic I, Yang J, Kinzler KW, et al: Profiling the effects of isocitrate dehydrogenase 1 and 2 mutations on the cellular metabolome. **Proc Natl Acad Sci U S A 108:**3270–3275, 2011

20. Santagata S, Eberlin LS, Norton I, Calligaris D, Feldman DR, Ide JL, et al: Intraoperative mass spectrometry mapping of an onco-metabolite to guide brain tumor surgery. **Proc Natl Acad Sci U S A 111:**11121–11126, 2014

21. Shankar GM, Francis JM, Rinne ML, Ramkissoon SH, Huang FW, Venteicher AS, et al: Rapid intraoperative molecular characterization of glioma. **JAMA Oncol 1:**662–667, 2015

22. Shi Y, Morgenstern N: Granular cell astrocytoma. **Arch Pathol Lab Med 132:**1946–1950, 2008

23. Søndergaard CB, Scheie D, Sehested AM, Skjøth-Rasmussen J: Finding of IDH1 R132H mutation in histologically nonneoplastic glial tissue changes surgical strategies, a case report. **Childs Nerv Syst 33:**1217–1220, 2017

24. Suzuki A, Maruyama T, Nitta M, Komori T, Ikuta S, Kawamata T, et al: Modified rapid immunohistochemical staining for intraoperative diagnosis of malignant brain tumors. **Brain Tumor Pathol 34:**141–148, 2017

25. Takáts Z, Wiseman JM, Gologan B, Cooks RG: Mass spectrometry sampling under ambient conditions with desorption electrospray ionization. **Science 306:**471–473, 2004

26. Tietze A, Choi C, Mickey B, Maher EA, Parm Ulhøi B, Sangill R, et al: Noninvasive assessment of isocitrate dehydrogenase mutation status in cerebral gliomas by magnetic resonance spectroscopy in a clinical setting. **J Neurosurg 128:**391–398, 2018

27. Yannell KE, Smith K, Alfaro CM, Jarmusch AK, Pirro V, Cooks RG: N-acetylaspartate and 2-hydroxyglutarate assessed in human brain tissue by mass spectrometry as neuronal markers of oncogenesis. **Clin Chem 63:**1766–1767, 2017

Disclosures

Author Contributions

Conception and design: Cohen-Gadol, Alfaro, Pirro, Hattab, Cooks. Acquisition of data: Alfaro, Pirro, Keating. Analysis and interpretation of data: Alfaro, Pirro, Keating. Drafting the article: Alfaro, Pirro, Hattab, Cooks. Critically revising the article: Cohen-Gadol, Hattab, Cooks. Reviewed submitted version of manuscript: all authors. Approved the final version of the manuscript on behalf of all authors: Cohen-Gadol. Statistical analysis: Alfaro, Pirro, Keating. Study supervision: Cohen-Gadol, Hattab, Cooks.

Supplemental Information

Online-Only Content

Supplemental material is available with the online version of the article.

  Supplemental Information. https://thejns.org/doi/suppl/10.3171/2018.8.JNS181207.

Previous Presentations

Portions of this work were presented in poster form at Translational Science 2018, Association for Clinical and Translational Science, April 20, 2018.

Correspondence

Aaron Cohen-Gadol: Indiana University School of Medicine, Indianapolis, IN. acohenmd@gmail.com.